RFSoC-Based Software-Defined Radio Systems for Frequency-Multiplexed Bolometer Readout

Zur Erlangung des akademischen Grades eines

DOKTORS DER INGENIEURWISSENSCHAFTEN (Dr.-Ing.)

von der KIT-Fakultät für Elektrotechnik und Informationstechnik des Karlsruher Instituts für Technologie (KIT)

angenommene

DISSERTATION von

DIPL.-ING. MANUEL E. GARCÍA REDONDO

geboren in: Daireaux, Argentina

Tag der mündlichen Prüfung:	27.05.2025
Hauptreferent:	Prof. Dr. Marc Weber
Korreferent:	Prof. Dr.-Ing. Manuel Platino

Karlsruher Institut für Technologie

UNSAM

RFSoC-Based Software-Defined Radio Systems for Frequency-Multiplexed Bolometer Readout

Para obtener el título académico de

DOCTOR EN CIENCIAS APLICADAS Y DE LA INGENIERÍA

de la Escuela de Ciencia y Tecnología de la Universidad Nacional de San Martín (UNSAM)

versión aprobada

DISERTACIÓN de

ING. MANUEL E. GARCÍA REDONDO

nacido en: Daireaux, Argentina

Fecha de la defensa oral:	27.05.2025
Director por UNSAM:	Prof. Dr.-Ing. Manuel Platino
Director por KIT:	Prof. Dr. Marc Weber

Karlsruher Institut für Technologie

UNSAM

Abstract

The Q & U Bolometric Interferometer for Cosmology (QUBIC) aims to detect the B-mode polarization of the Cosmic Microwave Background (CMB), which is one of the major challenges of observational cosmology. Given the extreme weakness of the signal to be observed, QUBIC proposes a novel Bolometric Interferometer. It combines the advantages of interferometry in terms of control of instrumental systematic effects with those of bolometric detectors in terms of Background-Limited Sensitivity (BLIP). To significantly enhance the sensitivity of the QUBIC instrument, its second phase proposes the use of a focal plane equipped with thousands of antenna-coupled Magnetic Micro-Bolometers (MMBs), multiplexed in the frequency domain by the novel Microwave SQUID Multiplexer (μMUX). The readout of thousands of bolometers multiplexed by means of the μMUX is a complex task that requires generating high-purity microwave signals over a broad bandwidth, as well as acquiring and processing them with minimal noise addition in order to avoid degrading the intrinsic sensitivity of the detectors. This is achieved through Software-Defined Radio (SDR) readout systems specially designed and optimized for such applications.

This thesis focuses on the development of two SDR prototypes for the multiplexed readout of MMBs, exploiting the unique features of Radio-Frequency System on Chip (RFSoC) platforms, which combine powerful processing systems with high-speed data converters. In the first part of this work, the functionalities and requirements of the SDR readout system are determined through simulations of both the MMBs and the μMUX. A dedicated simulation framework was developed to estimate the system's noise performance as a function of different readout parameters and the noise levels present in the SDR systems. From these results, the optimal readout parameters and maximum tolerable noise levels for MMB readout were determined. In the second part of this thesis, the development and evaluation of both proposed SDR prototypes is described. The first prototype, called the *Zero-IF SDR* prototype, is based on previous developments and utilizes the RFSoC together with an external frequency IQ Mixing board. The second prototype, titled the *Mixer-Less SDR*, takes advantage of the RFSoC's high-speed converters to directly generate and acquire signals in the GHz range. Both prototypes were characterized individually to determine their noise performance and then integrated into the readout and multiplexing system to demonstrate the readout of a μMUX device. The obtained results validate the outcomes from the simulation framework and demonstrate the feasibility of the SDR prototypes in MMBs readout, achieving the BLIP required for the next phase of the QUBIC project. The developed prototypes exhibit noise performance comparable to state-of-the-art SDR readout systems, while also providing a high level of integration, flexibility, customizability, and ease of use. These developments are in line with the latest SDR technologies and represent a significant contribution to the new generation of readout systems.

Zusammenfassung

Das Q & U Bolometrische Interferometer für Kosmologie (QUBIC) hat zum Ziel, die B-Modus-Polarisation des kosmischen Mikrowellenhintergrunds (CMB) zu detektieren, was eine der größten Herausforderungen der beobachtenden Kosmologie darstellt. Da das zu beobachtende Signal extrem schwach ist, schlägt QUBIC ein neuartiges bolometrischen Interferometer vor. Es kombiniert die Vorteile der Interferometrie in Bezug auf die Kontrolle instrumenteller systematischer Effekte mit denen bolometrischer Detektoren hinsichtlich der "Background-Limited Performance" (BLIP). Um die Empfindlichkeit des QUBIC-Instruments signifikant zu erhöhen, schlägt die zweite Phase des QUBIC-Experiments den Einsatz einer Fokalebene vor, die mit Tausenden von antennengekoppelten Magnetischen Mikro-Bolometern (MMBs) ausgestattet ist. Die Auslese von Tausenden von Bolometern, die im Frequenzbereich durch den neuartigen Mikrowellen SQUID Multiplexer (μMUX) gemultiplext werden, stellt eine komplexe Aufgabe dar. Diese Art der Auslese erfordert die Erzeugung von hochreinen Mikrowellensignalen sowie deren Verarbeitung mit minimaler Rauschbeimischung, um eine Verschlechterung der intrinsischen Empfindlichkeit der Detektoren zu vermeiden. Dies wird durch ein speziell für diese Anwendungen entwickeltes und optimiertes "Software-Defined Radio" (SDR)-Auslesesystem erreicht.

Diese Dissertation konzentriert sich auf die Entwicklung von zwei SDR-Prototypen für die multiplexierte Auslesung von MMBs. Dabei werden die einzigartigen Eigenschaften von "Radio-Frequency System on Chip" (RFSoC)-Plattformen ausgenutzt, welche leistungsstarke Verarbeitungssysteme mit Hochgeschwindigkeits datenwandlern kombinieren. Im ersten Teil dieser Arbeit werden die Funktionen und Anforderungen des SDR-Auslesesystems durch Simulationen der MMBs und des μMUX bestimmt. Ein spezielles Simulationsframework wurde entwickelt, um die Rauschleistung des Systems in Abhängigkeit von verschiedenen Ausleseparametern und den Rauschpegeln der SDR-Systeme abzuschätzen. Anhand dieser Ergebnisse wurden die optimalen Ausleseparameter und die maximal tolerierbaren Rauschpegel für die MMB-Auslese ermittelt. Im zweiten Teil dieser Dissertation wird die Entwicklung und Bewertung beider vorgeschlagener SDR-Prototypen beschrieben. Der erste Prototyp, genannt der *Zero-IF SDR*-Prototyp, nutzt das RFSoC gemeinsam mit einer externen Frequenz-IQ-Mischung. Der zweite Prototyp, das *Mixer-Less SDR*, nutzt die Hochgeschwindigkeitswandler des RFSoC, um Signale im GHz-Bereich direkt zu erzeugen und zu erfassen. Beide Prototypen wurden einzeln charakterisiert, um ihre Rauschleistung zu bestimmen, und anschließend in das Auslese- und Multiplexsystem integriert, um die Auslesung eines μMUX zu demonstrieren. Die Messungen validieren die Ergebnisse des Simulationsframeworks und demonstrieren die Machbarkeit der SDR-Prototypen für die MMB-Auslese, wobei die für die nächste Phase des QUBIC-Experiments erforderliche BLIP erreicht wurde. Die entwickelten Prototypen zeigen eine Rauschleistung, die mit der von modernen SDR-Auslesesystemen vergleichbar ist, und bieten gleichzeitig ein hohes Maß an Integration, Flexibilität und Anpassungsfähigkeit. Diese Entwicklungen stehen im Einklang mit den neuesten SDR-Technologien und stellen einen bedeutenden Beitrag zur neuen Generation von Auslesesystemen dar.

Resumen

El Q & U Bolometric Interferometer for Cosmology (QUBIC) tiene como objetivo detectar la polarización en modo B del Fondo Cósmico de Microondas (CMB, por sus siglas en inglés), uno de los principales desafíos de la cosmología observacional. Dada la extrema debilidad de la señal a observar, QUBIC propone un instrumento novedoso que combina las ventajas de la interferometría en términos de control de efectos sistemáticos instrumentales con las de los detectores bolométricos en términos de Sensibilidad Limitada por el Fondo (BLIP, por sus siglas en inglés). Para mejorar significativamente la sensibilidad del instrumento QUBIC, se propone el uso de un plano focal equipado con miles de Micro Bolómetros Magnéticos (MMBs) acoplados a antenas y multiplexados en el dominio de la frecuencia mediante el novedoso Multiplexor SQUID de Microondas (μMUX). La lectura de miles de bolómetros multiplexados mediante el μMUX es una tarea compleja que requiere la generación de señales de microondas de alta pureza sobre un amplio ancho de banda, así como su adquisición y procesamiento con mínima adición de ruido para evitar degradar la sensibilidad intrínseca de los detectores. Esto se logra mediante sistemas de lectura basados en Radio Definida por Software (SDR), especialmente optimizados para estas aplicaciones.

Esta tesis se centra en el desarrollo y evaluación de dos prototipos SDR para la lectura multiplexada de MMBs, aprovechando las características únicas de las plataformas Radio-Frequency System on Chip (RFSoC). Las mismas combinan potentes sistemas de procesamiento con conversores de datos de alta velocidad en un unico Sistema-en-Chip (SoC). En la primera parte de este trabajo, se determinan las funcionalidades y requerimentos del sistema de lectura SDR a través de simulaciones tanto de los MMBs como del μMUX. Se desarrolló un marco de simulación dedicado para estimar el rendimiento de ruido del sistema en función de diferentes parámetros de lectura y los niveles de ruido presentes en los sistemas de lectura SDR. A partir de estos resultados, se identificaron los parámetros de lectura óptimos y los niveles máximos de ruido tolerables para la lectura de MMBs. En la segunda parte, que constituye el núcleo de esta tesis, se describe la arquitectura de los dos prototipos SDR propuestos. El primer prototipo, denominado *Zero-IF SDR*, se basa en desarrollos previos y utiliza el RFSoC junto con una placa de conversión de frecuencias externa. El segundo,titulado *Mixer-Less SDR*, aprovecha los convertidores de alta velocidad del RFSoC para generar y adquirir directamente señales en el rango de GHz. Ambos prototipos fueron caracterizados de manera individual para determinar su rendimiento de ruido y luego integrados en el sistema de lectura y multiplexación para demostrar la lectura de un dispositivo μMUX. Los prototipos desarrollados exhiben un rendimiento de ruido comparable con los sistemas de lectura SDR de última generación, al mismo tiempo que ofrecen un alto nivel de integración, flexibilidad, personalización y facilidad de uso. Estos avances están en línea con las tecnologías SDR más recientes y representan una contribución significativa a la nueva generación de sistemas de lectura.

Acknowledgments

First and foremost, I would like to thank my thesis advisors, *Prof. Dr. Manuel Platino* and *Prof. Dr. Marc Weber*, for their guidance, support, and patience throughout this process. Their dedication, valuable advice, and constant motivation were crucial in overcoming difficult moments and bringing this long journey to a successful conclusion. The quality of their mentorship has been an inspiration to me. I am also immensely grateful to *Prof. Dr. Alberto Etchegoyen*, former head of the *ITeDA* institute, for providing me the opportunity to develop in an environment of excellence. His leadership enabled me to be part of the most important international projects, a truly invaluable experience.

I would like to extend my heartfelt gratitude to my colleagues at *ITeDA* and *IPE*, whose collaboration, support, and camaraderie have been invaluable throughout this journey. The many talented individuals at these institutes have generously shared their expertise and insights, and while it is impossible to name everyone, each of you has played a significant role in my work. It has been a true privilege to work alongside such a dedicated and knowledgeable group, and I am deeply grateful for the countless moments of learning, growth, and professional development, as well as the enjoyable and fun times of relaxation and friendship, which made the experience even more pleasant.

I am deeply grateful to my parents, *María Marta* and *Manuel Alfredo*, and my brother *Jonás*, for their love, understanding, and unwavering support throughout this journey. Their trust in me, along with the sacrifices they made to enable me to continue my studies, have been the cornerstone of my academic career. Without their encouragement, this work would not have been possible. I will be eternally thankful for their constant presence and belief in me.

I would also like to acknowledge the invaluable support provided by the doctoral programs *Helmholtz International School in Astroparticles and Enabling Technologies* and *Karlsruhe School of Elementary Particle and Astroparticle Physics: Science and Technology*, which have been essential to the development of my research and professional skills. The training and resources provided by these programs have been pivotal in shaping my academic path.

I am particularly grateful for the international collaborations in which I had the privilege to participate. Working with colleagues and researchers from *QUBIC Collaboration* has broadened my perspective, and their contributions have enriched this thesis in countless ways.

I would like to extend my sincere thanks to *Universidad Nacional de San Martín* and *Karlsruhe Institute of Technology* for providing the academic environment that enabled me to conduct research, contributing to both my professional and personal growth, as well as to the Argentinean institutions, the *Comisión Nacional de Energía Atómica* and the *Consejo Nacional de Investigaciones Científicas y Técnicas*, for granting me access to their resources, laboratories, and collaborative networks.

Finally, I would like to thank everyone who, in one way or another, contributed to this work, whether through emotional support, exchange of ideas, or direct collaboration. Each one of you has left an important mark on this process.

Contents

1. Introduction

According to the current dominant cosmological model, it is the scientific consensus that our Universe was born 13.8 billions years ago as a very hot and dense plasma, rapidly expanding and cooling down: this birth is commonly known as the Big Bang [1]. During the early ages, this plasma was so dense that light was tightly coupled to it and could not escape from it. According to this theory, when cooling, the Universe evolved from this very dense, optically thick state to a less dense and cooler state. The first atoms formed, and photons escaped: the Universe became transparent to light, 380 000 years after the Big Bang as can be seen in Figure 1.1. The first photons released are know as the Cosmic Microwave Background (CMB) and the moment when they escaped as the Last Scattering Surface. The photons that make up the CMB have travelled freely since that early time, and their wavelengths have been stretched with the expansion of the Universe to a few millimeters length, making them microwaves today. The CMB is almost smooth and uniform in all directions and its spectrum corresponds to a blackbody with an average temperature of 2.7 K, corresponding to the temperature of the initial plasma red-shifted by cosmic expansion. The observation and characterization of the CMB and its features is one of the major domain of interest in modern cosmology, providing cosmologists a wealth of information about the history, evolution, and contents of the Universe.

The CMB, the afterglow of the Big Bang, was first measured in 1964 by A. Penzias and R. Wilson [2] and since then, successive ground, balloon and satellite-based instruments have been improving its characterization [3, 4, 5, 6]. Today, several ongoing projects [7, 8] aim to make a leap forward in measuring the CMB with unprecedented precision, providing valuable new insights into a wide range of fundamental questions in physics. These measurements will enable the search for signatures of primordial gravitational waves, probe the nature of dark matter and dark energy, map the matter throughout the Universe, search for new light relic particles and set the neutrino mass scale [9].

1.1 Inflation and the Quest for B-modes

First observations of the CMB and of the Universe at large scale have led to huge breakthroughs in our comprehension of cosmic history, but have also brought new questions. Two main characteristics of our Universe are indeed that it is flat and isotropic [10, 11]. This means that its global geometry shows no curvature in the context of Einstein's general relativity and its properties are the same, regardless the direction of observation [12, 1]. However, according to the classic Big Bang model, regions of the sky separated by more than a few degrees should never have been in causal contact, so there is no particular reason for these regions to have a similar matter and energy content, or for the CMB to be almost uniform. Moreover, general relativity allows the Universe to have any curvature parameter between -1 (hyperbolic geometry) and 1 (spherical geometry), but experimental measurements yields zero curvature with a high level of confidence, which corresponds to the very particular case of flatness. In order to

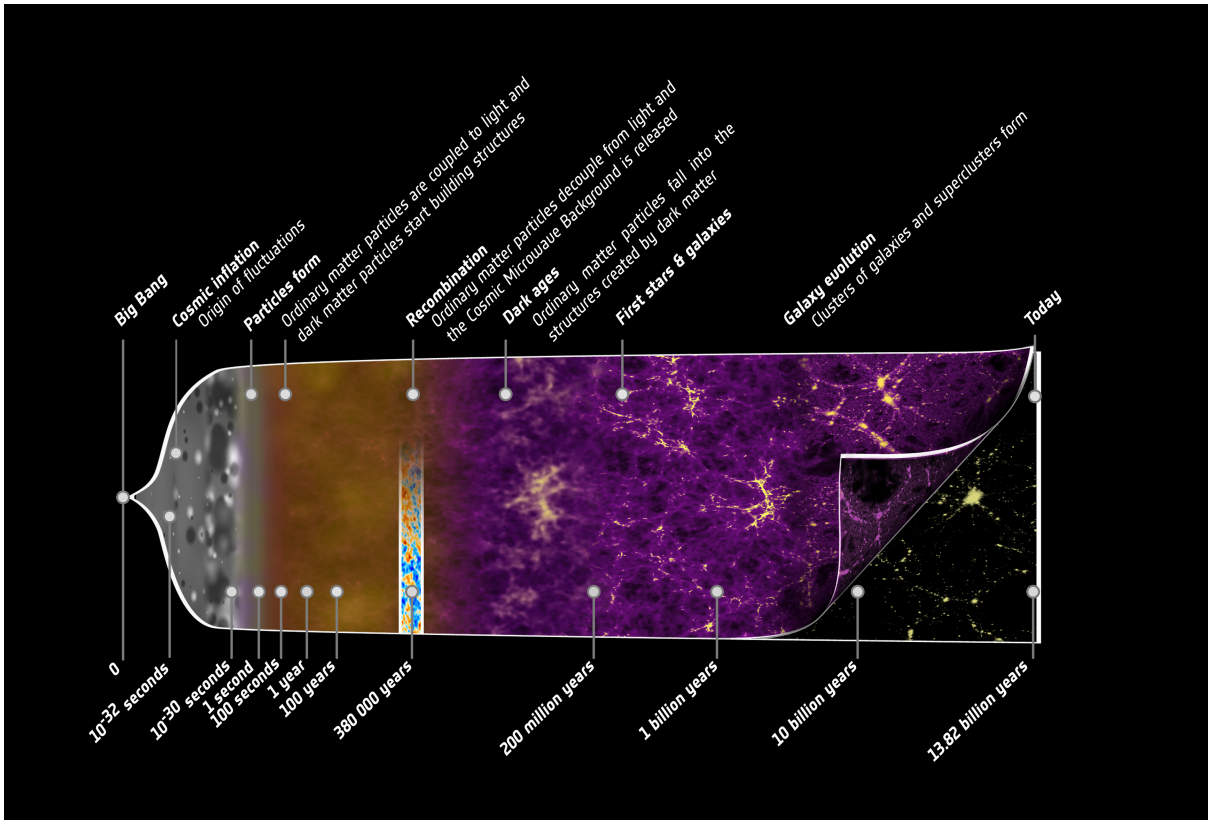

Figure 1.1: Evolution of the Universe since the Big Bang (Credit: European Space Agency).

answer these questions, an extremely short and rapid phase of expansion called *Inflation* was proposed [13]. This expansion would explain how regions of the sky could have been in causal contact even if they are far apart today, and also would have flattened the Universe. It would also explain how initial quantum fluctuations have been magnified to give birth to the actual large scale structures, such as galaxies and cluster of galaxies [9].

Observations of the CMB have provided several convincing arguments in favor of inflation [10, 14, 15, 16] but still there is a lack of direct observational evidence of inflation despite the 40 years that have passed since it was first proposed. One observable effect of Inflation is the generation of polarization B-modes in the CMB. In contrast to the E-mode polarization created by density fluctuations (scalar perturbations) in the early Universe, the intense gravitational waves during the exponential inflation (tensor perturbations) induced re-orientation of the primordial plasma. As a result, B-modes were imprinted in the CMB radiation as a subtle non-symmetric, rotational pattern of polarization across the sky. This symmetry in the polarization pattern gives the names to the E and B modes, based on their analogy with electric (E) and magnetic (B) fields. Measurement of B-mode polarization in the CMB would be clear evidence of the presence of primordial gravitational waves which are theoretically expected to be produced about 10^{-35} seconds after the Big Bang. Therefore, the quest for B-mode polarization of the CMB is among the main challenges in Observational Cosmology. A detection of this particular polarization pattern would open a completely new window into the physics of the early Universe and provide us with an additional relic left over from the hot big bang. This relic would constitute our most direct probe of the very early Universe and transform our understanding of several aspects of fundamental physics. However, as can be seen in Figure 1.2, primordial B-modes are extremely faint ($\Delta T/T \sim 10^{-7/-8}$), and their detection is even more challenging due to being overshadowed by various effects occurring along the line-of-sight between the last scattering surface and Earth. Some of them affect directly the CMB signal

while other are superimposed on the CMB signal, making it harder to distinguish from these external contaminants [9].

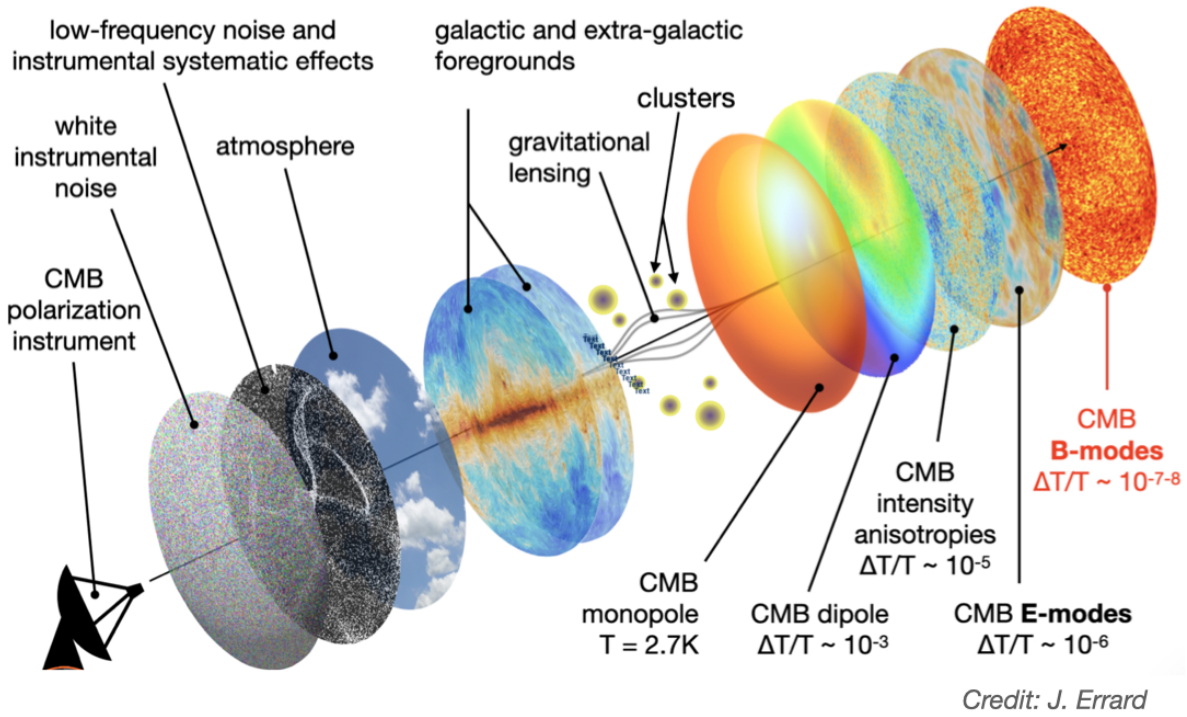

Figure 1.2: Illustration of systematic error sources in CMB B-mode detection (Credit: Josquin Errard).

CMB photons travelling to the present time interact with matter and are also affected by gravitational potentials creating the so called secondary anisotropies. The most important sources of secondary anisotropies from gravitational interactions comes from weak gravitational lensing of the CMB by galaxy clusters [17]. The effect of lensing is that it mixes CMB polarization E- and B-modes, and in particular it generates lensing B-modes from primordial E-modes that were created by scalar perturbations instead of tensor perturbations. This effect has thus to be carefully accounted for when looking for primordial B-modes, as the amplitude of lensing B-modes dominates those of primordial B-modes at the level that we are currently looking for. Another family of contaminants for precision measurement of the CMB comes from our very own galaxy. The Milky Way also emits in the sub-millimeter frequencies in which we observe the CMB. The main two contaminants are synchrotron radiation coming from electrons spiralling around galactic magnetic field, and thermal emission for interstellar dust. Even when choosing a clean patch of the sky away from the galactic plane, the low frequency synchrotron (dominant below 70 GHz) and the high frequency dust (dominant above 150 GHz) are very difficult to disentangle from the faint CMB signal. Locally on Earth, we are also affected by the atmosphere, as well as noise and contaminants coming from the instrument itself. Thus, detecting primordial B-modes is a complex instrumental and data analysis challenge of modern physics [18].

The next generation of ground-based CMB polarization experiments require: 1) Scaled-up superconductive detector arrays operated at extremely low temperatures with well-understood and robust material properties and processing techniques; 2) High-throughput mm-wave telescopes with low and high-angular resolution and optics with unprecedented precision and rejection of systematic contamination; 3) Full internal characterization of astronomical foreground emission; 4) A location for the experiment with an exceptionally stable and dry atmosphere; 5) Large cosmological simulations and theoretical modeling with accu-

racies yet to be achieved; and 6) Computational methods for extracting minute correlations in massive, multi-frequency data sets contaminated by noise and a host of known and unknown signals [18]. Some examples of ongoing and planned experiments are SPTPol [19], POLARBEAR [20], ACTPol [3], BICEP2 [21], CLASS [22], POLARBEAR2+Simons Array [23], advanced ACT [24], BICEP3/Keck array [25], Simons Observatory [8], PIPER [26], LSPE [27], CMB-S4 [7] and LiteBIRD [28].

1.2 The QUBIC Project

Among of the new generation of CMB polarization experiments, The *Q & U Bolometric Interferometer for Cosmology (QUBIC)* project proposes a novel kind of polarimeter optimized for the measurement of the B-mode polarization of the CMB. It combines the advantages of bolometers with high sensitivity and those of interferometers that have an excellent control of instrument systematic effects and signal identification. The interferometric nature of QUBIC (together with broadband observation and beam frequency dependence) also allows spectro-imaging and improved spectral resolution with respect to imagers, providing a significant advantage concerning foreground removal [29]. QUBIC is installed in its final observing site in Argentina. The site is located 4869 m a.s.l. in the Argentinean side of the Chajnantor-Plateau, in Alto Chorillos, province of Salta. This site has been studied for mm-wave astronomy for many years exhibiting excellent quality sky for CMB studies [30]. The QUBIC project is an international collaboration that involves universities, institutes and laboratories in France, Italy, Argentina, the United Kingdom and the United States of North America.

The use of bolometric interferometry to measure polarization B-modes in the CMB was proposed for a series of projects leading up to QUBIC [31, 32, 33, 34]. In order to achieve bolometric interferometry, QUBIC relies on an optical system consisting of back-to-back horns that select the relevant baselines and an optical combiner focusing on a bolometric focal plane. The optical combiner forms interference fringes while the bolometers average their intensity over timescales much longer than the period of the electromagnetic light. Being a bolometric device, the whole instrument operates at cryogenic temperatures thanks to a large cryostat [35]. A schematic of the design of QUBIC is shown in Figure 1.3. The sky signal first goes through a 56 cm diameter window made of plastic followed by a series of filters cutting off frequencies higher than the desired ones. The next optical component is a stepped rotating Half-Wave-Plate which modulates incoming polarization [36]. A single polarization is then selected thanks to a polarizing grid. Although reflecting half of the incoming photons may appear as a regrettable loss, it is in fact one of the key features of QUBIC for handling instrumental systematics, especially polarization-related ones. The following optical device in the chain is an array of 400 back-to-back corrugated horns. An array of mechanical shutters (RF switches) separates the two back-to-back horn arrangements in order to be able to close or open horns for self-calibration. Both front and back horns are identical, each with a field of view of 13 degrees Full Width at Half Maximum (FWHM) with secondary lobes below -25 dB [37]. The back-horns directly illuminate the two-mirror off-axis Gregorian optical combiner that focuses the signal onto the two perpendicular focal planes [38]. These are separated by a dichroic filter that splits the incoming waves into two wide bands centered at 150 GHz for the on-axis focal plane and 220 GHz for the off-axis one. The focal planes are each equipped with 1024 Niobium-Silicon (*NbSi*) Transition-Edge-Sensors (TES) cooled down to 300 mK using a sorption fridge [39]. A realistic view of the cryostat can be seen in the right panel of Figure 1.3. The cryostat has a height of approximately 1.6 meters and a diameter of 1.4 meters, weighing around 800 kg. With this unique instrument concept, the QUBIC project has the potential to make fundamental discoveries about the origin of our universe by detecting primordial gravitational waves and to open a new window into the early cosmos.

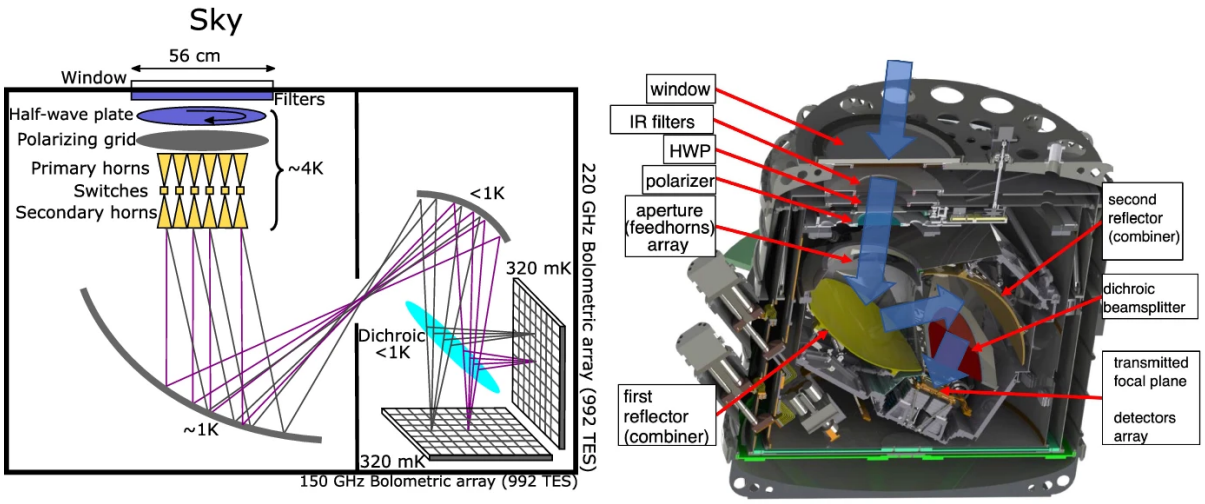

Figure 1.3: Left) Schematic of the QUBIC instrument and **Right)** Sectional cut of the cryostat showing the same sub-systems in their real configuration [40].

1.3 Upgrading the QUBIC Instrument

The QUBIC detection chain architecture is shown in Figure 1.4 each focal plane is composed of four 256-pixel arrays assembled together to obtain 1024-pixel *NbSi* Transition-Edge-Sensors. For each quarter focal plane, two blocks of 128 SQUIDs (Superconducting Quantum Interference Devices) are used at 1 K in a 128:1 Time Domain Multiplexing (TDM) scheme [41]. Each block is controlled and amplified by a full-custom ASIC cooled to 40 K while a warm FPGA board ensures the control and acquisition of the signal to the acquisition computer. Although the detection chain of the QUBIC project has demonstrated outstanding results in the first technical demonstrator [39], several drawbacks are still present limiting the full deployment of the system. One of them is the manufacturing of focal planes with their membrane-like bolometer, which due to their design complexity cannot be produced repetitively with high yield (more than 80%), thus limiting the number of useful pixels in the focal plane. Furthermore, this type of bolometer has a high time-constant due to it's massive suspended structure. This limits the scanning speed, and consequently, the scanning strategy. The cryogenic readout system makes use of commercial SQUIDs and ASICs located at 1 K and 40 K respectively, which are connected through superconducting ribbon cables to the detectors. With this scheme, not only the costs of superconducting ribbon *NbTi* cables are a strong limitation, it also imposes stringent requirements on the cryogenic systems responsible for cooling the SQUIDs and detectors to temperatures below 1 K. Additionally, the dichroic membrane, in charge of separating the observable frequency bands, lacks sufficient space for proper placement along the optical path. Thus, currently the instrument does not have the capacity to observe at multiple frequencies.

Since 2019, a group of researchers from the *Instituto de Tecnologías en Detección y Astropartículas (ITeDA)*, an active member of the QUBIC collaboration, have been working on the development of a new detection chain that overcomes the previously mentioned limitations and additionally extends the capabilities of the instrument. This new proposal pursues the development of three new key technologies: 1) Multichroic Antenna-Coupled Magnetic Micro-Bolometers (MMBs) [42], 2) A Multiplexing system in the frequency domain by means of the Microwave SQUID Multiplexer (µMUX) [43] and 3) A Software Defined-Radio readout system based on Radio-Frequency System-on-Chip devices (RFSoC) [44]. These three technologies comprise the next-generation detection chain and are being developed simultaneously. Throughout this thesis we will describe the development of each of these technologies and the advantages they offer over the existing detection chain. In particular, the work presented

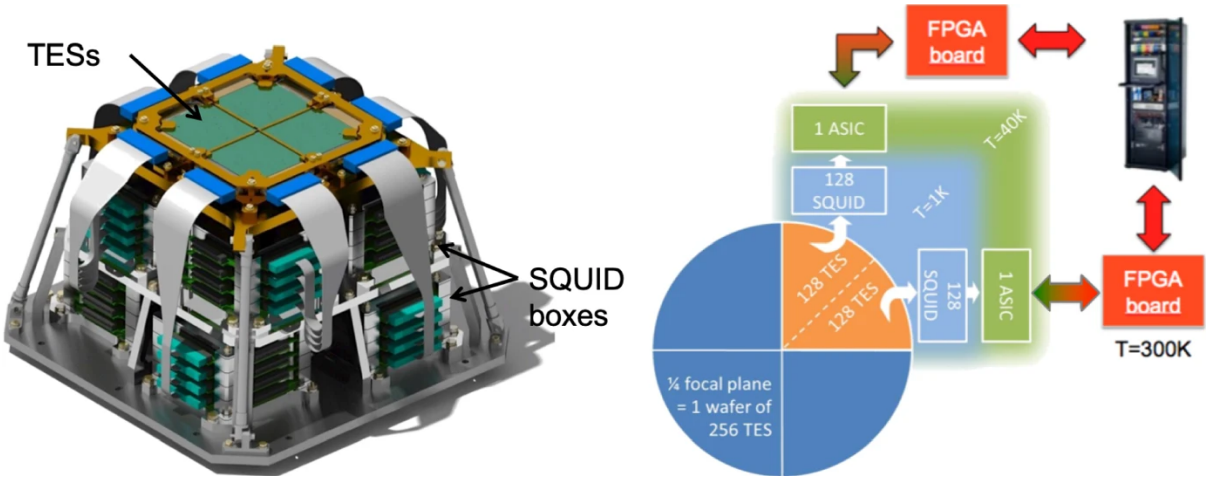

Figure 1.4: Left) QUBIC cryo-mechanical structure which supports one TES focal plane at 300 mK on top and the SQUID boxes at 1 K below. **Right)** Architecture of the QUBIC detection chain for one focal plane of 1024 channels [41].

along this document focuses on the Software-Defined Radio (SDR) systems for the multiplexed readout of MMBs using the µMUX and RFSoC devices [44]. The parallel development of these three technologies represents a great challenge not only because of the individual complexity, but also because of the strong connection between them. Thus, the doctoral research carried out had two clear objectives:

- First, understand and quantify the impact of the SDR system on the performance of the detection chain, and then define requirements based on the desired performance. Specifically, the focus will be on noise performance from the SRD readout point of view.
- Second, develop innovative SDR technologies that satisfy the requirements previously found by exploiting the unique characteristics of RFSoC devices.

The aforementioned developments were achieved in collaboration with the *Karlsruhe Institute of Technology (KIT)* under the program of Joint-Supervision of Doctoral Theses in Electrical Engineering and Information Technology between the *Department of Electrical Engineering and Information Technology (ETIT)* and the *Escuela de Ciencia y Tecnología (ECyT)* of the *National University of San Martin (UNSAM)*. This program is supported by the *Helmholtz International Research School for Astroparticle Physics and Enabling Technologies (HIRSAP)* and *The Karlsruhe School of Elementary Particle and Astroparticle Physics: Science and Technology (KSETA)*. Both graduate schools focused on the development and application of cutting-edge particle detection techniques and corresponding analysis methods in the fields of astronomy, astrophysics, elementary particle physics and cosmology. Geographically, the research was carried out mainly at the *ITeDA* facilities in the *Centro Atómico Constituyentes (CAC)*, part of the *National Atomic Energy Commission (CNEA)* of Argentina and partially at *Institute for Data Processing and Electronics (IPE)* over the course of two 9-month research stays. The fruitful collaboration with the KIT also involved the participation of the *Institute of Micro- and Nanoelectronic Systems (IMS)*. It is important to note that the developments presented are included in the framework of the development of superconductor-based quantum sensor systems and Data Acquisition (DAQ) systems for superconducting sensors and their application also extends to other projects which the *KIT* is part, for example, the Electron Capture ^{163}Holmium Experiment (ECHo) aiming to investigate the electron neutrino mass in the sub-eV range [45].

The thesis is structured following the waterfall approach shown in Figure 1.5. First, Chapter 1 presents the motivation for mapping the B-mode polarization and the proposed objectives to improve the capabilities of the QUBIC instrument. Second, Chapter 2 introduces the

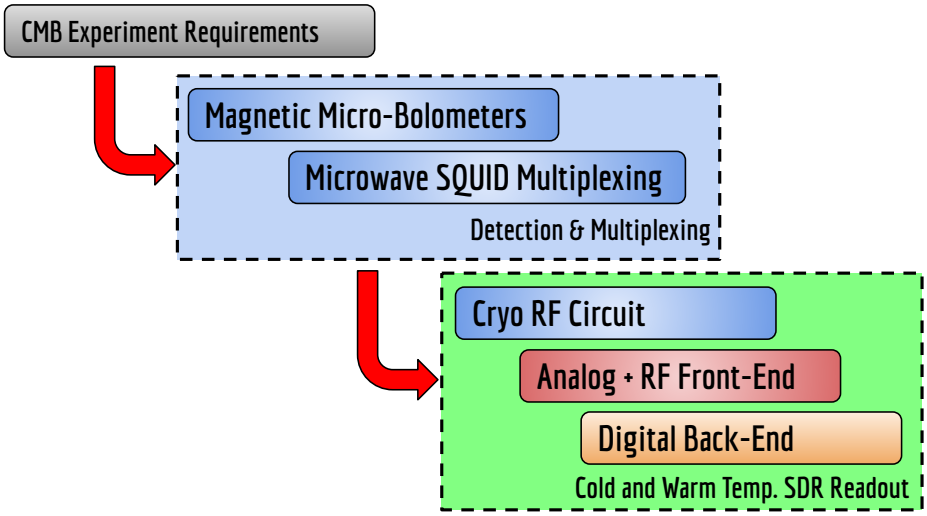

Figure 1.5: Waterfall structure for requirements extraction and development of the new detection chain for the QUBIC project.

sensitivity requirements for measuring the B-modes on the QUBIC instrument, the proposed Magnetic Micro-Bolometers (MMB), and their detection principles and properties. Next, Chapter 3 describes the frequency domain multiplexing scheme via the Microwave SQUID Multiplexer (μMUX), explaining its operating principle and advantages. Following this, the tasks that this work focuses on are discussed. Chapter 4 introduces the challenges of μMUX readout from the perspective of the readout system, its operation, and the associated noise sources. In Chapter 5, the readout scheme using SDR systems is presented, along with the implementation of two prototypes using the new Radio-Frequency System-on-Chip (RFSoC) technologies. Subsequently, Chapter 6 presents the experimental testing of the prototypes and compares the results with the requirements derived in the first three chapters. In Chapter 7, the SDR system is integrated with the cryogenic multiplexing system, and the readout demonstration is performed. Finally, conclusions are drawn based on the results obtained, and future research directions are discussed in Chapter 8.

2. Magnetic Micro-Bolometers for the QUBIC Project

The *Q & U Bolometric Interferometer for Cosmology (QUBIC)* project aims to measure the B-mode polarization of the CMB with unprecedented sensitivity. This is achieved with a focal plane equipped with thousands of ultra sensitive low-temperature bolometers. In this chapter, the basis properties of the CMB polarization and the required instrumental sensitivity are introduced. Later, the proposed Magnetic-micro-bolometers are presented as a technological solution, describing their working principle, properties and expected sensitivity.

2.1 CMB Anisotropies

The CMB is almost uniform, but nevertheless, it presents small variations in temperature and polarization. These variations can arise either from phenomena happening when CMB photons are emitted, called primary anisotropies, or from events happening between CMB emission and its detection on Earth, the secondary anisotropies. These small variations of temperature are more than five orders of magnitude smaller than the average blackbody temperature of 2.7 K and are due to initial density fluctuations in the early Universe where photons emitted by denser regions of the plasma have more energy than photons emitted by less dense regions. Temperature fluctuations of the CMB have been mapped with a high precision by the Planck satellite, as shown in Figure 2.1. CMB light is also polarized and shows polarization anisotropies that are even smaller than temperature anisotropies. Polarization anisotropies are created by Thompson scattering in the primordial plasma. The scattering of electromagnetic waves of different intensities by free electrons produces polarized light. This scattering can only happen when the plasma is thin enough to let light go through it, but there still needs to be free electrons (not recombined into atoms) to scatter the light. Therefore, only a small fraction (10%) of the CMB signal is polarized. Because the intensity of light coming from different directions is not the same, photons scattered in different regions of the sky do not result in the same polarization, creating polarization anisotropies as is represented by tiny black straight lines in Figure 2.1. These anisotropies find their origins in different physical processes, and cosmologists distinguish two types of resulting polarization: E-modes and B-modes [46].

Primary E-mode polarization is created by density fluctuations in the early Universe. These density fluctuations create a velocity gradient where photons are blue-shifted or red-shifted, and their scattering results in polarized light. The velocity perturbations are scalar, and create a symmetric, non-rotational pattern of polarization (curl-free even-parity) over the sky (see right side of Figure 2.1), called E-modes. E-modes have been detected and measured for the first time by the instrument DASI in 2002 [47], and since then have been studied by many experiments. The information content in this polarization probes the same cosmology and physical processes as temperature anisotropies. Contrary to E-modes, B-modes can only

be produced by tensor perturbations, which create a non-symmetric, rotational pattern of polarization (divergence-free odd-parity) as represented in Figure 2.1. Inflation is thought to have produced gravitational waves in the early Universe, thus generating B-modes polarization. The detection of primordial B-modes would therefore be a strong evidence for the existence of inflation [48].

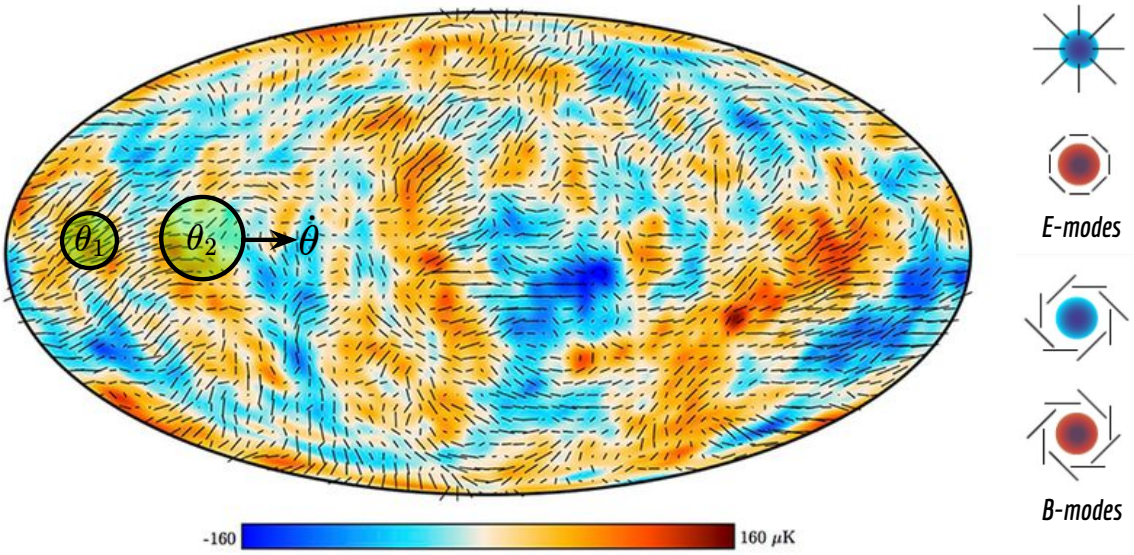

Figure 2.1: Left) Map of the CMB temperature and polarization anisotropies in the galactic coordinate system. θ_1 and θ_2 circles represent two different telescope angular scales while $\dot{\theta}$ the scanning speed. **Right)** Curl-free even-parity E-modes and divergence-free odd-parity B-modes decomposition of CMB polarization maps (Courtesy: Planck Collaboration).

2.1.1 B-mode Polarization Angular Spectrum

Useful CMB information is contained in the spatial intensity variations over the sky of the anisotropies in either temperature or polarization E or B-modes [46]. Similarly, a one-dimensional function can be represented by a Fourier series (i.e. sum of sines and cosines), any function on the surface of a sphere $f(\theta, \phi)$ can be written as a sum over complex functions on the sphere with well-defined wavelengths, the spherical harmonics $Y_{l,m}(\theta, \phi) = e^{jm\phi} \cos(\theta) P_l^m$. The azimuthal factor is simply $e^{jm\phi}$, while P_l^m are the Legendre Polynomials [12]. In this way, the B-mode polarization anisotropies $\Delta T^{BB}(\theta, \phi)$ can be represented in spherical harmonics through the following expression:

$$\Delta T^{BB}(\theta, \phi) = \sum_{l=0}^{\infty} \sum_{m=-l}^{l} a_{l,m} Y_{l,m}(\theta, \phi). \tag{2.1}$$

Here, θ and ϕ are the coordinates on the surface of the sphere (polar and azimuthal angles respectively), while l and m are the principal and azimuthal indices, respectively. $a_{l,m}$ are the coefficients of the spherical harmonics. The sum over l ranges from 0 to infinity and the sum over m ranges from $-l$ to $+l$. The angular distribution of the coefficients $a_{l,m}$ provides useful information about the properties and evolution of the early universe. The theory of the temperature fluctuations predict that each coefficient $a_{l,m}$ should have an average that depends only on l and the distribution of the values should be Gaussian [46]. Therefore, the

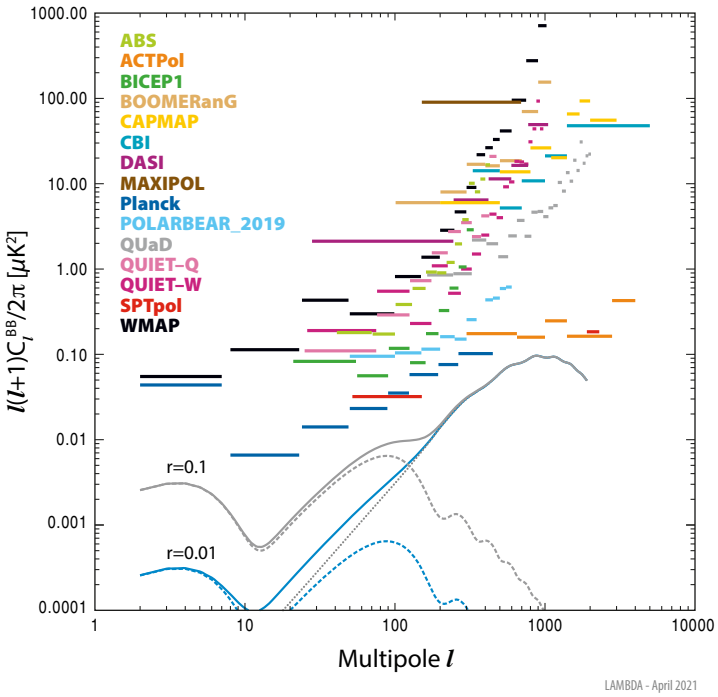

Figure 2.2: Upper limits for the B-mode power spectrum with 95% confidence level from different CMB experiments. For comparison, theoretical curves are shown for a ΛCDM model with tensor-to-scalar ratio $r = 0.1$ and $r = 0.01$. The gravitational lensing component is shown as a dotted curve and inflationary components are shown as dashed curves (Credit: NASA LAMBDA).

angular distribution of the B-mode polarization can be completely characterized by defining the following average:

$$C_l^{BB} = \langle |a_{l,m}|^2 \rangle = \frac{2\pi}{l(l+1)} \sum_{m=-l}^{l} |a_{l,m}|^2. \tag{2.2}$$

This is the B-mode polarization angular power spectrum C_l^{BB}. It characterizes the amplitude of the fluctuations as a function of the angular frequency l, also known as the multipolar number. The reciprocal of l corresponds to the angular scale called the angular fluctuation wavelength λ that gives typical sky spot size of $\theta \approx \pi/l$. For example $l = 10$ corresponds to roughly 20 degrees on the sky, while $l = 100$ corresponds to roughly 2. This is exemplified in the Figure 2.1 with two black circles, where θ_1 represents an angular resolution higher than θ_2 (i.e. $\theta_2 > \theta_1$).

The intensity of primordial B-modes is related to the energy scale of the inflationary process, and depends on the intensity of tensor perturbations compared to scalar perturbations [48]. The ratio between these two quantities, called the tensor-to-scalar ratio and usually denoted as r, is one of the crucial parameters that gives information about the intensity of the primordial gravitational waves, and is intended be to measured through B-modes. The B-mode power spectrum C_l^{BB} has been intensely measured by several experiments at different angular scales (see Figure 2.2). During the last decade, convincing several upper limits for the tensor-to-scalar ratio in the range $0.032 < r < 0.13$ have been measured, but these are still insufficient for the CMB community to distinguish between competing inflationary models with greater confidence[1]. In the case of improving only an order of magnitude the current limits, it would significantly advance our understanding of the inflation period. It potentially would discard the most popular and most widely studied models and dramatically impact the current cosmology theory.

[1] https://lambda.gsfc.nasa.gov/

2.1.2 Instrumental Sensitivity

The expected level of the B-mode signal is very low and therefore requires the development of highly sensitive instruments with low systematic errors specially designed to cover particular multipole l ranges. Accordingly with the Standard cosmological model (Lambda Cold Dark Matter or ΛCDM), decreasing the current upper limits of tensor-to-scalar ratio by an order of magnitude require improving the instrument sensitivity by one order of magnitude as well [9]. By examining the gray and blue dashed lines in Figure 2.2, it can be observe that a decrease in r from 0.1 to 0.01 results in a reduction of the power spectrum intensity, form $\frac{l(l+1)}{2\pi}C_l^{BB} = 5 \cdot 10^{-2}\mu K^2$ to $5 \cdot 10^{-3}\mu K^2$ for $l \approx 100$. The QUBIC project seeks to make a leap forward in instrumental sensitivity making use of bolometric interferometry to measure polarization B-modes [29]. This technique combines the advantages of an interferometer (i.e. spectral-imaging and self-calibration) with the amazing sensitivity of low-temperature bolometers. In the case of QUBIC bolometric interferometer, the variance ΔC_l^{BB} in the estimation of the B-mode power spectra C_l^{BB} is given by [49]

$$\Delta C_l^{BB} = \sqrt{\frac{2}{2l f_{sky} \Delta l}} \left(C_l^{BB} + 8 \frac{N_h}{N_t} \frac{NET_{BI}^2 \Omega}{N_{eq}^2} \right). \tag{2.3}$$

Where f_{sky} is the fraction of the sky accessible from the telescope, Ω is defined as the solid angle covered in the sky $\Omega = 4\pi f_{sky}$, Δl is the width of the l-space binning, N_h is the number of entry horns, N_{eq} is the number of equivalent baselines, N_t is the number of time samples, and NET_{BI} is the Noise Equivalent Temperature of the bolometric interferometer. Due to the fact that the CMB power spectrum is measured in terms of temperature fluctuations on the sky, it is useful for astronomers and physicist to express the instrumental sensitivity in temperature units. NET_{BI} is defined as the incident signal temperature that gives a signal-to-noise ratio of 1 in a 1 Hz output bandwidth and it is usually expressed in units of $\mu K/\sqrt{Hz}$ or $\mu K\sqrt{s}$. Most of the parameters of Equation 2.3 are fixed by the CMB statistical properties, the observation site, the sky scanning strategy, the observation period, and the optics of the instrument described in the Section 1.2. Therefore, they are not affected by the proposed upgrade in Section 1.3. However, this is not the case of the NET_{BI}, which is one of the most important parameters in the detection chain and a direct indicator of the instrumental sensitivity.

CMB polarization experiments are equipped with sensitive bolometers that measure the power of the incident radiation $P_{h\nu}$ directly. Therefore, power is a more suitable unit for instrument scientists and designers. Considering the CMB as a thermal radiation with black-body spectrum [50], it is possible to transform temperature fluctuations in power fluctuations using the following expression [51]:

$$NEP_{BI} = \frac{NET_{BI}}{\frac{\sqrt{2}\eta c^2 \Delta\nu}{\nu^2} \frac{\partial B_\nu(T_{CMB},\nu)}{\partial T}}. \tag{2.4}$$

Here, η is the instrument optical efficiency, c the speed of light in a vacuum, ν the frequency of the radiation, $\Delta\nu$ the spectral bandwidth and $B_\nu(T_{CMB},\nu)$ the spectral radiance of the CMB black-body temperature T_{CMB}. Analogous to NET_{BI}, NEP_{BI} is defined as the incident signal power that gives a signal-to-noise ratio of 1 in a 1 Hz output bandwidth and it is usually expressed in $aW/\sqrt{Hz}$. Commonly for a CMB instrument, NEP_{BI} is dominated by two noise sources. One is the photon or background noise $NEP_{h\nu}$ and the other is the intrinsic noise NEP_{det} of the detector itself. Since the two sources are not correlated, the total NEP_{BI} is calculated as a quadrature addition using [51]

$$NEP_{BI}^2 = NEP_{h\nu}^2 + NEP_{det}^2. \tag{2.5}$$

Background noise is produced by statistical fluctuations in the arrival of photons at the detector and generally is the dominant source in ground-Based CMB experiments. $NEP_{h\nu}$

depends on the average incoming optical power $P_{h\nu}$. Thus, in order to estimate it, all radiation sources incoming into the detectors need to be accounted. Optical components, as well as the atmosphere (for ground-based experiments) present a contribution to $P_{h\nu}$ corresponding to their emissivity, optical efficiency and spillover losses [52]. Once $P_{h\nu}$ is known, $NEP_{h\nu}$ can be calculated assuming a single-mode detector using [53]

$$NEP_{h\nu}^2 = 2h\nu P_{h\nu} + \frac{2P_{h\nu}^2}{m\Delta\nu}. \tag{2.6}$$

Here h is Planck's constant, ν is the radiation frequency, $\Delta\nu$ is the spectral bandwidth and m the number of polarizations detected. In the case of polarimetric measurements of the CMB, $m = 1$. For the QUBIC case study, which observes the sky in the frequency band of $\nu = 150$ GHz (radiance peak of the CMB) with a 25% of bandwidth ($\Delta\nu \approx 38$ GHz) and considering a typical aperture size of the instrument of 0.3 m, implying $\theta_{beam} = 0.39$ degrees at the central frequency, the calculated average incoming optical power is around $P_{h\nu} \approx 6$ pW. Hence, the estimated photon or background is $NEP_{h\nu} \approx 56$ aW$/\sqrt{Hz}$ [52]. This value of $NEP_{h\nu}$ is commonly reported in CMB instruments like QUBIC [39], POLARBEAR [20] and BICEP2 [21]. It is equivalent to $NET_{BI} \approx 120\ \mu K/\sqrt{Hz}$ calculated using Equation 2.4 and considering an optical efficiency of $\eta = 0.5$. This estimate is extremely important because it is the starting point for the design of the detection system. The design criterion used is

$$NEP_{det} \ll NEP_{h\nu}. \tag{2.7}$$

Typically, a factor of ten times smaller is sufficient to meet this criterion. Under this condition the detector is said to be background-limited. The sensitivity of a background-limited instrument can only be improved by increasing the integration time, either by planning longer experiments or increasing the number of detectors that measure simultaneously in the array (i.e. N_t in Equation 2.3). This is why, for CMB instruments, it is generally required to have both background-limited and scalable detectors. In this thesis, the design and contribution of each part of the detection chain to the NEP_{det} will be described satisfying the condition imposed by Equation 2.7. In the next section, the recently proposed Magnetic Microbolometers will be described as an improvement for the QUBIC detection chain.

2.2 Magnetic Micro-Bolometers

The current QUBIC detection chain architecture shown in Figure 1.4 uses a focal plane composed of four 256-pixel arrays of *NbSi* Transition-Edge-Sensors (TES). Nowadays, TES are the state-of-the-art for CMB detector arrays [41]. A TES is a resistive temperature sensor that consists of a superconducting structure made from a thin film superconducting material biased at its normal to superconducting state transition. This transition presents a sudden and abrupt drop in resistance to zero; therefore, small changes in temperature can be measured as large resistance variations. Even though these detectors are continuously used not only in CMB observations but various other applications, they do still present challenges when implemented in large detector arrays. The transition temperature, T_c, and critical current, I_c, of superconducting layers become difficult to control even in modern micro-fabrication facilities. Particularly in the case of QUBIC, the TES sensor is coupled to a massive metallic grid which is responsible for coupling the mm-wave radiation. This type of TES, called absorber-coupled TES, have two additional disadvantages. First, due to the mechanical weakness of the structure, it does not allow large-scale manufacturing with high yields. Second, the high volume of the metal absorber reduces the speed of the sensor [39].

As a solution to the aforementioned problems, a new detector technology called Magnetic Micro-bolometer (MMB) was proposed. It is the bolometric version of the well-known Magnetic Micro-calorimeters (MMCs) extensively used in the field of high-resolution X-ray

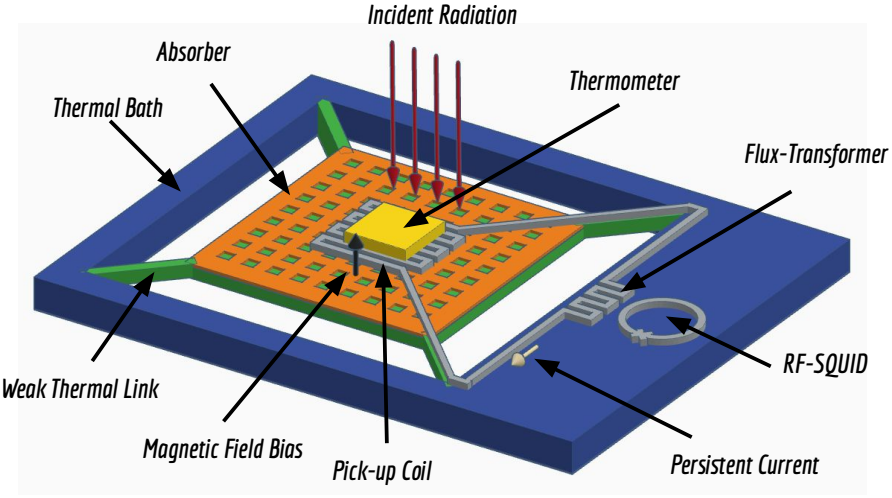

Figure 2.3: Schematic representation of a Magnetic Micro-bolometer consisting of a mesh-like mm-wave absorber and a paramagnetic temperature sensor.

spectroscopy and the investigation of the neutrino mass [45]. In order to understand this new technology, a comprehensive study of its working principle, characteristics and prototype design is presented in the next section following reference [42].

2.2.1 Working Principle

A Magnetic Micro-bolometer depicted in Figure 2.3 consists of an absorber or thermal mass that absorbs incident radiation power $P_{h\nu}$ and thermalizes the energy, a weak thermal link to a heat bath that keeps the absorber temperature at some defined value in the absence of a power input, and a thermometer in tight thermal contact to the absorber that measures its temperature increase ΔT given small variations in the incident power $\Delta P_{h\nu}$ [51]. In contrast to the TES, instead of using a resistive thermometer to measure the temperature change, the Magnetic Micro-bolometer uses a paramagnetic sensor that is biased with a weak dc-magnetic field B. Paramagnetic materials exhibit a magnetic field and temperature dependent magnetization $M(B,T)$; therefore, any change in sensor magnetization ΔM resulting from a temperature rise ΔT, induces a flux change $\Delta\Phi$ in associated superconducting pick-up coil with the sensor as its paramagnetic core. This flux change $\Delta\Phi$ can be measured through a Superconducting Quantum Interference Device (SQUID), which is a precise magnetometer capable of converting a magnetic flux signal into a voltage signal with quantum-limited accuracy [54] as will be described in further chapters. The flux change $\Delta\Phi$ is given by

$$\Delta\Phi \propto \Delta M = \frac{\partial M}{\partial T}\Delta T = \frac{\partial M}{\partial T}\frac{\Delta P_{h\nu}}{G_{\text{bath}}}. \tag{2.8}$$

The flux change $\Delta\Phi$ is determined by the thermal conductance of the weak thermal link G_{bath} and the slope of the magnetization curve $\partial M/\partial T$. In recent years, dilute alloys of gold (Au) or silver (Ag) as host materials that are doped with erbium (Er) have been established as state-of-the-art paramagnetic temperature thermometers for MMCs [55] and naturally adopted for MMBs. An in-depth study of the thermodynamic properties of the resulting alloys Au:Er or Ag:Er can be found in references [56] and [57] but they are mostly limited to temperatures below 100 mK and thus outside of the range where MMCs are typically operated. For this reason, several researchers within the *ITeDA* group have been developed a simulation framework to determine the thermodynamic properties of a Au:Er- or Ag:Er-based paramagnetic

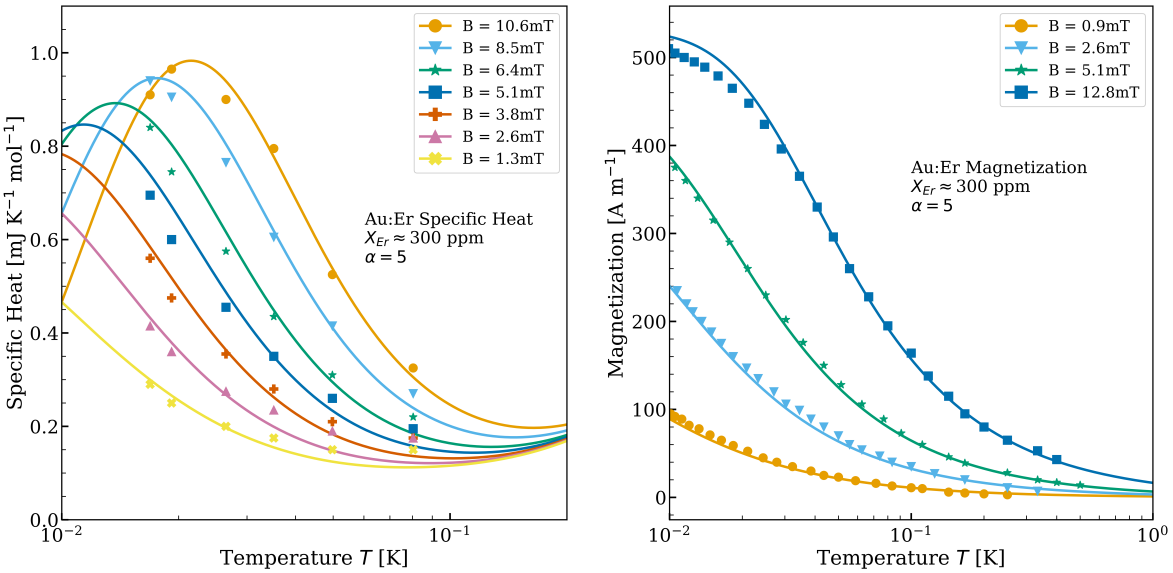

Figure 2.4: Left) Results of a Monte-Carlo calculation of the specific heat as a function of temperature. **Right)** Results of the simulation for the magnetization. The Au:Er sample has a concentration $x_{Er} \approx 300$ ppm and is biased with various magnetic fields B. Solid lines represent simulation results. The data points are taken from measurements presented in reference [57].

thermometer being operated in a bolometric application for CMB surveys (i.e. $T > 100$ mK). Figure 2.4 shows the specific heat $C_s(B,T)$ (left) and magnetization $M(B,T)$ (right) as a function of temperature and magnetic field for a paramagnetic sensor made out of Au:Er with an Er concentration of $x_{Er} \approx 300$ ppm. Solid lines correspond to the simulation results while dotted lines represent measurements taken from [57]. The specific heat shown also accounts for the free electron contribution. This electron component shows a linear dependence with temperature and can be estimated as $C_e = \gamma T$, where $\gamma = 6.9 \times 10^{-4} J \cdot mol^{-1} K^{-2}$ is the Sommerfeld constant of gold [58]. This realistic thermodynamic model of Au:Er or Ag:Er considers the influence of the interactions between the magnetic moments in the lattice and both mechanisms of spin-spin interaction, i.e. dipole-dipole (α) and RKKY interactions [56]. While the slope of the magnetization curve $M(B,T)$ sets how sensible the thermometer is, it cannot be dissociated from the specific heat curve $C_s(B,T)$. Both properties are proportional to the effective number of effective spins N_s in the paramagnetic material, so an increase in magnetization also represents an increase in specific heat. Therefore, the MMB design faces this trade-off between thermometer sensitivity and time response as will described below.

2.2.2 Detector Proprieties

CMB experiments impose two main constraints on the detectors, low response time τ and high responsivity or gain $\mathfrak{R}_{MMB}$. Fast response is required to avoid distortion of the point-source response of the telescope. CMB experiments are designed with a specific observation strategy depending on the mechanical limitations of the instrument, required angular scale resolution and avoidance of atmosphere $1/f$ noise, typically present in this type of observation. Therefore, it imposes the scan speed $\dot{\theta}$ at which the telescope must be slewed throughout the portion of the sky that is observed. In order to minimize distortion and satisfy the Nyquist-Shannon theorem, the time constant τ of the detector must be [59]:

$$\tau < \frac{\theta_{\text{beam}}}{2\pi\dot{\theta}}, \tag{2.9}$$

where θ_{beam} is the FWHM telescope beam-width and $\dot{\theta}$ the scanning speed. The time constant of a bolometer, i.e. the time the detector takes to return to heat bath temperature after switching off the constant power input $P_{h\nu}$, sets the speed of the bolometer and is given by

$$\tau = \frac{C_{\text{tot}}}{G_{\text{bath}}}. \tag{2.10}$$

Where the C_{tot} is the total bolometer heat capacity and G_{bath} the thermal conductance of the weak thermal link.

The MMB's responsivity $\mathfrak{R}_{MMB}$ accounts for the ratio between flux variation at the SQUID loop $\Delta\Phi_{\text{sq}}$ (i.e. the detector output) and the variation in the incoming power $\Delta P_{h\nu}$. A high responsivity value allows considerably higher signal levels compared to the noise sources present helping to achieve background-limited performance (BLIP). The MMB's responsivity $\mathfrak{R}_{MMB}$ is described by

$$\mathfrak{R}_{MMB} = \frac{\Delta\Phi_{\text{sq}}}{\Delta P_{h\nu}} = \frac{\partial T_s}{\partial P_{h\nu}} \frac{\partial \Phi_{\text{ft}}}{\partial T_s} \frac{\partial \Phi_{\text{sq}}}{\partial \Phi_{\text{ft}}}. \tag{2.11}$$

Each of the terms in the right side can be described in detail using the schematic shown in Figure 2.3. The first term in the right side correspond to the thermal steady-state dynamic response $\partial T/\partial P_{h\nu}(\omega)$ that describes how harmonic oscillations in incoming power with amplitude $\Delta P_{h\nu}$ and angular frequency ω are converted to variations in temperature ΔT in the paramagnetic thermometer. The thermal steady-state dynamic response of the bolometer can be derived from the differential equations that describe the linearized equivalent circuit model shown in Figure 2.5, arriving to the following expression:

$$\frac{\partial T_s}{\partial P_{h\nu}} = \frac{1}{G_{\text{bath}}} \left[1 - \frac{C_e C_s}{G_{\text{se}}}\omega^2 + \frac{C_s(G_{\text{bath}} + G_{se}) + C_e G_{se}}{G_{\text{bath}} G_{se}} j\omega \right]^{-1}. \tag{2.12}$$

Where G_{bath} and G_{se} are the thermal conductances between the thermal bath and the absorber, and between the absorber and the paramagnetic thermometer, respectively. C_e and C_s are the absorber and thermometer heat capacities, respectively. The choice of subscripts is based on the fact that the heat capacity of metallic absorbers at low temperatures is dominated by electron systems, while in paramagnetic materials by the spin systems. Generally, in a well-designed bolometer, dynamics are dominated by the absorber, since the absorber heat capacity $C_e \gg C_s$ and the thermometer is strongly linked to the absorber $G_e \gg G_{\text{bath}}$. Therefore, the time constant is $\tau \approx C_s/G_{\text{bath}}$. It is important to note from Equations 2.10 and 2.12 that decreasing the value of G_{bath} increases the thermal gain at the expense of increasing the time constant τ, representing an inherent trade-off between gain and speed when optimizing a bolometer.

The second term in Equation 2.11, $\partial\Phi_{\text{ft}}/\partial T_s$, characterizes how the temperature variation ΔT_s is converted to a change of sensor magnetization ΔM and consequently to a magnetic flux variation $\Delta\Phi_{\text{ft}}$. It is mostly determined by pickup coil geometry and the magnetic field distribution within the paramagnetic sensor. In most state-of-the-art MMCs the geometry used is a meander-shaped planar inductor as can be seen in 2.3. A persistent supercurrent, I_{field}, circulating through this superconducting coil magnetizes the sensor and simultaneously reads out flux variations. The factor $\partial\Phi_{\text{ft}}/\partial T_s$ is determined by integrating the magnetization's derivative with respect to temperature over the entire sensor volume using the following expression:

$$\frac{\partial \Phi_{\text{ft}}}{\partial T_s} = \int_V \frac{|\vec{B}(\vec{r})|}{I_{\text{field}}} \frac{\partial M}{\partial T}\bigg|_{|\vec{B}(\vec{r})|} d^3r. \tag{2.13}$$

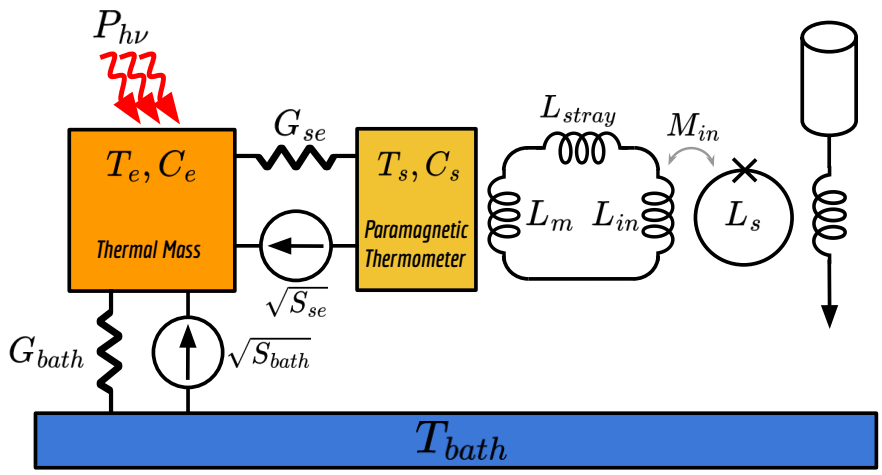

Figure 2.5: Schematics of the thermal model and readout scheme of a MMB. Incoming power $P_{h\nu}$ is absorbed by a thermal mass with heat capacity C_e that is therefore heated to a temperature T_e. This thermal mass is linked to a thermal bath with temperature T_{bath} by the weak thermal link G_{bath}. A paramagnetic temperature sensor with heat capacity C_s is strongly linked to the thermal mass by a second thermal link G_{se} and is heated to a temperature T_s. The paramagnetic thermometer signal is transduced by a superconducting pickup coil magnetically coupled to a sensitive rf-SQUID amplifier part of the multiplexing system. Additionally, the model includes the respective thermal noise sources, S_{bath} and S_{se}, related to the heat conductance.

Maximizing the flux response is also necessary and implies the optimization of the magnetic field distribution through the meandering inductor geometry (i.e. pitch p_m, linewidth w_m) as well as the sensor height h.

The last term in Equation 2.11 is the superconducting flux transformer transfer function $\partial\Phi_{\text{sq}}/\partial\Phi_{\text{ft}}$. It specifies the change of magnetic flux $\Delta\Phi_{\text{sq}}$ within the SQUID loop due to the change of magnetic flux $\Delta\Phi_{\text{ft}}$ threading the pickup coil. The superconducting flux transformer is created by the connection of the pickup coil with the SQUID input coil as can be seen in 2.5. Due to flux conservation in the superconducting loop, when $\Delta\Phi_{\text{ft}}$ changes, an excess current is generated preserving the flux value. This current, at the same time, produces a flux $\Delta\Phi_{\text{sq}}$ within the SQUID with value $\Delta\Phi_{\text{sq}}$ given by

$$\frac{\partial\Phi_{\text{sq}}}{\partial\Phi_{\text{ft}}} \approx \frac{k\sqrt{L_{\text{in}}L_{\text{s}}}}{L_{\text{m}} + L_{\text{stray}} + L_{\text{in}}}. \tag{2.14}$$

Where L_m is the inductance of the pickup coil, L_{in} is the SQUID's input coil, L_s is the SQUID's loop inductance, k is the coupling factor between L_{in} and L_s. L_{stray} is the parasitic inductance derived from the superconducting lines and wire bonds that connects the detector to the readout circuit.

2.2.3 Noise Sources

As outlined in Section 2.1.2, the detector noise contributions need to be estimated in order to decide whether the instrument will be capable of performing BLIP detection on the sky. The main contributions that must be considered for the MMB are the Thermodynamic Fluctuation Noise (TFN), magnetic Johnson noise, Erbium $1/f$ excess noise and readout noise. These contributions referred to the detector input (i.e. where radiation $P_{h\nu}$ is impinging) result in

$$NEP_{\text{det}}^2 = \frac{S_{\text{th}}}{\left|\frac{\partial T_s}{\partial P_{h\nu}}\right|^2} + \frac{S_{\text{J}}}{\left|\frac{\partial T}{\partial P_{h\nu}}\frac{\partial \Phi}{\partial T_s}\right|^2} + \frac{S_{\text{Er}}}{\left|\frac{\partial T_s}{\partial P_{h\nu}}\frac{\partial \Phi}{\partial T_s}\right|^2} + \frac{S_{\text{read}}}{\left|\frac{\partial T_s}{\partial P_{h\nu}}\frac{\partial \Phi_{\text{ft}}}{\partial T_s}\frac{\partial \Phi_s}{\partial \Phi_{\text{ft}}}\right|^2}. \tag{2.15}$$

The terms $S_{\text{th}}(f)$, $S_{\text{J}}(f)$, S_{Er} and $S_{\text{read}}(f)$ denote the spectral densities of the respective noise sources. The factors in the denominators correspond to the gains between the detector input and the point of the circuit where the noise source is located. Regarding the TFN, there are two contributions: one represents the thermal fluctuation of phonon energy in the thermal link due to the heat bath $S_{\text{bath}}(f)$, and the other the phonon energy fluctuations between the conduction electrons and the spin subsystems within the sensor $S_{\text{e}}(f)$. Both are represented as current sources in the electro-thermal equivalent circuit depicted in Figure 2.3. The phonon noise spectral density $S_{\text{bath}}(f)$ is given by [60]

$$S_{\text{bath}}(f) = 4\epsilon k_B T^2 G_{\text{bath}}. \tag{2.16}$$

where k_B is the Boltzmann constant and ϵ is a numerical factor derived for materials at low temperatures that depends on the geometry and heat transport proprieties of the thermal link. In the case of weak thermal link made of Si_3N_4 at $T_{\text{bath}} < 300$ mK there is only phonon transport of heat and no electronic contribution, therefore $\epsilon = 3$. The energy fluctuations between the conduction electrons and the spin subsystems can be modeled and estimated by a similar method, arriving to the following expression [57],

$$S_{\text{e}}(f) = 4k_B T^2 G_{\text{se}}. \tag{2.17}$$

The second noise source affecting the MMB is produced by the thermally excited random movement of conducting electrons in the paramagnetic sensor, generating a fluctuating magnetic field that couples to the pickup coil seemingly as a part of the measured signal. It is called Magnetic Johnson Noise and its spectral density can be calculated as [57],

$$S_{\text{J}}(f) = \mathfrak{K}\sigma k_B T. \tag{2.18}$$

Here $\mathfrak{K}$ is a constant that depends on the geometry of the detector, σ is the electrical conductance of the paramagnetic sensor and T is the sensor temperature.

As an extra noise source, each erbium ion in the sensor presents a fluctuating magnetic moment in the form of flicker noise, the origin of this magnetic fluctuation is not fully understood to date and is experimentally determined to be independent of temperature. Since it is a flicker noise it appears predominantly at low frequencies following a $1/f$ shape. It is commonly referred to as erbium $1/f$ excess noise. The spectral density of this contribution is given by

$$S_{\text{Er}}(f) = N_{\text{Er}} \frac{|\vec{B}(\vec{r})|^2}{I_{\text{field}}^2} S_m(f). \tag{2.19}$$

N_{Er} stands for the number of erbium ions in the sensor and $S_m(f)$ stands for the spectral density noise power of the vertical component of the magnetic moments of the erbium ions, $S_m(f) = 0.12\mu_B^2/f^\eta$ where η is in the range of 0.8 to 1, μ_B is the Bohr Magneton [55].

Finally, the last contribution $S_{\text{read}}(f)$ corresponds to the noise spectral density of the multiplexing and readout system. For this thesis the proposed multiplexing and readout system consist of the Microwave SQUID multiplexer (μMUX) and the associated Software-Defined Radio readout system. This is the most important contribution regarding this thesis and defines the requirements of the system (see Figure 1.5). Similarly to Equation 2.7 and taking into account that the denominator in the last contribution is $\mathfrak{R}_{MMB}^2$, the following design condition can be defined for the multiplexing and readout system:

$$S_{\text{read}}(f) \ll S_{\text{det}}(f) = NEP_{\text{det}}^2 \Re_{MMB}^2. \tag{2.20}$$

Equivalently, this condition means that the readout contribution is much smaller than the rest of the detector noise contributions (i.e. TFN, Johnson, 1/f). At this point a clarification should be made in order to avoid misuse of the nomenclature and confusion in units used to express the noise. Strictly, the spectral flux density S_Φ is expressed in Φ_0^2/Hz. However, within the low-temperature detector community flux noise is mostly expressed using $\sqrt{S_\Phi}$ which is expressed in $\mu\Phi_0/Hz$. It is equivalent to the NET, NEP and could be defined as the Noise Equivalent Flux. This unit allows for quick conversion between different units such as current, power and temperature and will be the unit of choice in later chapters when expressing flux noise level. In the next paragraphs a numeric estimation for Equation 2.20 is derived based on the proposed MMB prototype's parameters.

2.2.4 Detector Prototype

The bolometer design chosen for the first prototypes is an antenna-coupled bolometer. Its simplified diagram is shown in Figure 2.6. In contrast to the absorber-coupled bolometer shown in Figure 2.3, the proposed bolometer uses a wide-band antenna that couples the mm-wave radiation. Using a pair of transmission lines, the electrical signal is guided to a series of diplexers. These devices not only split the signal, but also define the desired frequency bands. The different transmission lines are routed to the central part of a suspended H-like structure, where the electrical signal is dissipated in a matched resistor, thermalized and finally measured by a paramagnetic thermometer as described in [42]. Unlike the absorber-coupled bolometer currently used in QUBIC, this new type of bolometer presents several advantages. First, the H-like structure does not primarily serve to electromagnetically couple the radiation, and therefore its dimensions are not determined by the radiation wavelength $\lambda_{h\nu}$. Therefore, the suspended H-like structure is considerably smaller representing less manufacturing complexity than the absorber membrane. The reduction in size also means heat capacity reduction and implies a faster detector. Second, this scheme is multichroic, i.e. allows to measure simultaneously several frequency bands and polarizations depending on the antenna and filters configuration, without the need for a dichroic membrane. These characteristics make the MMBs suitable for foregrounds removal in the next generation of CMB experiments [61, 62].

The design parameters of the first antenna-coupled MMB prototype were taken from reference [42] and are summarized in Table 2.1. Niobium (Nb) is the superconductor of choice for these devices, silicon oxide (SiO_x) for the insulator and silicon nitride (Si_3N_4) for the suspended structure. Considering a thermal bath temperature of $T_{bath} = 250$ mK, corresponding to the base temperature of cryostats commonly used in CMB experiments, the H-like structure is suspended using four legs with a length of $l_{\text{bath}} = 700$ µm and cross-sectional area $A_{\text{bath}} = 30$ µm^2. The paramagnetic sensor is a volume of $Au{:}Er$ with an Er concentration of $x_{Er} \approx 1000$ ppm that will lie over a meander-like superconducting pick-up coil with a linewidth of $w_m = 2.5$ µm and a pitch of $p_m = 5$ µm. An insulating SiO_x layer of 300 nm separates the sensor from the pick-up coil. The sensor itself would have an area of $A = 180 \times 180$ µm^2 and a height of $h = 1$ µm while the selected magnetic bias field current is $I_{\text{field}} = 100$ mA as used in other MMC designs [63]. The pickup coil design was optimized based on the detector input characteristics of the rf-SQUIDs used by the proposed multiplexing system. The rf-SQUID presents an input inductance $L_{in} = 2$ nH, self-screening inductance $L_s = 50$ pH and a coupling factor $k = 0.57$. For the first designs, the wire stray inductance was neglected. A detailed analysis of the multiplexing system will be presented in the following chapter.

The simulation results for the MMB prototype described in Table 2.1 are shown in Figure 2.7. All different noise contributions can be referred to any part of the system, here, each source was referred to the input using Equation 2.15. Another point commonly used

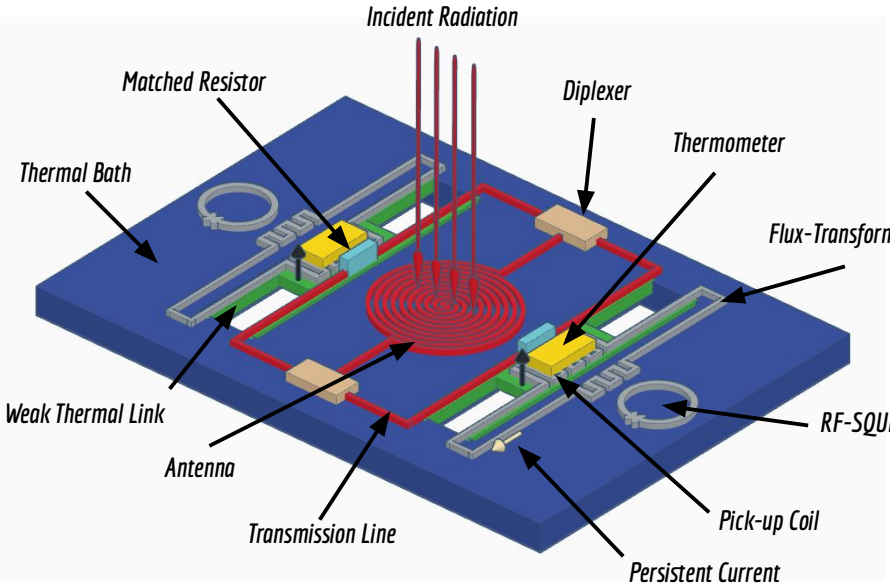

Figure 2.6: Schematic representation of a multichroic antenna-coupled Magnetic Micro-bolometer. It consists of a planar antenna that couples radiation onto a microstrip transmission line terminated with a matched resistor thermally coupled to a paramagnetic sensor.

Table 2.1: Antenna-coupled Magnetic Micro-Bolometer prototype design parameters.

Parameter	Symbol	Value	Unit
Thermal link length	l_{th}	700	μm
Thermal link area	A_{th}	30	μm^2
Au:Er thermometer dimensions	$l \times l$	180×180	μm
Au:Er sensor height	h	1	μm
Au:Er thermometer concentration	x_{Er}	1000	ppm
Meander width	w_m	2.5	μm
Meander pitch	p_m	5	μm
Persistent current	I_{field}	100	mA
rf-SQUID self-screening inductance	L_{s}	30	pH
rf-SQUID input inductance	L_{in}	2	nH
Coupling factor	k	0.57	-

to compare the equivalent noise contributions, and more convenient for multiplexing system designers, is the flux threaded within the SQUID. The noise at the SQUID loop is characterized by the flux-noise spectral density $S_\Phi(f)$. The left side of Figure 2.7 shows each contribution to the $NEP(f)$ as a function of the frequency, while equivalently in the right side, each contribution to the flux-noise spectral density is $S_\Phi(f)$. The blue solid line represents the previously calculated background noise $NEP_{hv}(f) \approx 56$ aW$/\sqrt{Hz}$, or equivalently a flux-noise $\sqrt{S_\Phi(f)} \approx 20\ \mu\Phi_0/\sqrt{Hz}$ at the detector output, given the detector responsivity of $\Re_{MMB} \approx 0.35\ \mu\Phi_0/aW$ when $f \to 0$. The total detector noise lies underneath the background noise for frequencies above 1 Hz, implying that the MMB prototype presents background-limited performance (BLIP) in that bandwidth. It is important to note that the unavoidable 1/f atmospheric noise is not included in these plots and therefore all 1/f noise contributions from the detector appear predominant towards the low frequency end of the spectrum. The main component of this low frequency noise is the erbium excess noise and can be minimized

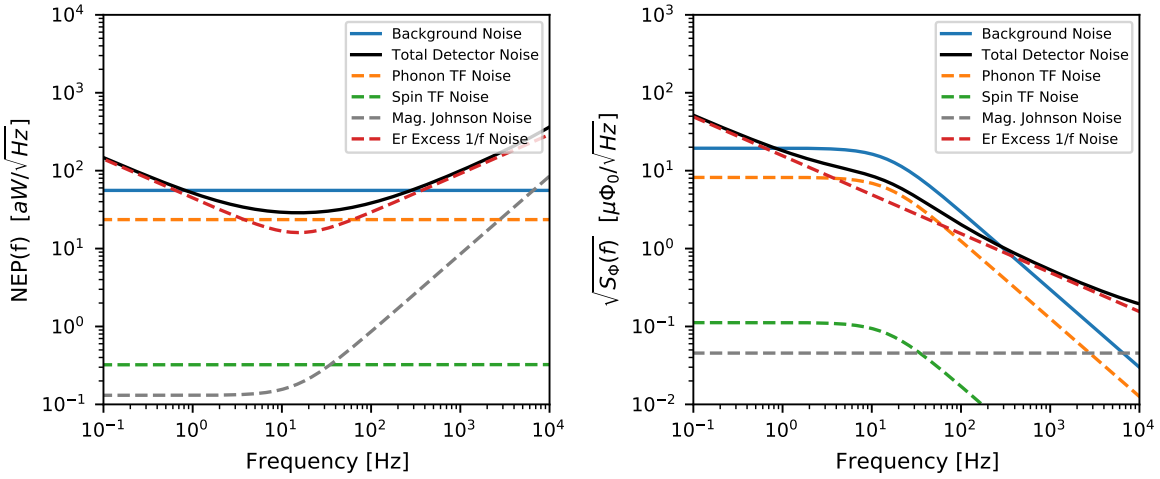

Figure 2.7: Left) Noise Equivalent Power $NEP(f)$ and **Right)** Flux noise level $\sqrt{S_\Phi(f)}$ contributions at the SQUID as a function of frequency for the proposed antenna-coupled MMB. The solid blue line represents the background NEP/flux noise as a function of the frequency, while the solid black line represents the total detector NEP/flux noise without considering the multiplexing and readout noise. Dashed lines represent the detector's NEP/flux noise contributions discussed in Section 2.2.3.

enhancing the MMB responsibility by increasing I_{field}. The time constant can be derived from the roll-off present in the background flux noise. The cut-off frequency sets the bolometer bandwidth of $f_{BW} \approx 15$ Hz and therefore the time constant is $\tau = 1/(2\pi f_{BW}) = 11$ ms, consistent with a total heat capacitance of $C_{\text{tot}} = 1.7$ pJ/K and a thermal link conductance of $G_{\text{bath}} = 163$ pW/K. This value remains well below the $\tau < 62$ ms requirement imposed by Equation 2.9 when considering a scanning speed of $\dot{\theta} = 1$ deg/s and a telescope FWHM beamwidth of $\theta \approx 0.39$ deg.

The readout noise $S_{\text{read}}(f)$ was not considered in Figure 2.7 because it depends on the multiplexing and readout system which will be described in detail in the following chapters. The motivation for obtaining the above results was to find a maximum readout noise limit based on the sum of the dominant detector noise contributions as expressed in equation 2.20. In this case, the minimum detector noise within the readout bandwidth is $\sqrt{S_{\text{det}}(f)} \approx 10\ \mu\Phi_0/\sqrt{Hz}$. Therefore, for the design of the readout and multiplexing system, a ratio of 10 times less than the noise of the multiplexing and readout system was imposed as a rule of thumb, this means $\sqrt{S_{\text{read}}(f)} < 1\ \mu\Phi_0/\sqrt{Hz}$ for a readout bandwidth of $f_{BW} > 15$ Hz.

3. Microwave SQUID Multiplexing of MMB Arrays

In this chapter the Microwave SQUID Multiplexer (μMUX) is introduced as the proposed multiplexing system for the new detection chain of the QUBIC project. The need for CMB experiments to multiplex large arrays of low-temperature bolometers is discussed in Section 3.1. This section enumerates the advantages and disadvantages of the currently used multiplexing techniques and the rationale for the choice of the μMUX. The next sections describe the most important elements of the μMUX such as the Coplanar Waveguide (CPW) superconducting resonators in Section 3.2 and the Josephson junctions and rf-SQUIDs in Section 3.3. Finally, in Section 3.4, the μMUX operation principle is explained and its design parameters are presented.

3.1 Low-Temperature Bolometers Array Multiplexing

The most demanding CMB polarization experiments requires focal planes populated with tens of thousands of ultra-sensitive bolometers. As explained in Section 2.1.2, the sensitivity of a CMB instrument depends on the instrument noise performance NEP_{ins} as well as the number of acquired time samples N_t. Using bolometers operating at temperatures in the order of milli-Kelvins, as for example the MMB described in Section 2.2, it is possible to reach the BLIP where $NEP_{BI} \approx NEP_{h\nu}$. Beyond that limit, the only way to improve the sensitivity is to increase the number of N_{det} detectors observing the sky simultaneously [18]. In this way N_t would increase proportionally to N_{det} without the need to increase the total observing time. However, operating a large number of detectors at cryogenic temperatures is a major challenge given the reduced cooling powers at sub-Kelvin stages. The use of a cryogenic multiplexing system such as the one shown on the left side of the Figure 3.1 is proposed to overcome this limitation. In this scheme, a multiplexing system located in the lower temperature stages collects the signals from all the bolometers in a single channel connecting the stages at different temperatures. Outside the cryostat, a readout system (demultiplexer) splits the signals from each detector again for processing and storage. The primary figures of merit of these multiplexing systems are the multiplexing factor (i.e. number of detectors per communication channel), the number of connections and interfaces per detector number, the thermal load due to wiring and electrical dissipation and the readout noise which should be sub-dominant with respect to detector noise and background noise as specified in Equations 2.20 and 2.7.

In order to overcome the aforementioned problems and achieve the best figures of merit, different cryogenic multiplexing techniques have been developed during the last decades. Figure 3.1 shows the most widely used multiplexing techniques for CMB instruments, similar to the ones used in communications systems [64]. Time-division multiplexing (TDM) is the most mature technique. In TDM, given a group of N bolometers, each bolometer signal is sequen-

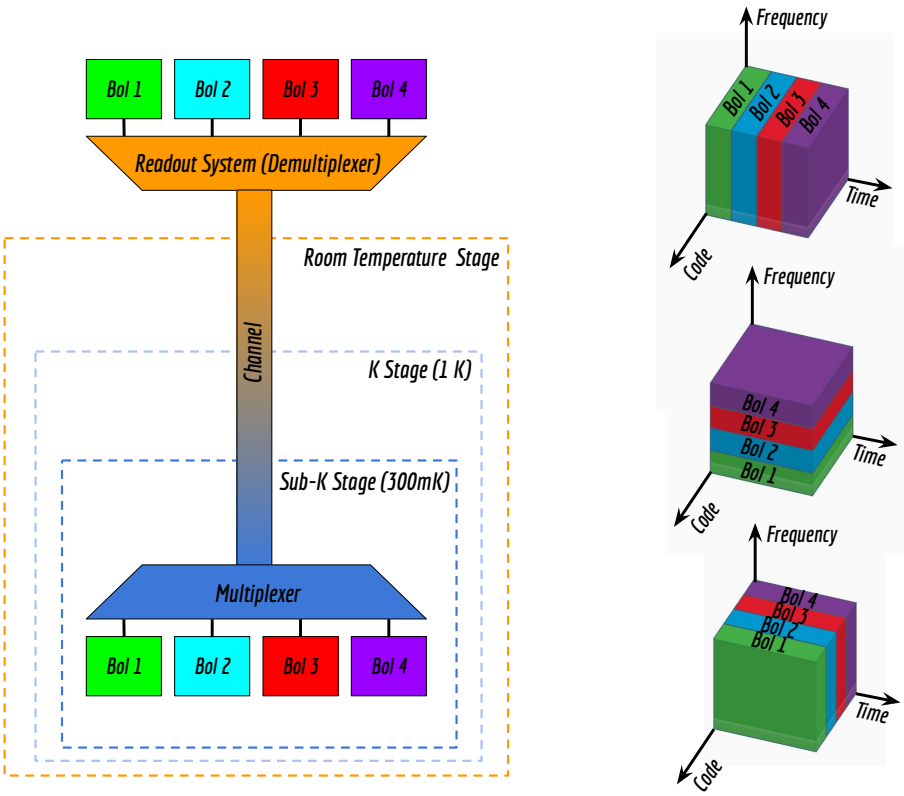

Figure 3.1: Left) Scheme of the most common multiplexing systems used in CMB instruments. Bolometers located at sub-kelvin stages are multiplexed and their signals transmitted outside the cryostat sharing a single communication channel. A room temperature readout system recovers the signal of each bolometer. **Right)** Typical multiplexing techniques used in CMB instruments: **Top)** Time-Division Multiplexing (TDM). **Middle)** Frequency-Division Multiplexing (FDM). **Bottom)** Code-Division Multiplexing (CDM).

tially transmitted through the communication channel at different times (i.e. $t_1, t_2, ..., t_{N-1}, t_N$). This transmission must be fast enough so that the number of samples from each detector is at least twice the bandwidth of the bolometer signal in order to satisfy the sampling theorem. Generally for bolometric applications this bandwidth is in the order of $\sim$ 100 Hz [18]. For the case of FDM, each detector signal is coupled to a frequency encoding element where each detector has a unique assigned frequency (i.e. $f_1, f_2, ..., f_{N-1}, f_N$); all signals are added and sent through the communication channel simultaneously. The channel requires a bandwidth higher that N times the detector bandwidth in order to avoid losing information or cross-talk due to overlapping channels. Finally, in CDM each detector signal is multiplied by an unique code (i.e. $c_1, c_2, ..., c_{N-1}, c_N$ for N detectors), all signals are added together and transmitted through the communication channel. Since these codes have no projection between them (i.e. they are orthogonal), the information can be retrieved later using each code regardless of whether the signals overlap in the frequency domain.

Several of these multiplexing techniques were extensively tested in the field as for example TDM with dc-SQUIDs [65], FDM using MHz LC resonators (DfMUX) [66], and Walsh-code CDM [67]. Most of them can achieve multiplexing factors of $\mathcal{O}(100)$ detectors per wire operating at $\sim$MHz frequencies, but are limited by high cost, complexity, or noise degradation for higher multiplexing factors [18]. However, this is not the case of the Microwave SQUID Multiplexing (μMUXing) technique inspired in the intrinsic multiplexed principle of the Mi-

crowave Kinetic Inductance Detectors (MKIDs) [68]. In this method, each detector is inductively coupled to an rf-SQUID terminating an unique GHz-frequency resonator and all of them coupled to a single feedline. Each rf-SQUID acting as a flux-dependent inductor shifts the resonance frequency proportionally to the detector signal. Therefore recovering the signals from each detector is straightforward and "only" requires monitoring the resonant frequencies [69]. Nowadays, the high quality factors achieved by current superconducting nano-fabrication techniques along with the exquisite sensitivity rf-SQUIDs and the large readout bandwidth supported by the cryogenic Low Noise Amplifiers (LNA) of several GHz enable multiplexing factors on excess of $\mathcal{O}(1000)$ [70].

As mentioned at the beginning of this document in Section 1.3, this new technology is proposed as an alternative to the multiplexing system used in the QUBIC instrument. Currently, QUBIC uses a TDM scheme achieving a multiplexing factor of $N_{det} = 128$ TES by means of a 4×32 dc-SQUID matrix placed at 1 K [41]. A custom cryogenic Application-Specific Integrated Circuit (ASIC) placed at 40 K and room temperature readout electronics amplify the detectors signals again and provide the necessary feedback signal in order to keep the most sensitive dc-SQUID operational point. A diagram of the multiplexing scheme is shown in the right side of Figure 1.4. Although this architecture adapts very well to the readout of TES, one of the characteristics that makes this architecture unsuitable for the readout of MMBs is the high stray inductance L_{stray} introduced by the cables connecting the detectors located at $\sim$ 300 mK with the multiplexing matrix at 1 K. This inductance dilutes the responsivity of the detector $\mathfrak{R}_{MMB}$, given the Equation 2.14. In addition, to avoid thermal loading at sub-Kelvin stages, expensive *NbTi* superconducting ribbon cables are required. In contrast, the µMUX, given its small size and low thermal dissipation in order of few $\sim$ pW per channel, can be connected directly to the detectors using aluminum wire bonds or even integrated into the detectors themselves as for MMCs readout [71]. This would increase system integration and reduce thermal load and cost. Additionally, like other TDM systems, the QUBIC multiplexing system sufferers of an aliasing noise penalty due to the fact that both the amplification system and the detectors have bandwidths greater than the sampling frequency [39]. While the detector bandwidth can be reduced by adding filters, the degradation due to channel noise grows with $\sqrt{N_{\text{det}}}$. In the case of µMUX this does not occur and the only limitation to multiplexing a large number of channels in one coaxial cable is their arrangement, avoiding the accidental overlap between them or crosstalk. In the following sections, this multiplexing technology is explained in detail starting from each element and then concluding with the design focused on the bolometric applications.

3.2 Superconducting Microwave Resonators

One of the most important parts of the µMUX are the superconducting microwave resonators. These are used as frequency encoding elements, and therefore, their properties determine the µMUX response and define the achievable multiplexing factor. In this section, the basic theory of coplanar superconducting resonators (CPW) is introduced and their dependence on the geometries and materials proprieties described. Then, their behavior when terminated inductively and then capacitively coupled to a transmission line is analyzed, following the references [43, 72, 73, 74].

3.2.1 Surface Impedance in Superconductors

The superconductivity phenomenon was discovered in 1911 by the Dutch physicist *Heike Kamerlingh Onnes*. Superconductivity is a set of physical properties observed in certain materials where electrical resistance vanishes and magnetic fields are expelled from the material (Meissner effect). Unlike an ordinary metallic conductor, whose resistance decreases gradually

as its temperature is lowered, even down to near absolute zero, a superconductor has a characteristic superconducting transition temperature T_c at which the resistance drops abruptly to zero [75]. This is valid for dc currents, but not for ac currents. Microwave properties of superconductors can be described by the two-fluid model, which is consistent with experiment and qualitatively in agreement with full microscopic theory [76]. This model describes a superconductor as a two independent fluids coexisting simultaneously but not interacting, one consist of superconducting electrons, the other of normal electrons. The relative abundance of these two fluids changes as a function of temperature and it is described by the superconducting and normal fluid densities $n_s(T)$ and $n_n(T)$ respectively. The total number density is equal to that of the metal in the normal state: $n_s(T) + n_n(T) = n$, a number density fixed by the nature of the metal. The microscopic theory of superconductivity (BSC) calls superconducting electrons *Cooper pairs* that are made of two paired electrons of opposite momentum and spin [77]. When a variable electromagnetic field is applied to the superconductor, it accelerates both types of electrons, but only normal electrons (quasiparticles) suffer scattering processes causing ohmic losses and hence the surface resistance R_s. Analogously to normal conducting metals, the current flow produces a magnetic field that opposes the changes in the current representing a magnetic inductance L_m. This factor is related to the geometry of the superconductor material. In contrast, superconducting electrons (Cooper pairs) do not experience those scattering mechanisms and flow through the material without energy dissipation. However, due to their inertia, they cannot follow the time varying electromagnetic field instantaneously, which manifests in a kinetic inductance L_kin. Therefore, for a microwave excitation with angular frequency ω superconductors show a finite surface impedance Z_s given by

$$Z_s = R_s + j\omega(L_m + L_\mathrm{kin}). \tag{3.1}$$

The density of quasiparticles in a superconductor $n_n(T)$ decreases exponentially with the temperature, and consequently, so does the surface resistance R_s. Thus, for temperatures far below the superconducting transition temperature T_c, the surface impedance Z_S is dominated by the surface inductance $L_S = (L_m + L_\mathrm{kin})$. A more detailed description of surface impedance Z_s can be given using the complex conductivity of a superconductor $\sigma_s(\omega, T) = \sigma_1(\omega, T) - j\sigma_2(\omega, T)$ at angular frequency ω and temperature T. Accordingly to the Mattis–Bardeen theory [78] these two quantities can be calculated in relation to the normal conductivity σ_n using the following equations:

$$\frac{\sigma_1}{\sigma_n} = \frac{2}{\hbar\omega}\int_{\Delta(T)}^{\infty} \frac{[f(\epsilon) - f(\epsilon - \hbar\omega)][\epsilon^2 + \Delta^2(T) + \hbar\omega\epsilon]}{\sqrt{\epsilon^2 - \Delta^2(T)}\sqrt{[\epsilon + \hbar\omega]^2 - \Delta^2(T)}} d\epsilon \tag{3.2}$$

$$\frac{\sigma_2}{\sigma_n} = \frac{1}{\hbar\omega}\int_{\Delta(T)-\hbar\omega}^{\Delta(T)} \frac{[1 - 2f(\epsilon - \hbar\omega)][\epsilon^2 + \Delta^2(T) + \hbar\omega\epsilon]}{\sqrt{\Delta^2(T) - \epsilon^2}\sqrt{[\epsilon + \hbar\omega]^2 - \Delta^2(T)}} d\epsilon. \tag{3.3}$$

Here, $\hbar$ denotes the reduced Planck constant and $f(x) = (1 + e^{x/k_B T})^{-1}$ indicates the Fermi-Dirac distribution. These equations are only valid for small angular frequencies where the energy of a single photon is not sufficient to break a Cooper pair (i.e $\hbar\omega < 2\Delta(T)$, with $\Delta(T)$ the binding energy or superconducting gap).

The solution to these equations depends mostly on three characteristic length scales inside the superconductor. First, the magnetic penetration depth λ that represents the decay length of magnetic field in the superconductor. Second, the coherence length ξ_0 that measures the interaction distance between electrons forming a Cooper pair. Third, the electron mean free path l_e describing the quality or amount of impurities in the superconductor. For a superconducting thin film of thickness t in the dirty limit, $l_e \ll \xi_0$, and in the particular case of $\sigma_2 \gg \sigma_1$ and $T \ll T_c$ the surface impedance Z_s can be expressed as [72, 79],

$$R_s = \mu_0 \lambda_\mathrm{eff} \omega \beta \frac{\sigma_1}{2\sigma_2}, \tag{3.4}$$

$$L_s = \mu_0 \lambda_{\text{eff}}, \tag{3.5}$$

where $\lambda_{\text{eff}} = \lambda \coth(t/\lambda)$ denotes the effective magnetic penetration depth. All these parameters are strongly dependent on the material, temperature and deposition technique, therefore a cryogenic material characterization is required in order to experimentally determine the superconducting proprieties. In the case of µMUX, the superconducting thin film is made of $\sim$ 300 nm Niobium (Nb) deposited through the sputtering technique yielding a critical temperature of $T_c < 8$ K. Typical values for Nb are $\xi_0 = 39$ nm and $\lambda = 36$ nm with $T \to 0$.

3.2.2 Superconducting Coplanar Waveguides (CPW)

Nowadays, microwave cryogenic amplification technologies provide a bandwidth in the order of several GHz. To use this bandwidth efficiently, the µMUX makes use of low-bandwidth microwave resonators. The reduced bandwidth is obtained by minimizing the losses in the resonator using superconducting films as described in the previous section. Therefore, the geometry chosen for the resonator has to be compatible with the micro-fabrication techniques. One of the geometries most widely used to create a superconducting resonator is the coplanar waveguide (CPW), sometimes also called CPW transmission line. The geometry of the CPW is shown in Figure 3.2 and consists of a centre strip of width s separated by a distance s from two ground-planes at both sides. Here, the superconducting film of thickness t is placed on top of a dielectric substrate with relative permittivity ϵ_r. The most significant advantage of CPW over other kinds of planar transmission line geometries, like microstrips, is the ability to connect active and passive circuit components in shunt from the centre conducting strip to the ground plane on the same side of the substrate [80]. The superconducting thin film deposition, patterning and etching required in this structure can be easily carried out using traditional micro- and nano-fabrication techniques.

The characteristics of lossless transmission lines are described by the characteristic impedance Z_0 of the phase velocity of the wave in the transmission line v_p given by

$$Z_0 = \sqrt{\frac{L'}{C'}} \tag{3.6}$$

$$v_p = \frac{1}{\sqrt{L'C'}}. \tag{3.7}$$

Here, L' and C' denotes the inductance and capacity per unit length respectively. The characteristic impedance Z_0 is the ratio between the voltage and current amplitudes of a wave travelling in one direction along the line, while the phase velocity describes the time it takes for voltage and current waves to propagate from one point to another along the line. Characteristic impedance and phase velocity are determined by the geometry and materials of the transmission line and, for a uniform line, are not dependent on its length. In the case of a CPW, conformal mapping techniques (angle-preserving transformations) are used in order to calculate L' and C', and consequently Z_0 and v_p. For the ideal case when the ground planes are very wide relative to the slot width w and the dielectric substrate is very thick $h \gg t$, the distributed magnetic inductance per unit length L'_{m} and the capacitance per unit length C' are calculated as

$$L'_{\text{m}} = \frac{\mu_0}{4} \frac{K(k')}{K(k)} \tag{3.8}$$

$$C' = 4\epsilon_0 \epsilon_{\text{eff}} \frac{K(k)}{K(k')}. \tag{3.9}$$

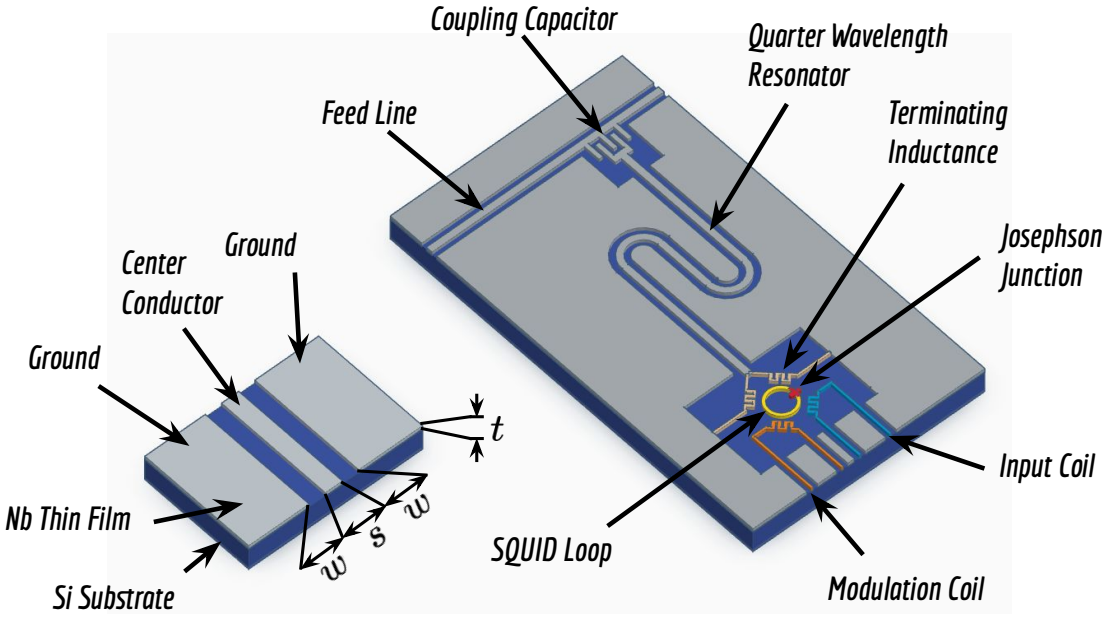

Figure 3.2: Left) Sketch of a coplanar waveguide geometry made from a superconducting film with thickness t placed on top of a dielectric substrate with height h and dielectric constant ϵ_r. The centre conductor exhibits a width s and the slots a width w. **Right)** Sketch of a µMUX channel where a quarter-wave CPW resonator capacitively coupled to a transmission line using an inter digital capacitor. At the same time, the resonator is inductively terminated with an rf-SQUID. The rf-SQUID is magnetically coupled using different coils to the detector (blue), modulation line (orange) and resonator (gold). The rf-SQUID is conceptually represented only for explanatory purposes but does not represent the real geometry.

here ϵ_0 is the vacuum permittivity, μ_0 the vacuum permeability. Then, $\epsilon_{\text{eff}} \approx (1+\epsilon_r)/2$ is the effective permittivity assuming a quasi-Transverse Electromagnetic Mode (quasi-TEM) wave propagating between air and substrate with permittivity ϵ_r. Finally, $K(x)$ is the complete elliptic integral of the first kind with the arguments, $k = w/(w+2s)$ and $k' = \sqrt{1-k^2}$ [81]. Due to the fact that Equation 3.8 only considers the magnetic inductance, the kinetic inductance of the superconducting film described before needs to be accounted for using [72]

$$L'_{\text{kin}} = (g_c + g_g)\mu_0\lambda_{\text{eff}}, \tag{3.10}$$

where g_c and g_g represent the contributions from the centre conductor and ground planes respectively. λ_{eff} is the effective magnetic penetration depth described in previous paragraphs. Thus, the total inductance per unit length is $L' = L'_{\text{m}} + L'_{\text{kin}}$.

3.2.3 Inductively Terminated and Capacitively Coupled CPW Resonators

The input impedance of a CPW transmission line with impedance Z_0 and length l_0 terminated with a load Z_l is given by [82]

$$Z_{\text{in}} = Z_0 \frac{Z_l + Z_0 \tanh(\gamma_p l_0)}{Z_0 + Z_l \tanh(\gamma_p l_0)}, \tag{3.11}$$

where γ_p stands for the propagation constant. Considering a superconducting CPW with negligible losses ($\gamma_p = j\beta_p$) and shorted at the end (i.e. $Z_l = 0$), $Z_{\text{in}} \approx jZ_0 \tan(\beta_l l_0)$. This

value diverges $Z_{\text{in}} \to \infty$ when the length of the resonator approaches $l_0 = \lambda/4$. Using the fact that $\lambda = v_p/f$, the resonance frequency of a quarter-wavelength resonator is given by

$$f_0 = \frac{v_p}{4l_0}. \tag{3.12}$$

For resonance frequencies in the range between 1 to 10 GHz, the lengths of the CPW quarter-wave resonators are in the order of tens of millimeters for silicon wafers (Si), making them compatible with 1 to 3-inches diameter silicon wafers commonly used in university/research clean rooms and allowing to pack several resonators in small areas of a few square centimeters. These resonators provide the frequency selectivity required to be used as frequency encoding elements. However by themselves they do not have any mechanism that allows them to modify their properties according to the detector signal to be read through a single communication channel. This is achieved by replacing the termination by an inductor whose value varies according to the signal to be detected and capacitively coupling the resonator to a single transmission line. The variable inductor consists of a rf-squid and is explained in the next section. Figure 3.3 shows a schematic of a quarter-wave resonator terminated in an inductor L_T and capacitively coupled to a feedline through a capacitor C_c. Both resonator and feedline have the same characteristic impedance Z_0. The impedance at the capacitor terminals as a function of the angular frequency ω is given by

$$Z_c = \frac{1}{j\omega C_c} + Z_0 \frac{j\omega L_T + Z_0 \tanh(\gamma_p l_0)}{Z_0 + j\omega L_T \tanh(\gamma_p l_0)}. \tag{3.13}$$

The first term represents the capacitor series impedance and the second term the inductively terminated resonator using Equation 3.11. The coupled resonance frequency f_r in terms of the quarter wave resonator f_0 can be found by expanding Z_c and finding $\text{Im}(Z_c) = 0$ as explained by Mates [43]. The expression for f_r can be written as

$$f_r = \frac{f_0}{1 + 4f_0(C_c Z_0 + L_T/Z_0)}. \tag{3.14}$$

This expression is valid only for the case of $2\pi f_0 C_c Z_0 \ll 1$ and $2\pi f_0 L_T \ll Z_0$. At microwave frequencies it is more useful to describe the frequency response of a network using the scattering parameters (S-parameters) instead of impedances (Z-parameters) or admittances (Y-parameters). The scattering parameters describe the frequency response in terms of the relation between incident a_i and reflected b_i travelling waves at network ports. The transmission scattering parameter $S_{21}(f)$ as a function of the frequency $f = \omega/(2\pi)$, measured between port 1 and 2 in Figure 3.3 can be derived from the narrow-band approximation of Z_c using $S_{21} = 2/(2 + Z_0/Z_c)$ yielding [82]

$$S_{21}(f) = \frac{S_{21}^{\min} + 2jQ_l\left(\frac{f-f_r}{f_r}\right)}{1 + 2jQ_l\left(\frac{f-f_r}{f_r}\right)}. \tag{3.15}$$

Here $S_{21}^{\min}$ is the minimum scattering parameter, also called resonance depth and occurs at the resonant frequency $f = f_r$. Q_l is the loaded quality factor and it takes into account the resonator losses included in the real part of the propagation constant $\gamma_p = \alpha_p + j\beta_p$ and the capacitively coupling. α_p include all loss mechanisms like ohmic losses in the superconductor, dielectric losses, radiation and Two-Level System (TLS) losses [72]. The loaded quality factor calculated in terms of the quality factors of each contribution can be written as

$$\frac{1}{Q_l} = \frac{1}{Q_c} + \frac{1}{Q_i}. \tag{3.16}$$

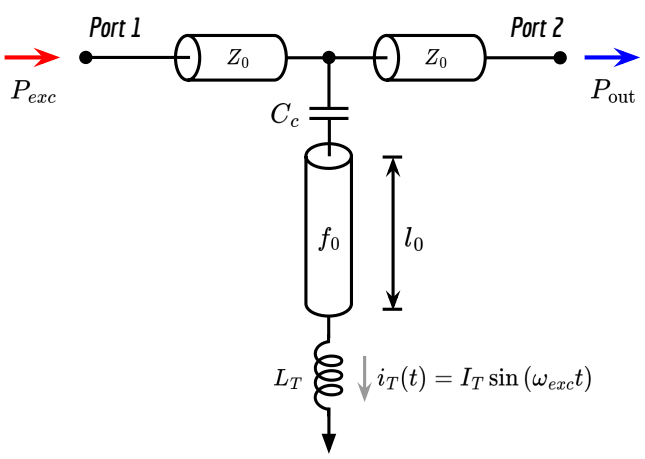

Figure 3.3: Circuit diagram of a quarter-wave resonator as shown in 3.2, with length l_0, inductively terminated with L_T and coupled to a feed-line via a capacity C_c. The resonator and the transmission line exhibit the same characteristic impedance Z_0.

Where Q_i is the intrinsic quality factor of the resonator and Q_c is the coupling quality factor. Q_i includes the aforementioned loss mechanisms and is a metric used to determine the quality of the superconducting resonators. For a CPW microwave resonator made of Nb, Q_i is in excess of 10^5. On the other hand, the coupling quality factor is given by

$$Q_c = \frac{2\pi}{(4\pi f_r Z_0 C_c)^2}. \tag{3.17}$$

The resonator bandwidth is defined as $BW_{\text{res}} = f_2 - f_1$ where $|S_{21}(f_1)|^2 = |S_{21}(f_2)|^2 = (S_{21}^{\min} + 1)^2/2$. This results in the following expression for the resonator bandwidth in terms of the loaded quality factor

$$BW_{\text{res}} = \frac{f_r}{Q_l}. \tag{3.18}$$

Generally, $Q_c \ll Q_i$ and therefore $BW_{\text{res}} \approx f_r/Q_c$. As a design parameter, Q_c is used to define the resonator bandwidth depending on the multiplexing factor as will be discussed in the following sections. Additionally, given a excitation power P_{exc} at the input of the feed-line (port 1), the capacitive coupling determines the power entering in the resonator P_{int} and also the intensity of the current I_T circulating through the terminating inductance L_T. For frequencies $f_{\text{exc}} \approx f_r$ close to the resonance frequency, the internal power can be approximated as [79]

$$P_{\text{int}} = \frac{2}{\pi}\frac{Q_l^2}{Q_c^2} P_{\text{exc}}. \tag{3.19}$$

Based on Equation 3.19, the amplitude of the current running through the inductive load is given by

$$I_T = \sqrt{\frac{16}{\pi}\frac{Q_l^2}{Q_c^2}\frac{P_{\text{exc}}}{Z_0}}. \tag{3.20}$$

The importance of the internal power P_{int} lies in the fact that it is proportional to the power dissipated P_{diss} in the resonator and the cooling power required by the multiplexing system [43]. Generally, the dissipated power per channel is less than 10 pW [18]. I_T defines the μMUX frequency response dependence on the readout power P_{exc}.

3.3 Radio-frequency Superconducting Quantum Interference Device (rf-SQUID)

One of the resonator parameters needs to be modulated in order to encode the detector signal into the resonator frequency response. For example, in the case of the Microwave Kinetic Inductance Detector (MKID), the incident photons with energy higher than the binding energy $2\Delta(T)$ break Cooper pairs increasing the amount of quasiparticles. Therefore, the kinetic inductance changes and consequently the resonance frequency and loaded intrinsic factor also change [72]. Inspired by this principle, the µMUX uses an rf-SQUID as a variable inductor proportional to the detector signal. On the right side of Figure 3.2 a sketch of the µMUX channel is shown where a quarter-wave CPW resonator inductively terminated and capacitively coupled to the feed-line by means of an inter-digital capacitor. At the same time, the terminating inductance previously defined as L_T is coupled to a rf-SQUID which in turn is coupled to two coils. One corresponds to the flux transformer described in Section 2.2 and the other to a modulation coil used to linearize the rf-SQUIDs response. This section explains the operation of a non-hysteretic unshunted rf-SQUID, starting by describing the operation of the Josephson junctions and of the SQUID.

3.3.1 Josephson Junctions

The behavior of superconductors suggests that electron pairs are coupled forming Cooper pairs. These Cooper pairs took the character of a bosons and condense into the ground state [75], where the whole superconductor can be described by a single macroscopic wave function Ψ,

$$\Psi = |\psi| e^{j\varphi}. \tag{3.21}$$

Here $|\psi|$ represents the magnitude and φ the phase of the wave function Ψ. When two superconductors are connected through an insulation barrier sufficiently thin, as illustrated in the left side of Figure 3.4, the macroscopic wave functions of the two superconductors overlap, allowing for coherent tunnelling of Cooper pairs [83]. This effect is named Josephson effect after the British physicist *Brian Josephson* predicted it in 1962 and postulated the mathematical relationships for the current and voltage across the junction. The junction has the same name as the effect, *Josephson junction*. It is an example of a macroscopic quantum phenomenon, where the effects of quantum mechanics are observable at ordinary, rather than atomic, scale. The mathematical relationships for the current and voltage across the junction can be expressed in terms of the wave functions phase difference $\varphi = \varphi_2 - \varphi_1$ of the two superconductors. The expression for the superconducting current I_S through the barrier (first Josephson equation) can be written as [84]

$$I_S = I_c \sin(\varphi). \tag{3.22}$$

Here, I_c stands for the junction critical current. While the current applied to the junction does not exceed the critical current $I_S \leq I_c$, the total current flowing through the barrier is carried only by tunneling Cooper pairs. The voltage drop V across the junction is described by the second Josephson equation [84],

$$V = \frac{\Phi_0}{2\pi}\dot{\varphi} \tag{3.23}$$

Where $\Phi_0 = h/2e$ denotes the magnetic flux quanta. The time derivative of the phase difference $\dot{\varphi}$ sets the voltage V across the junction. If an alternating ac current with amplitude $I_S < I_c$ is applied to the junction, it is possible to calculate the time derivative of Equation 3.22 and insert it in Equation 3.23 yielding a voltage drop V of

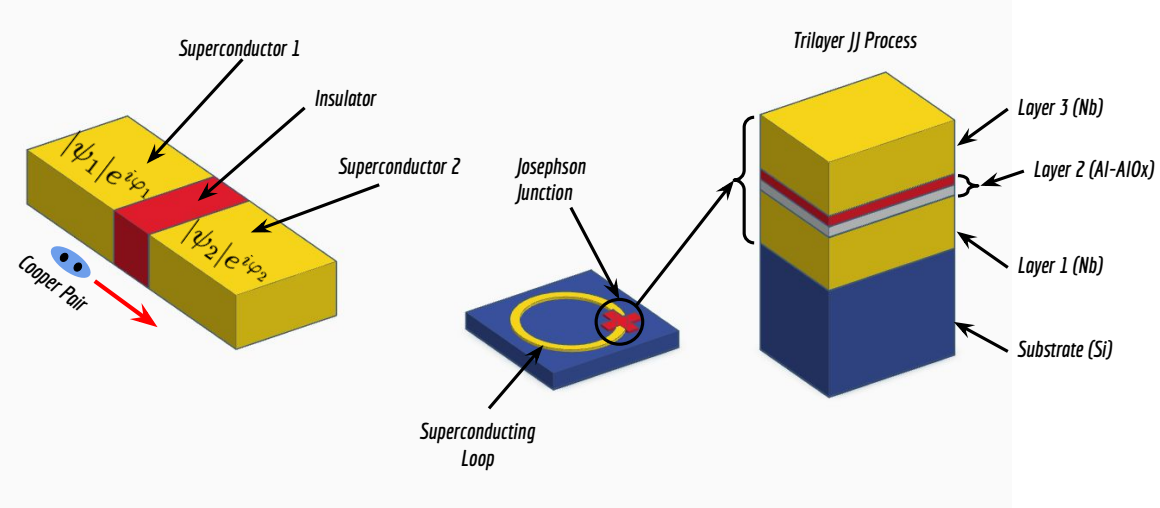

Figure 3.4: Left) Sketch of Josephson Junction (JJ). The yellow blocks are the superconducting electrodes with their respective wave functions $|\psi_1|e^{j\varphi_1}$ and $|\psi_2|e^{j\varphi_2}$. The red block represents the insulator through which cooper pairs can tunnel. **Right)** Sketch of a rf-SQUID consisting of superconducting loop (yellow) interrupted by a Josephson Junction (red cross). The Josephson junction is made of a trilayer of $Nb/Al-AlO_x/Nb$, the superconducting electrodes are made of Nb while the AlO_x insulating barrier is created oxidizing a thin layer the Al film.

$$V = \frac{\Phi_0}{2\pi I_c \cos(\varphi)} \dot{I}_s. \tag{3.24}$$

Using the fact that $V = L\dot{I}$, the proportionality factor linking the voltage and the time derivative of the current is by definition an inductance. Particular, it is a phase-dependent non-linear inductance $L(\varphi)$ which can be written as

$$L(\varphi) = \frac{\Phi_0}{2\pi I_c \cos(\varphi)} = \frac{L_J}{\cos(\varphi)}, \tag{3.25}$$

where L_J is the Josephson inductance [84]. The Josephson junction is one the most important building blocks in superconducting electronics and has many applications in the fields of metrology, quantum computing and astronomy [85]. A typical way to fabricate these junctions is through the trilayer process. The basis of the trilayer structure is shown on the right side of Figure 3.2. The first base Nb layer ($\sim$ 300 nm) is deposited via sputtering over a Si wafer and, on top of it, a thin ($\sim$ 30 nm) Al layer. The Aluminium surface is then oxidized by letting oxygen enter into the chamber creating a thin layer of AlO_x that acts as an insulating barrier and defines the junction properties. Finally, the Nb counter electrode ($\sim$ 300 nm) is sputtered on top of AlO_x. All deposition processes are done in situ without breaking the vacuum, ensuring a high quality superconductor and insulation barrier. Finally, the trilayer is patterned and electrodes conformed using UV projection lithography and different etching techniques [86].

3.3.2 Non-hysteretic Unshunted rf-SQUIDs

An unshunted rf-SQUID consists of a superconducting loop with a characteristic inductance L_S, interrupted by a single Josephson junction. The Josephson Junction inductance $L(\varphi)$ depends on the wave function phase difference φ between the superconductor electrodes (eq 3.25). When the junction is interrupting a superconducting loop, as a consequence of the

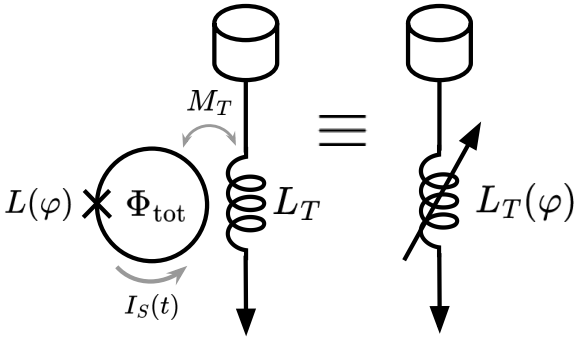

Figure 3.5: Schematic of an unshunted rf-SQUID inductively coupled to a coil characterized by an inductance L_T and by a mutual inductance M_T between the coil and the rf-SQUID loop.

flux quantization ($\varphi = 2\pi n$) the phase difference can be related with the flux through the SQUID loop Φ_{tot} using the following Equation [75],

$$\varphi + \frac{2\pi\Phi_{\text{tot}}}{\Phi_0} = 2\pi n \quad \forall \quad n \in \mathbb{Z}. \tag{3.26}$$

Figure 3.5 shows a schematic of an unshunted rf SQUID inductively coupled to a coil characterized by an inductance L_T and by a mutual inductance M_T between the coil and the rf-SQUID loop. The term *unshunted* refers to the fact that the junction is not shunted by any resistive element that modifies its behavior [54]. Inserting Equation 3.26 into the first Josephson Equation 3.22, the supercurrent I_S flowing through the rf-SQUID, as a function of the total magnetic flux Φ_{tot} is

$$I_S = -I_c \sin\left(2\pi\frac{\Phi_{\text{tot}}}{\Phi_0}\right). \tag{3.27}$$

The total magnetic flux Φ_{tot} comprises two contributions $\Phi_{\text{tot}} = \Phi_{\text{ext}} + \Phi_{\text{scr}}$. The first contribution is the external flux Φ_{ext}, generated either by a current applied through the modulating coil L_{mod} or by the current running through the terminating inductance L_T (see Figure 3.5). The second contribution is the screening flux $\Phi_{\text{scr}} = L_S I_S$ induced by the screening current I_S, a consequence of the flux quantization. Using $\varphi_{\text{tot}} = 2\pi\Phi_{\text{tot}}/\Phi_0$, $\varphi_{\text{ext}} = 2\pi\Phi_{ext}/\Phi_0$, and defining the screening parameter $\beta_L = 2\pi L_S I_c/\Phi_0 = L_S/L_J$, the total phase, also called normalized flux φ_{tot}, can be rewritten as

$$\varphi_{\text{tot}} = \varphi_{\text{ext}} - \beta_L \sin(\varphi_{\text{tot}}). \tag{3.28}$$

The screening parameter β_L allows us to define two different operation modes. As can bee seen in Figure 3.6, when $\beta_L \leq 1$, there is a one-to-one correspondence (i.e. bijective function) between the total magnetic flux φ_{tot} and the external magnetic flux φ_{ext}, so the rf-SQUID is defined as non-hysteretic. On the other hand, when β_L takes larger values, i.e. when $L_S > L_J$, a single value of the external flux is not linked uniquely to a single value of the total flux (i.e. set-valued function), leading to a hysteretic behaviour of the rf-SQUID. An hysteretic rf-SQUID can have flux jumps between metastable states, therefore a resistive shunt of the junction is necessary to make these transitions predictable. Most rf-SQUIDs use resistive shunts, at the cost of making them dissipative. In order to avoid dissipation, a not hysteretic rf-SQUID is chosen [43].

The μMUX uses an non-hysteretic unshunted rf-SQUID inductively coupled to a CPW resonator. As can be seen in Figure 3.5, there is a mutual inductance M_T between the rf-SQUID and the terminating inductance L_T. Therefore the inductance seen by the resonators as a function of flux $L_T(\varphi_{\text{tot}})$ is given by [43],

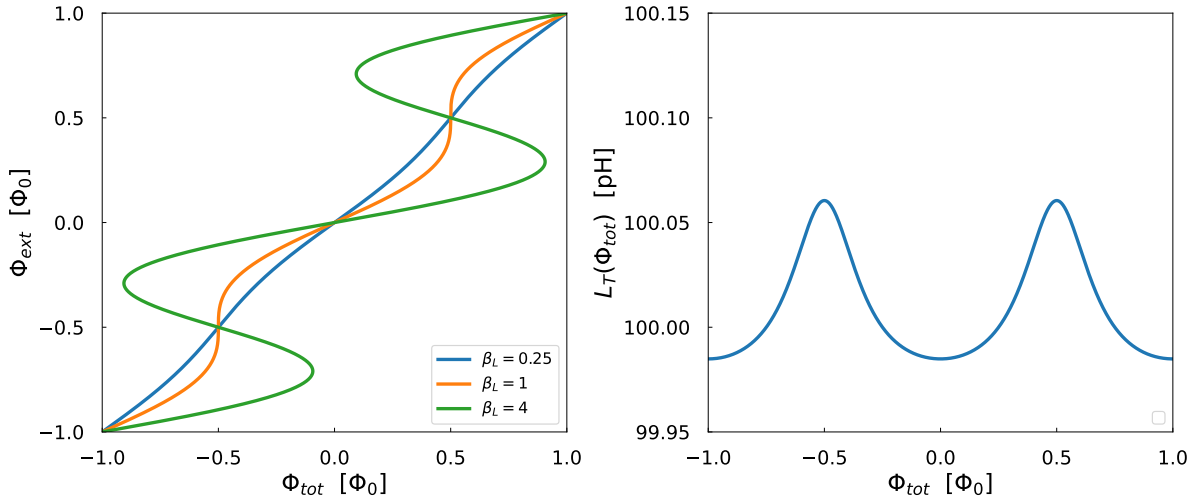

Figure 3.6: Left) Relation between the total magnetic flux φ_{tot} through the rf-SQUID loop and the external magnetic flux φ_{ext} for different values of the screening parameter β_L. **Right)** Terminating inductance $L_T(\varphi_{\text{tot}})$ as a function of the total flux φ_{tot} threaded in the rf-SQUID loop.

$$L_T(\varphi_{\text{tot}}) = L_T - \frac{M_T^2}{L_S} \frac{\beta_L \cos(\varphi_{\text{tot}})}{1 + \beta_L \cos(\varphi_{\text{tot}})} \tag{3.29}$$

As an example, the right side of Figure 3.6 shows the periodic response $L_T(\varphi_{\text{tot}})$ using $L_T = 100$ pH, $L_S = 30$ pH and $M_T = 1.3$ pH and $\beta_L = 0.6$. Equation 3.29 in conjunction with Equation 3.14 leads to a flux-dependent resonance frequency $f_r(\varphi_{\text{tot}})$ and consequently a flux-dependent frequency response $S_{21}(f, \varphi_{\text{tot}})$. This will be described in detail in the following section.

3.4 The Microwave SQUID Multiplexer (µMUX)

In this section the Microwave SQUID Multiplexer (µMUX) is introduced using the topics previously described and following references [43, 73]. A sketch of the µMUX used for the FDM of a MMB array is shown in Figure 3.7. The building block of the µMUX are the frequency encoding elements consisting of a CPW resonator inductively coupled to a non-hysteretic unshunted rf-SQUID as described in previous sections. A set of N resonators is capacitively coupled to a single feedline, where each resonator by design is assigned a single resonance frequency (i.e. $f_1, f_2, ..., f_{N-1}, f_N$). This is done by selecting the resonator lengths l_i and coupling capacitance C_i values. Each resonator is coupled to a rf-SQUID that exhibits a flux-dependent termination inductance given by Equation 3.29. If a detector is magnetically coupled to it, it will modify the flux and therefore the resonant frequency proportionally. Thus, by coupling N bolometers to each rf-SQUID as shown in Figure 3.7, the bolometers signals will be encoded in the resonance frequencies of each resonator. Since in principle the frequency responses of each resonator (Equation 3.15) do not overlap, the change in the resonance frequencies of each resonator (equivalently called channel) can be monitored individually through the feedline. This is the working principle of µMUX, and achieves a multiplexing factor of N detectors in a single pair of coaxial cables entering the cryostat [69, 43]. The resonators are read out by injecting a frequency comb P_{exc} tuned to the frequencies of each resonator as shown on the right side of the Figure 3.7. The time-varying frequency response modifies the phase and amplitude of each tone according to the detector signal producing sidebands (P_{out} spectrum in Figure 3.7). In the

cryostat output path, a cryogenic low-noise amplifier amplifies the signals while maintaining the signal-to-noise level imposed by the detectors. Subsequently, the ambient temperature readout system (demultiplexer in Figure 3.1) separates each channel and recovers the scientific signals.

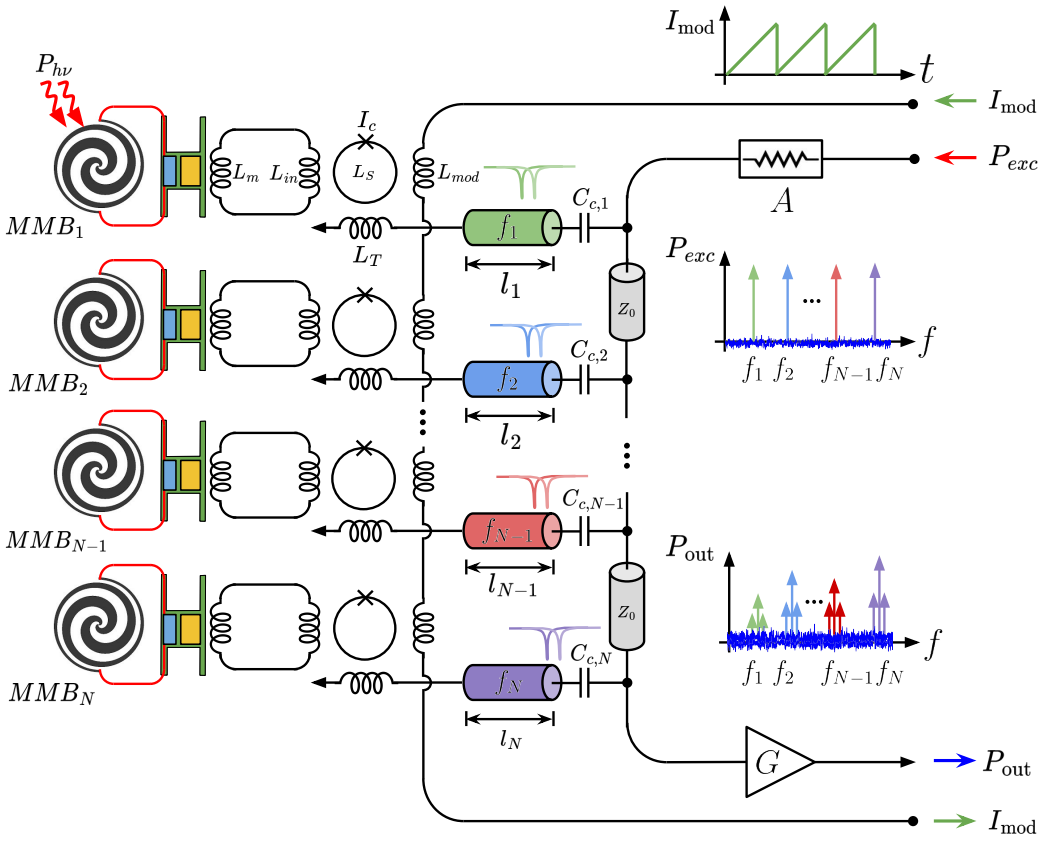

Figure 3.7: Sketch of a N channel quarter-wave resonator-based Microwave SQUID Multiplexer (μMUX) connected to the Antenna-Coupled MMB array. Each resonator is characterized by a unique resonance frequency (i.e. $f_1, f_2, ..., f_{N-1}, f_N$), and is coupled capacitively to a common transmission line and inductively to a rf-SQUID. Each rf-SQUID is coupled inductively to a common modulation line and to an individual MMB. The resonance frequency monitoring is performed by means of a frequency comb P_{exc}, where each tone is tuned to read a particular resonator. At the multiplexer output, each tone is modulated in amplitude and phase containing the detector information P_{out}. An additional saw-tooth current I_{mod} is injected in order to linearize the SQUID responses.

Figure 3.8 shows the flux dependent frequency response $S_{21}(f, \Phi_{\mathrm{tot}})$ of a μMUX channel. Due to the SQUID periodicity with Φ_0, resonator amplitude and phase also oscillates with the same periodicity. Amplitude and phase frequency responses are shown in the left side of Figure 3.8 for $\Phi_{\mathrm{tot}} = n\Phi_0$ and $\Phi_{\mathrm{tot}} = (n + 1/2)\Phi_0$ flux values. The minimum frequency of resonance f_r^{min} corresponds to $\Phi_{\mathrm{tot}} = (n + 1/2)\Phi_0$ while the maximum frequency f_r^{max} corresponds to $\Phi_{\mathrm{tot}} = n\Phi_0$. When a probe tone is placed at a fixed frequency f_{op}, its amplitude and phase will change as a function of the flux as shown on the right side of the Figure 3.8. Since the detector flux varies over time $\Phi_{\mathrm{det}}(t)$, amplitude and phase modulation generates side bands in the output tones. However, usually the detector signals Φ_{det} are very small compared to Φ_0 and would not produce any modulation if the total flux is located close to where the variations of the frequency response $S_{21}(f_{\mathrm{op}}, \Phi_{\mathrm{tot}})$ are zero (i.e. $\partial S_{21}(f_{\mathrm{op}}, \Phi_{\mathrm{tot}})/\partial\Phi_{\mathrm{tot}} \approx 0$). This generally

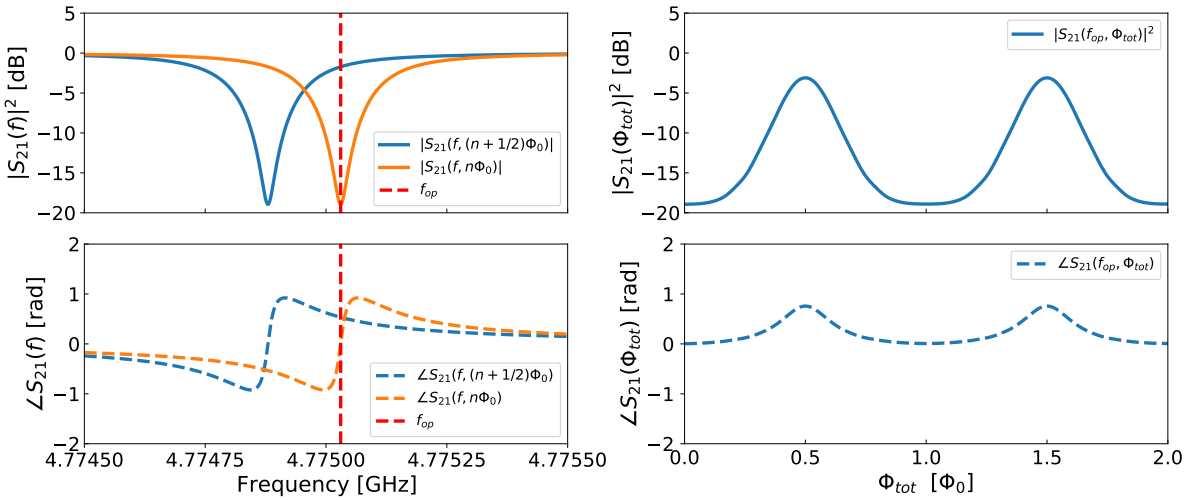

Figure 3.8: Left) Resonator frequency response $S_{21}(f, \Phi_{\text{tot}})$ for both flux values $\Phi_{\text{tot}} = n\Phi_0$ and $\Phi_{\text{tot}} = (n + 1/2)\Phi_0$. Resonator amplitude $|S_{21}(f, \Phi_{\text{tot}})|$ and phase $\angle S_{21}(f, \Phi_{\text{tot}})$ as a function of the frequency. **Right)** Resonator amplitude $|S_{21}(f_{\text{op}}, \Phi_{\text{tot}})|$ and phase $\angle S_{21}(f_{\text{op}}, \Phi_{\text{tot}})$ flux dependent responses evaluated at the operation frequency f_{op} indicated by dashed red line in the left hand side.

occurs near $\Phi_{\text{tot}} = n\Phi_0$ and $\Phi_{\text{tot}} = (n + 1/2)\Phi_0$. In order to avoid this insensible point of operation, a saw-tooth current I_{mod} is injected through an additional modulation coil. It sweeps all the possible SQUIDs operational points ensuring that the detector signal is not located at the point of lower sensitivity [87]. This linearization method is called flux-ramp modulation and is represented by the green signal in the Figure 3.7. The demodulation process as well as the flux-ramp modulation will be presented in the next Chapter 4.

3.4.1 Flux and Power-Dependent Frequency Response

Figure 3.9 shows a simplified schematic circuit diagram of a single readout channel of the µMUX depicted in Figure 3.7. Monitoring the resonator response requires a microwave tone applied to the input of the µMUX with frequency f_{exc} close to the resonance frequency. As explained before, this probe tone creates a current $i_T(t) = I_T \sin(2\pi f_{\text{exc}})$ running through the terminating inductance L_T given by Equation 3.20. Consequently, a time-varying flux component $\Phi_{\text{exc}}(t)$ is induced in the SQUID. Considering this additional flux contribution, the supercurrent in the rf-SQUID given by Equation 3.27 can be rewritten in term of the normalized fluxes as

$$I_S(t) = -I_c \sin\left[\varphi_{\text{mod}} + \varphi_{\text{exc}} \sin(\omega_{\text{exc}} t) + \beta_L \frac{I_S(t)}{I_c}\right]. \tag{3.30}$$

Here $\varphi_{\text{exc}} = 2\pi M_T I_T/\Phi_0$ is the amplitude of the time-variant magnetic flux induced by the probing tone through M_T, $\varphi_{\text{mod}} = 2\pi M_{\text{mod}} I_{\text{mod}}/\Phi_0$ is a quasi-static magnetic flux contribution induced by a current source I_{mod} coupled through M_{mod}, and I_c the critical current of the Josephson junction. The term $\varphi_{\text{scr}}(t) = \beta_L I_S(t)/I_c$ represents the self-screening flux. According to Lenz's law, a voltage $u_{\text{ind}}(t) = -M_T dI_s(t)/dt$ is created which opposes the flux changes and hence the current $i_{\text{ind}(t)}$ is induced in the resonator termination. Both currents $i_T(t)$ and $i_{\text{ind}}(t)$ are represented with grey arrows in Figure 3.9. Therefore, the total current at the resonator termination $i_{\text{tot}}(t) = i_T(t) + i_{\text{ind}}(t)$ is a superposition of two contributions originating from the microwave probing tone and the supercurrent flowing through the SQUID loop. In this way, the total voltage across the resonator termination is $u_{\text{ind}}(t) = L_T di_{\text{tot}}(t)/dt$

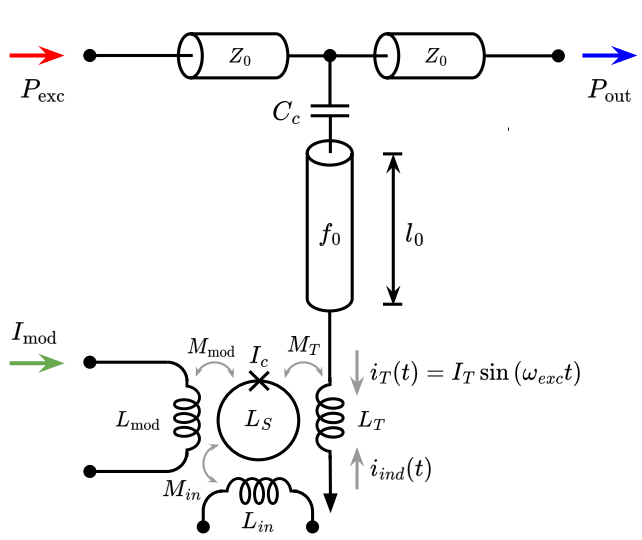

Figure 3.9: Simplified schematic circuit diagram of a single readout channel of the μMUX. The CPW resonator is terminated by an inductance L_T which is coupled to the rf-SQUID. In turn, the rf-SQUID is simultaneously coupled to the modulation L_{mod} and detector L_{in} coils respectively. The mutual coupling between each coil and the SQUID are denoted as M_T, M_{mod} and M_{in}. The probing tone with frequency f_{exc} and power P_{exc} produces a current $i_T(t)$ running at the inductive termination L_T.

and can be expressed by an effective termination inductance,

$$L_{T,\text{eff}}(\varphi_{\text{exc}}, \varphi_{\text{mod}}) = L_T \left[1 + \frac{i_{\text{ind}}(t, \varphi_{\text{exc}}, \varphi_{\text{mod}})}{i_T(t)}\right] \tag{3.31}$$

Due to the transcendental nature of Equation 3.30, there is no analytical solution for $I_S(t)$ that can be directly inserted into Equation 3.31. The required approximations and expansions of $I_S(t)$ in order to obtain a useful expression for $L_{T,\text{eff}}$ are described in analytical power-dependent model of the μMUX developed by Wegner [88]. The derived expression can be directly related to the Equation 3.14 yielding to the following resonance frequency expression as a function of the normalized fluxes $f_r(\varphi_{\text{exc}}, \varphi_{\text{mod}})$,

$$f_r(\varphi_{\text{exc}}, \varphi_{\text{mod}}) \approx f_{\text{off}} + \frac{4 f_0^2 M_T^2}{Z_0 L_S} \frac{2\beta_L}{\varphi_{\text{exc}}} \sum_{i,j} p_{i,j}(\varphi_{\text{exc}}, \varphi_{\text{mod}}), \tag{3.32}$$

where $f_{\text{off}} = f_0 - 4f_0^2(C_c Z_0 + L_T/Z_0)$ stands for the unaltered resonance frequency and $p_{i,j} = a_{i,j}\beta_L^{b_{i,j}} J_1(c_{i,j}\varphi_{exc}) \cos(c_{i,j}\varphi_{mod})$ the Taylor expansion coefficients. Here, i denotes the expansion order and j the number of contribution of each order, while J_1 is the first order Bessel function of the first kind [89]. It is not the purpose of this text to derive the model equations in detail again, but to give the basic necessary elements to understand the following sections. The $p_{i,j}$ coefficients as well as a detailed analysis can be found in the following references [88, 90]. The validity of this model sets an upper limit for $\beta_L \leq 0.6$ and assumes a probing tone frequency f_{exc} close to the resonance frequency of the resonator f_r, leading to a maximum oscillating anti-node current amplitude given by Equation 3.20. The previously introduced expression can be inserted into the resonator transmission scattering parameter (Equation 3.15) in order to find the flux dependence of the resonator frequency response $S_{21}(f_{\text{exc}}, \varphi)$. The expression becomes,

$$S_{21}(f_{\text{exc}}, \varphi_{\text{exc}}, \varphi_{\text{mod}}) = \frac{S_{21}^{\min} + 2jQ_l\left(\frac{f_{\text{exc}} - f_r(\varphi_{\text{exc}}, \varphi_{\text{mod}})}{f_r(\varphi_{\text{exc}}, \varphi_{\text{mod}})}\right)}{1 + 2jQ_l\left(\frac{f_{\text{exc}} - f_r(\varphi_{\text{exc}}, \varphi_{\text{mod}})}{f_r(\varphi_{\text{exc}}, \varphi_{\text{mod}})}\right)}. \tag{3.33}$$

3.4.2 Resonance Circle

Expression 3.33 represents a perfectly symmetric lossy resonator [91, 92]. This equation describes a Lorentzian shaped frequency response, while in the complex plane follows a semi-circular trajectory with a center at $(x_c, 0)$ and radius $r = 1 - x_c$, with $x_c = (1 - S_{21}^{\min})/2$. The S_{21} parameter is shown in Figure 3.10, where the axes represent the real part $\mathrm{Re}(S_{21})$ and imaginary part $\mathrm{Im}(S_{21})$ of the scattering parameter. This trajectory is approximately the same for flux or frequency sweeps in the case of a negligible junction sub-gap resistance [93]. The symmetric frequency response described by Equation 3.33 is a consequence of good impedance matching between the resonator and the associated feed-line [91]. The orange trajectory in Figure 3.10 describes the trajectory $S_{21}(f, \varphi_0)$ as a function of frequency for constant flux φ_0. At resonance, the scattering parameter $S_{21}(f_r) = S_{21}^{\min} \approx Q_l/Q_i$ is real-valued while for frequencies $f \to \infty$ and $f \to 0$, the scatter parameter approaches the off-resonance point $(1, 0)$. Analogously, the blue trajectory represents a constant frequency as a function of flux $S_{21}(f_{\mathrm{exc}}, \varphi)$. In this case, the amplitude of the excursion depends on the peak-to-peak resonance frequency variation given by Equation 3.32. Using the resonance circle, two useful quantities can be defined. One is the amplitude of the scattering parameter γ represented with a red arrow in Figure 3.10 and defined as

$$\gamma = |S_{21}(f)| = \sqrt{\mathrm{Re}(S_{21})^2 + \mathrm{Im}(S_{21})^2}. \tag{3.34}$$

The second one is the resonator phase θ measured from the resonator rotating frame $(x_c, 0)$ given by

$$\theta = \arctan\left(\frac{\mathrm{Im}(S_{21})}{x_c - \mathrm{Re}(S_{21})}\right). \tag{3.35}$$

These two quantities are shown as a function of frequency and flux in Figure 3.8 demonstrating the μMUX working principle. While the resonator circle is defined by γ and θ, when using a Vector Network Analyzer (VNA) to characterize the frequency response, θ is not directly measured. Instead, the VNA measures the power ratios and phases difference between incident and transmitted waves, therefore it measures ϕ defined as

$$\phi = \arctan\left(\frac{\mathrm{Im}(S_{21})}{\mathrm{Re}(S_{21})}\right). \tag{3.36}$$

For the purpose of this thesis, ϕ is called readout phase and the resonator phase is calculated at post-processing using γ and ϕ or equivalently the S_{21} coordinates. In the next chapter, these three quantities will be used to explain the readout and noise performance of a μMUX device.

3.4.3 Bandwidth and Maximum Frequency Shift

The extensions of the trajectory for a constant probing frequency f_{exc} represented in blue in Figure 3.10 yields a maximum frequency shift $\Delta f_r^{\max} = f_r^{\max} - f_r^{\min}$. This quantity can be calculated by finding the maximum $f_r^{\max}$ and minimum $f_r^{\min}$ values of the resonance frequency given by Equation 3.32. This quantity is usually expressed in relation to the resonator bandwidth BW_{res} using a dimensionless parameter η defined as

$$\eta(P_{\mathrm{exc}}) = \frac{\Delta f_r^{\max}(P_{\mathrm{exc}})}{BW_{\mathrm{res}}}. \tag{3.37}$$

Along with the resonance frequency, η also depends on the probing tone power. In the case of high power levels, $\eta(P_{\mathrm{exc}}) \to 0$, and consequently the μMUX becomes insensitive to flux changes. On the other hand, for vanishing powers η reaches a constant value given by

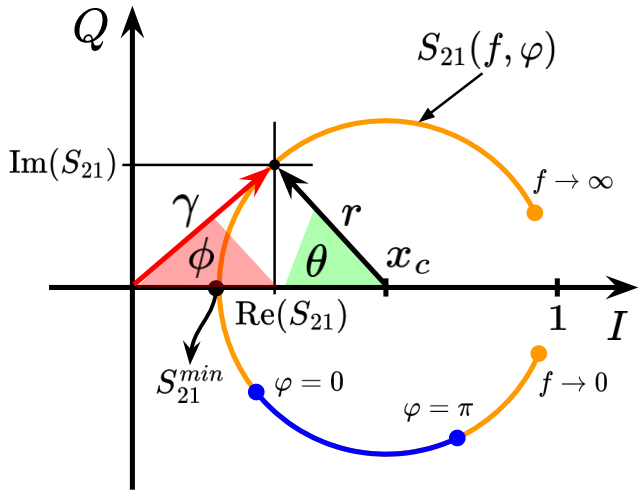

Figure 3.10: Complex Plane representation of the transmission scattering parameter $S_{21}(f,\varphi)$ given by Equation 3.33. I and Q represent the real and imaginary axis respectively. The response describes a circle with radius r centered at $(x_c, 0)$. The $S_{21}(f,\varphi_0)$ as function of frequency for constant flux φ_0 is represented in orange, while the trajectory for constant frequency as function of flux $S_{21}(f_{\mathrm{exc}},\varphi)$ is blue. $\gamma = |S_{21}(f)|$ and θ are the resonator amplitude and phase, respectively, while ϕ is the readout phase.

$$\lim_{P_{\mathrm{exc}}\to 0} \eta(P_{\mathrm{exc}}) = \eta_0. \tag{3.38}$$

Larger values $\eta_0 \gg 1$ are not commonly used because several resonator bandwidths BW_{res} away from the resonance frequency, the Lorentzian response $S_{21}(f)$ becomes constant and again insensitive to flux changes. Additionally, low power levels represent a degradation in signal-to-noise as will be explained in detail later. Values between $0.8 < \eta(P_{\mathrm{exc}}) < 1$ have been proved to be good compromises between sensitivity and noise performance [43, 92].

3.4.4 Crosstalk and Resonance Spacing

One of the main limitations in the μMUX multiplexing factor is the crosstalk between resonators. For example, the tail of the Lorentzian response of a resonator at f_1 extends over the frequency response of a neighbour resonator at f_2. The crosstalk level between resonators placed at frequencies f_1 and f_2 separated n number of resonators bandwidths BW_{res} (i.e. $n = (f_2 - f_1) = BW_{\mathrm{res}}$) can be estimated using [94]

$$\chi_{\mathrm{res}} \approx \frac{1}{2}\frac{S_{21}^2(f_2)}{n^2}. \tag{3.39}$$

This simplification illustrates the $1/n^2$ dependence of Lorentzian crosstalk on the frequency separation between resonators and the suppression of crosstalk when the probe tone is on resonance. In order to maintain crosstalk between frequency adjacent resonators below 0.1%, an average space resonances by roughly 10 times their bandwidth is required. In the context of this thesis, a resonator bandwidth of $BW_{\mathrm{res}} \approx 200$ kHz, 4 MHz resonator spacing (i.e. $n = 20$) and an available LNA bandwidth of $BW_{\mathrm{LNA}} = 4$ GHz is considered, yielding a maximum multiplexing factor of $N_{\mathrm{mux}} \approx 1000$ compatible with the focal plane requirements for QUBIC for a single polarization. In case of implementing dual polarized pixels, the number of RF chains will be doubled. It is important to note that spacing resonators closer than 1 MHz represents a major challenge given the tolerances of current nano-fabrication processes [70]. Another mechanism of crosstalk to be considered is the electromagnetic coupling between SQUIDS χ_{mag} and Inter-Modulation Distortion (IMD) generated by cryogenic LNA χ_{imd} that

overlaps with other channels, nevertheless they can be partially mitigated using adequate frequency placement and improving the linearity of the cryogenic set-up [94].

3.4.5 µMUX Prototype Parameters

Similar to Chapter 2, the design parameters of a prototype µMUX were defined and used as the starting point for the design of the readout system. The design parameters are listed in Table 2.1. A maximum crosstalk level of $\chi_{res} < 0.1\%$ was defined, representing a total amount of $N_{mux} = 1000$ channels in the available bandwidth given the available cryogenic LNA[1]. This condition was based on a resonator bandwidth of $BW_{res} \approx 200$ kHz compatible with the achievable intrinsic quality factors and with the required readout bandwidth. In order to maintain the constant bandwidth BW_{res} for all frequencies in the range 4 to 8 GHz, the coupling factors are adjusted by the capacitance C_i given by the interdigital capacitor shown in Figure 3.2. Generally, each multiplexer has a fixed number of N_{chan} channels and the total multiplexing N_{mux} factor is achieved by cascading several chips $N_{chip} = N_{mux}/N_{chan}$. Today the maximum number of channels per chip is $N_{chip} = 65$ [70], but the first prototype used in this thesis has $N_{chan} = 9$ channels. Although the multiplexer has several channels, by design they all have the same frequency response, only shifted in frequency. For the purpose of extracting parameters for the readout system, it has been assumed that the individual behavior of all channels is the same and can be represented by the parameters of a single channel described by the parameters in the Table 3.1.

Table 3.1: µMUX prototype channel parameters used during simulations. These are the typical design parameters for a µMUX optimized for bolometric applications.

Parameter	Symbol	Value	Unit
Unloaded resonator resonance frequency	f_0	5	GHz
Resonator characteristic impedance	Z_0	50	Ω
rf-SQUID inductance	L_S	30	pH
Terminating inductance	L_T	100	pH
Screening parameter	β_L	0.6	-
rf-SQUID to resonator mutual inductance	M_T	1.2	pH
rf-SQUID to modulation line mutual inductance	M_{mod}	20	pH
rf-SQUID to detector line mutual inductance	M_{in}	100	pH
Resonator intrinsic quality factor	Q_i	$2 \cdot 10^5$	-
Coupling capacitance	C_c	5	fF

It is important to highlight that in a real multiplexer, variations in the characteristics of the materials and the manufacturing process produce dispersion in the characteristics of the channels. Therefore, it is the job of the µMUX developers either by design, fabrication or subsequent adjustment to equalize the response of the channels [90, 95]. If this is not possible, the readout should be optimized for each channel individually.

The µMUX analytical model described by Equations 3.32 and 3.33 was numerically implemented using Python and tested with device parameters typical for a µMUX device used in bolometric applications [70] (see Table 3.1). Using Equation 3.32 the unaltered resonance frequency was calculated yielding $f_{off} \approx 4.775$ GHz, while the peak-to-peak frequency shift Δf_r^{mod} for vanishing readout powers $P_{exc} \to 0$ matches the resonator bandwidth $BW_{res} \approx 200$ kHz (i.e. $\eta_0 \approx 1$). The resulting resonance depth for this resonator bandwidth is $S_{21}^{min} \approx -18$ dB. Figure 3.11 shows the maximum f_r^{max} and minimum f_r^{min} resonance frequencies as a function of the probe tone power P_{exc}. The difference between both corresponds

[1] https://lownoisefactory.com/product/lnf-lnc4_8g/

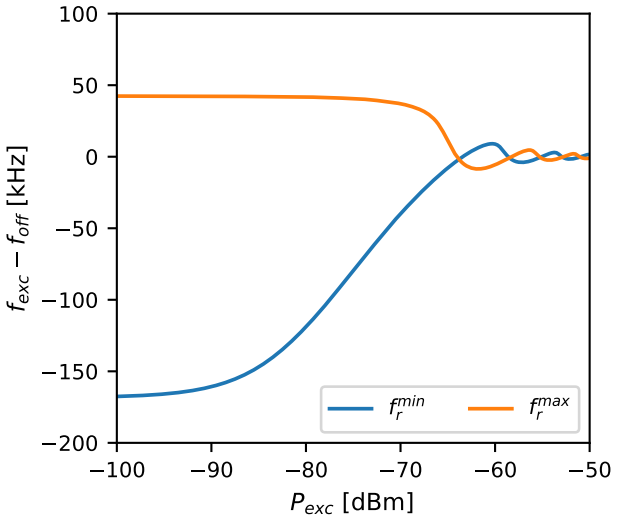

Figure 3.11: Maximum $f_r^{\max}$ (orange) and Minimum $f_r^{\min}$ (blue) resonance frequencies as a function of the probe tone power P_{exc} for µMUX parameters described in Table 3.1. At $P_{\text{exc}} \approx -64$ dBm both frequencies intersect, meaning that the µMUX channel becomes insensitive to flux. Both curves are represented in relation to the unaltered resonance frequency f_{off}.

to Δf_r^{mod}. Since the probing tone frequency f_{exc} is commonly placed close to the unaltered resonant frequency f_{off}, it is more convenient to express it in terms of the difference $f_{\text{exc}} - f_{\text{off}}$ instead of its absolute frequency. This metric was adopted for the graphs in this work. Accordingly to the analytical model predictions at a power levels around $P_{\text{exc}} \approx -64$ dBm the resonator becomes insensitive to the modulation flux φ_{mod} [88]. For this reason, simulations performed in this work were limited to a power range between -90 dBm and -60 dBm. It should be noted that the required condition of a probe tone frequency f_{exc} close to the resonance frequency f_r cannot be always satisfied, yielding to an overestimation of the radio-frequency flux induced within the rf-SQUID when the probing tone is far away from it. In this case, an analytical calculation of $I_T(f_{\text{exc}})$ cannot be found due to the recursive relation between $f_r(\varphi_{\text{exc}})$ and $\varphi_{\text{exc}}(f_r)$. Therefore, a similar solution to that used in previous articles [92] was adopted. But in this case, the maximum value of the anti-node current I_T given by Equation 3.20 was scaled using narrow-band approximation of the transmission line resonator frequency response given by expression 3.33. This iterative process starts at the condition of zero readout power $P_{\text{exc}} \to 0$ to derive a first guess $f_r^{i=0}$ and then executes the power-dependent model sequentially using the previous results f_r^{i-1} until the equilibrium are reached or equivalently the convergence criteria is satisfied $f_r^{i-1} \approx f_r^i + \epsilon$.

Despite the advantages of the µMUX, reducing integration complexity and achieving manageable thermal loads, challenges in both cold and warm components, hinder these systems from achieving their full multiplexing potential and maintaining the readout noise subdominant to the intrinsic detector noise [70]. In the case of high-count bolometric applications like QUBIC, the μMUX covers a huge bandwidth of several GHz and requires higher drive powers due to the total amount of channels. For a cold readout, this represents strong requirements for linearity and noise factors [96], while for the warm electronics, it imposes the requirement to generate and acquire high-frequency, high-purity broadband signals, typically in the range between 4 and 8 GHz and process them in real time without degrading the performance imposed by cold readout. In the next chapter, the µMUX readout system is introduced as well as the noise performance analysis for the particular case of QUBIC using MMBs.

4. Microwave SQUID Multiplexer Read-out System

The microwave SQUID multiplexer combines the frequency selectivity of superconducting resonators with the sensitivity of rf-SQUIDS to encode the detector signals at the resonant frequencies of different resonators. As explained above, the state of each resonator and therefore, of the detector, can be monitored individually through only two coaxial lines entering the cryostat. In this way, it is possible to reduce the thermal load, complexity and increase the integration level. However, like every element of the detection chain, the multiplexer and the required readout system inevitably also contribute to the overall noise present in the scientific data. Therefore, it is important to understand the associated noise sources in order to design the multiplexing and readout systems without degrading the intrinsic performance of the detectors.

The readout system is responsible for generating a probing tone for each channel and then, once modulated by the μMUX, demodulate the detector signals. While this sounds simple, it imposes stringent requirements for generating and acquiring high-purity wide-band microwave signals. Similarly to communications systems, the noise performance of these systems depends on the type of modulation used, the signal strength and the noise sources. This chapter aims at evaluating the impact of the readout electronics systems in the overall readout performance in order to determine the requirements for its subsequent design and characterization. With this objective in mind, a new simulation framework for the readout of Microwave SQUID Multiplexers was developed extending the capabilities of the available ones [97, 92]. Previously developed frameworks solely consider additive noise, commonly attributed to the cryogenic LNA. However, characterizations preformed over different readout systems unveil the presence of multiplicative noise [98, 99, 100]. These extra noise sources were included and their impact in the system performance was evaluated as a function of the readout parameters. Since the noise sources added act in different domains, the most commonly used demodulation domains, i.e. resonator phase and amplitude, were also included. Along this chapter and by means of single channel noise simulations, the maximum readout system noise levels accepted to satisfy the design condition given by Equation 2.20 were found.

This chapter is based on reference [101] and is organized as follows: Section 4.1 presents the readout signal model and the different noise sources attributed to the readout system. Section 4.2 describes the different demodulation schemes. In Section 4.3, through simulations, the minimum-noise readout parameters for additive noise in both demodulation schemes are found and the impact of the remaining noise sources under these conditions using a variety of different demodulation parameters are evaluated. In addition, the impact of a typical readout system is analyzed as an example. Finally, in Section 4.4 a description and characterization of the cryogenic microwave read-out chain installed in our dilution refrigerator is given.

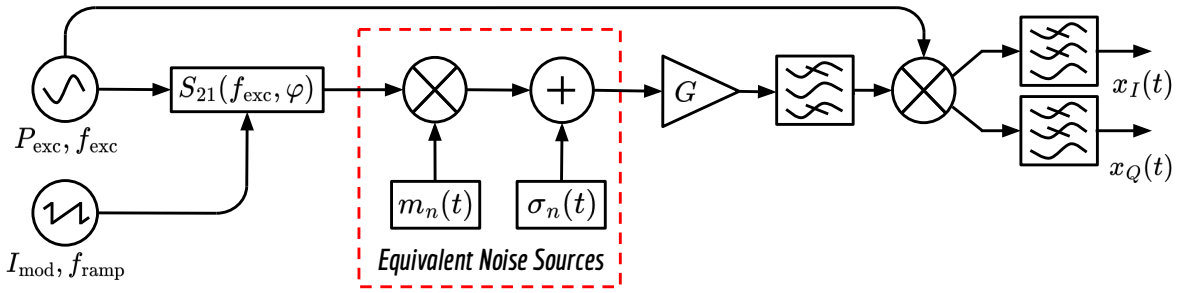

Figure 4.1: Block diagram of the homodyne readout system used for the readout of a Microwave SQUID Multiplexer. **From left to right)** Microwave and arbitrary signal generators in charge of generating the probing tone and flux modulation, μMUX device, equivalent noise sources, low-noise amplifiers, filters and IQ mixer for signal conditioning and down-conversion. The noise sources inside the red rectangle $\sigma_n(t)$, $m_n(t)$ represent the additive and multiplicative noise sources attributed to the readout system and referred to the μMUX output.

4.1 Readout System Model

A simplified block diagram of the homodyne system used for the readout of a single μMUX channel is shown in Figure 4.1. For the sake of simplicity, several of the microwave/RF components comprising the cold and the warm-temperature electronics were condensed into single blocks while preserving its functionality. They will be described in detail later. Generally the terms "cold" and "warm" are used to differentiate the microwave/RF components of the readout system that are inside or outside the cryostat, respectively. The most important components of this system are: 1) a microwave synthesizer capable of generating the probing tone with frequency f_{exc}, and available power P_{exc} at the μMUX input port, 2) an arbitrary current waveform generator able to provide the required flux modulation φ_{mod} with frequency f_{ramp}, 3) the μMUX device described by the behavioral model explained in Section 3.4.1, 4) a set of noise sources representing all noise contributions attributed to the readout system (dashed red box), 5) low-Noise amplification and filtering stages in charge to boost the signals and filter out unwanted components maintaining the Signal-to-Noise Ratio (SNR) and, 6) a complex IQ mixer that down-converts the signal in order to be processed later.

4.1.1 Measured Signals

In this section a continuous-time analytical signal model is used to describe the readout process. Therefore, the time-dependence is introduced considering a time varying modulation flux $\varphi_{\text{mod}}(t)$. The quasi-static flux condition imposed for Equation 3.30 is fulfilled ensuring flux variations considerably slower compared to the resonator ring-down time $\tau_{\text{down}} \approx 1/2\pi BW_{\text{res}}$ and consequently even slower than $\tau_{\text{exc}} = 1/2\pi f_{\text{exc}}$. This condition allowed the resonator to keep track of the flux variations while maintaining the steady-state frequency response described by Equation 3.33 [92, 87]. Nevertheless, our simulation model allows a first order approximation of the dynamic response by means of a low-pass filtered version of S_{21}. In order to simplify the nomenclature and facilitate the following analysis, the time dependence of the transmission parameter $S_{21}(t)$ as a consequence of the flux variations $\varphi(t)$ will only be explicitly shown. In these conditions, the complex base-band signal $x(t) = x_I(t) + jx_Q(t)$ at the output of the homodyne readout system shown in Figure 4.1 can be expressed as

$$x(t) = G' V_{\text{exc}} S_{21}(t) m_n(t) + G' \sigma_n(t). \tag{4.1}$$

Where $V_{\text{exc}} = \sqrt{2P_{exc}Z_0}$ is the amplitude of the probing tone, while $\sigma_n(t)$ and $m_n(t)$ are

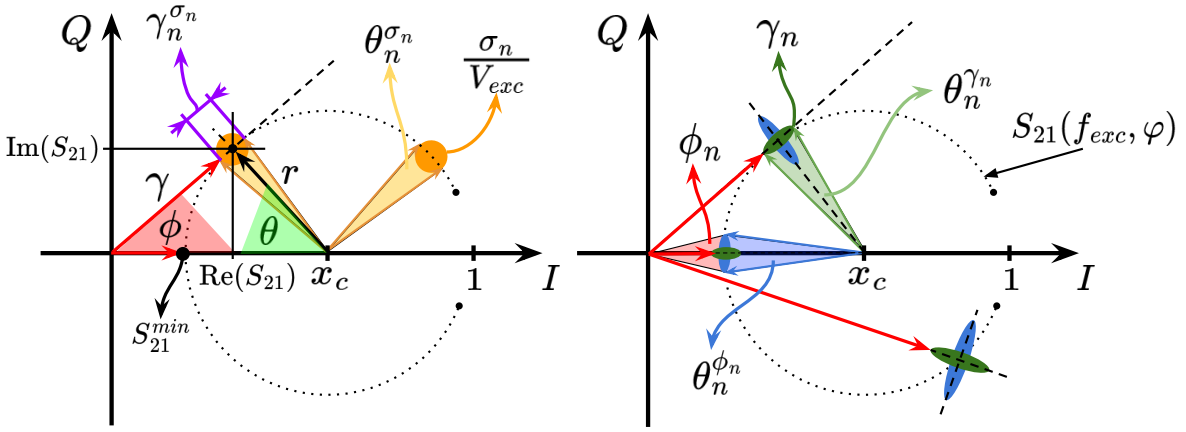

Figure 4.2: Complex plane representation of the scattering parameter $S_{21}(f_{\text{exc}}, \varphi)$ in its canonical form, with the readout noise sources. Red arrows represent the normalized measured signal phasor with amplitude γ and phase ϕ, while θ is the resonator phase measured from its rotating frame. **Left)** Additive source: Johnson–Nyquist noise $\sigma_n(t)/V_{\text{exc}}$ represented as a circular orange noise cloud. **Right)** Multiplicative sources: Phase $\phi_n(t)$ and Amplitude $\gamma_n(t)$ noises represented with the blue and green ellipses respectively. The projection of each noise source into the resonator phase and amplitude demodulation domains are denoted as: $\gamma_n^{\sigma_n}(t)$, $\theta_n^{\sigma_n}(t)$, $\theta_n^{\gamma_n}(t)$ and $\theta_n^{\phi_n}(t)$. The superscript stands for the noise source that is being projected.

the additive and multiplicative noise terms, respectively. Here, an ideal IQ mixer and a gain factor $G' = Ge^{j\alpha}e^{2j\pi f_{\text{exc}}\tau}$ including the overall gain G, phase offset α and time delay τ added by the RF components and cables were considered. In the context of a real measurement, G' can be determined during the calibration process as it will be described later. For the purpose of this chapter, all of the aforementioned parameters are assumed to be known and constant over time for the probing tone frequency f_{exc}. During the down-conversion process the time dependence of the excitation signal $e^{-j2\pi f_{\text{exc}}t}$ was removed keeping only the complex envelope of the modulated probing tone being equal to the scaled transmission parameter time-trace $G'S_{21}(t)$. When f_{exc} is located out of resonance, the transmission parameter is close to unity and the measured average signal amplitude approximately equals to $x^{\text{off}}(t) \approx G'V_{\text{exc}}$. This value is used to define a normalized signal as

$$\frac{x(t)}{x^{\text{off}}(t)} = S_{21}^{\text{meas}}(t) = S_{21}(t)m_n(t) + \frac{\sigma_n(t)}{V_{\text{exc}}}. \tag{4.2}$$

Thus, the normalized signal is basically an estimation of the actual transmission parameter $S_{21}(t)$. Figure 4.2 shows the complex representation of S_{21}^{meas} where, as was mentioned in Section 3.4.2 and for the noise-less case, the measured signal (red arrow) describes a semi-circle centered at x_c with radius r as a consequence of a flux sweep. Contrarily, in a real scenario represented by Equation 4.1, noise sources produce a deviation from this trajectory that cannot be distinguished from the flux variations produced by the detector signal and are interpreted as a flux noise. Therefore, a detailed description of the noise sources affecting the system is required in order to calculate the error in the transmission parameter determination and consequently derive the equivalent flux noise represented by each one.

4.1.2 Noise Sources

As it was done for the MMB in Section 2.2.3, all noise sources acting on the μMUX and readout system must be identified. Since the objective of this thesis is to evaluate the impact of

the readout system on the total noise, the noise sources were divided in two groups. The first group is composed by the noise sources specific to the readout system, including both the noise generated in the probing tones given the analog or digital processing and the noise present in the modulation current needed to modulate the rf-SQUID flux. The second group represents the noise sources intrinsic to the µMUX such as the Two-Level System Noise (TLS) and the SQUID noise. This section will only focus on the noise present in the probing tones and TLS. This is due to two reasons: first, the flux-ramp modulation system represented with a current generator in Figure 4.1 is being designed in parallel by other researchers and is not part of the work of this thesis. Assuming its proper design, we consider its contribution to the overall system noise negligible. Second, when determining the optimal readout domain, only noise sources that affect the phase or amplitude of the probing tones in different ways were considered. This is exclusively the case for TLS noise.

Readout System Noise

Readout noise refers to all types of noise affecting the probing tones which creates a modulation that cannot be distinguished from the multiplexer's own modulation. This noise can be present from the moment the tones were generated or can be added at each stage of the modulation/demodulation process progresses. Generally, the most common noise sources are divided into two categories based on how they affect the signal. These are additive or multiplicative. Additive noise refer to all kinds of noise sources that are directly added to the desired signals and remain even if the desired signal is not present. Considering the scope of this work, and based on previous articles [92, 102], only Johnson–Nyquist noise $\sigma_n(t)$ was considered. Johnson–Nyquist noise can be modeled as

$$\sigma_n(t) = \sigma_I(t) + j\sigma_Q(t), \tag{4.3}$$

where the real and imaginary components of $\sigma_n(t)$ are both zero-mean, finite power, Independent and Identically Distributed (IID) Gaussian random variables. A normalized version $\sigma_n(t)/V_{\text{exc}}$ can be seen as an orange circular noise cloud in Figure 4.2. This model is well-suited to describe a wide range of noise sources present in readout electronics systems such thermal, electric or quantization. In a properly designed system, the additive noise is typically dominated by the cryogenic High-Electron Mobility Transistor (HEMT) amplifier [103]. Because of their importance, many groups are actively trying to improve the HEMT amplifiers or even replace them with new amplification technologies such as quantum-limited parametric amplifiers [104, 102]. While these new technologies represent an important reduction of the additive noise level, they make evident the presence of other types of sources such as those described below. Additionally to the Johnson–Nyquist noise, spurious signals generated by the electronics [105] can be also included as additive interferences, but for the scope of this work they will not be included because unlike noise, they are localized in frequency and can be mitigated using a properly frequency planning [106] or increasing the linearity of the processing chain.

Contrary to additive sources, multiplicative noise sources depend on the presence of the desired signal. Their amplitude depend on the signal strength and mathematically, as the name implies, the noise is multiplied with the desired signal $S_{21}(t)$ as

$$m_n(t) = [1 + \gamma_n(t)]e^{j\phi_n(t)}. \tag{4.4}$$

This work will only focus on amplitude $\gamma_n(t)$ and phase $\phi_n(t)$ noise which are the most common multiplicative noise sources present in readout electronics systems [107, 108]. Both are real random variables described by their auto-correlation function as explained in Subsection 4.1.3. A simplified and magnified representation of these noises using colored ellipses is shown in the right side of Figure 4.2. The term $\gamma_n(t)$ represents small signal variations (green

ellipses) parallel to the measured signal phasor (red arrow), while $e^{j\phi_n(t)}$ can be seen as perpendicular signal variations (blue ellipses). Due to their multiplicative nature, when the measured signal amplitude decreases (i.e., at resonance), the voltage fluctuations decrease proportionally, keeping the amplitude and phase variations constant. Traditionally, amplitude and phase noise are terms used to describe short-term variations or instabilities, with "short-term" referring to time intervals of the order of seconds or less [109]. These are commonly generated when some system parameter randomly fluctuates (e.g. due to thermal or flicker noise) translating that variation to the desired signal. This process called parametric up-conversion does not differ too much from the μMUX working principle where the resonance frequency (system parameter) is modulated proportionally to the detector signal.

Two-Level Systems Noise

This manuscript additionally includes the Two-Level System Noise. Although TLS noise is not generated by the readout electronics, it can act differently depending on the demodulation domain and readout parameters as well as the readout noise sources. The evidence suggest that this noise is caused by Fluctuating Two-Level Systems (TLS) in dielectric materials, either the bulk substrate or its exposed surface, the interface layers between the metal films and the substrate, or any oxide layers on the metal surfaces that comprises the transmission line resonator [110, 111]. This noise affects the distributed capacitance and therefore produces fluctuations in the resonance frequency that are seen as rotations of the resonance circle around its center. As well as amplitude noise in Equation 4.4, it can be expressed as frequency fluctuations $f_r \cdot f_{\mathrm{TLS}}(t)$ around the resonance frequency f_r using

$$f_{\mathrm{r}}(t) = f_r[1 + f_{\mathrm{TLS}}(t)]. \tag{4.5}$$

4.1.3 Noise Metrics

Due to its random nature, noise is analyzed as a stochastic process. For a wide-sense-stationary and ergodic random process $y(t)$, the Wiener-Khinchin theorem says that a power spectral density can be defined in terms of the Fourier transform of the statistical expected value, e.g. the auto-correlation function [112, 107] as follows

$$S_y(\Delta f) = \mathcal{F}\left\{R_{yy}(\tau)\right\} = \mathcal{F}\left\{\langle y(0), y(\tau)\rangle\right\}. \tag{4.6}$$

Thus, spectral features of noise are entirely determined by the Noise Spectral Density $S_y(\Delta f)$ (NSD). The requirement that noise be stationary and ergodic are the equivalent of "repeatable" and "reproducible" in experimental physics. Particularly in this case where the noise around the probing tones is being analyzed, $S_y(\Delta f)$ is the base-band representation of the NSD measured at a frequency offset Δf from the probing tone frequency f_{exc}. In other words, it is the complex noise envelope. For the case of Johnson–Nyquist noise, the statistic independence implies white noise with constant NSD equals to $S_N = k_B T_{\mathrm{n}}$, where T_{n} is the so called noise temperature and k_B the Boltzmann's constant. Therefore, the NSD of the normalized Johnson–Nyquist noise respect to the probing tone amplitude $\sigma_n(t)/V_{\mathrm{exc}}$ is

$$S_{\sigma_n}(\Delta f) = \frac{k_b T_{\mathrm{n}}}{P_{\mathrm{exc}}}. \tag{4.7}$$

This quantity is usually expressed in dBc/Hz, and T_{n} is the noise equivalent temperature referred to the μMUX output (see Figure 4.1). In the context of this work, a distinction between T_{n} and T_{sys} is required due to the fact that T_{sys} is commonly experimentally determined and, as will be explained later, corresponds to an equivalent noise temperature that takes into account all the different noise sources acting simultaneously and producing the same system noise level [102].

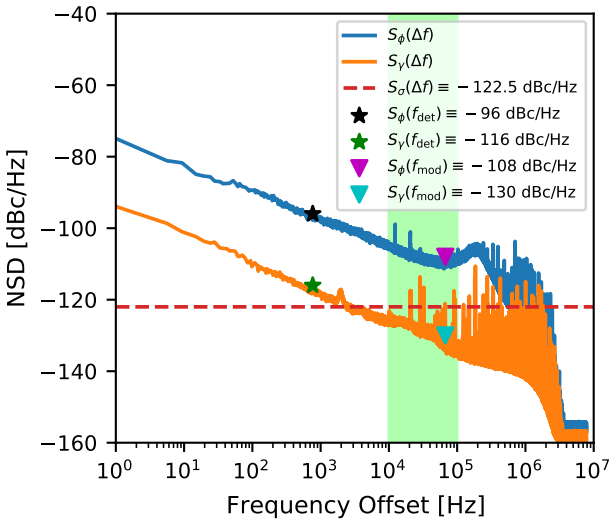

Figure 4.3: Noise spectral densities for typical cold and warm-temperature readout systems at a frequency of $f_{exc} \approx 5.4$ GHz. Blue and orange solid lines are the residual phase and amplitude noise spectral densities. The dashed red represents the additive NSD calculated by Equation 4.7 using an equivalent noise temperature of $T_n = 4$ K and probing power $P_{exc} = -70$ dBm.

On the other hand, amplitude, phase or TLS noise exhibits certain degree of correlation between realizations yielding to colored noise spectral densities. They are commonly described by a power law such as

$$S_y(\Delta f) = \sum_n b_n (\Delta f)^n. \tag{4.8}$$

With values of $n = [-4, 0]$ for phase, $n = [-2, 0]$ for amplitude [107] and $n = [-1, -1/2]$ for TLS [110]. As in the case of Johnson–Nyquist, phase and amplitude noises are expressed in dBc/Hz and represent the noise power integrated in a 1 Hz bandwidth at a Δf offset from f_{exc} relative to the probe tone power. In the TLS case, it is expressed in fractional frequency fluctuations $S_{f_r}(f)/f_r^2$ in units of Hz^{-1}. Unlike uncorrelated noise sources, depending on the degree of correlation, correlated noise can be removed. This is the case for phase noise in radio systems which use different oscillators and clocks locked to the same frequency reference during up-and down-conversion processes as well as during generation and sampling. Therefore, $\phi_n(t)$ used in Equation 4.4 stands for the so-called "residual" phase noise [108]. Since it is a multiplicative quantity, it can be arbitrarily referred to any part of the circuit yielding the same behavior.

4.1.4 Readout System Noise Example

As an example, Figure 4.3 shows readout residual amplitude $S_\gamma(\Delta f)$ and phase $S_\phi(\Delta f)$ noise spectral densities for a Software-Defined Radio (SDR) readout system based on the RFSoC ZCU216 evaluation kit [113]. Black and green stars represent phase and amplitude noise measured at $f_{det} \approx 762$ Hz. The green region covers the possible modulation frequencies f_{mod} where the signal of interest is typically located in the case of bolometric applications [105]. Particularly, for a modulation frequency $f_{mod} \approx 62$ kHz phase and amplitude noise takes values represented by the magenta and cyan triangles respectively. These measurements were taken at a frequency of $f_{exc} \approx 5.4$ GHz using a loop-back cable connecting transmitter (Tx) and receiver (Rx) ensuring that most of the coherent noise is removed in the down-conversion/sampling process [105]. A power sweep was performed until the amplitude and phase spectra reached power-independent values consistent with the nature of the multiplicative noise. At frequency offsets below 10 kHz, amplitude and phase noise densities have -10 dB/decade slopes demonstrating the colored behavior described by Equation 4.8, while the roll-off at frequencies above 1 MHz is due to the low-pass filter applied during

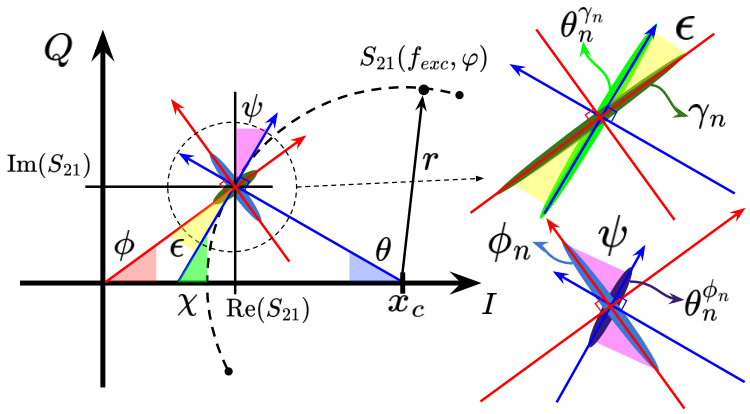

Figure 4.4: Detailed description of the projections of each noise source for both demodulation domains. Amplitude γ and phase θ measured form the resonator rotating frame.

signal channelization. In contrast to the multiplicative sources, the additive noise spectral density, which is generally dominated by the cold readout system, was theoretically calculated using Equation 4.7, assuming $T_{\text{n}} = 4$ K and probing power $P_{\text{exc}} = -70$ dBm yielding $S_\sigma(\Delta f) \approx -122.5$ dBc/Hz. The noise values shown in Figure 4.3 are used in the last section of this chapter along with the μMUX model (Table 3.1) with the goal of estimating the expected readout noise performance. The system characterization procedure, as well as the origin of these noise sources will be explained in detail in Chapters 6 and 7.

4.2 Demodulation Domains and Schemes

The error term in the determination of the transmission scattering parameter as a function of time $S_{21}(t)$ can be written as

$$\delta S_{21}(t) = S_{21}(t)\gamma_n(t)e^{j\phi_n(t)} + \frac{\sigma_n(t)}{V_{\text{exc}}}. \tag{4.9}$$

Slow variations in the flux, given either by a modulation $\varphi_{\text{mod}}(t)$ or a detector $\varphi_{det}(t)$, lead to variations of the resonator frequency response as described by equation 3.33 and depicted in Figure 4.2. The most widely used domains in which these variations are demodulated are: 1) The resonator phase measured from its rotating frame $\theta(f_{\text{exc}}, \varphi)$ defined by Equation 3.35 [114, 115, 102] and 2) The amplitude of the transmission scattering parameter $\gamma(f_{\text{exc}}, \varphi)$ defined using Equation 3.34 [116, 92]. A representation of both domains is shown again on the left side of Figure 4.2 together with the different sources of noise. While both domains are used showing outstanding performance, at the time of this doctoral research, there was no analytical or simulation framework to allow the comparison of their performance in the presence of readout noise, especially multiplicative noise as described in the previous Subsection 4.1.2, hence the interest in developing this simulation framework. With the help of equations 3.34 and 3.35 it is possible to define the projection of the error term $\delta S_{21}(t)$ in the aforementioned domains. Considering that noise amplitudes are considerably small compared to $S_{21}(t)$ variations produced by flux changes, each noise source can be geometrically projected into the corresponding demodulation domain.

The nomenclature adopted to describe these projections is the following: $\theta_n^{\sigma_n}(t)$, $\gamma_n^{\sigma_n}(t)$ correspond to the resonator phase and scattering amplitude error due to additive noise $\sigma_n(t)$, while $\theta_n^{\phi_n}(t)$ and $\theta_n^{\gamma_n}(t)$ correspond to the resonator phase error due phase $\phi_n(t)$ and amplitude $\gamma_n(t)$ noise respectively. In other words, the superscript indicates the noise source that is being projected. Unlike the rest, amplitude noise $\gamma_n(t)$ is already projected into the amplitude domain by definition. These projections are depicted in the right side of Figure 4.2 using shaded yellow, green, red and blue triangles. Figure 4.4 shows a detailed description of Figure 4.2.

Using triangles properties, it can be easily demonstrated that $\psi = \pi/2 - \epsilon = \theta + \phi$, therefore, using the adequate trigonometric relations the projections of amplitude $\gamma_n(t)$ and phase $\phi_n(t)$ readout noise into the resonator phase $\theta(t)$ can be written as follows,

$$\theta_n^{\gamma_n}(t) \approx \gamma_n(t)\cos(\epsilon) = \gamma_n(t)\frac{\gamma}{r}\sin(\theta+\phi), \tag{4.10}$$

$$\theta_n^{\phi_n}(t) \approx \phi_n(t)\cos(\psi) = \phi_n(t)\frac{\gamma}{r}\cos(\theta+\phi), \tag{4.11}$$

where the approximation $\theta \approx \Delta_\perp / r$ was used to convert absolute voltage variations into phase units. r stands for the resonance circle radius, while $\Delta_\perp$ represents voltage variations perpendicular to r or, equivalently, tangent to the resonance circle. Considering that for a given scaling factor g applied to signal $y(t)$, the resulting power spectral density of the scaled signal $z(t)$ is equal to $S_z(\Delta f) = g^2 S_y(\Delta f)$. The respective noise spectral densities were calculated and are shown in Table 4.1.

Table 4.1: Spectral densities of additive and multiplicative noise sources projected in both demodulation domains. S_θ represents the flux spectral density in resonator phase readout while S_γ in the scattering parameter amplitude. The dependence of the parameters with f_{exc}, φ and Δf was removed in order to avoiding a complex notation.

Readout Domain	Additive Noise σ_n	Amplitude Noise γ_n	Phase Noise ϕ_n
S_θ	$\frac{1}{r^2}\frac{k_b T_n}{P_{\text{exc}}}$	$\frac{\gamma^2 \sin^2(\phi+\theta)}{r^2} S_\gamma$	$\frac{\gamma^2 \cos^2(\phi+\theta)}{r^2} S_\phi$
S_γ	$\frac{k_b T_n}{P_{\text{exc}}}$	$\gamma^2 S_\gamma$	–

Expressions in Table 4.1 corresponding to additive noise represent the easiest cases to analyze because it describes a constant radius noise cloud independent of the trajectory described by the resonator response. Therefore, its projections either in resonator phase or scattering parameter amplitude are constant. Conversely, multiplicative noise projections depend on the position in the resonance circle $S_{21}(f_{\text{exc}}, \varphi)$ in which they are calculated (i.e. scattering amplitude γ, readout phase ϕ and resonator phase θ). Particularly in these cases can be a condition for minimum or zero projection depending on the readout domain and readout parameters chosen. For example, in the case of readout amplitude noise $\gamma_n(t)$ there is no projection into the resonator phase domain when the readout phasor (red arrow in Figure 4.2) is parallel to the circle radius ($\theta + \phi = 0$). In contrast for readout phase noise $\phi_n(t)$, there is no projection into the resonator phase domain when the readout phasor is tangent to the resonance circle ($\theta + \phi = \pi/2$). In addition, using the expressions in Table 4.1 it is possible to conclude that additive noise is the dominant noise source due to the fact that when considering equal noise densities (i.e. $S_\gamma = S_\phi = \frac{k_B T_n}{P_{\text{exc}}}$), multiplicative sources are scaled by factors lower than unity compared to the additive case. Despite these expressions allow for the calculation of the resonator phase and amplitude noise projections, an additional step is required in order to convert them to flux noise for a later comparison. This step depends on the demodulation scheme used and will be explained below.

4.2.1 Open-Loop Demodulation

When a detector signal is coupled to the rf-SQUID through the input coil L_{in} (see Figure 3.9), it creates a flux component $\varphi_{\text{det}}(t)$ that is added to the modulation flux $\varphi_{\text{mod}}(t)$. For a given constant f_{exc}, P_{exc}, and flux φ_{mod}, small flux variations $\delta\varphi_{\text{det}}(t)$ will lead to resonator phase $\theta(t)$ and amplitude $\gamma(t)$ variations described by

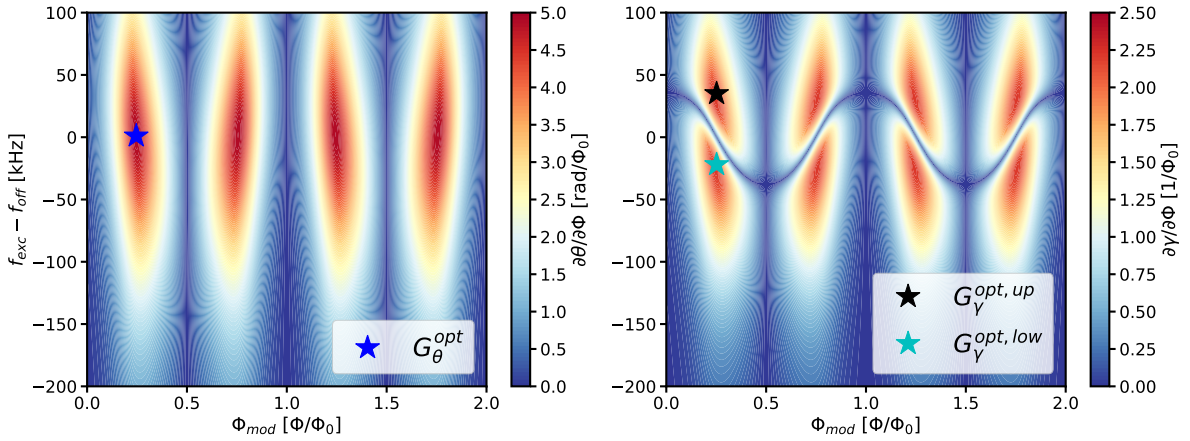

Figure 4.5: Open-loop gains corresponding to the μMUX model shown in Table 3.1 as a function of probe frequency f_{exc} and modulation flux φ_{mod} for a constant probing power $P_{\text{exc}} = -70$ dBm. **Left)** Resonator phase gain, black star represents the maximum gain G_θ^{opt}. **Right)** Scattering amplitude gains, the black and cyan stars represent the both upper $G_\gamma^{\text{opt,up}}$ and lower $G_\gamma^{\text{opt,low}}$ local maximum gains.

$$\theta(t) \approx \delta\varphi_{\text{det}}(t)\frac{\partial\theta}{\partial\varphi}\bigg|_{f_{\text{exc}},P_{\text{exc}},\varphi_{\text{mod}}} \tag{4.12}$$

$$\gamma(t) \approx \delta\varphi_{\text{det}}(t)\frac{\partial\gamma}{\partial\varphi}\bigg|_{f_{\text{exc}},P_{\text{exc}},\varphi_{\text{mod}}}. \tag{4.13}$$

This readout scheme is called open-loop and the demodulated signals $\theta(t)$ and $\gamma(t)$ are scaled copies of $\delta\varphi_{det}(t)$. The scaling factors are denoted as open-loop gains, or transfer coefficients equivalently, being equal to the partial derivatives of the corresponding demodulation domain with respect to the normalized flux evaluated at f_{exc}, P_{exc} and φ_{mod}. Consequently, the maximum demodulated signal amplitudes are obtained when the maximum partial derivatives are achieved. Figure 4.5 shows the simulated resonator phase (left) and amplitude (right) derivatives for the μMUX model described in Section 3.1 as a function of the modulation flux φ_{mod} and probing tone frequency f_{exc} for a specific probing power $P_{\text{exc}} = -70$ dBm. The absolute maximum gain for the resonator phase G_θ^{opt} is represented by the blue star, while upper $G_\gamma^{\text{opt,up}}$ and lower $G_\gamma^{\text{opt,low}}$ local maximum open-loop gains with black and cyan stars respectively.

These gain factors can be used to calculate the resonator phase and amplitude variations, but also in the reverse way to derive the equivalent flux change for given resonator phase and amplitude variations. Therefore, the NSD of the noise projections listed in Table 4.1 can be translated into an equivalent flux noise density for resonator phase $\sqrt{S_\Phi^\theta}$ and amplitude $\sqrt{S_\Phi^\gamma}$ readout using

$$\sqrt{S_\Phi^\theta} \approx \sqrt{S_\theta(\Phi)}\left|\frac{\partial\theta(\Phi)}{\partial\Phi}\right|^{-1}, \tag{4.14}$$

$$\sqrt{S_\Phi^\gamma} \approx \sqrt{S_\gamma(\Phi)}\left|\frac{\partial\gamma(\Phi)}{\partial\Phi}\right|^{-1}. \tag{4.15}$$

Simplifying the notation for reading purposes, the dependence of the noise projection with probing frequency and power was avoided only preserving the explicit dependence of

the magnetic flux Φ. A similar expression for the flux noise $\sqrt{S_\Phi^{TLS}}$ can be found for TLS noise [43, 74]. Since it acts directly in the resonance frequency, it can be related to the flux using

$$\sqrt{S_\Phi^{TLS}} \approx \sqrt{S_{f_r}} \left| \frac{\partial f_r(\Phi)}{\partial \Phi} \right|^{-1}, \tag{4.16}$$

where $\frac{\partial f_r(\Phi)}{\partial \Phi}$ is the derivative of Equation 3.32 with respect to the flux and S_{f_r} the frequency NSD. Although it is experimentally possible to determine the optimum flux bias necessary to obtain the maximum transfer coefficients, one of the main disadvantages of this method is that the information lies in the modulation side-bands. They are located at a frequency offset equal to f_{det} where generally the phase $S_\gamma(f_{det})$, amplitude $S_\phi(f_{det})$ and TLS $S_{f_r}(f_{det})$ noise sources are considerably large compared to Johnson–Nyquist noise $\frac{k_B T_n}{P_{exc}}$ as it can be seen in Figure 4.3 represented with green and black stars. Therefore, special care should be given to multiplicative and TLS noise sources in the case of bolometric applications where the detector signal is extremely slow and faint [42, 70] or a different readout method to overcome this problem should be used.

4.2.2 Flux-Ramp Demodulation

In addition to the aforementioned problem, random flux offsets trapped inside the SQUID loop would require individual flux tuning of every channel in order to achieve the maximum open-loop gain, re-introducing the multiplexing problem. A technique called Flux-Ramp Modulation (FRM) was introduced as a solution to overcome this limitation [87]. In it, a common flux line is shared among all SQUIDs and a sawtooth-shaped flux with amplitude $M_{\text{mod}} I_{\text{mod}} = n_{\Phi_0} \Phi_0$ and reset frequency f_{ramp} is applied sweeping all possible operating points. This flux-ramp line can be seen in Figure 3.7 and it is connected to the current AWG present in Figure 4.1. The flux-ramp signal is shown in the upper plot of Figure 4.6. Due to the SQUID periodic response, resonator phase $\theta(t)$ and scattering amplitude $\gamma(t)$ will have the same periodicity equal to $f_{\text{mod}} = n_{\Phi_0} f_{\text{ramp}}$. Therefore, a considerably slow detector signal $\varphi_{\text{det}}(t)$ added to the the sawtooth-shaped modulation can be be seen as a phase modulation, where $\varphi_{\text{det}}(t)$ determines the instantaneous phase changes of the periodic responses. The solid lines in the middle plot of Figure 4.6 represent the resonator phase and scattering amplitude when there is no detector signal applied, while the dashed lines are the shifted versions produced when the detector signal is introduced. As a consequence of FRM, detector information is up-converted to the frequency $f_{\text{mod}} = n_{\Phi_0} f_{\text{ramp}}$ avoiding in this way noise levels close to the probe tone frequency f_{exc}. Figure 4.7 shows the simulated resonator phase and scattering amplitude spectrum corresponding to the probing tone complex envelope where the detector signals are contained in the modulation side-bands around the carrier signal produced by the flux-ramp modulation. Detector sidebands are hardly visible because they are located $f_{det} \approx 762.90$ Hz away from the carrier frequency at $f_{\text{mod}} = n_{\Phi_0} f_{\text{ramp}} \approx 61.03$ kHz. However, an additional phase demodulation step is required in order to recover the detector signal (Flux-Ramp Demodulation or FRD). In the context of this work the linearity-improved quadrature demodulation was adopted [117]. The demodulated flux for the resonator phase $\theta(t)$, and scattering amplitude $\gamma(t)$ demodulation can be written respectively as

$$\varphi_\theta(t') = \arctan\left[\frac{\int \sin(2\pi p f_{\text{mod}} t) w(t) \theta(t) dt}{\int \cos(2\pi p f_{\text{mod}} t) w(t) \theta(t) dt} \right], \tag{4.17}$$

$$\varphi_\gamma(t') = \arctan\left[\frac{\int \sin(2\pi p f_{\text{mod}} t) w(t) \gamma(t) dt}{\int \cos(2\pi p f_{\text{mod}} t) w(t) \gamma(t) dt} \right]. \tag{4.18}$$

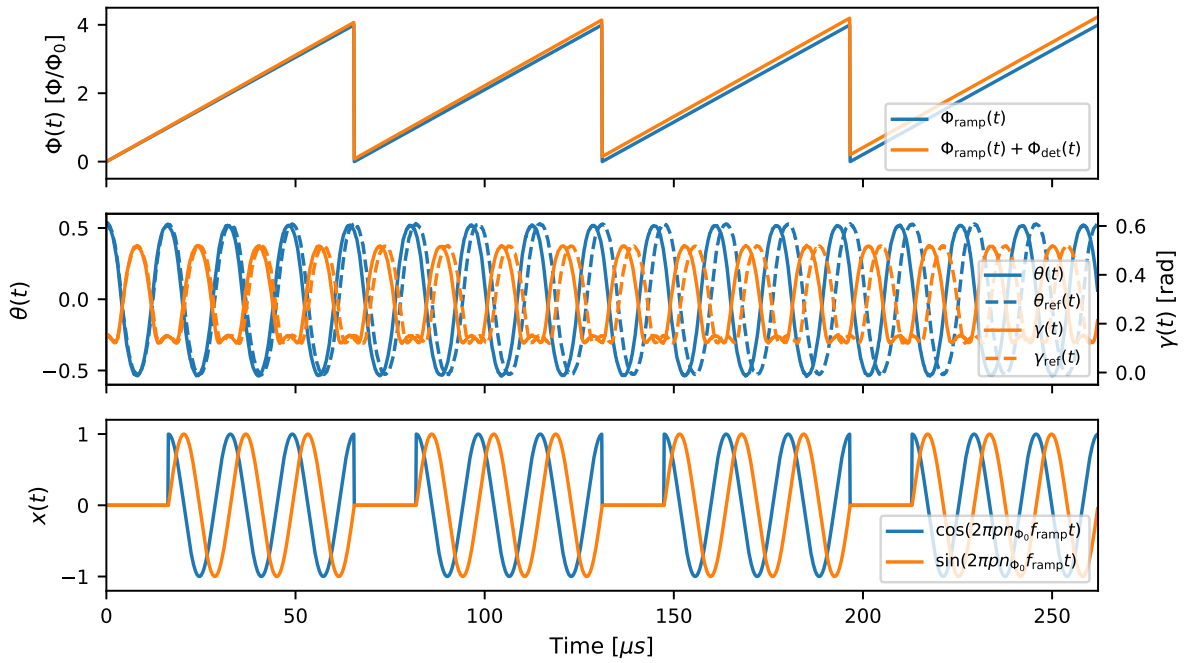

Figure 4.6: Signals associated with the Flux-Ramp Demodulation process (FRD) of the μMUX model presented in Table 3.1 for a particular f_{exc} and P_{exc}. **Top)** Flux-Ramp Modulation signal spanning $n_{\Phi_0} = 4$ with $f_{\text{ramp}} \approx 15.25$ kHz with and without detector flux added. **Middle)** Resonator phase and amplitude signals before FRD. Dashed and solid lines represent amplitude and phase signals without and with detector signal respectively. **Bottom)** Reference signals used for demodulation including the discarded period $n_{\text{disc}} = 1$ and using the first harmonic component $p = 1$.

Here, $w(t)$ represents both the discarding window, where a number of SQUID periods n_{disc} is set to zero avoiding the sawtooth-shaped flux non-ideal transition, and the window function used to attenuate the non-linearity components. An integer number p was also added allowing the demodulation of higher order FRM harmonics as will be used later in Section 4.3.2. The bottom part of Figure 4.6 shows the cosine and sine reference signals used for FRD. Particularly in this example one of a total of four periods is discarded and a boxcar window is used. These signals serve as references to detect the phase change produced by the detector signal. In this scheme, the integration is performed over a flux-ramp period setting an effective sampling rate of f_{ramp}. Here, a continuous time notation is used for explanatory purposes and t' to explicitly show this implicit decimation.

In contrast with open-loop demodulation, FRM sweeps all possible flux values varying the open-loop gains from its maximum to minimum values. As a consequence, Equations 4.15 and 4.14 need to be integrated over a one flux-ramp period in order to get the demodulated noise level. As a natural solution, a gain-weighted average noise value may be used, but expressions 4.14, 4.15 and 4.16 diverge for the case of zero gain. This is the reason why a Root-Mean-Square (RMS) gain over a flux-ramp period is defined [87, 92] and flux noise density in the case of resonator phase and amplitude is calculated using

$$\sqrt{S_\Phi^\theta} \approx \sqrt{S_\theta} \left\{ \frac{1}{n_{\Phi_0}\Phi_0} \int_{n_{\text{disc}}\Phi_0}^{n_{\Phi_0}\Phi_0} \left(\frac{\partial\theta(\Phi)}{\partial\Phi} \right)^2 d\Phi \right\}^{-1/2}, \tag{4.19}$$

$$\sqrt{S_\Phi^\gamma} \approx \sqrt{S_\gamma} \left\{ \frac{1}{n_{\Phi_0}\Phi_0} \int_{n_{\text{disc}}\Phi_0}^{n_{\Phi_0}\Phi_0} \left(\frac{\partial\gamma(\Phi)}{\partial\Phi} \right)^2 d\Phi \right\}^{-1/2}. \tag{4.20}$$

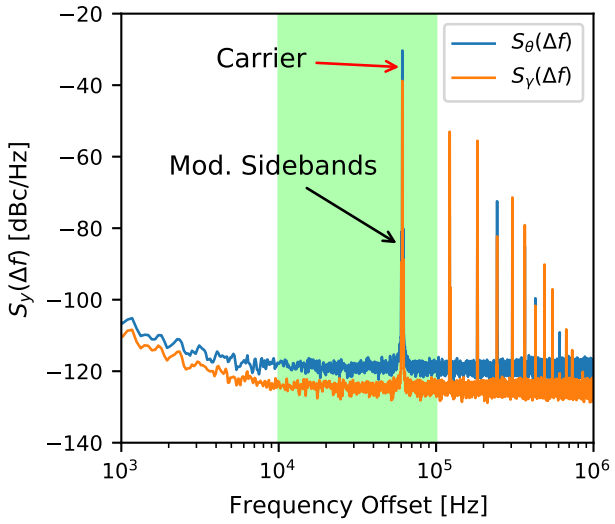

Figure 4.7: Simulated resonator phase and scattering parameters amplitude spectrum of the probing tone complex envelope. The carrier is located at a frequency $f_{\text{mod}} = n_{\Phi_0} f_{\text{ramp}} \approx 61.03$ kHz while the modulation side-bands are located $f_{\text{det}} \approx 762.90$ Hz away from the carrier. White and $1/f$ noise components similar to Figure 4.3 were included for a more realistic representation.

Similarly, for TLS a flux noise density can be calculated as

$$\sqrt{S_\Phi^{TLS}} \approx \sqrt{S_{f_r}} \left\{ \frac{1}{n_{\Phi_0}\Phi_0} \int_{n_{\text{disc}}\Phi_0}^{n_{\Phi_0}\Phi_0} \left(\frac{\partial f_r(\Phi)}{\partial \Phi} \right)^2 d\Phi \right\}^{-1/2}, \tag{4.21}$$

where expressions between brackets are the gain-mean squares over a flux-ramp period and S_θ, S_γ and S_{TLS} are the noise spectral densities evaluated at f_{mod}. Due to the fact that n_{disc} periods of a total of n_{Φ_0} are discarded and a window function is applied, a degradation equal to $\sqrt{\kappa/\alpha}$ is expected. Where $\alpha = (n_{\Phi_0} - n_{\text{disc}})/n_{\Phi_0}$ and κ is a factor that accounts for the degradation caused by the applied window. When a boxcar window is used, $\kappa = 1$. While these expressions give a rough estimation of the noise level, they have several limitations that this work aims to overcome. Unlike additive and TLS noise, these expressions do not apply to the case of multiplicative noise where both spectral densities and gains are flux dependent (i.e. $S_{\theta,\gamma}(\Phi)$). Another limitation is that due to the non-sinusoidal resonator phase and amplitude responses, the information is not only contained in a single side-band, but spread out in harmonics of f_{mod} which cannot be demodulated using the quadrature demodulation method (see Figure 4.7). Additionally, an extra challenge lies in the analytical calculation of the derivatives with respect to the flux, for the given conditions of readout power and frequency using the model presented in Section 3.4.1 and their integration over a flux-ramp period, especially when multidimensional optimization criteria must be found. That is why throughout this chapter, the evaluation of the optimal readout parameters that match the lowest noise condition in both domains and demodulation methods were carried out by means of numerical simulations.

4.3 System Noise Simulation

In this section, several simulations were carried out in order to evaluate the demodulated noise for different readout conditions. Previously, for sake of simplicity a continuous-time signal model of the readout system was introduced. From now on, this model was replaced by its discrete-time equivalent using adequate sampling frequency f_s that satisfies the sampling theorem. This migration was not only motivated by the numerical simulation, but also because the demodulation is typically done in the digital domain using Software-Defined Radio (SDR) Systems [118, 116]. The readout system simulation framework was implemented completely in Python and making use of several available libraries. Table 4.2 enumerates the parameters

used in the following simulations. The general simulation procedure to obtain a demodulated signal time-trace can be summarized as follows:

1. The total modulation flux $\varphi_{\text{tot}}[m]$ is created adding the modulation flux $\varphi_{\text{mod}}[m]$ to the detector flux $\varphi_{\text{det}}[m]$.
2. Given fixed f_{exc} and P_{exc}, $f_r[m]$ is iteratively calculated using Equation 3.32 and $f_{TLS}[m]$ is added.
3. Then, $S_{21}[m]$ is calculated through Equation 3.15 for a particular f_{exc}, low-pass filtered and the readout noise sources $\sigma_n[m]$, $\phi_n[m]$ and $\gamma_n[m]$ included.
4. Finally, and after a new step of signal conditioning, $\theta[m]$ and $\gamma[m]$ are available to be demodulated using some of the methods presented in previous section.

Table 4.2: Readout system parameters used during demodulated noise simulations.

Parameter	Value	Unit
f_s	≈7.82	MHz
N_s	2^{20}	Samples
BW_{readout}	2	MHz
f_{det}	≈762.90	Hz
A_{det}	1	mΦ_0
f_{ramp}	≈15.25	kHz
n_{Φ_0}	4	-
n_{disc}	1	-
p	1	-
$w[n]$	Hamming	-

4.3.1 Open-Loop Demodulation Noise Performance

Using our simulation framework, the measurement process that is carried out in the laboratory during characterization was replicated. This allowed us to not only evaluate the noise performance, but also to know the required functionalities of our SDR readout system. Particularly, the parameters described in Table 4.2 are in agreement with the SDR systems presented in the following chapters. For the determination of the noise density in the open-loop scheme described by Equations 4.14 and 4.15, we must know the value of the open-loop gains (transfer coefficients) which depend on the readout frequency f_{exc} and power P_{exc} as well as the applied constant modulation flux φ_{mod}. First, for each value of frequency and power, one period of the transmission scattering parameter $S_{21}(f_{\text{exc}}, P_{\text{exc}}, \varphi_{\text{mod}})$ was calculated sweeping φ_{mod}. Then, we get the resonator phase $\theta(f_{\text{exc}}, P_{\text{exc}}, \varphi_{\text{mod}})$ and amplitude $\gamma(f_{\text{exc}}, P_{\text{exc}}, \varphi_{\text{mod}})$ to consequently obtain the partial derivatives with respect to flux as can be seen in Figure 4.5. For the next process, the maximum gains $G_\theta^{\text{opt}}(f_{\text{exc}}, P_{\text{exc}})$ and $G_\gamma^{\text{opt}}(f_{\text{exc}}, P_{\text{exc}})$ along with the correspondent fluxes $\varphi_{\text{mod}}^{\text{opt}}$ and resonance circle parameters (i.e. radius r and center x_c) are stored. Resonance circle parameters determine the rotating frame required to calculate the resonator phase using Equation 3.35 when detector signal is present. This calibration procedure allows us to get all parameters required to obtain a demodulated signal time-trace.

Optimum Readout Parameters for Open-Loop

In order to find the optimum readout parameters, for each frequency f_{exc} and power P_{exc}, a small detector signal $\varphi_{\text{det}}[m]$ was added to the fluxes corresponding to the maximum gains

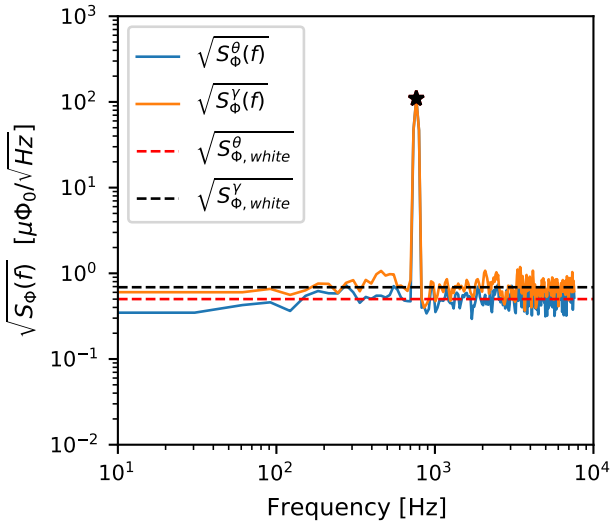

Figure 4.8: Simulated flux spectra demodulating the resonator phase $\sqrt{S_\Phi^\theta(f)}$ and the scattering parameter amplitude $\sqrt{S_\Phi^\gamma(f)}$. The detector signal is located at a frequency $f_{\text{det}} \approx 762.90$ Hz. The dashed red and black lines represents the estimated white flux noise levels for the case of the resonator phase $\sqrt{S_{\Phi,\text{white}}^\theta}$ and amplitude demodulation $\sqrt{S_{\Phi,\text{white}}^\gamma}$.

$\varphi_{\text{mod}}^{\text{opt}}$. The transmission parameter is calculated and the readout noise sources were included. Consequently, depending on the selected domain, resonator phase $\theta[m]$ and amplitude $\gamma[m]$ time-traces calculated and $\varphi_\theta[m]$ and $\varphi_\gamma[m]$ were derived dividing them by their correspondent optimum open-loop gain coefficients. As can be seen in Figure 4.8, by means of the Welch's method [119], the flux spectral density was calculated for both domains and the white noise density components estimated (i.e. $\sqrt{S_{\Phi,\text{white}}^\theta}$ and $\sqrt{S_{\Phi,\text{white}}^\gamma}$). The results of these simulations for both domains are shown in Figure 4.9 for the case of a typical noise equivalent temperature of the cryogenic HEMT amplifier [103] of $T_n = 4$ K. Red and green dashed lines in Figure 4.9 represent maximum and minimum resonance frequencies according with Equation 3.32, while dash-dotted blue, black and cyan represent the minimum noise $(P_{\text{exc}}, f_{\text{exc}})$ trajectories. These three trajectories describe the position followed by the optimum open-loop gains previously shown in Figure 4.5. Colored stars are the local noise minimums at $P_{\text{exc}} = -70$ dBm, exactly at the same positions where the maximum gains were calculated in Figure 4.5. As previously mentioned, only additive noise was considered. Therefore, the optimum readout parameters are valid for this condition.

As can be seen in Figure 4.9, the noise minimums for low powers always lie within the maximum and minimum resonant frequencies and the optimum conditions for amplitude are symmetrically located on both sides of the optimum condition for the resonator phase. In order to compare the demodulated noise values for both demodulation domains, the minimum noise levels corresponding to these trajectories were simulated again for two different additive noise temperatures. In line with new amplification technologies, simulations in the Standard Quantum Limit (SQL) condition with $T_n = hf_{\text{exc}}/k_B$ along with the $T_n = 4$ K previously used [120, 102] were performed. The results are plotted in Figure 4.10. For these cases, flux noise levels can be estimated by using the additive noise version of Equations 4.14 and 4.15

$$\sqrt{S_\Phi^\theta} \approx \frac{1}{r}\sqrt{\frac{k_B T_n}{P_{\text{exc}}}}\left|\frac{\partial\theta}{\partial\Phi}\right|^{-1}, \tag{4.22}$$

$$\sqrt{S_\Phi^\gamma} \approx \sqrt{\frac{k_B T_n}{P_{\text{exc}}}}\left|\frac{\partial\gamma}{\partial\Phi}\right|^{-1}. \tag{4.23}$$

In accordance with these equations, at low power the transfer coefficients remain constant and the noise level decreases proportionally to $\sqrt{S_{\Phi,white}} \propto 1/\sqrt{P_{\text{exc}}}$ until it reaches a plateau in which both open-loop gain values reach a level of around $P_{\text{exc}} \approx -63$ dBm where

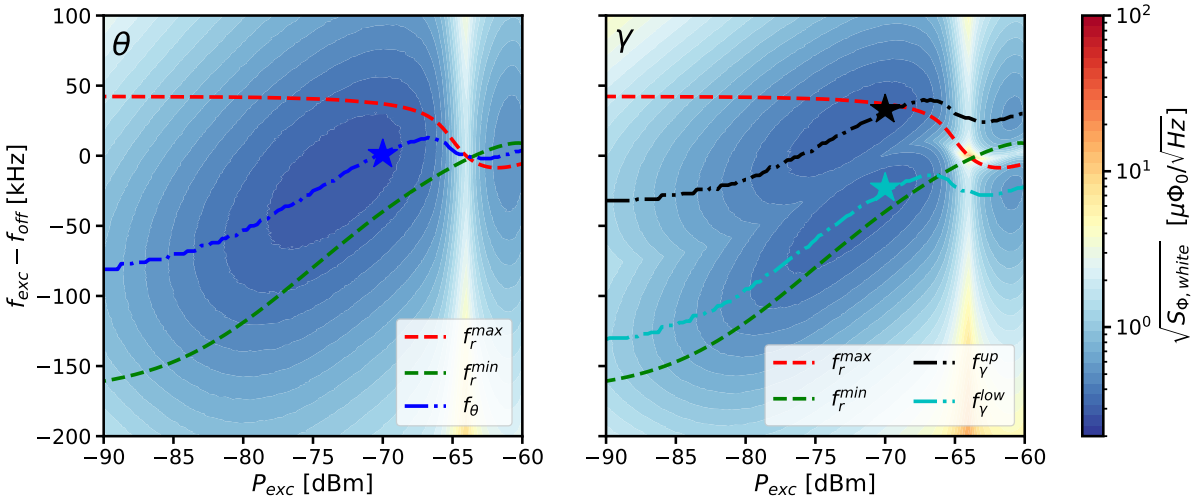

Figure 4.9: Open-loop demodulated white noise flux density $\sqrt{S_{\Phi,white}}$ for both demodulation domains as a function of probe tone frequency f_{exc} and power P_{exc} for an additive noise temperature of $T_n = 4$ K. Red and green dashed lines represent maximum $f_r^{\max}$ and minimum $f_r^{\min}$ resonance frequencies respectively. **Left)** Resonator phase demodulation. Dash-dotted blue f_θ line is the optimum trajectory to achieve minimum noise. **Right)** Scattering amplitude demodulation. Dash-dotted black and cyan curves are the optimum trajectories to achieve both upper f_γ^{up} and lower f_γ^{low} local minimum noise values.

the µMUX becomes insensitive to flux variations. Using $P_{\text{exc}} = -70$ dBm, simulated optimum gain values yielded $G_\theta^{\text{opt}} = 4.90\ rad/\Phi_0$ and $G_\gamma^{\text{opt,up}} = G_\gamma^{\text{opt,low}} = 2.21/\Phi_0$ (see Figure 4.5). Thus, for a resonance circle radius $r \approx Q_l/2Q_c \approx 0.49$ the calculated noise values results are $\sqrt{S^\theta_{\Phi,SQL}} \approx 0.071\mu\Phi_0/\sqrt{Hz}$ and $\sqrt{S^\gamma_{\Phi,SQL}} \approx 0.08\mu\Phi_0/\sqrt{Hz}$ for the SQL, in contrast to $\sqrt{S^\theta_{\Phi,4K}} \approx 0.30\mu\Phi_0/\sqrt{Hz}$ and $\sqrt{S^\gamma_{\Phi,4K}} \approx 0.34\mu\Phi_0/\sqrt{Hz}$ with $T_n = 4$ K, in well agreement with the simulations. Dotted red and grey lines in Figure 4.10 represent the aforementioned noise values in the case of resonator phase readout. Leaving aside technical difficulties that may be encountered when implementing the demodulation of one of the domains, which will be discussed in the next subsections, there is no strong argument based on noise performance to decide for either domain. This is given by the non-appreciable noise differences in the simulation results. Therefore, the impact of the remaining noise sources were evaluated in order to find considerable differences that would indicate the existence of a preferential domain.

TLS and Multiplicative Noise Impact for Open-Loop

In order to quantify the impact of the non-additive noise sources, individual simulations were carried out for each noise source under the optimum readout parameters for additive noise, represented with stars in Figure 4.9. As mentioned earlier, Two-Level Systems noise is one of the most common noise sources and particularly important in open-loop readout due to its frequency dependence [110]. Here, TLS noise was represented by its fractional frequency density S_{f_r}/f_{off}^2 with a frequency slope of $1/f$ and taking values from $6.25 \cdot 10^{-20}$ Hz^{-1} to $6.25 \cdot 10^{-14}$ Hz^{-1} when evaluated at 1 Hz. Due to the TLS noise saturation as a function of the readout power [110], it is worth to mention that TLS noise is specified for $P_{\text{ext}} = -70$ dBm. Simulations results for each domain measured at detector frequencies of $f_{\text{det}} \approx 762$ Hz are shown in the left side of Figure 4.11. As in the previous plots, the minimum noise values for the SQL and $T_n = 4$ K were included as reference. These results allows to set maximum TLS

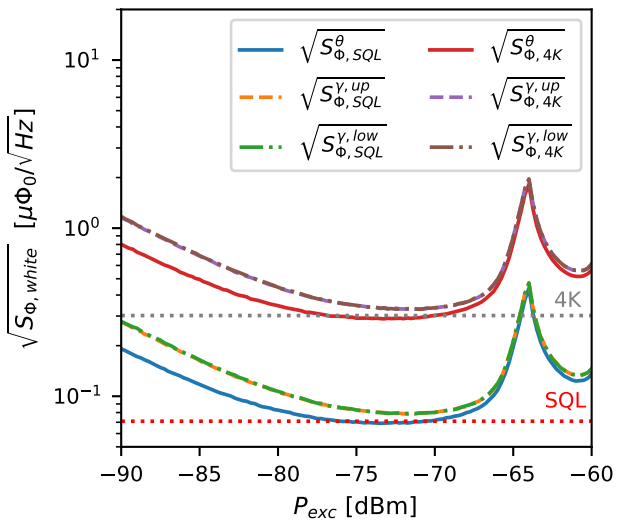

Figure 4.10: Open-loop demodulated minimum white noise flux density $\sqrt{S_{\Phi,white}}$ for every demodulation domain as a function of power P_{exc} for both SQL and $T_n = 4$ K cases. Solid lines correspond to minimum noise for resonator phase readout, while dashed and dashdotted lines are upper and lower local minimums for scattering amplitude readout.

noise levels of $S_{f_r}(1Hz)/f_{\text{off}}^2 = 3 \cdot 10^{-18}$ Hz^{-1} and $S_{f_r}(1Hz)/f_{\text{off}}^2 = 6.6 \cdot 10^{-17}$ Hz^{-1} for the SQL and $T_n = 4$ K respectively avoiding the TLS as dominant noise source, but once again, showing no preferential demodulation domain.

Contrary to the TLS noise, multiplicative and additive noise sources can be compared directly in the same NSD units. Therefore, the simulations were performed as function of the NSD values for each noise source in the same conditions as before using $P_{\text{exc}} = -70$ dBm. Equivalent noise temperatures starting from the SQL with $T_n = hf_{\text{exc}}/k_B \approx 0.24$ K, to $T_n = 8$ K, corresponding to NSDs from -135 dBc/Hz to -120 dBc/Hz were used in the case of additive noise. While for phase and amplitude readout noise, NSD going from -130 dBc/Hz to -100 dBc/Hz. Since both local minimums for amplitude yield the same demodulated noise for open-loop demodulation, only the upper local minimum is considered in the following analysis. The results of these simulations as a function of the NSD are shown in the right side of Figure 4.11. As demonstrated previously, resonator phase readout lead to a slightly lower noise than amplitude readout for the same NSD. In addition, as expected from Table 4.1, noise levels scales proportional to NSD with $\sqrt{S_\Phi} \propto \sqrt{NSD}$ being additive noise the dominant noise source compared with multiplicative sources for equal NSD values. When considering non-correlated noise sources acting together, the total system noise is the quadrature summation all individual contributions. Therefore, a rejection factor A for each noise source and demodulation domain was defined, equal to the NSD difference with respect to the additive NSD that would result in the same demodulated noise level. This factor is represented with a black arrow in the right side of Figure 4.11 for the case of resonator amplitude demodulation and is equal to the distance in NSD units between parallel dashed lines for a constant flux noise density. Thus, for amplitude demodulation there is a ≈ 10 dB rejection of amplitude noise. In contrast using resonator phase demodulation, there are ≈ 19 dB and more than 40 dB rejection values for phase and amplitude noise respectively. Particularly, amplitude demodulation is more sensitive than phase demodulation to amplitude noise because the readout tone is positioned further away from the resonance where its projection is considerably greater compared with phase noise and the amplitude open-loop gain lower. On the contrary, resonator phase demodulation is more sensitive to phase noise because the maximum open-loop gain requires the probe tone on resonance where phase noise projection is maximum (see Figure 4.2).

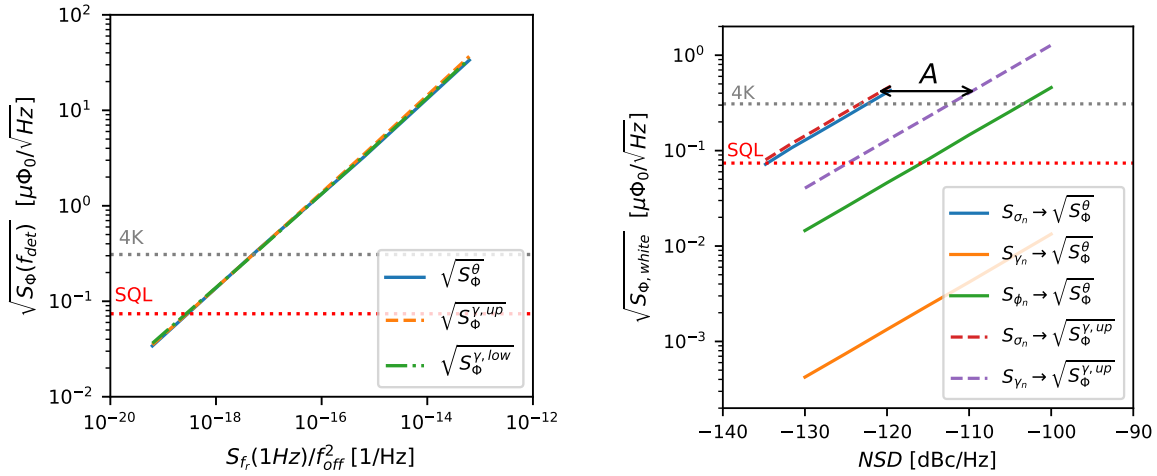

Figure 4.11: Left:) Open-loop demodulated white noise flux density $\sqrt{S_{\Phi,\text{white}}}$ as a function of the Two-Level Systems (TLS) noise level of $S_{f_r}(1Hz)/f_{\text{off}}^2$ for both demodulation domains in the minimum additive noise condition for a constant $P_{\text{exc}} = -70$ dBm. **Right)** Open-loop demodulated white flux noise density $\sqrt{S_{\Phi,white}}$ for every demodulation domain as a function of the noise spectral densities (NSD) for each noise source in the minimum additive noise condition for a constant $P_{\text{exc}} = -70$ dBm. Dashed lines correspond to scattering amplitude domain, while solid lines are for resonator phase readout. As a reference, dotted red and grey lines represent the minimum noise values for resonator phase demodulation in the case of the SQL and $T_n = 4$ K respectively.

Optimum Domain for Open-loop

Previous results suggest that maximum sensitivity is achieved in the resonator phase domain due to the lower demodulated noise level in the additive noise case and high rejection to multiplicative noise sources compared to amplitude domain. Unfortunately, this is not a realistic scenario in the case of open-loop readout. Phase and amplitude noise spectral components (Equation 4.8) usually grow rapidly for small frequency offsets far exceeding additive noise, impacting directly in the detector signal. As an example, in order to determine the expected open-loop performance of a real SDR readout system [113], the measured noise values shown in Figure 4.3 were included in our simulation framework. Since the TLS noise did not show a preferential readout region and assuming a proper resonator design, it was not included in this case. The results of the demodulated noise for every domain for both SQL and $T_n = 4$ K additive noise conditions are shown in Figure 4.12.

Clearly, the demodulated noise is dominated by the multiplicative noise and its effect is most noticeable at high powers and near the SQL [120]. The resonator phase domain is completely dominated by the multiplicative noise values of $S_\phi(f_{\text{det}}) \approx -96$ dBc/Hz and $S_\gamma(f_{\text{det}}) \approx -116$ dBc/Hz for phase and amplitude respectively. Both are considerably larger than the additive noise at the detector frequency $S_\sigma(f_{\text{det}})$ (see colored stars in Figure 4.3). Noise levels at $P_{\text{exc}} = -70$ dBm are $\sqrt{S_\Phi^\theta(f_{\text{det}})} \approx 0.82\mu\Phi_0/\sqrt{Hz}$ and $\sqrt{S_\Phi^\gamma(f_{\text{det}})} \approx 0.24\mu\Phi_0/\sqrt{Hz}$ for the SQL, $\sqrt{S_\Phi^\theta(f_{\text{det}})} \approx 0.87\mu\Phi_0/\sqrt{Hz}$ and $\sqrt{S_\Phi^\gamma(f_{\text{det}})} \approx 0.40\mu\Phi_0/\sqrt{Hz}$ for the $T_{\text{n}} = 4$ K case. All of them are consistent with the values shown in the left side of Figure 4.11 for their respective NSD levels. Based on these results and Equations 4.22 and 4.23, it is possible to calculate an equivalent system temperature which reflects the measured noise. This would be the temperature that one would measure and attribute it directly to the additive noise, not knowing

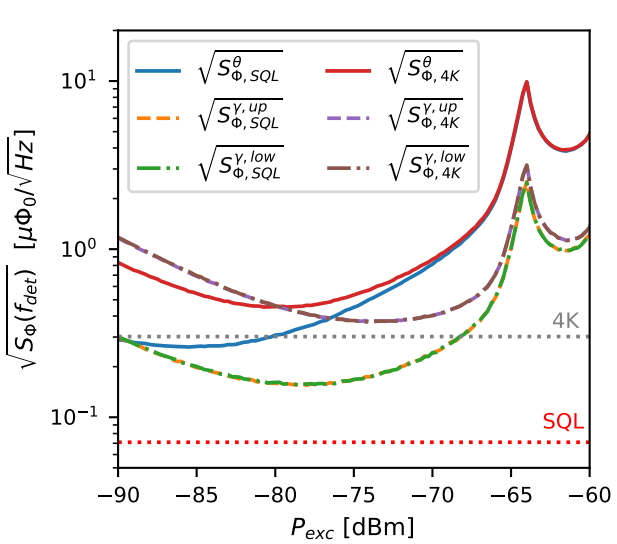

Figure 4.12: Open-loop demodulated flux noise density $\sqrt{S_\Phi(f_{\text{det}})}$ for every demodulation domain as a function of power P_{exc} for both SQL and $T_n = 4$ K cases and using the example SDR readout System. Solid lines correspond to minimum noise for resonator phase readout, while dashed and dash-dotted lines are upper and lower local minimums for scattering amplitude readout.

that it is produced by the multiplicative noise. In the case of phase noise, measurements were $T_{\text{sys}}^{\theta,SQL} \approx 29$ K and $T_{\text{sys}}^{\theta,4K} \approx 33$ K, as for amplitude $T_{\text{sys}}^{\gamma,SQL} \approx 2$ K and $T_{\text{sys}}^{\gamma,4K} \approx 5.6$ K, considerably higher than the real additive noise equivalent temperature T_{n}.

While phase and amplitude noise can be reduced at lower frequencies using an ultra low-noise frequency reference [107], and TLS strongly reduced properly choosing resonator materials and geometry [110], they are still a problem specially in the case of bolometric applications. Therefore, the FRM technique mentioned above in 4.2.2, can be used to mitigate these effects along with other limitations previously mentioned.

4.3.2 Flux-Ramp Demodulation Noise Performance

Similarly to the open-loop demodulation, the noise characterization procedure of a real μMUX device was replicated. For the determination of the noise density in the FRD scheme described by Equations 4.18, 4.17. First, the modulation flux $\varphi_{\text{mod}}[m]$ and the detector signal $\varphi_{\text{det}}[m]$ was generated using the parameters described in Table 4.2. Both fluxes were added, $f_r[m]$ and the transmission parameter $S_{21}(f_{\text{exc}}, P_{\text{exc}}, \varphi_{\text{mod}})[m]$ consequently iteratively calculated. Then, and using the circle parameters previously stored, resonator phase $\theta(f_{\text{exc}}, P_{\text{exc}}, \varphi)[m]$ and amplitude $\gamma(f_{\text{exc}}, P_{\text{exc}}, \varphi_{\text{mod}})[m]$ time traces were obtained. Finally, the FRD was applied for both domains in order to get the detector signal time-traces $\varphi_\theta[n]$ and $\varphi_\theta[n]$. Here, n instead of m was used, as a consequence of the decimation produced by the FRD [87, 117] (see Figure 4.6).

Optimum Readout Parameters for FRD

The demodulated detector time-traces $\varphi_{\text{det}}[n]$ for both domains were calculated as a function of the frequency f_{exc} and power P_{exc} considering only additive noise with $T_{\text{n}} = 4$ K. As before, the white flux noise spectral density $\sqrt{S_{\Phi,white}}$ was estimated for both domains as it is shown in Figure 4.8. The results of these simulations for both domains are shown in Figure 4.13. Red and green dashed lines represent maximum and minimum resonance frequencies, while dashed-dot blue, black and cyan represent the minimum noise $(P_{\text{exc}}, f_{\text{exc}})$ trajectories. Colored stars are the absolute noise minimums at $P_{\text{exc}} \approx -70$ dBm for both domains.

In principle, we would assume that the noise minima will also follow the trajectories previously found for the open-loop scenario (Figure 4.9). But this is not the case, the trajectories mainly differ when approaching each other at high powers. This behavior is mainly determined by the spectral components of the resonator phase and amplitude time-traces described by their Fourier series as

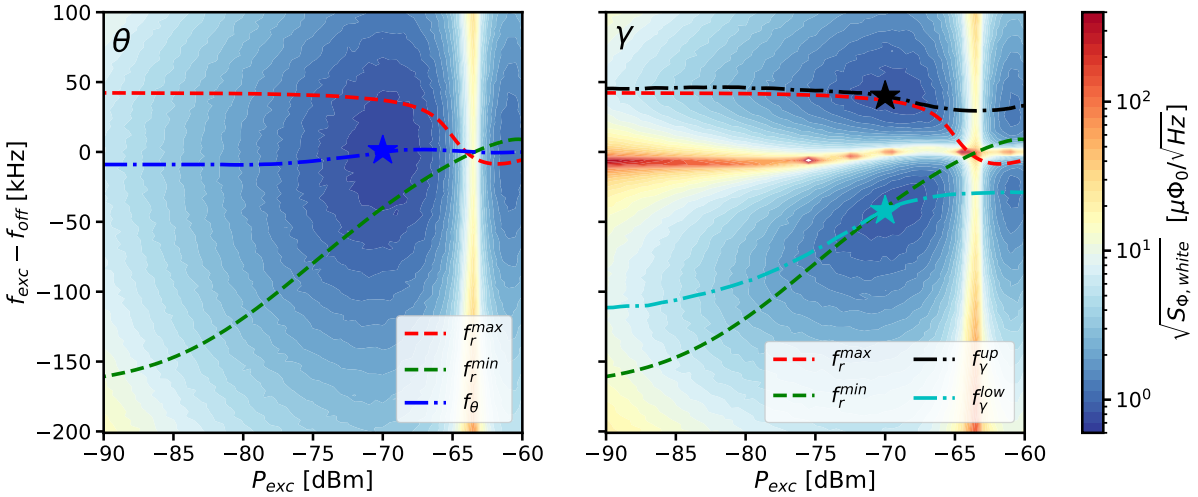

Figure 4.13: Flux-ramp demodulated white flux noise density $\sqrt{S_{\Phi,white}}$ for both demodulation domains as a function of probe tone frequency f_{exc} and power P_{exc}. **Left)** Resonator phase demodulation. Red and green dashed lines represent maximum $f_r^{\max}$ and minimum $f_r^{\min}$ resonance frequencies respectively. Dashdotted blue lines f_θ show the optimum trajectory to achieve minimum noise. **Right)** Scattering amplitude demodulation, dashdotted black and cyan curves are the optimum trajectories to achieve both upper f_γ^{up} and lower f_γ^{low} local minimum noise values. Hamming windows function with $n_{\text{disc}} = 1$ and $n_{\Phi_0} = 4$ were used.

$$\theta(t) \approx \Theta_0 + \sum_{p=1}^{\infty} \Theta_p \sin(2\pi p f_{\text{mod}} t + \lambda_p), \tag{4.24}$$

$$\gamma(t) \approx \Gamma_0 + \sum_{p=1}^{\infty} \Gamma_p \sin(2\pi p f_{\text{mod}} t + \epsilon_p). \tag{4.25}$$

Here, the fundamental frequency is $f_{\text{mod}} = n_{\Phi_0} f_{\text{ramp}}$ (also called SQUID frequency) and Θ_p, Γ_p, λ_p, ϵ_p amplitude and phase spectral coefficients. Based on the FRM [87], we can assume that the detector signal changes the instantaneous frequency of each harmonic component $f_{\text{dem}} = p \cdot f_{\text{mod}}$ and consequently each component is phase modulated. However, while the modulation index is given by the detector signal, the carrier power depends on the amplitude spectral components of each domain (i.e. Θ_p and Γ_p). Due to the fact that the first component is usually demodulated, noise values increase when either Θ_p or Γ_p decreases. In order to test this, f_{exc} was swept at constant power of $P_{\text{exc}} = -70$ dBm, and the detector signal was demodulated for each harmonic component changing p in Equations 4.17 and 4.18. Only one period was discarded considering that the flux-ramp transient lasts less than one period of the highest modulating frequency harmonic. The results of the simulation are shown in Figure 4.14.

Blue traces in both panels of Figure 4.14 correspond to the demodulation of the first harmonic component $p = 1$, consistent with the results of Figure 4.13. Dotted red and grey lines are the minimum demodulated white flux noise for resonator phase and amplitude respectively, achieved at conditions represented by the blue, black an cyan stars. Like in the open-loop scheme, resonator phase domain gives the lowest possible noise although the difference with amplitude demodulation is not considerable. In the case of the phase, we can see that demodulated noise for the first component is always lower than the rest. On the contrary, in the case of amplitude readout, when the probe tone f_{exc} is close to the unaltered resonance frequency f_{off} noise diverges for the first and third demodulated component while

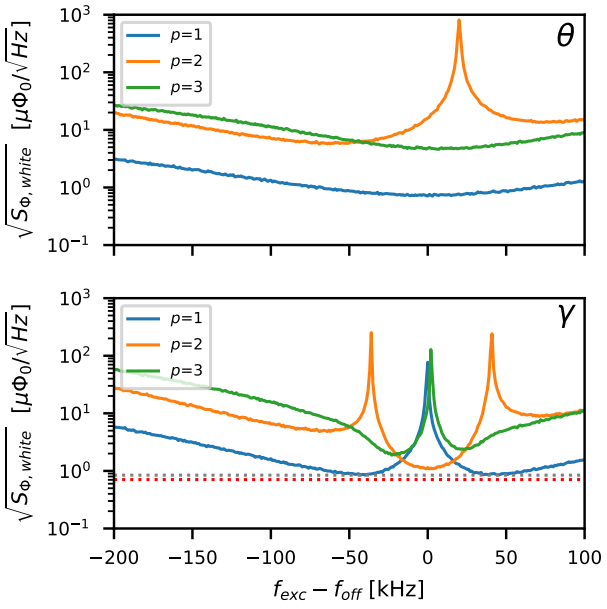

Figure 4.14: Flux-ramp demodulated white flux noise density $\sqrt{S_{\Phi,white}}$ as a function of f_{exc} for every demodulated domain and selected FRM component $f_{\text{dem}} = p \cdot f_{\text{mod}}$ for constant $P_{\text{exc}} = -70$ dBm and additive noise temperature of $T_n = 4$ K. **Top)** Resonator phase demodulation. **Bottom)** Scattering amplitude demodulation. Red and grey lines show resonator phase and scattering amplitude noise minimums respectively. Hamming window functions with $n_{\text{disc}} = 1$ and $n_{\Phi_0} = 4$ were used.

for the second there is a minimum in accordance with the available literature [92]. Therefore, achieving the minimum noise condition involves demodulation of the first harmonic at its maximum amplitude (i.e. Θ_1^{max} and Γ_1^{max}). Since the to total power is spread out between harmonics, this is fulfilled when the sum of the powers of the other harmonics reach their minimums. On the other hand, for a fixed f_{exc}, the spectral components are determined by P_{exc} [88]. When power increases P_{exc}, both β_{eff} and η decrease, leading again to a sinusoidal response in resonator phase and amplitude, until there is no response (i.e. $\Theta_p \approx \Gamma_p \approx 0$). Taking advantage of the fact that resonator phase and amplitude behave as sinusoidal signals at high powers, Equations 4.19 and 4.20 in the additive noise case can be easily calculated considering $\theta(\Phi) \approx \Theta_1 \sin(2\pi\Phi/\Phi_0)$ $\gamma(\Phi) \approx \Gamma_1 \sin(2\pi\Phi/\Phi_0)$ yielding to [102]

$$\sqrt{S_\Phi^\theta} \approx \frac{1}{r} \frac{\sqrt{2\kappa/\alpha}}{2\pi\Theta_1} \sqrt{\frac{k_B T_n}{P_{\text{exc}}}}, \tag{4.26}$$

$$\sqrt{S_\Phi^\gamma} \approx \frac{\sqrt{2\kappa/\alpha}}{2\pi\Gamma_1} \sqrt{\frac{k_B T_n}{P_{\text{exc}}}}. \tag{4.27}$$

To verify the validity of these expressions, and later use them to estimate system temperature T_{sys}, first the amplitude of the fundamental resonator phase and amplitude components were numerically determined, yielding $\Theta_1 \approx 0.63$ rad and $\Gamma_1^{\text{up}} \approx \Gamma_1^{\text{low}} \approx 0.27$. Second, we demodulated white flux noise for both domains as a function of probe tone frequency f_{exc} at constant power $P_{\text{exc}} \approx -70$ dBm for three different cases: 1) Boxcar window $w[n]$ without discarding, 2) Boxcar window and one period discarded and 3) Hamming window with one period discarded. For all cases, $n_{\Phi_0} = 4$ and the parameters in Table 4.2 were used. The results presented in Figure 4.15 for the non-discarding case were $\sqrt{S_\Phi^\theta} \approx 0.52\mu\Phi_0/\sqrt{Hz}$ and $\sqrt{S_\Phi^\gamma} \approx 0.62\mu\Phi_0/\sqrt{Hz}$ for resonator phase and amplitude demodulation respectively, while in the second case $\sqrt{S_\Phi^\theta} \approx 0.61\mu\Phi_0/\sqrt{Hz}$ and $\sqrt{S_\Phi^\gamma} \approx 0.72\mu\Phi_0/\sqrt{Hz}$. Lastly, using Hamming window, $\sqrt{S_\Phi^\theta} \approx 0.71\mu\Phi_0/\sqrt{Hz}$ and $\sqrt{S_\Phi^\gamma} \approx 0.84\mu\Phi_0/\sqrt{Hz}$. These values are in well

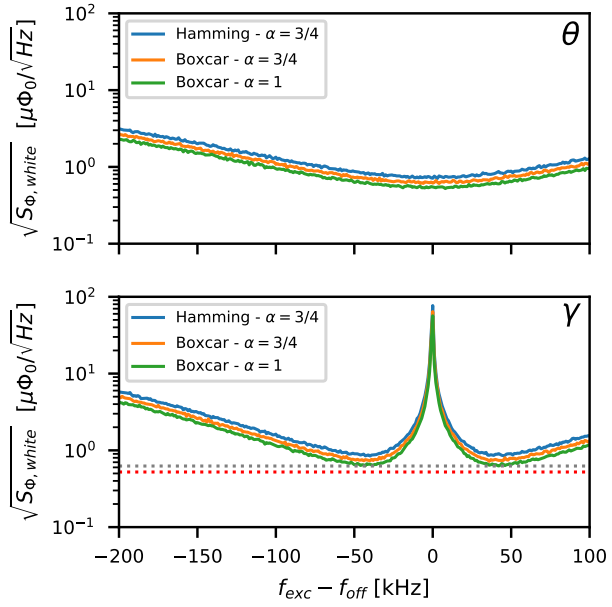

Figure 4.15: Flux-ramp demodulated white flux noise density $\sqrt{S_{\Phi,\text{white}}}$ as a function of f_{exc} for different window functions $w(t)$ and number of discarded periods n_{disc} with constant $P_{\text{exc}} = -70$ dBm and additive noise temperature of $T_{\text{n}} = 4$ K. **Top)** Resonator phase and **Bottom)** Scattering amplitude. Red and grey lines show phase and amplitude noise minimums respectively for a Boxcar window function, without periods discarded.

agreement with expressions 4.26 and 4.27 using the aforementioned Θ_1 and Γ_1 values. As expected, discarding a period yielded a degradation of $\sqrt{4/3} \approx 1.15$, while the Hamming window $\sqrt{4\kappa/3} \approx 1.35$. This corresponds to a factor $\kappa = 1.37$ coincident with the equivalent noise bandwidth of the Hamming window with respect to the Boxcar. Although the Hamming window improves linearity [117], its main-lobe is wider compared to the boxcar window leading to an increase in the noise level. For the purpose of this work, this degradation is not important since it affects both domains equally.

Similar to the open-loop demodulation, the noise in the optimal trajectories for both domains was determined for the SQL and $T_{\text{n}} = 4$ K. The results are shown in Figure 4.16. Again, resonator phase readout provides the best performance and noise densities decreases with $\sqrt{S_{\Phi,\text{white}}} \propto 1/\sqrt{P_{\text{exc}}}$ for both domains reaching minimums at $P_{exc} = -70$ dBm. Unlike the open-loop case, both amplitude minima differ at low powers, while at high powers they coincide due to the sinusoidal behavior explained earlier. In agreement with Equations 4.26 and 4.27 noise values in the SQL are $\sqrt{S^{\theta}_{\Phi,SQL}} \approx 0.18\mu\Phi_0/\sqrt{Hz}$ and $\sqrt{S^{\gamma}_{\Phi,SQL}} \approx 0.22\mu\Phi_0/\sqrt{Hz}$ being $\sqrt{T_{4K}/T_{SLQ}} \approx 4$ lower than the $T_n = 4$ K case. As expected, these values represent a degradation of $c^{\theta}_{\text{deg}} \approx 2.53$ and $c^{\gamma}_{\text{deg}} \approx 2.8$ with respect to open-loop demodulation. Smaller values can be achieved removing the windows or not discarding periods depending on the linearity requirements or flux-ramp transient duration. Despite the imposed degradation, FRM provides other advantages as is demonstrated below using our simulation framework in the following sections.

TLS and Multiplicative Noise Impact for FRD

As shown in Section 4.3.1, simulations to evaluate the impact of both TLS noise and multiplicative readout system noise for FRD were performed. Starting with TLS, the demodulated noise $\sqrt{S_{\Phi,white}}$ at the detector frequencies f_{det} was determined for the same fractional frequency densities $S_{f_r}(1Hz)/f^2_{\text{off}}$ values used before. The results are shown in the left side of Figure 4.17 for both domains at the optimum conditions represented by stars in Figure 4.13. It can be seen that although the noise level increased with respect to the un-modulated case, for the same noise density TLS noise represents a lower impact with respect to the additive noise levels represented by the red and grey dotted lines. This is due to the demodulation process that

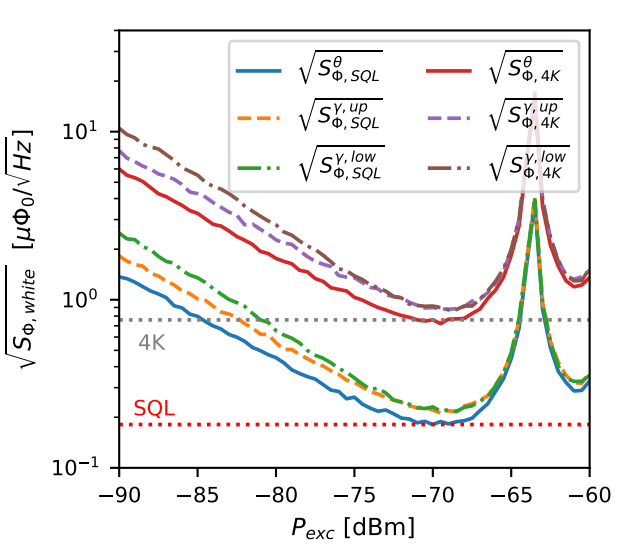

Figure 4.16: Flux-ramp demodulated minimum white flux noise density $\sqrt{S_{\Phi,white}}$ for every demodulation domain as a function of power P_{exc} and additive noise temperature of $T_n = 4$ K. Solid lines correspond to minimum noise for resonator phase readout while dashed and dashdotted lines are upper and lower local minimums for scattering amplitude readout.

down-converts the information signal from the carrier frequency $f_{\mathrm{mod}} \approx 61$ kHz, and therefore the noise evaluated at the same frequency $S_{f_r}(f_{\mathrm{mod}})/f_{\mathrm{off}}^2$. This value is considerably lower than the value at $S_{f_r}(f_{\mathrm{det}})/f_{\mathrm{off}}^2$ due to the $1/f$ TLS dependency. Therefore, relaxing the maximum TLS noise requirements to $S_{f_r}(1Hz)/f_{\mathrm{off}}^2 = 2 \cdot 10^{-17}$ Hz^{-1} and $S_{f_r}(1Hz)/f_{\mathrm{off}}^2 = 4 \cdot 10^{-16}$ Hz^{-1} for the SQL and $T_n = 4$ K respectively. As far as the readout domain is concerned, results show again no preference for resonator phase or amplitude demodulation at higher powers, leaving multiplicative noise the main factor to decide if there is an optimal readout domain.

Demodulated noise results for multiplicative sources under the optimum readout condition for additive noise found in Section 4.3.2 as a function of NSD are shown in the right side of Figure 4.17. As seen in previous results, resonator phase domain is the optimal domain for the additive noise case while the other noise sources remain negligible for the same NSD values. All noise demodulated values increase with respect to the open-loop case, following the same dependence with $\sqrt{S_\Phi} \propto \sqrt{NSD}$. However, all previously defined rejection factors decreased from 10 dB to 8 dB for amplitude noise in the amplitude domain, while for the resonator phase demodulation from 19 dB to 18 dB and from 40 dB to 14 dB for phase and amplitude noise respectively. As expected, all rejection factors decreased as a consequence of the FRM. Particularly, phase demodulation became more sensitive to amplitude noise when the readout tone is positioned further away from the resonance, where its projection is considerably greater and the gain lower. On the contrary, phase noise in these positions is lower, therefore it has less impact. However, as demonstrated before, system noise depends on the characteristics of the readout hardware used.

Optimum Domain for FRD

Similar to the open-loop demodulation case, the simulation framework was used in order to predict the system noise performance of the SDR system used as an example. Measured noise values shown in Figure 4.3 using magenta and cyan triangles were included in our simulation framework and again, TLS noise was not considered. The results of the flux-ramp demodulated noise for every domain and both SQL and $T_{\mathrm{n}} = 4$ K additive noise conditions are shown in Figure 4.18. Once again, amplitude readout shows the best performance when a real SDR readout system is used, and the impact of multiplicative noise became more relevant for the SQL scenario. The resonator phase domain is completely dominated by the phase noise of the readout system which has a value of $S_\phi(f_{\mathrm{mod}}) \approx -108$ dBc/Hz at the frequency f_{mod}. Amplitude noise at the same frequency with $S_\gamma(f_{\mathrm{mod}}) \approx -130$ dBc/Hz does not have NSD to

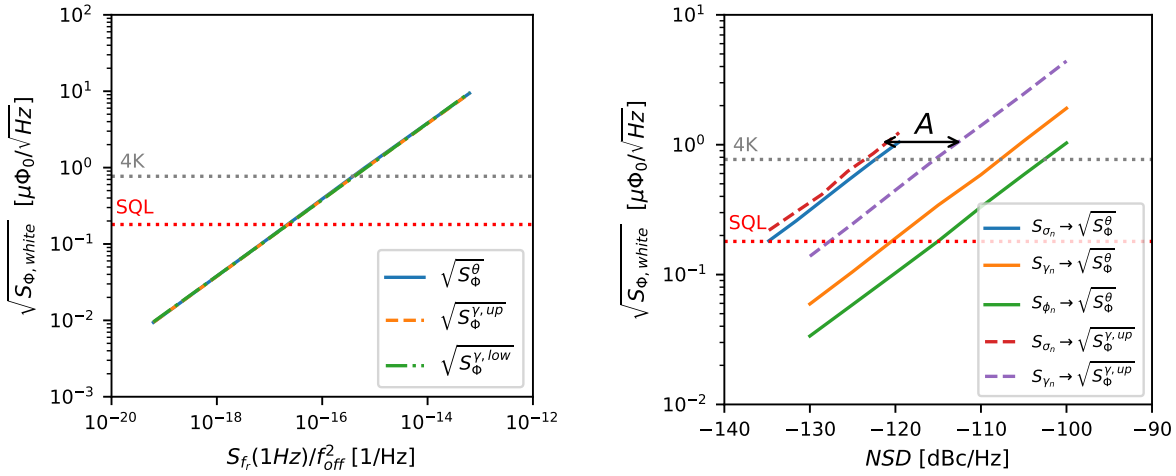

Figure 4.17: Left:) Flux-ramp demodulated white flux noise density $\sqrt{S_{\Phi,\text{white}}}$ as a function of the Two-Level Systems (TLS) noise level of S_{f_r}/f_{off} for both demodulation domains in the minimum additive noise condition for a constant $P_{exc} = -70$ dBm. **Right)** Flux-ramp demodulated white flux noise density for every demodulation domain and power for additive noise with $4K$. As a reference, dotted red and grey lines represent the minimum noise values for resonator phase demodulation with a power of $P_{\text{exc}} = -70$ dBm in the case of the Standard Quantum Limit (SQL) and $T_n = 4$ K respectively. Hamming window functions with $n_{\text{disc}} = 1$ and $n_{\Phi_0} = 4$ were used. As an example, black arrow represents the amplitude noise rejection factor A in scattering amplitude domain readout.

represent a considerable degradation for any of both scenarios. Clearly, like TLS, FRM helped to reduce the low-frequency multiplicative noise compared to the open-loop scheme. Quantitatively, noise levels at $P_{\text{exc}} = -70$ dBm are $\sqrt{S_\Phi^\theta} \approx 0.43\mu\Phi_0/\sqrt{Hz}$ and $\sqrt{S_\Phi^\gamma} \approx 0.26\mu\Phi_0/\sqrt{Hz}$ for the SQL and $\sqrt{S_\Phi^\theta} \approx 0.84\mu\Phi_0/\sqrt{Hz}$ and $\sqrt{S_\Phi^\gamma} \approx 0.90\mu\Phi_0/\sqrt{Hz}$ for the $T_{\text{n}} = 4$ K case, all of them consistent with the values shown in the right side of Figure 4.17 for their respective NSD levels. Using these results and Equations 4.26 and 4.27, it is also possible to calculate an additive equivalent system temperature. In the resonator phase demodulation case the measurements are $T_{\text{sys}}^{\theta,SQL} \approx 1.4$ K and $T_{\text{sys}}^{\theta,4K} \approx 5.1$ K, as for amplitude $T_{\text{sys}}^{\gamma,SQL} \approx 0.4$ K and $T_{\text{sys}}^{\gamma,4K} \approx 4.5$ K. Where only in the SQL case multiplicative noise represents considerably higher system temperature T_{sys} than the additive temperature T_{n}.

Previous simulations contributed to improve system noise estimations finding the maximum noise values that can be managed for a given sensitivity, thus enabling the optimization of the associated µMUX, cold and warm-temperature readout systems. Although for this work the criterion for the selection of optimal parameters was found to be based on the condition of minimum readout noise, two important factors must be taken into account. First, for a large number of channels N, the total power at the output of the µMUX grows with $P_{\text{out}} \propto N$ and can saturate the HEMT amplifier degrading the noise performance [103]. This problem is described in the next section along with the cryogenic Microwave Readout chain characterization. Second, while the phase demodulation yielded better results for the additive noise case, amplitude demodulation is robust to other types of noise, and does not require a resonance circle transformation which can be affected by phase variations [121] of the RF components and requires more digital resources to be implemented [114, 116].

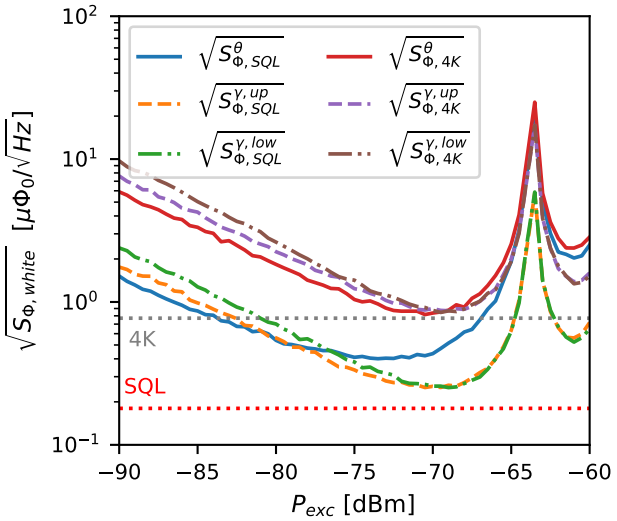

Figure 4.18: Flux-ramp demodulated white flux noise density $\sqrt{S_{\Phi,white}}$ for every demodulation domain as a function of power P_{exc} and additive noise temperature of $T_n = 4$ K and using the noise parameters of the example SDR readout System. As a reference, dotted red and gray lines represent the minimum noise values for resonator phase demodulation with a power of $P_{\text{exc}} = -70$ dBm in the case of the Standard Quantum Limit (SQL) and $T_n = 4$ K respectively.

The main objective of the developed simulation framework is to predict the system noise performance of a multiplexer channel with certain characteristics for a particular readout system and under different demodulation domains and readout parameters. The secondary objective is to be able to determine if the SDR readout system used has the appropriate performance to achieve the noise levels required by a given application. Although the results obtained are consistent with experimental results found in the available literature, this thesis also aims to experimentally validate the simulation results and at the same time determine the performance of the developed SDR systems. Among the parameters necessary for the validation, one of the most important ones is the additive noise temperature T_n. This temperature is typically dominated by the cryogenic RF chain of which the cryogenic HEMT amplifier is a major part. For this purpose, in the following sections, its design and characterization are described. The reset of the input parameter such as multiplicative noise levels and the μMUX parameters are described in Chapters 6 and 7.

4.4 Cryogenic Microwave Readout Chain

In order to achieve the required sensitivity, MMBs and their associated multiplexing systems require to be cooled down to sub-kelvin temperatures. Continuous cooling at these extremely low-temperatures cannot be performed with traditional cooling techniques using cryogenic liquids like Helium or Nitrogen, therefore special cooling techniques are required. This is the case of the dilution refrigerators that use a mixture of two isotopes of Helium achieving temperatures as low as 2 mK, with no moving parts in the low-temperature stages [122]. While these dilution systems can be operated for months without the necessity of Helium refill or recycling, they are limited by the cooling power available at the different cooling stages (Cooling power is defined as the maximum power that can be dissipated inside the refrigerator without increasing the temperature). This imposes several limitations on the design of the required cryogenic microwave readout chain that communicates the detectors and multiplexing systems with the readout electronics at room temperature as shown in the Figure 4.1, and therefore a strong trade-off between electrical and thermal performance which must be taken into account.

In this section, first the working principle of the dilution fridges and the heat load con-

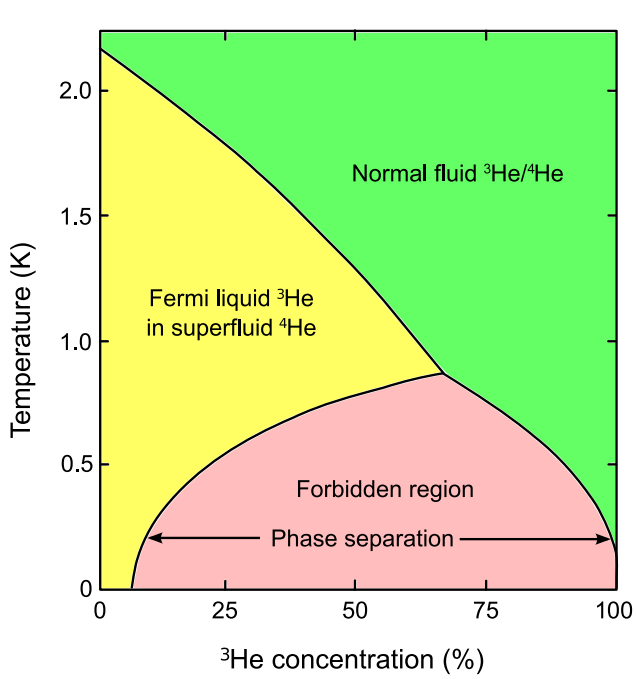

Figure 4.19: Phase diagram of ^3He-^4He mixture. Below $T \approx 0.87$ K at their saturated vapor pressure, a mixture of the two isotopes undergoes a phase separation into a normal fluid (mostly ^3He) that floats on a denser superfluid consisting mostly of ^4He. This phase separation happens because the overall mass of liquid helium can reduce its thermodynamic enthalpy by separating.

siderations at the time of dimensioning the microwave readout chain required for the μMUX readout are described. Later, the available cryogenic microwave readout chain layout is presented together with the gain, noise and linearity measurements.

4.4.1 Dilution Refrigerators and Heat Load Considerations

A cryogen-free dilution refrigerator is a closed-loop cooling system that provides cooling to temperatures in the order of milli-kelvins. These systems are used for instance in quantum computing, materials science, astrophysics, and fundamental research [122]. Temperatures below 10 mK are enabled by the dilution unit inside the system, which provides the necessary cooling to reach these ultra-low temperatures. The cooling power of the dilution unit comes from the mixture of Helium-3 (^3He) and Helium-4 (^4He) isotopes. Whereas other fluids tend to separate completely at sufficiently low temperatures, these two isotopes can remain dissolved even down at the lowest temperatures. ^3He and ^4He represent two different fundamental particles. ^4He isotope is a Boson and can undergo a phenomenon called Bose-Einstein condensation, where multiple particles can occupy the lowest quantum mechanical energy state. This phenomenon is responsible for the superfluidity of ^4He at ≈ 2.17 K [123]. On the other hand, ^3He is a fermion, therefore the superfluidity phenomenon is not possible for it since only two fermions (with opposite spins) are allowed to occupy the same quantum mechanical energy state. As can be seen in Figure 4.19, at temperatures of around ≈ 0.87 K depending on the ^3He concentration, the ^3He–^4He mixture will separate into two phases: an ^3He rich phase (concentrated phase - green region) and an ^3He poor phase (dilute phase - yellow region). Approaching the absolute zero temperature, the concentrated phase becomes pure ^3He while in the dilute ^4He rich phase remains 6.6% of ^3He. The enthalpy of ^3He in the dilute phase is larger than in the concentrated phase. Hence energy is required to move ^3He atoms from the concentrated to the dilute phase. This energy is taken from a well isolated environment where the mixing of the isotopes happens and is called the Mixing Chamber (MXC), the place where the cooling occurs when the ^3He is pumped through the phase boundary [124].

The entire dilution refrigerator consists of different temperature stages, with the dilution unit located in the lowest stages, as can be seen in the left side of Figure 4.20. The stages are easily recognizable as they are made of large metallic plates. These are conventional named:

the room temperature flange, the 50 K flange, the 4 K flange, the Still flange, the Cold Plate flange, and the Mixing Chamber flange. Below that there is the experimental space where the samples are attached, enabling their characterization at milli-Kelvin temperatures. The stages are separated by non-conductive supports and heat switches allowing to thermally connect or disconnect them. It should be mentioned that all stages are encapsulated in different vessels which provide shielding for thermal radiation between stages, as well as the necessary sealing to achieve high vacuum levels. In this way, the system can be thermally isolated from the environment avoiding heat transport by convection [123].

In normal operation, ^3He comes to the dilution unit pumped with a Gas Handling System (GHS). It enters the dilution unit precooled by the Pulse Tube Cryocooler (PTC) down to about 3 K, and through the main flow impedance in the still chamber. From there it is transported to the continuous flow heat exchanger and then to the step heat exchangers, which cool the ^3He going to the mixing chamber. From the mixing chamber the ^3He goes into the still chamber and in a gas phase it is evaporated through a still pumping line, eventually coming back to the start of the process. The available cooling power is determined by the circulation rate of ^3He. The larger the flow, the larger the cooling power, provided that the heat-exchangers are capable of handling the increased flow rate. The circulation rate of ^3He is controlled by the still heater in order to increase the evaporation. As ^3He has larger vapor pressure than ^4He, this process distills ^3He out of the mixture (the ^3He concentration in the gas phase is 90%) After the ^3He gas evaporates from the still, it is pumped back to the GHS, in which it is purified and then allowed back into the condensing line [122].

For the development of this work, a *Bluefors LD250*[1] dilution cryostat was used. A detailed view of its parts can be seen on the left side of Figure 4.20. Although in the future the detection system under development will be installed in the cryostat specially designed for the QUBIC project [35], the design of the cryogenic microwave readout chain required for monitoring the resonators state from the room temperature stages will be designed based on the available cryostat. The cryogenic microwave chain has two main objectives: first, to transmit the tones generated by the readout system to the μMUX, adapting the necessary readout powers; second, to amplify the signals at the output of the μMUX in order to be received by the readout system while maintaining the low noise levels provided by the lower temperature stages. Not only it is necessary to provide a chain capable of transmitting microwave signals, but also the low frequency lines needed to bias the detectors and to inject the modulation current. While these electrical connections are essential for the functioning of the detection chain, they must be selected carefully in order to avoid having high thermal loads that would impede the necessary temperatures to be reached.

Two types of thermal loads are considered when designing the cryogenic electrical circuits. One is called *Passive load*, and is determined by the conduction of heat from higher to lower temperature stages through the materials constituting the electrical connections. The other is the *Active load*, represented by all the electrical dissipation of the elements inside the cryostat such as amplifiers and attenuators. To ensure correct operation of the cryostat at the desired temperature, the sum of both contributions must be less than the cooling power of the respective stage in which they are thermally anchored. The cooling powers provided for the aforementioned device at their nominal temperatures are: $\sim$ 30 W for the 50 K flange, $\sim$ 1.5 W for the 4 K stage, $\sim$ 50 mW for the Still Plate, and $\sim$ 500 μW for the Cold Plate [125, 90]. For the particular case of the mixing chamber, although the manufacturer specifies 250 μW at 100 mK, the available cooling power for this particular cryostat and configuration is $\sim$ 380 μW. It should be noted that the values mentioned are those of the cryostat purchased, which is factory equipped with microwave coaxial lines and low-frequency twisted pair (TWP) lines. In particular, eight coaxial lines and twelve twisted pairs are provided between the room temperature stage (RT) and the mixing chamber (MXC). Additional DC lines are provided for

[1] https://bluefors.com/products/dilution-refrigerator-measurement-systems/

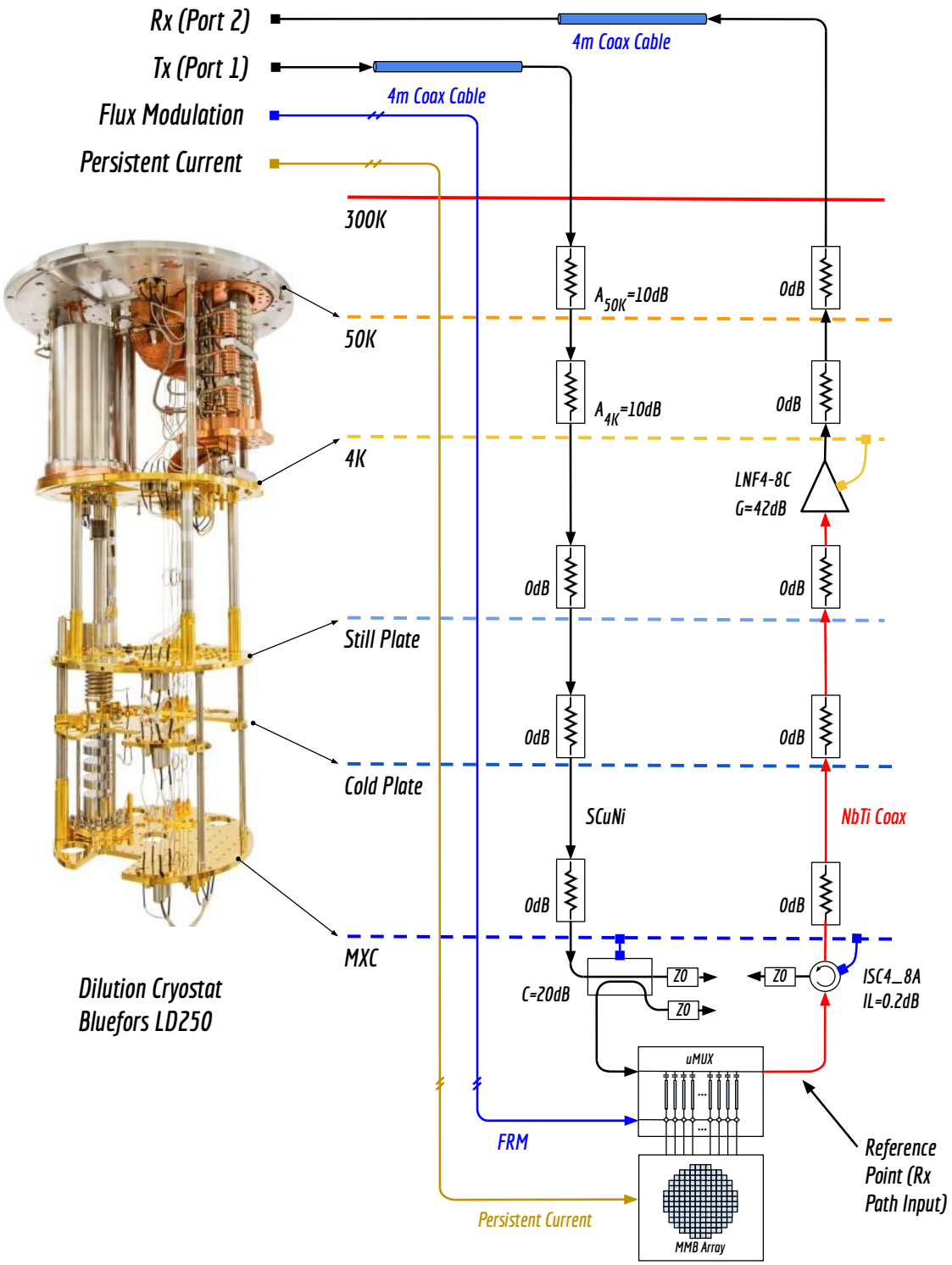

Figure 4.20: Cryogenic Microwave Readout Chain mounted on a *Bluefors LD250* dilution cryostat. On the transmission side (Tx) a set of cold attenuators and coupler reduce the thermal noise coming form the higher temperature stages, while at the same time adapts the required readout power P_{exc}. On the receiver side (Rx) a set of amplifiers bust the signals while maintaining the signal-to-noise ratio (SNR). Additionally, twisted pair lines are used to inject the persistent current and provide the Flux-Ramp modulation (FRM).

biasing the cryogenic HEMT amplifiers in the 4 K flange. The Access to the coaxial lines is via SMA feedthroughs mounted on a ISO-K63 flange, while the DC lines are accessed via 24-pin FISCHER connectors through a KF40 flange.

The thermal and electrical conductance of the electrical connections is determined by the material used as well as the cross section and length. For electrical connections it is preferable to use materials with high electrical conductivity, but at the same time good conductors generally represent a high thermal load due to the high thermal conductivity [123]. For this purpose, alloys of different metals, superconductors or special coatings are used in order to satisfy simultaneously electrical and thermal requirements. In the case of coaxial lines, Copper-Nickel ($CuNi$) wires of both 2.19 mm and 0.86 mm diameter are used. The denominations used by the manufacturer of these cables[2] are $SC219/50 - SCuNi/CuNi$ and $SC086/50 - SCuNi/CuNi$, where $SCuNi$ indicates that the inner conductor made of $CuNi$ is Silver-plated (S), thus reducing electrical losses produced by the skin effect at high frequencies. The respective thermal conductivities for these sections at 4 K are $4.11 \cdot 10^{-4}\ W \cdot m/K$ and $7.07 \cdot 10^{-5}\ W \cdot m/K$ respectively [126]. Larger cable cross-sections can be used to connect stages where more cooling power is available. Therefore, 2.19 mm cables connect room-temperature (RT) and 4K stages, while 0.86 mm cables connect to the rest of the stages. As will be explained below, in certain cases, cables with low or even negligible electrical losses are required. For this purpose, superconducting Niobium-Titanium ($NbTi$) cables are also used. The manufacture denomination in this case is $SC086/50 - NbTi/NbTi$. These cables present low electrical losses and low thermal conductivity, which makes them ideal for low noise applications at mK temperatures. Although these cables are the preferred choice, they are orders of magnitude more expensive than normal cables and only they can be used below their critical temperature (i.e. below 4 K) [126]. In our case, these cables will only be used in microwave coaxial chains equipped with amplifiers. For TWP lines, Phosphor-Bronze cables which represent a good trade-off between thermal conductivity and electrical resistance are used. The provider of these cables specifies a resistance $< 2\Omega$, which is suitable for the injection of modulating signals.

With respect to the active load, it can be divided into two contributions. One part is given by the dissipation of the LNA amplifiers which are placed at 4 K, the other by the dissipation of the electrical signals introduced by the cables. In the case of the amplifiers used for this thesis (LNF-LNC4-8C), they have a dissipation of about $\sim$ 12 mW, representing a total of 24 mW [127]. This dissipation is negligible with respect to the cooling power of the 4 K stage which is of the order of $\sim$ 1 W. Of the eight coaxial lines available, only two of them are equipped with two cryo LNA amplifiers. Therefore, only two microwave coaxial chains can be used for the readout of the µMUXes. In spite of the cooling power excess, particular attention must be paid to LNA amplifiers. They must be properly thermally anchored, and the center conductor of the SMA connector must be thermalized. The low thermal conductivity of the central pin with respect to fridge flanges may represent a heat flow from the 4 K stage to the lower temperature ones. For this reason, the microwave chains are provided with 0 dB attenuators which allow to thermally anchor the center conductor to the flange where they are attached.

The second contribution to the active load is determined by the dissipation of electrical signals inside the cryostat. This is the case of the monitoring tones which enter the cryostat through the coaxial cables. Due to the fact that the tones need to be generated at high powers by the readout system to obtain the required quality, they inevitably need to be attenuated by the cryogenic microwave chain in order to achieve the powers allowed by the µMUX. Therefore, it represents an active thermal load dependent on the tone power, the number of tones and the attenuation values. Along with the active load, the noise level and the linearity of the chain also depend on these same factors. This represents a trade-off when designing the microwave chain. In the following subsections the design and characterization of the cryo-

[2] http://www.coax.co.jp/en/

genic microwave readout chain will be described. It is important to highlight, that the design strategy employed in this thesis was aimed at optimizing the noise performance. Then, under this condition, the maximum number of tones for which the linearity and active thermal load requirements are satisfied was determined. This design strategy ensures the availability of a cryogenic microwave chain that enables optimal readout of at least a small number of channels during the development phase of the multiplexing and SDR readout systems.

4.4.2 Cold Attenuation, Gain and Noise Temperature

On the right side of Figure 4.20, the diagram of the microwave readout chain is shown. This is a detailed representation of the components in Figure 4.1, which are located inside the cryostat. The chain can be divided into two paths: the transmission (Tx) path and the reception (Rx) path. The Tx path allows the interrogation tones generated by the readout system to be sent to the multiplexer and adjusts the power levels, while the Rx path amplifies the low-power signals to acceptable levels for the readout system. As explained in Section 4.3, each component in the chain contributes electrical noise, which can be modeled by an equivalent noise temperature. In the case of passive components, their electrical noise is generated by the agitation of charge carriers due to the physical temperature of the element. For the case of a cables or attenuators at a physical temperature T_p, the equivalent noise temperature T_{eq} can be calculated using the following expression [82]:

$$T_{eq} = (A_L - 1)T_p, \tag{4.28}$$

where A_L represents the insertion losses or attenuation. In the case of an attenuator matched to the reference impedance Z_0, the insertion losses coincide with the squared magnitude of the scattering parameter, $A_L = 1/|S_{21}|^2$. In the case of a lossless cable, $A_L = 1$, the noise temperature is $T_{eq} = 0$ K, and therefore, the device does not contribute any electrical noise. Clearly, this is not the usual behavior of microwave components. The equivalent noise temperature is also used to describe the additive noise of active devices. In this case, the noise will be described by an equivalent noise temperature, often related to the physical temperature, but not described by Equation 4.28. The equivalent noise temperature is usually determined experimentally by the device manufacturers and provided in the data-sheet. When several components are connected in cascade, the equivalent noise temperature of the chain is determined by the noise added by each component and its relative position in the chain. The noise equivalent temperature T_e of a cascaded chain of components can be calculated based on the well-known Friis formula[128], which takes the following form:

$$T_e = T_1 + \frac{T_2}{G_1} + \frac{T_3}{G_1 G_2} + ... \tag{4.29}$$

For the example of only two components in cascade, which have power gains G_1, G_2 and equivalent noise temperatures T_1, T_2, as shown in Figure 4.21, the equivalent component has a power gain $G_{eq} = G_1 G_2$ and an equivalent noise temperature $T_e = T_1 + \frac{T_2}{G_1}$. Equation 4.29 suggests that the first component in the chain should have a high gain and low noise temperature in order to dominate the total equivalent noise temperature. Considering that the first elements in the chain are attenuators and cables (Tx path), it is natural to think that the noise temperature will be dominated by them and will be much higher than the physical temperature. However, this is not the case for a cold attenuation chain, which, in addition to matching the readout powers, aims to attenuate the thermal noise of the components at room temperature to the levels of the MXC [125]. As an example, consider the first attenuator in the chain, with attenuation A_1 and thermalized at $T_p = 50$ K, which directly receives thermal noise corresponding to the temperature $T_{Tx} = 300$ K. Using Equation 4.29, it is possible to calculate the noise temperature and refer it to the output, resulting in:

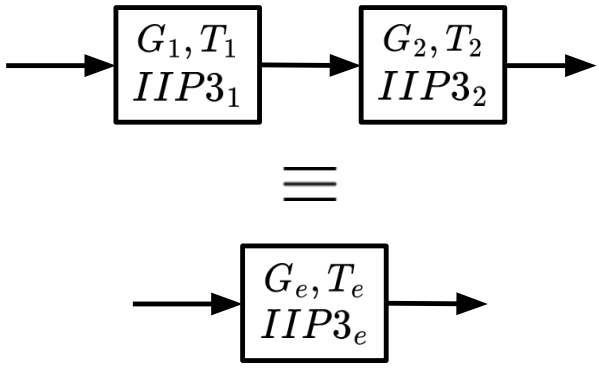

Figure 4.21: Cascade of two microwave components and its equivalent representation. Gain, noise and linearity of each block are characterized by its power gain G_i, noise equivalent temperature T_i and the 3rd order intercept point referred to the input $IIP3_i$. The equivalent block has gain G_e, equivalent noise temperature T_e and 3rd order intercept point $IIP3_e$.

$$T_{out} = \frac{T_{300K}}{A_1} + (1 - \frac{1}{A_1})T_{50K}. \tag{4.30}$$

In the limit case where the attenuation $A_1 \to \infty$, the noise temperature tends to the temperature at which the attenuator is anchored, $T_{out} \to T_{50K}$. While this is not a practical case, as no signal would be transmitted, typically an attenuation in the order of the temperature difference between stages is required (i.e. $A_1 \approx \frac{T_{300K}}{T_{50K}}$). In this case, 10 dB was used between the 300 K and 50 K stages, 10 dB between 50 K and 4 K, and finally 20 dB between 4 K and the MXC. The attenuation chain must be designed not only in terms of noise performance but also considering the active thermal load as explained before. Prioritizing the noise performance, the best option is to place all the attenuation in the lower temperature stages, but the dissipation of the interrogation tones could exceed the cooling capacity of that stage. For example, in the case of $N = 1000$ tones with an excitation power of $P_{exc} \approx -75$ dBm (i.e. $P_{Tx} \approx -35$ dBm), this would result in a dissipation of $P_{active} \approx 316\mu$W if the 40 dB were placed in the MXC. This value represents more than 80% of the cooling power of the stage. This is not feasible, so the attenuation was distributed between the stages for an intermediate solution. The requirements were to not exceed 20% of the cooling power of the stage and to achieve a noise temperature referred to the MXC that is at least five times lower than the noise temperature of the cryogenic LNA. It should be noted that 0 dB attenuators were also used, which have no effect on the noise but allow for proper thermalization of the central conductor of the coaxial cables. Particularly, as can be seen in Figure 4.20 a directional coupler *QMC-CRYOCOUPLER-20-4*[3] with a coupling value of $C = 20$ dB was used instead of an attenuator at MXC level. This device has additional functionalities compared to an attenuator. First, the SMA central conductor is galvanically isolated, thereby reducing the heat conduction to the µMUX device. Second, it presents a cold termination load to the µMUX, as the Z_0 load seen by the input port is not the same as the load in which the power of the tones reflected by the µMUX is dissipated [43, 90].

For the design of the transmission path (Tx), special attention was given to the components prior to the cryogenic LNA. This includes the cables connecting the MXC to the 4 K stage and the microwave circulator. Any loss in these cables would result in an increase in the noise temperature, as described by Equation 4.29. Therefore, superconducting *NbTi* lines were used (highlighted in red in Figure 4.20). Regarding the circulator, it is a passive, non-reciprocal, three-port device that allows the transmission of signals in one direction with almost no loss

[3] https://quantummicrowave.com/wp-content/uploads/2020/03/QMC-CRYOCOUPLER-20-4.pdf

(e.g., from port 1 to port 2 or from port 2 to port 3) and has high isolation when signals are injected in the opposite direction (i.e., from port 2 to port 1 or from port 3 to port 2). Isolators are two-port devices with one of the ports terminated with a Z_0 load that allow signals to pass in only one direction [82, 80]. This device is particularly useful at the output of the μMUX, as it allows signals to pass with attenuation less than 0.2 dB, which has small impact on the noise performance and helps isolate the device from the noise of the HEMT amplifier, as well as from unwanted signal reflections due to poor input matching of the cryogenic amplifier. Typically, these devices have isolation around 20 dB for a simple junction isolator. For our set up a circulator model *LNF-CIC4_8A*[4] terminated at one port with a load *LNF-TERM4_12A*[5] was used, both from the same manufacturer of the cryogenic LNA. A circulator was acquired instead of an isolator, as it offers greater versatility for use in a variety of experiments. The isolation of the circulator, combined with more than 20 dB of reverse isolation from the LNA, provides more than 40 dB of attenuation for ambient temperature noise entering the from transmission path (Port 2). The main component of the transmission chain is the cryogenic LNA, which amplifies the weak signals coming from the μMUX without degrading the SNR. As mentioned earlier, this setup makes use of Low Noise Factory amplifier, model *LNF-LNC4_8C*. The specifications for this amplifier show a gain of $G_{LNA} \approx 42$ dB and an equivalent noise temperature of $T_{LNA} \approx 2$ K for frequencies between 4 and 8 GHz and working at 4 K. It is important to note that the previous components were also selected to operate within the same frequency range. The HEMT amplifier, the coupler, and the circulator are all properly thermalized using cooper brackets with strong thermal contact to the respective plates. For the sake of simplicity, the LNAs low noise power supplies *LNF-PS3b* and cables for biasing were not included in Figure 4.20 but were required in order to ensure the correct LNA operation.[6]

For the fast and accurate noise estimation of the microwave chain, a Python script was developed to automate the cascade noise calculation and enable its optimization. As inputs, the script takes the values for attenuation A^i, physical temperature T_p^i, noise equivalent temperature of active devices T_e^i, cooling power P_{cool}^i, and readout tone power at the Tx input port P_{tone}^{Tx}. The outputs are the power gain, total noise equivalent temperature, active thermal load per stage, and received power at the Rx port. For the simulation, the attenuation values of the cables were added to the attenuators nominal values. Additionally, the attenuation and noise values used correspond to a frequency of $f = 6$ GHz and were considered frequency independent. In the future, the estimation will be improved by considering frequency-dependent attenuation and noise values, as well as the noise introduced by the cables due to the temperature gradient between stages. While for room temperature electronics the Johnson–Nyquist noise power is calculated using $P_n = KT_n$, these approximations are not valid for high-frequency devices working at low temperatures and quantum effects given by the SQL need to be taken into account. Consequently, a quantum correction factor $n(f)$ was included in the calculations. The expression for the correction factor is

$$n(f) = \frac{hf/k_B T_p}{e^{hf/k_B T_p} - 1} + \frac{hf}{2k_B T_p}. \tag{4.31}$$

The first factor considers Johnson–Nyquist noise temperature and frequency dependence, while the second accounts for the Standard Quantum Limit [129, 120]. At low-frequencies and high temperatures $hf/k_B T_p \to 0$, therefore $n(f) \to 1$ yielding to the classical approximation.

Figure 4.22 shows the contribution to the total noise temperature of each component in the microwave cryogenic chain, T_n^i. The values marked with red stars refer to the output of the μMUX, as this is the reference point used by the simulation framework described in Section 4.1.

[4] https://lownoisefactory.com/product/4-8-ghz-single-junction-isolator-circulator/
[5] https://lownoisefactory.com/product/lnf-term-4_12a/
[6] https://lownoisefactory.com/product/lnf-ps3b/

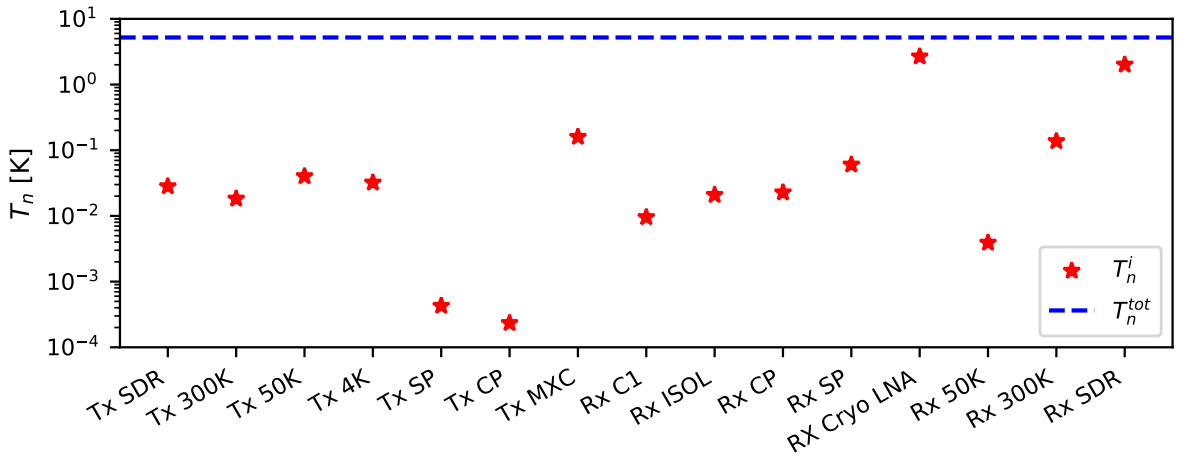

Figure 4.22: Additive noise equivalent temperature contributions T_n^i for each of the components shown in Figure 4.20 referred to the µMUX output (Red Stars). The blue dashed line represents the total noise equivalent temperature T_n^{tot}. C1 refers to the first superconducting cable after the µMUX, while Tx SDR and Rx SDR the transmitter and receiver noise equivalent temperatures of the readout system respectively.

The blue dashed line represents the sum of all contributions, T_n^{tot}, which, as required by design, is dominated by the temperature of the cryogenic LNA with $T_n^{RX-SDR} \approx 2.66K$ at the µMUX output. The total noise temperature is approximately $T_n^{tot} \approx 5.21$ K, while the total gain is $G_{tot} \approx -11$ dB. In addition to the LNA, the second most important contribution is the SDR receiver, which was included using a reference value of $T_e = 2500$ K, and represents a noise temperature of $T_n^{RX-SDR} \approx 2K$ when it is refereed to the µoutput. This value is an estimate and must be determined through the characterization of the readout system. This will be addressed later in Chapter 6.

In order to verify the correct design of the microwave chain shown in Figure 4.20, power gain and noise temperature measurements were performed using the *Keysight PNA-X N5242B* vector network analyzer (VNA) [130]. The cryostat circuit includes two 4-m coaxial cables that connect the SMA feedthroughs to the racks where the instruments are located. Power gain measurements between the Tx (Port 1) and Rx (Port 2) were carried out using a cable that connects the transmission and reception paths at the µMUX level, which is equivalent to measuring the resonators off-resonance. The VNA was previously calibrated in order to de-embed VNA cables and adapters. The measurement results in the 3 to 9 GHz range are shown in Figure 4.23. The blue line represents the total gain value $G_{\text{tot}}(f)$ as a function of frequency, while $G_{\text{fit}}(f)$ is a linear fit over the operating range. The gain is approximately -11.5 dB at 6GHz and decreases at a rate of 1.5 dB per GHz. This slope is primarily determined by the cabling and passive RF components [126], rather than by the cryogenic amplifier, which has a positive slope of approximately 2 dB [127]. These results represent a -2.5 dB difference with the simulation results of our simulation framework using the nominal values of each component. Despite this difference, the results demonstrate the proper functioning of the active devices in the cryogenic microwave chain.

The results from Figure 4.23 allow for the calculation of the tone power at the cryostat output. However, this total gain value does not distinguish between the contributions from the transmission and reception paths (i.e. $G_{tot} = G_{Tx} + G_{Rx}$). In our case, it is necessary to determine the transmission gain G_{Tx} in order to estimate the tone power P_{exc} interrogating the µMUX. Additionally, it is required to refer the noise temperature measured from the readout

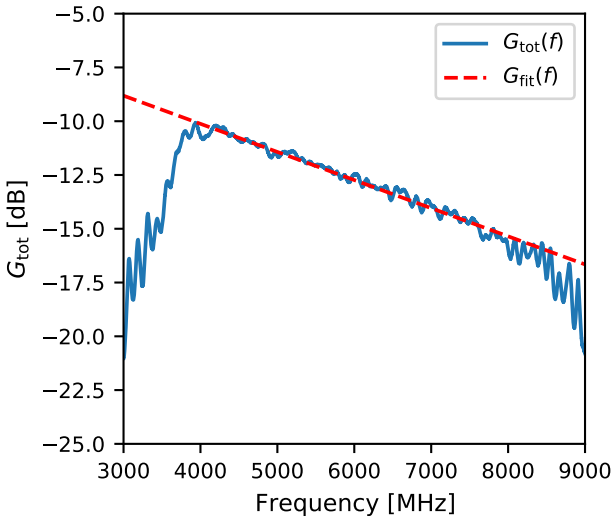

Figure 4.23: Measured total gain $G_{\text{tot}}(f)$ between transmitter (Tx) and receiver port (Rx) of the set-up shown in Figure 4.20 as function of frequency. The dashed red line represents the gain linear fit $G_{\text{fit}}(f)$ in the operational range. The operational frequency band is defined between 4 and 8 GHz.

system to the μMUX adopted as the reference in the readout model discussed in the previous Section 4.3. For the purposes of this work, the transmission path gain can be assumed to be no higher than 3 dB above the total attenuation calculated using the nominal values of the RF components. The calculations with the nominal values give $A_{Tx}^{nom} = 45$ dB (40 dB of cold attenuation plus 5 dB the cables). Thus, the attenuation value will range between two extremes values: $A_{Tx}^{min} = 45$ dB and $A_{Tx}^{max} = 48$ dB.

Using the PNA-X VNA, while the gain was determined, noise measurements were also performed using the Cold-Source Method [131]. Unlike the Y-factor method (also known as the hot/cold-source method), a noise source is not used during Device Under Test (DUT) measurements. Instead of measuring the DUT's output noise power under two different input-noise conditions generated from a noise source, the cold-source method combines S-parameter measurements with a single output-noise-power measurement of the DUT. First, the DUT's S-parameters are measured using the internal sinusoidal source and standard S-parameter receivers. From this data, the available gain of an amplifier or the conversion gain/loss can be calculated. Then, the sinusoidal source is turned off, a nominal 50Ω termination is presented to the input of the DUT, and a single output-noise-power measurement is taken using the VNA's receiver. From the S-parameter and noise-power data, the DUT's noise temperature is then calculated. In our case, the PNA-X is equipped with a particular low-noise receiver, which allows us to make precise noise-equivalent temperature measurements [131]. Prior to taking measurements, the VNA power was calibrated using a power meter directly connected to Port 1, followed by an extensive low-noise receiver calibration routine to achieve the required accuracy. The results of the noise temperature measurements as a function of frequency are shown in Figure 4.24. It is important to note that, unlike the results shown in Figure 4.22, this measurement excludes the noise temperatures of the transmitter and receiver due to the calibration performed. Given that the VNA provides a result referenced to the input of the DUT (e.g., Port 1), the measured value of T_n^{meas} was divided by the attenuation values A_{Tx}^{min} dB and A_{Tx}^{max}, thus referencing it to the output of the μMUX for both conditions. The results where the attenuation is the maximum, $T_n^{min} = T_{meas}/A_{Tx}^{min}$, are shown in orange, while results for the minimum attenuation, $T_n^{min} = T_{meas}/A_{Tx}^{max}$, are shown in blue. The result corresponding to T_n^{max} is close to those reported by the LNA manufacturer, which could indicate an overestimation of the attenuation in the case of $A_{Tx}^{max} = 48$ dB. A more precise measurement of the gain and noise temperature could be carried out using cryogenic noise sources and calibration kits at the MXC level. Regarding the objectives of this work, and given the lack of these devices, a value of $T_n^{max} \approx 4$K at 6 GHz was adopted, which is similar to the values typically reported

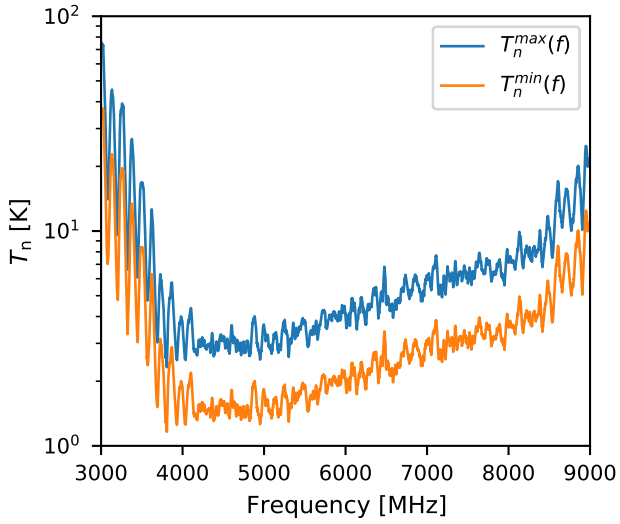

Figure 4.24: Cryogenic microwave chain noise equivalent temperature T_{n} as a function of frequency and transmitter attenuation A_{Tx}. The measured noise equivalent temperature initially referred to the input port (Rx) was referred to the μMUX output using the Tx path attenuation G_{Tx}. The blue line is calculated using the minimum expected attenuation $A_{Tx}^{min} \approx 45$ dB, while orange using the maximum $A_{Tx}^{max} \approx 48$ dB.

in the literature and close to the values obtained in the simulations presented. Additionally, this is a conservative value due to the fact that it represents an upper bound for the cryogenic microwave chain noise equivalent temperature.

4.4.3 Inter-modulation Distortion

The superposition principle states that, for all linear systems, the net response caused by two or more stimuli is the sum of the responses that would have been caused by each stimulus individually. At low reading powers, generally all the components in the RF chain behave in a linear fashion. The most common case is that of the amplifier, which, from an input signal, generates an amplified copy at its output $y(t) = a_1 x(t)$. Where a_1 is the voltage gain, which is commonly expressed as power gain $G_1 = |a_1|^2$ in high-frequency amplifiers. Real components deviate from this behavior at high signal levels. In particular, nonlinear effects become more evident in active components that use diodes and transistors. While nonlinearities give rise to microwave devices such as mixers and frequency multipliers, they are a problem in amplification devices because they can cause undesirable effects such as gain compression and generation of spurious frequency components. Generally, the output response of a nonlinear circuit can be modeled as a Taylor series in terms of the input signal voltage [82]

$$y(t) = a_0 + a_1 x(t) + a_2 x(t)^2 + a_3 x(t)^3 + ... \tag{4.32}$$

For a single input tone at f_0, the output will in general consist of harmonics of the input frequency of the form nf_0 , for $n = 0, 1, 2, ...$ created by the high order Taylor terms. Often these harmonics lie outside the pass-band of the device and they don't interfere with the desired signal at frequency f_0 . When considering a two-tone input signal $y(t) = X_0 \cos(2\pi f_1 t) + X_0 \cos(2\pi f_2 t)$ with closely spaced frequencies f_1 and f_2 the output $y(t)$ can be written as

$$
\begin{aligned}
y(t) = a_0 &+ a_1 X_0 \cos(2\pi f_1 t) + a_1 X_0 \cos(2\pi f_2 t) \\
&+ \frac{a_2 X_0^2}{2}\left[1 - \cos(4\pi f_2 t)\right] + \frac{a_2 X_0^2}{2}\left[1 - \cos(4\pi f_1 t)\right] \\
&+ a_2 X_0^2 \cos\left[2\pi(f_1 - f_2)t\right] + a_2 X_0^2 \cos\left[2\pi(f_1 + f_2)t\right] \\
&+ a_3 X_0^3 \left\{ \frac{3}{2}\cos(2\pi f_1 t) + \frac{3}{4}\cos\left[2\pi(2f_1 - f_2)t\right] + \frac{3}{4}\cos\left[2\pi(2f_1 + f_2)t\right] \right\} \\
&+ a_3 X_0^3 \left\{ \frac{3}{2}\cos(2\pi f_2 t) + \frac{3}{4}\cos\left[2\pi(2f_2 - f_1)t\right] + \frac{3}{4}\cos\left[2\pi(2f_2 + f_1)t\right] \right\} + \ldots
\end{aligned} \tag{4.33}
$$

This expansion shows that the output spectrum consists of harmonics of the form $nf_1 + mf_2 + \ldots$, with $m, n = 0, \pm 1, \pm 2, \pm 3, \ldots$. These combinations of the two input frequencies are called inter-modulation products, and the order of a given product is defined as $|m| + |n|$. Products of order $|m| + |n| = 1$ are the amplified input signals, while those with $|m| + |n| > 1$ are inter-modulation products, which are undesirable in the case of an amplifier. Particularly, third-order products located at $2f_1 - f_2$ and $2f_2 - f_1$ are the most problematic in amplification chains due to their proximity to the desired signals (f_1 and f_2) and their inability to be adequately filtered. As can be verified from Equation 4.33, first-order products scale linearly with input power $P_{f_1} = P_{f_2} = a_1^2 X_0^2/2$, while the power of Third-Order Inter-modulation products ($IM3$) increases with the cube of the input power $P_{2f_1-f_2} = P_{2f_2-f_1} = 9a_3^2 X_0^6/32$. The input power at which these powers are equal, $P_{f_1} = P_{2f_1-f_2}$, is defined as the Third-Order Input Intercept Point ($IIP3$). This value can be calculated based on the Taylor series coefficients as follows

$$
IIP3 = \frac{2a_1}{3a_3}. \tag{4.34}
$$

Although it is not possible to reach this point in practice, as other first-order products reduce the power of the tones at f_1 and f_2 (called gain compression), this parameter is widely used to describe the linearity of a microwave component chain and to estimate the value of third-order inter-modulation products. Just as the total noise of a cascade of components was calculated above using 4.29, there is an equivalent expression for calculating the equivalent third-order intercept point $IIP3_e$. For example, in the case of a two-element cascade as shown in figure 4.21, with third-order intercept points for each element $IIP3_1$ and $IIP3_2$, it is possible to calculate its equivalent using the following expression:

$$
IIP3_e = \left(\frac{1}{IIP3_1} + \frac{G_1}{IIP3_2} \right)^{-1}. \tag{4.35}
$$

In contrast to the Johnson-Nyquist noise, the inter-modulation products generated by the different blocks are coherent with the signals that produce them. This can lead to constructive or destructive combination of the products depending on the evolution of their phases and amplitudes along the chain. The expression 4.35 considers the most conservative case where the products are assumed to be coherent. A similar expression, assuming random phases, can be found in the available literature [82].

Considering that the inter-modulation products are inevitable, it is possible to design the cryogenic microwave chain in such a way that it has the necessary linearity or finding the maximum tone power levels that allow maintaining the inter-modulation products below a certain level, in order not to affect the readout of the µMUXes. The linearity of the RF chain was characterized again using the available VNA, using two independent signal sources, to allow the generation and combination of two RF tones with arbitrary powers and frequencies on the same port. These signals were sent through the Tx path and, using one of the receivers

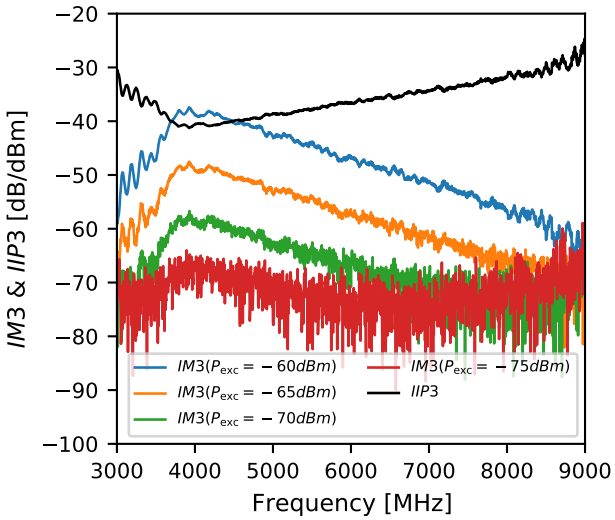

Figure 4.25: Third order inter-modulation products as a function of the frequency $IM_3(f)$ for different powers at the µMUX output. These values are referred to the power of the carrier signals. The solid black line represents Third Order Intercept point as function of frequency $IIP_3(f)$, referred to the input.

connected to the Rx port, the power of the desired signals and the inter-modulation products were measured [132]. The measurement results as a function of frequency and tone power are shown in Figure 4.25. As with the noise temperature, all results were referred to the input of the Rx circuit (i.e. µMUX output) using $A_{Tx} = 45$ dB. The blue, orange, green, and red curves correspond to the power of the third-order inter-modulation products ($IM3$) for different signal power levels in the range from -60 to -75 dBm at the µMUX output. These are expressed in dB, as they reflect the power difference between the inter-modulation product and the power of the tones generating it. As can be seen, a 5 dB increase in power results in a 10 dB increase in the inter-modulation product power. This happens because, while the desired signal grows linearly, the inter-modulation product grows cubically, and therefore, their difference grows quadratically. In the case of the red curve, this effect can only be observed at low frequencies, as the power of the products is higher than the receiver noise.

Based on these measurements, the software provided by the PNA-X VNA is capable of deriving the third-order intercept point [132]. The black trace represents the $IIP3$ as a function of frequency. Since this represents a power value, it is expressed in dBm. The results are consistent with the data-sheet of the cryogenic amplifier and the literature [127, 133]. Passive components can be considered completely linear ($IIP3 \rightarrow \infty$) and, therefore, are not included in Equation 4.35. In this way, the LNA is the only active element and the first one within the chain, thus dominating the linearity of the readout chain.

The two-tone signal represents the simplest case to analyze, but this analysis can be extended to a multi-tonal signal. In this case, it is possible to calculate the number of combinations of tone pairs that can be found in an N-tone comb. The number of inter-modulation products is $2N(N-1)$. Given the variability in the fabrication process of the resonators, it can be assumed that the interrogation tones will randomly be located across the entire bandwidth, thus affecting neighboring channels. This can be considered crosstalk between channels, similar to what is explained in Chapter 3.4. The crosstalk level due to inter-modulation distortion χ_{imd} can be calculated with the following expression [134, 94]

$$\chi_{imd} = 4\frac{P_{\text{tot}}}{IIP3}. \tag{4.36}$$

Here, P_{tot} is the total peak power transmitted to the the Rx path with the $IIP3$ third-order intercept point determined before. Along with the FRD noise simulations presented in Section 4.3.1, the average power of P_{exc}^{avg} and peak power of P_{exc}^{peak} at µMUX output over a flux-ramp period was calculated. The simulation results are shown in Figure 4.26. The simu-

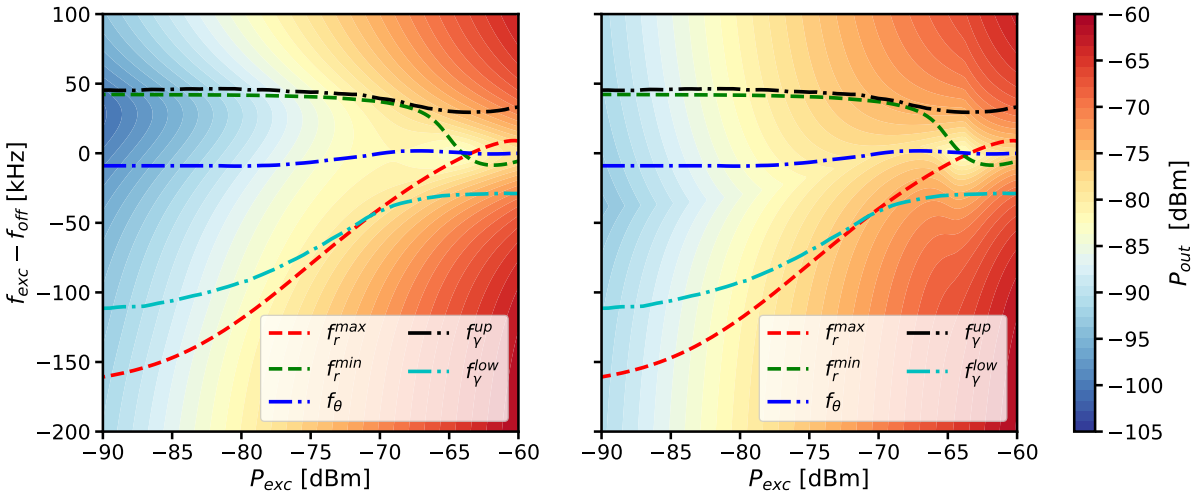

Figure 4.26: Output power at the μMUX presented in Table 3.1 as a function of f_{exc} and P_{exc}. **Right)** Average power P_{out}^{avg} at the μMUX output over a flux-ramp period. **Left)** Peak power P_{out}^{peak} at the μMUX output. Red and Green dashed line represent the maximum and minimum resonance frequencies, while dash-dotted lines the optimum trajectories for both demodulation domains.

lation results presented in Section 4.3.2 suggest an optimal readout of $P_{exc}^{opt} \approx -70$ dBm, which corresponds to an average μMUX output power of $P_{out}^{avg} \approx -80$ dBm and a peak power of $P_{out}^{peak} \approx -75$ dBm for the resonator phase domain. Considering that all the channels of the μMUX have random offset fluxes, it would be very conservative to assume that all channels will simultaneously present the peak power at the μMUX output. Therefore, in order to calculate the total peak power at the μMUX output (Rx path input) the average output power per channel multiplied by the number of channels was used (i.e., $P_{\text{tot}} = N_{det} P_{\text{out}}^{\text{avg}}$). The proposed improvement for the QUBIC project plans the readout of approximately $N = 1000$ detectors. Thus, the total average power at the output of the μMUX is $P_{tot} \approx -50$ dBm. Using Equation 4.36, this power represents a 40% crosstalk for $IIP3 \approx -40$ dBm, which could be excessive for the application. Therefore, one must opt to reduce the readout power and accept a degradation in the demodulated flux noise or directly limit the maximum number of channels. A 10 dB lower readout power would reduce the crosstalk to values close to 4%, and the noise would increase from $\approx 0.77\mu\Phi_0/\sqrt{Hz}$ to $\approx 2\mu\Phi_0/\sqrt{Hz}$, according to the results shown in Figure 4.18. Equivalently to reduce the power 10 dB, the number of tones can be reduced to $N = 100$ without noise performance degradation at the 4% crosstalk level. Although this value is an order of magnitude lower than the required one for the QUBIC project, it is an adequate value for the development stages. At the time of writing this thesis, the maximum number of multiplexer channels per coaxial line is $N = 16$.

Additionally to the aforementioned options, there are other intelligent solutions to overcome this issue. Clearly, the reception chain could be modified to improve its linearity. Although this represents a high cost, it has been adopted in several applications [103, 133]. This improvement uses a low-gain, high-linearity cryogenic LNA amplifier (e.g. *LNF-LNC4_8F_LG*) followed by a medium-gain cryogenic LNA at the 50K stage. This configuration provides ~ 10 dB improvement in the microwave chain $IIP3$. Finally, as an additional solution, a readout scheme that reduces the peak power at the multiplexer's output can be used. This is the case of Tone-Tracking [135], which consists of a feedback loop that tracks the movement of each resonator to continuously keep the readout tone in resonance and thus minimize the output power. Analyzing and implementing any of these options is beyond the scope of this thesis and will be considered in future works.

In summary, throughout this chapter, the readout procedure for a µMUX channel was described. The readout system was presented along with its noise sources and a simulation framework that allows us to determine the optimal readout parameters for two different readout schemes and domains was developed. To demonstrate the functionality of the simulation framework, and as an example, the noise levels shown in Figure 4.3 were used during the simulations. These levels were extracted from the previous characterization of the SDR readout system, except for the additive noise temperature T_n, which was considered a free parameter to evaluate its impact with different amplification techniques. As part of the validation of the simulation framework, the second part of this chapter described the operation of the cryogenic microwave chain and its characterization. From this, important parameters could be obtained such as the equivalent noise temperature T_n and linearity parameters $IIP3$. These results will be compared with the results of the characterization using the developed SDR systems.

In later chapters, the experimental validation of this framework will be carried out by measuring the demodulated noise of a µMUX channel using two different readout systems. These measurements also aim to verify that the SDR systems meet the necessary requirements for the frequency-multiplexed readout MMBs presented in Chapter 2 by means of the µMUX. The two prototypes of the SDR readout systems will be presented in the following Chapter 5. Then, their individual characterization will be shown in Chapter 6. Finally, the integration of the SDR system with the cryogenic microwave chain, the characterization of a single µMUX channel, and the measurement of demodulated noise as a function of the readout parameters will be presented in Chapter 7.

5. Software-Defined Radio Readout Systems

The readout system shown in Figure 4.1 provides the basic functionalities for the readout of a single μMUX channel. Typically, this scheme is composed of both microwave components and bench top instruments. While these provide exceptional performance required during the development phases of the multiplexers, they are too costly, bulky, and not versatile enough for the simultaneous readout of multiple channels. Technological advances in the telecommunications field offer a variety of specific solutions to this problem, representing lower cost, higher integration, and the necessary adaptability that such applications require.

Figure 5.1 shows several of the approaches used to address the MUX readout challenge. The natural solution would be to replicate the scheme in Figure 4.1 as many times as N channels are required. The combination/separation of the channels would be performed analogically using combiners and filters. The schematic of this solution is shown at the top of Figure 5.1. This scheme would require a large number of components, and analog channels separation would be impractical given the proximity between the channels ($\sim$ MHz). This problem also appears in other areas of telecommunications where it is necessary to separate narrow communication channels that are multiplexed in the frequency domain [136]. In line with Moore's Law, the rapid evolution of digital systems enables more sophisticated processing of radio signals [137]. The aforementioned complex tasks that previously could not be carried out in the analog domain started being implemented successfully in the digital domain, giving rise to the concept of Software-Defined Radio (SDR) [138]. These systems offer high customizability, large I/O bandwidths, and real-time processing, making them particularly suitable for the readout of μMUX devices. The aim of this chapter is to present one of the most important contributions to this work, which focuses on the development of two SDR system prototypes for the readout of MMBs in the frequency domain by means of the μMUX. As we will see later, these novel SDR systems are based on the latest generation of Radio-Frequency Systems on Chip (RFSoC) technologies.

5.1 Software-Defined Radio Readout Systems

The diagrams shown in the middle and bottom parts of Figure 5.1 correspond to widely used SDR schemes for the readout of multiplexed detectors in the frequency domain, such as MKIDs or TES/MMCs using the μMUXing technique [98, 139, 105, 135, 140]. While these schemes will be explained in detail later, a brief introduction is provided here to give an understanding of their general structure. In both schemes (middle and bottom), a series of Digital-to-Analog Converters (DACs) are responsible for generating the frequency comb, where each tone is tuned to the resonance frequency of each resonator. Typically, given the large bandwidth to be covered (on the order of several GHz) high-speed DACs are used, which help reduce the

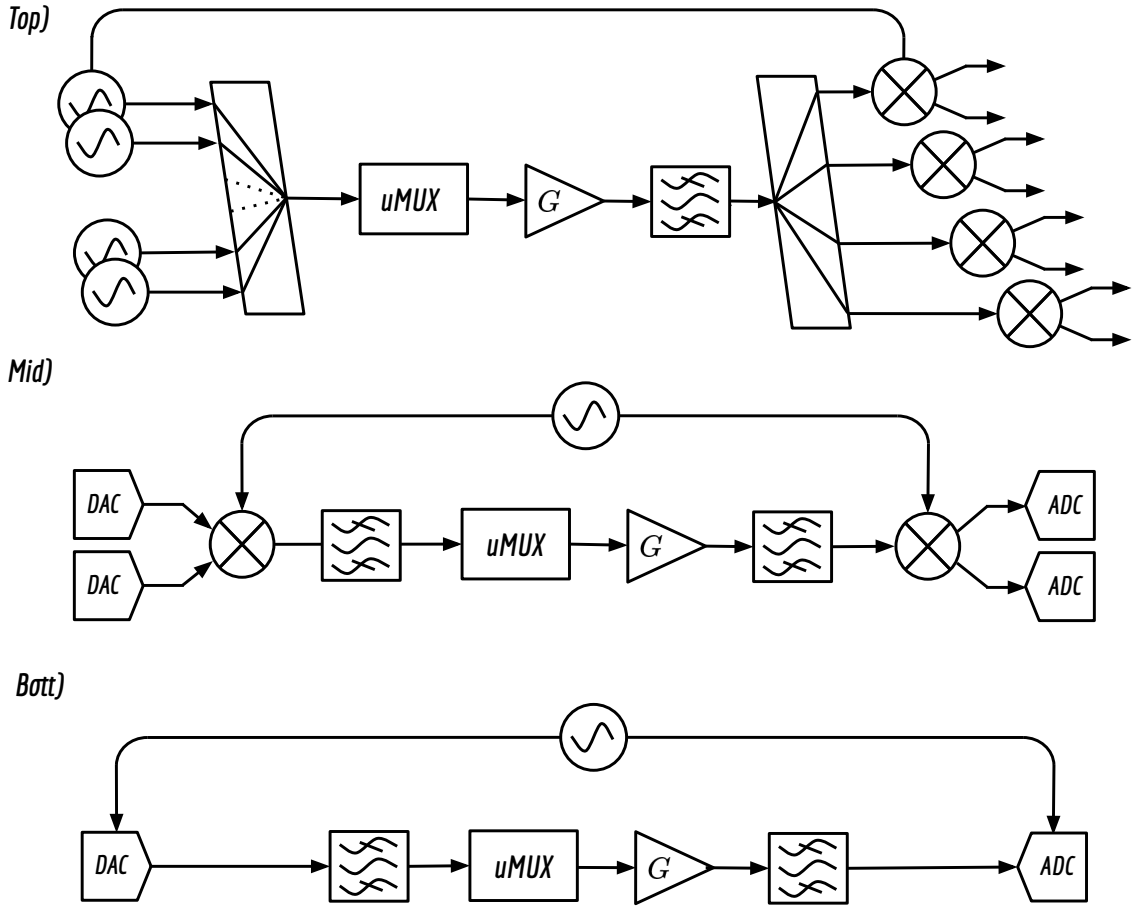

Figure 5.1: Different approaches implementing the µMUX readout system shown in Figure 4.1. **Top)** Multi-channel Homodyne systems using N generators and Mixer pairs. **Middle)** Zero-IF SDR Readout System. A pair of Complex Mixers are used to up/down convert the frequency comb form/to the operation frequency band. The frequency comb is generated/acquired in baseband by the DACs/ADCs respectively. **Bottom)** Mixer-Less SDR readout system. The frequency comb is directly generated by the High-Speed DAC and acquired in a High-order Nyquist zone by the High-Speed ADCs.

number of converters required to cover the total bandwidth. Depending on the sampling frequency, the frequency comb may require a frequency translation stage that shifts the comb to the operating frequency during transmission and brings it back to baseband during reception. This is the case of the scheme shown in the middle of Figure 5.1. To achieve the frequency translation, a pair of complex mixers, also known as IQ mixers, are employed. To efficiently utilize the bandwidth of the converters, the IQ mixer shifts the signals from the operating frequency f_c to baseband $f_{IF} = 0$, unlike other systems where signals are shifted to an intermediate frequency $f_{IF} \neq 0$. That is why, this scheme is also known as Direct-Conversion SDR or Zero-IF SDR [138, 141].

In recent years, the miniaturization of digital electronics has enabled even higher operational speeds, leading to a new generation of DACs capable of operating at frequencies on the order of several GHz. It allows the implementation of systems like the one shown in the lower part of Figure 5.1. In this scheme, the tones are generated and acquired directly in the operating band without the need for mixers. Therefore, from now on we will refer to it as a Mixer-Less or Direct-RF SDR system [141]. Both schemes require a series of filters to eliminate spurious signals produced during generation and frequency translation. Additionally, amplifiers are required to adapt the signal levels needed by each component throughout the cascade. Each type of scheme employed involves different requirements for the analog filters, as we will see later. Once the tones are generated with the appropriate power and signal quality, they are transmitted to the µMUX, where each tone is modulated by the respective resonator. They are then sent to the receiver, previously amplified by the cryogenic LNA. Next, in the case of the Zero-IF SDR system, the signals are converted to baseband and acquired by a pair of high-speed Analog-to-Digital Converters (ADCs). In contrast, in the Mixer-Less scheme, microwave signals are acquired directly after an aggressive band-pass filtering stage. At this point in the process, all channel signals coexist in a single digital signal and must be separated for subsequent demodulation, as mentioned in Section 4.2.

Given the high data rates involved, the channelization separation process (demultiplexing) is traditionally performed in parallel using an In-Field Programmable Gate Array (FPGA). This allows for a reduction in the data rate so that it can be stored, either in memory or on disk, or transmitted to other systems for further processing (e.g., Ethernet). Generally, in such systems, the FPGA configuration, hardware control and monitoring, networking, storage management, as well as the execution of calibration and measurement routines are carried out by a Central Processing Unit (CPU). Unlike the FPGA, the CPU is capable of performing all these specific complex tasks sequentially in an efficient manner with low energy consumption. The Figure 5.2 shows the hardware implementation of two SDR solutions. The solution shown above is the traditional implementation of the SDR system. It consists of an RF front-end that contains the DACs and ADCs along with the necessary RF components to fulfill the functionalities of the systems shown in Figure 5.1. The ADCs and DACs are driven by an FPGA, which is generally connected to the RF front-end using high-speed serial digital interfaces (transceivers using the JESDx standard [142]). In the FPGA, the intensive digital signal processing (DSP) work and data decimation are performed in parallel. On the other hand, initialization, programming, control, data storage, and network management are handled by a CPU, which connects to the FPGA via another high-speed digital interface (e.g., PCIe [143]). The CPU runs an operating system that allows for the execution of SDR software applications and the management of the different subsystems. Although the combination of these two processing platforms provides a wide range of functionalities, this type of implementation has the disadvantages of high design complexity and use of high-speed serial interfaces, along with a large footprint and high transceiver power consumption [141].

In February 2017, AMD® (formerly Xilinx®) announced the introduction of a new technology called RFSoC[44]. This technology provides a solution to this problem by integrating high-speed DACs and ADCs, along with a powerful FPGA and Hard processors, into a single

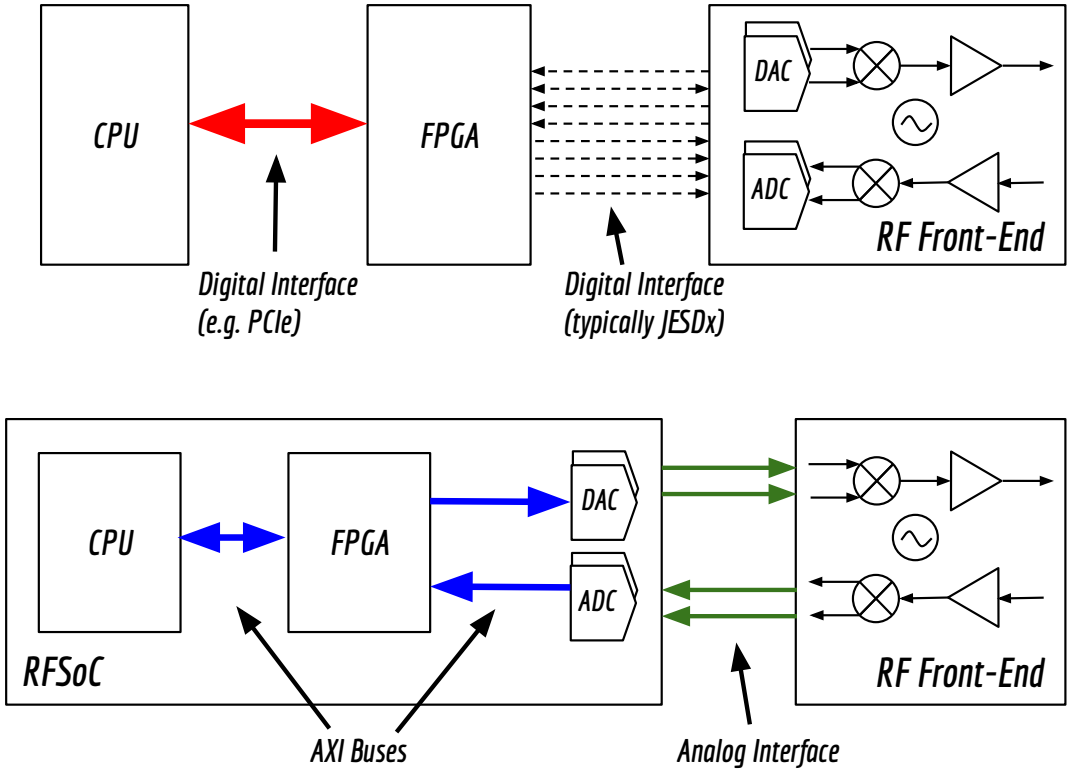

Figure 5.2: Comparison between different SDR solutions. **Bottom)** Traditional SDR solution comprising an RF Front-End, FPGA and CPU Boards. The Data Converters are usually interfaced with the FPGA via a Digital Serial interface using the JESDx standard, while the communication between FPGA and CPU is dome by means of a High-Speed PCIe standard. **Top)** SDR solution using the RF-System on Chip. Data converters, FPGA and CPU are contained in a Single Chip and connected via on-chip AXI buses. If a RF Front-End is required, it can be connected to the Data converters analog input/outputs.

system-on-chip. The lower part of Figure 5.2 shows the diagram of a SDR based on RFSoC. As shown, the DACs, ADCs, FPGA, and CPU are integrated within a single chip and communicate via AXI buses. AXI stands for Advanced eXtensible Interface (AXI[1]), an on-chip communication bus protocol that is part of the Advanced Microcontroller Bus Architecture specification (AMBA). These types of devices not only solve the previously mentioned issues, but also combine memory subsystems, interconnect resources for CPU-FPGA connections, and external interfaces supporting multiple popular standards (USB, I2C, HDMI®, DisplayPortTM, and others) [144]. This provides the RFSoC with very low latency and flexibility for a wide variety of SDR applications. It is worth noting that RFSoC is the evolution of the series of Heterogeneous Processing platforms Zynq™ UltraScale+™ MPSoCs (ARM processor enhanced family of high-performance FPGAs), with the removal of graphic and video coding features [145].

These types of platforms are ideal for the development and implementation of SDR readout systems for frequency-multiplexed detectors. Throughout the following sections, we will describe the functionalities of the latest generation of RFSoC devices and present the implementation of the schemes in Figure 5.1 based on these innovative devices.

[1] https://developer.arm.com/documentation/102202/0300/AXI-protocol-overview

5.2 Zynq UltraScale+ RFSoC Architecture Overview

Before the development of a SDR based on RFSoC, we will review the basic architecture of the RFSoC and its most important parts. This will later allow us to understand the implementation of the RFSoC-Based SDR system prototypes. Figure 5.3 shows the block diagram of the ZCU216 evaluation kit of third-generation RFSoC devices, where the high-level overview of the Zynq UltraScale+ RFSoC Architecture can be observed. Here, the three most important constituent blocks are detailed: the Processing System (PS), the Programmable Logic (PL), and the RF Data Converters Block (RFDC). All of these are connected via the fourth iteration of the AXI standard (AXI4). These buses provide high-speed, high-performance communication between the different blocks within the chip. This ensures that data can be transferred between components with low latency and efficiently. Since AXI is a scalable and flexible protocol, it allows the interconnection between components to adapt to the needs of the application. In turn, its large bandwidth enables the movement of large volumes of data in parallel without stopping the processes, ensuring that signals are processed continuously and without interruption. These advantages make it ideal for high-performance applications such as SDR systems. Three types of AXI4 buses are supported in RFSoC, AXI4 and AXI4-Lite (both of these are memory-mapped interfaces, for burst transfers and single transactions, respectively), as well as AXI4-Stream, which enables the direct flow of data from source to destination. Next, we will detail the internal architecture of each of the three components previously mentioned.

5.2.1 Processing System

As can be seen inside the blue rectangle in Figure 5.3, the Processing Unit (PU) consists of several different types of hardened processing resources. Among them are the Application Processing Unit (APU), the Real-Time Processing Unit (RPU), and the Platform Management Unit (PMU). Each of them has different complementary functionalities to execute software stacks for SDR applications. Each one can be used together with a programmable logic to create a complete SDR system.

The Application Processing Unit (APU) consists of a Quad-core Arm Cortex-A53 processor, which hosts four processing cores, each with its own dedicated computational units. These include a Floating-Point Unit (FPU), a Neon Media Processing Engine (MPE), Cryptography Extension (Crypto), Memory Management Unit (MMU), and dedicated Level 1 cache memory per core. These four Arm Cortex-A53 cores are capable of running a fully featured Operating System (OS) alongside software applications. This is an important feature because the SDR Readout software, presented later, will run on this APU. Along with the APU, the RFSoC also includes a Real-Time Processing Unit (RPU) containing two Arm Cortex-R5 cores for real-time applications and deterministic system control, providing low-latency performance. The RPU contains a number of computational units and memories, which include an FPU, Tightly Coupled Memories (TCMs), two local caches, and a Memory Protection Unit (MPU). While this RPU is available, it is not used for our developments [144, 141]. Additionally, a Platform Management and Security Unit (PMU) and Configuration Security Unit (CSU) are also present in the SoC. The Platform Management Unit (PMU) controls the power-up, reset, and monitoring of resources within the system. It contains several memories, as well as firmware that enables effective management of the RFSoC device. The CSU consists of a Secure Processor Block (SPB) and Cryptography Interface Block (CIB). These manage the secure boot of the ARM processors and several other security features, such as Physically Unclonable Functions (PUFs) and tamper protection [144, 141].

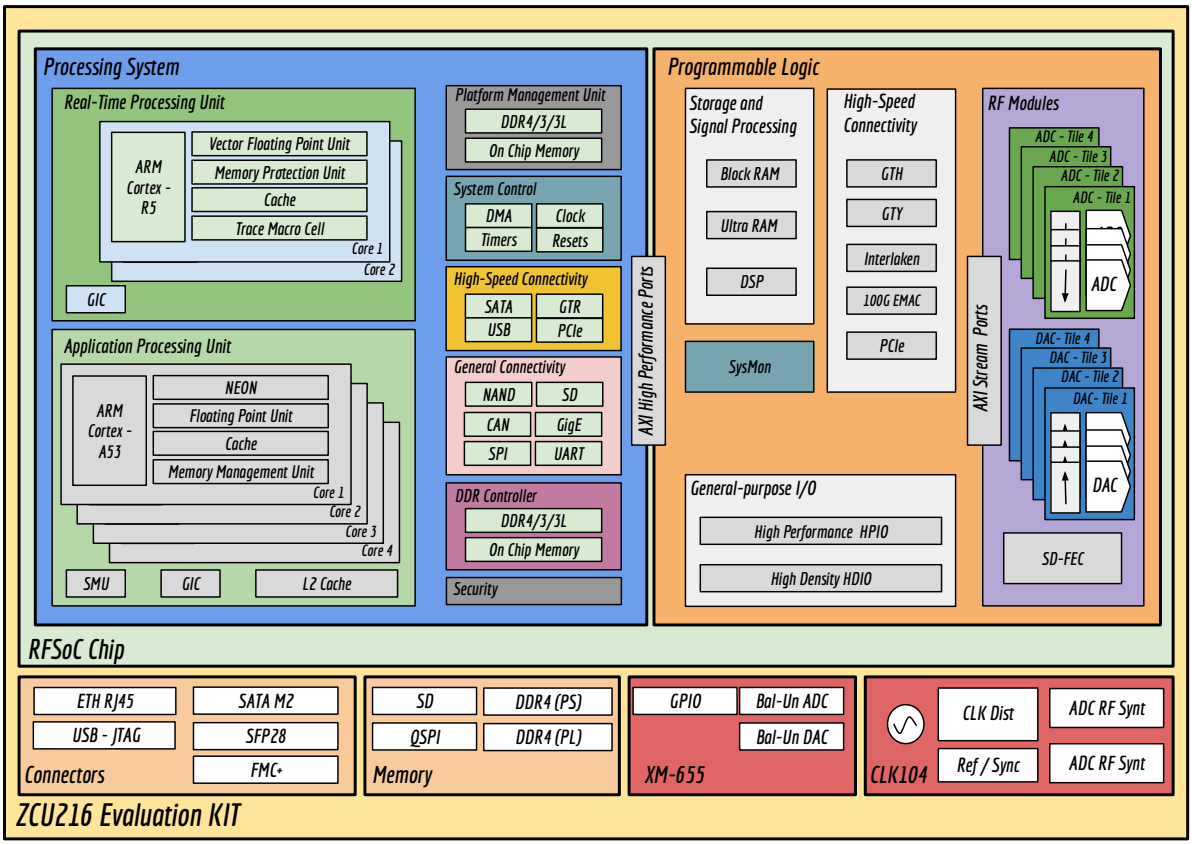

Figure 5.3: Block Diagram of the ZCU216 Evaluation Kit together with the High level overview of the Zynq Ultrascale+ Radio-Frequency System on Chip architecture. The RFSoC chip is divided in two: the Processing System (PS) and the Processing Logic (PL). Both domains are connected via High Performance AXI interfaces. The Radio-Frequency Data Converters IP core is accessible from the Processing Logic via AXI Stream Ports.

5.2.2 Programmable Logic

The PL is the most important element when designing the SDR system because it is responsible for interfacing with the high-speed converters and performing the first stage of intensive data processing. The number of available elements of each type is a factor that can limit the signal processing capabilities required for a given application. Table 5.1 lists the key features of some of the most powerful SoCs offered by AMD. This table includes SoCs from both the MPSoC and RFSoC families, as well as several generations of RFSoC. The RFSoC family provides a common set of resources including CLBs, DSP slices, Block RAMs, and UltraRAMs. These building blocks are also shown in Figure 5.3 inside the orange block corresponding to the Programmable Logic region.

A configurable logic block (CLB) is a fundamental building block of a Field-Programmable Gate Array (FPGA). It comprises a number of Lookup Tables (LUTs) and Flip-Flops (FFs) than can be arranged in order to implement logic functions, Shift Registers (SRL), Read Only Memory (ROM) and Random Access Memory (RAM). They can be used to create larger logic functions as well as small local memories also know as Distributed RAM. Due to its highly programmable nature, the RFSoC logic fabric is suitable for the implementation of almost any desired digital circuit [144].

Some SDR systems, such as systems that we will show later, require the implementation of intensive Digital Signal Processing (DSP) algorithms. Some of them can be Fast

Fourier Transforms (FFT), Finite Impulse Response (FIR) filters, or Frequency Conversion. The DSP48E2 slices within the PL are particularly valuable for implementing these functions. DSP48E2 slices provide high speed Multiply Accumulate (MAC) hardware, supporting word lengths of up to 48 bits, optimized for high-speed and low-power operation. The RFSoC was specifically designed to carry out this type of task in accordance with modern SDR systems and offers a huge amount of DSP Slices as can be seen in Table 5.1.

Table 5.1: Comparison of Key Features of AMD SoC Devices.

Parameter	ZU28DR	ZU48DR	ZU49DR	ZU11EG	ZU19EG
Family	RFSoC	RFSoC	RFSoC	MPSoC	MPSoC
Generation	Gen1	Gen3	Gen3	-	-
DAC Number	8	8	16	-	-
DAC Sample Rate	6.554GHz	9.850GHz	9.850GHz	-	-
DAC Bits	14	14	14	-	-
ADC Number	8	8	16	-	-
ADC Sample Rate	4.096GHz	5.000GHz	2.500GHz	-	-
ADC Bits	12	14	14	-	-
DDCs per RF-ADC	1	1	1	-	-
DUCs per RF-DAC	1	1	1	-	-
Logic Cells	930K	930K	930K	653K	1143K
CLB FFs	425K	850K	850K	598K	1045K
CLB LUTs	425K	425K	425K	299K	522K
Max. Dist. RAM	13Mb	13Mb	13Mb	9.1Mb	9.8Mb
Total Block RAM	38Mb	38Mb	38Mb	24.1Mb	34.6Mb
UltraRAM	22.5Mb	22.5Mb	22.5Mb	22.5Mb	36Mb
DSP Slices	2272	4272	4272	2928	1968

5.2.3 RF Data Converters

The most prominent and disruptive difference of RFSoCs compared to the MPSoC family is the inclusion of high-speed Data Converters within the SoC. Both ADCs, DACs, and their clock distribution are part of the so-called RF Data Converters IP Logic core [146]. Figure 5.3 shows this block within the violet box. Over the last few years, the different generations of RFSoCs have increased the number of available DACs and ADCs, raised their maximum sampling rates, and the number of bits offered. Table 5.1 shows the RFDC key features of generations 1 and 3. Throughout this thesis, we will make use of the RFSoC ZU49DR device, which is part of the third generation (Gen3). It features 16 DACs and 16 ADCs with maximum sampling rates of 9.85 GHz and 2.50GHz respectively.

The RFDC block not only provides the ability to convert signals from the analog to the digital domain and vice-versa, but each element also offers a series of DSP hardened blocks, which provide functionalities comparable to those of Mixed-Signal Front Ends (MxFE)[2]. The RFDC converters are grouped into tiles. Particularly, for the ZU49DR device each tile consists of 4 ADCs or DACs, which can be interconnected to achieve different configurations. Figure 5.4 shows a simplified representation of the ADCs and DACs Gen 3 block pipelines. The signal flow is from right to left for the ADC and from left to right for the DAC.

In the case of the ADC, after the Analog-to-Digital conversion, a Threshold Detection and Quadrature Modulation Correction (QMC) enable adjustments of the input signal level and correct analog signal imbalances in a complex configuration. Then, a Crossbar block al-

[2] https://www.analog.com/en/product-category/mixed-signal-frontends.html

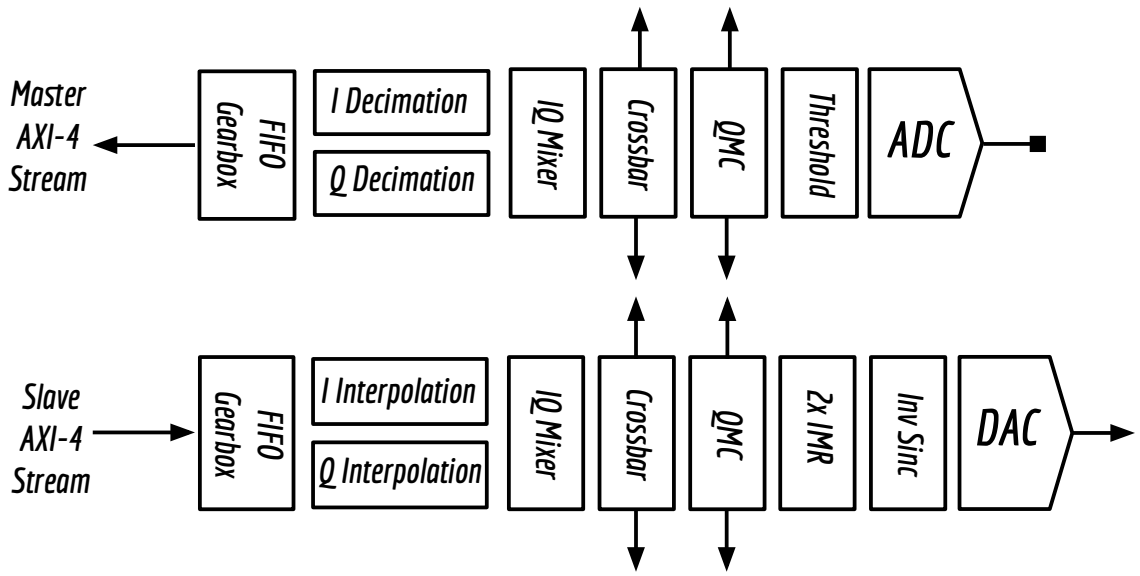

Figure 5.4: Simplified representation of ADCs and DACs Gen 3 block pipelines.

lows to interconnect different ADCs in order to achieve complex or multi-band operation. Then, a Digital Down-Converter (DDC) consisting of a Digital IQ Mixer, Numeric Controlled Oscillator (NCO) and Decimation Filters can be used to select the desired frequency-band and at the same time relaxing the data rate to the PS. Two operation modes can be used for the NCO. In the coarse mode, the frequency can be $\pm f_s/2$ or $\pm f_s/4$, while in the fine mode a 48-Bit NCO is used. The decimation filter can be selected from a plethora of different decimation values (1x, 2x, 3x, 4x, 5x, 6x, 8x, 10x, 12x, 16x, 20x, 24x, 40x). Finally, the output signals passes through a gearbox FIFO, which enables conversion between the different data rates of the ADCS and PL.

The DAC configuration is similar but instead of a DDC, A Digital-Up Converter is used. Instead of Decimation filters, Digital Interpolators with factors 1x, 2x, 3x, 4x, 5x, 6x, 8x, 10x, 12x, 16x, 20x, 24x, 40x are provided. As well as the ADCs, the NCO also can work in the aforementioned mentioned modes, different DACs within a tile can be connected for multi-band or complex operation and QMC application. Contrary to the ADC, two additional blocks can be used. An Image Rejection Filter (IMR) and Inverse Sinc compensation. IMR can be configured as either low or high pass, which aids in suppressing images in the second and first Nyquist zones, respectively. The IMR filter can only be used in combination with the DUC, and introduces an additional 2x interpolation to the pipeline. The Inverse-Sinc Compensation Filter is used to correct the frequency response of the DAC reconstruction waveform used to bust the signals in the different Nyquist zones. All blocks can be bypassed if not used, as long as the maximum allowed data rates are met.

As well as the different DSP functionalities, each tile contains a Phase Locked Loop (PLL), which can be used to generate the clocks required within the tile. The PLL requires an external, low-jitter, off-chip frequency reference to operate effectively. This PLL can be by-passed when high-spectral purity is required, allowing to directly feed an off-chip high-Quality sampling clock. RFSoC development boards often host these external clocks which features an add-on clocking board as it will be explained later.

It is important to mention that, both ADCs and DACs use differential signaling at the external interface. Therefore, Baluns (Balanced-Unbalanced) must be used to convert between differential signals and single-ended signals. As well as an add-on clocking board, an add-on Balun board is provided with the development board. The configuration of the RFDC

converters is a key part of this work and it is explained in Sections 5.4 and 5.5.

5.2.4 Miscellaneous Components

In addition to the previously mentioned blocks, RFSoC devices include a wide range of features, such as high-speed connectivity, high performance and high-density input/output interfaces (e.g., 100G Ethernet, PCIe, GTH, USB 3.0, or SATA). Some of the devices also are equipped with Soft-Decision Forward Error Correction (SD-FEC) blocks. These blocks support Low Density Parity Check (LDPC) encoding and decoding, as well as Turbo code decoding.

5.2.5 ZCU216 Evaluation Kit

RFSoC devices require several external components to correctly achieve all the functionalities previously mentioned. For this purpose, the manufacturer provides various evaluation kits specific to each RFSoC chip series. Such boards combine an RFSoC device with supporting features such as additional DDR memory, I/O connectors, external clocking, and baluns [113].

The ZCU216 evaluation kit is specifically designed for the evaluation of the RFSoC ZU49DR device and will be used throughout this thesis. This kit has three basic components: the base board that houses the RFSoC chip, the clock generation and distribution board (CLK104), and the balun and filtering board (XM655). These components are shown at the bottom of Figure 5.3. Among the most important components on the base board are the memory subsystems and connectors. The kit is equipped with 4 GB of 64-bit DDR4-DIMM memory (attached to PL) and 4 GB of 64-bit DDR4 SODIMM (attached to PS). It also includes 4 GB of dual Quad-SPI flash memory for non-volatile storage. Non-volatile storage can be expanded using the SD card connector or an SSD connected through the M.2 SATA port. Among the accessible connectors are USB and JTAG for platform programming and debugging, as well as RJ45 and Small Form-factor Pluggable (SFP28) connectors for high-speed networking.

Analog and digital connections are made possible via one FMC+ and two RFMC 2.0 connectors. The 560-pin FMC+ provides connectivity for up to 160 single-ended or 80 differential user-defined signals, 24 transceiver differential pairs, 6 transceiver differential clocks, 4 differential clocks, 239 ground connections, and 19 power connections. The RFMC 2.0 connectors are particularly important as they form the interface between the 32 data converters and the external world. The DACs and ADCs are routed individually to two different RFMC 2.0 connectors. These connectors are connected to the XM655 balun board.

Clock Generation and Distribution Board

The CLK104 RF clock add-on board is designed for use with ZCU216 evaluation board. It generates an ultra low-noise, wideband RF clock source for the ADCs and DACs. The CLK104 board provides the low frequency reference clocks for the on-chip integrated PLL or one RF sampling clock for all ADC channels and one RF sampling clock for all DAC channels [147]. The CLK104 also supports multi-tile and multi-board synchronization. A High Level block diagram of the CLK104 is shown in Figure 5.5.

The LMK04828B is a dual loop jitter cleaner and clock generator. The first stage PLL is driven by either an external reference clock f_{EXT}, or the on-module TCXO 10 MHz reference clock f_{TXCO}, or the recovered reference clock from the RFSoC. An external 160 MHz VCXO provides a frequency-accurate, low-phase noise reference clock for the second stage PLL. The second PLL operates with a wide-loop bandwidth and generates the input references and SYNC signal for the ADC/DAC RF PLLs, the PLL reference clocks, the SYSREF signal for the RFSoC ADC/DAC, the reference clocks for the RFSoC PL banks, and the output reference clock for multi-tile and multi-board synchronization. The second PLL of the LMK04828B chip can be configured in dual-loop mode if synchronization is not required between the outputs and

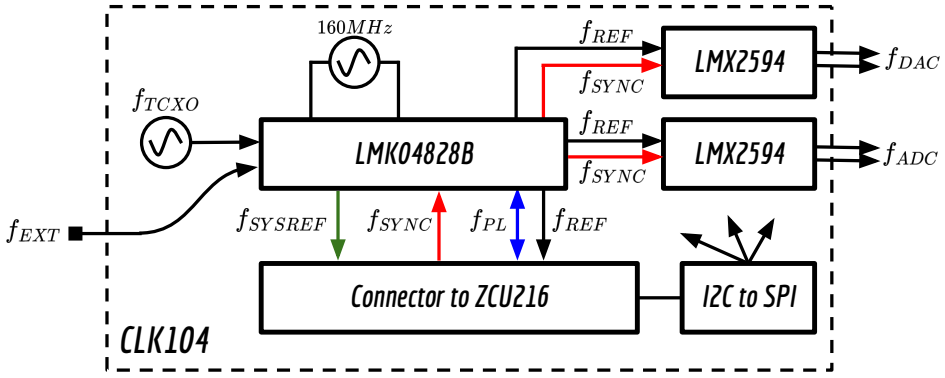

Figure 5.5: High level block diagram of the CLK104 Add-On card. The first double PLL Loop LMK042828B clock synthesizer provide a smooth, jitter-free clock f_{REF}, generated from either a reference clock on the card f_{TXCO}, or from an external clock f_{EXT}. The second stage composed by two LMX2594 synthesizers are driven by the LMK chip, and provide ultra low-noise dedicated RF clocks f_{DAC} and f_{ADC} to the DACs and ADCs on the RFSoC. Reference f_{PL} and synchronization signals f_{SYNC} and f_{SYSREF} are also provided to/from the ZCU216 board.

reference input. In contrast, if configured in nested 0-delay mode, a fixed deterministic phase relationship of the phase of the input reference to the phase of the outputs is achieved.

When the performance of the on-chip PLLs within the RFSoC device is not sufficient, the data converters sampling clocks can be provided by two dedicated RF Synthesizers present in the CLK104. The LMK04828B drives two high-performance, wideband RF synthesizers LMX2594 that can generate f_{ADC} and f_{DAC} sampling clocks. The LMX2594 can operate in integer or fractional mode outputting frequencies between 10MHz and 15 GHz. These sampling clocks are supplied to the RFSoC chip in a differential fashion using two pairs of Carlisle SSMP loopback cables.

Bal-Un Board

DACs and ADCs transmit and receive using differential signals, and conversion is required to and from a single-ended analog signal format, in many applications. These conversions can be achieved using baluns. Each of the RFSoC evaluation Boards fulfill this interfacing requirement providing a BalUn daughter board which can be directly attached to the development board. The XM655 is an RFMC 2.0 add-on board for use with the ZCU216 evaluation board. This add-on board enable ZCU216 connectivity from the DAC and ADC for loopback evaluation and for instrumentation use.

The XM655 is equipped with sixteen baluns optimized for four different frequency ranges, 10 MHz to 1 GHz (*Minicircuits TCM2-33WX+*), 1 to 4 GHz (*Anaren BD1631J50100AHF*), 4 to 5 GHz (*Anaren BD3150N50100AHF*) and 5 to 6 GHz (*BD4859N50100AHF*). Each frequency range contains four baluns accessible through SMA connections. The connections between any of the 16 ADCs or 16 DACs with the baluns is done via the Carlisle Core HC2 8 Channel to 3.5 mm Male cables (*TM40-0157-00*). An additional pin header on the XM655 side gives access to I2C, different I/O pins and supply voltages [113]. The different Baluns of the XM655 will be used to interface the ZCU216 kit with external RF components, as shown later in this thesis.

5.3 SDR Firmware and Software Overview

This thesis focuses on the development of two SDR readout systems based on the RFSoC platforms. The design flow of a complete SDR system requires the interaction of several specialties in electrical/telecommunications engineering. First, a system engineer defines the global requirements of the SDR system, as done in Chapters 2, 3 and 4. Then, an RF engineer carries out the frequency planning and specifications of the RF hardware components. Later, an FPGA/hardware engineer implements the signal processing algorithms either in hardware or software. Finally, a testing engineer uses the previous developments to verify if the proposed requirements are met. Given the complexity of the associated tasks, the approach used in this work suggests the reuse of previous developments, their migration/adaptation to the RFSoC platforms, and the verification of their analog performance. Particularly, we used as a starting point the firmware and software architecture developed for The Electron Capture in ^{163}Ho experiments such as ECHo [139]. The hardware architecture is based on a multi-band, double-conversion, zero-IF RF-mixing board, which divides the total bandwidth into five 800 MHz complex base-bands. This architecture plans to use ten DACs and ten ADCs (five IQ pairs) sampling at $f_s = 1$ GHz in order to to cover the total bandwidth [148].

A block diagram of the SDR Firmware implemented in the RFSoC is shown in Figure 5.6. This corresponds to the firmware capable of processing a single 800 MHz band. Therefore, it needs to be replicated five times to cover the total bandwidth 4 GHz. All blocks except those shaded within the yellow block were inherited from previous developments using the MPSoC platform [149]. Specifically, these were integrated into the *DTS-100G* platform developed jointly between KIT and DESY (Deutsches Elektronen-Synchrotron) within the Detector Technologies and Systems (DTS) program of Helmholtz [150]. The platform is designed as a universal and flexible platform and can be equipped with the most powerful versions of MPSoCs, such as the ZU11EG and ZU19EG, listed in Table 5.1. The hardware architecture used for the ECHo project employs a daughterboard which features ten ADCs and ten DACs (AD9144 and AD9680 from Analog Devices® respectively) along with its clock distribution system [148]. This board communicates with the *DTS-100G* through 24 high-speed lanes, using a scheme similar to the one shown at the top of Figure 5.2.

The yellow block corresponds to the Radio-Frequency Data Converters IP core presented in Section 5.2.3 and is one of the most important components of this thesis. To ensure firmware compatibility, the input (DACs) and output (ADCs) interfaces of the RFDC block, as well as the data rate, were maintained with respect to the previous developments. The DACs interface is determined by the tone generation block (comb-generator), which provides a continuous stream of complex data at a rate of 1 GSPS. The implementation of this block will be detailed later. This interface is implemented using one or two AXI4-stream buses, where the number of samples per AXI clock cycle can be configured. This allows balancing the bus operating speed and its bit width, depending on whether timing or congestion issues arise during implementation. The decision of using a single bus or two buses is contingent on whether one bus transports complex data or two buses carry real data. Regarding reception, each pair of ADCs performs IQ sampling at a rate of 1 GSPS. The AD9680 has an internal structure similar to the one shown at the top of Figure 5.4 and is configured to split the total 1 GSPS bandwidth into two bands of 500 MSPS by decimating by two. This is done by frequency shifting and applying a filter, as described in Section 5.4. From the PL side, the polyphase channelizer and spectrum shift blocks (see Figure 5.6) each receive one of these complex data streams at a rate of 500 MSPS. Similar to the comb-generator, this interface is implemented through an AXI4-stream, where the bus width and the number of words per AXI clock cycle can also be configured.

Before presenting the SDR prototypes, we will detail the operation of the most important blocks of the SDR firmware. These will be used to demonstrate the correct operation of

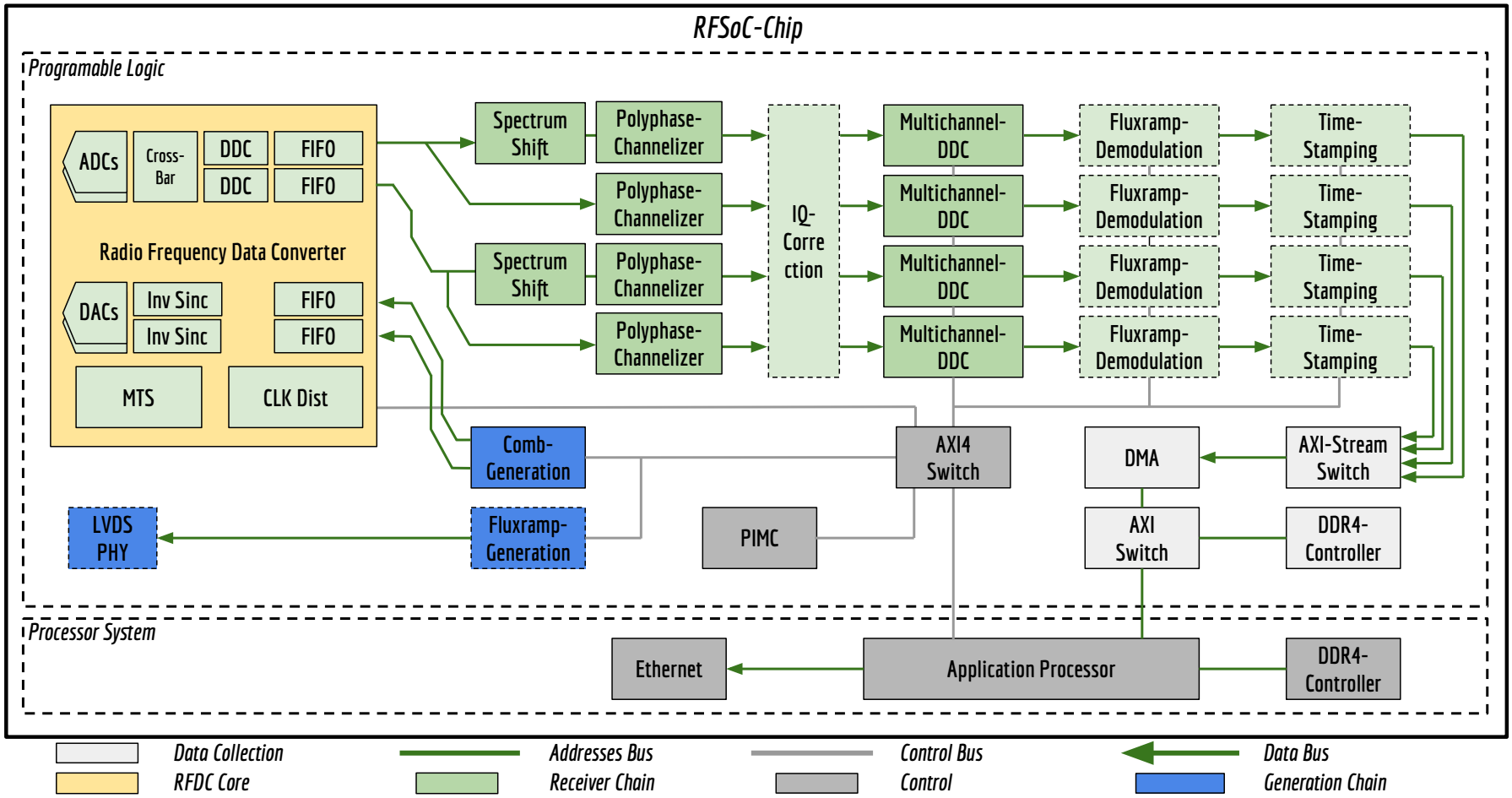

Figure 5.6: Block diagram of the SDR Firmware implemented in the RFSoC Chip. The yellow block corresponds to the Radio-Frequency Data Converters IP core which was configured to implement the SDR architectures shown in Figure 5.1 while also being compatible with the firmware and software previously developed. The blocks boxed with dotted lines were not used in this thesis, consequently, they were by-passed.

the SDR prototypes. The blocks boxed with dotted lines were not used in this thesis, they were bypassed. At the same time, the blocks previously responsible for handling the physical communication of the MPSoC with the Data-converters were removed.

5.3.1 Comb-Generation

The first block in the SDR chain is responsible for generating the interrogation tones for the µMUX (see comb-generator in Figure 5.6). The tones themselves are generated in complex base-band using a pair of DACs and are shifted to the operating frequency using IQ mixers. For the case of N tones, the in-phase component $x_{Tx,I}(t)$ and the quadrature component $x_{Tx,Q}(t)$ of the frequency comb can be expressed as follows:

$$x_{Tx,I}(t) = \sum_{k=1}^{N} A_k \cos\left(2\pi f_k t + \phi_k\right), \tag{5.1}$$

$$x_{Tx,Q}(t) = \sum_{k=1}^{N} A_k \sin\left(2\pi f_k t + \phi_k\right). \tag{5.2}$$

Here, k is the index of each interrogation tone, A_k and ϕ_k are the amplitude and phase of the k-th tone, respectively, and t is the time. To satisfy the sampling theorem, the condition $|f_k| < f_{DAC}/2$ must be met, where f_{DAC} is the sampling frequency of the DAC. The IQ mixer takes the components $x_{Tx,I}(t)$ and $x_{Tx,Q}(t)$ and mixes them with two local oscillators $\cos(2\pi f_{LO} t)$ and $-\sin(2\pi f_{LO} t)$, resulting in the transmitted signal $x_{Tx}(t)$

$$x_{Tx}(t) = x_{Tx,I}(t)\cos(2\pi f_{LO} t) - x_{Tx,Q}(t)\sin(2\pi f_{LO} t), \tag{5.3}$$

where f_{LO} is the local oscillator frequency to which the frequency comb is to be shifted. A scaling factor could be considered depending on the conversion losses of the mixer. It is easy to see that the previous equation is equivalent to

$$x_{Tx}(t) = \sum_{k=1}^{N} A_k \cos[2\pi(f_{LO} + f_k)t + \phi_k]. \tag{5.4}$$

It can be demonstrated that the generated tones lie within the range $[f_{LO} - f_{DAC}/2 < f_k < f_{LO} + f_{DAC}/2]$. Therefore, the frequency range covered is approximately $\approx f_{DAC}$. Generally, at the output of the IQ mixer, other spurious signals also appear due to imbalances between its branches and the low isolation between its ports. These phenomena, known as IQ imbalance and LO leakage, are described in Appendix E.

From equation 5.1, it can be seen that the maximum amplitude of the signal $\max|x_{Tx,I}(t)|$ depends on the amplitude A_k and the phase of each tone ϕ_k. In the case of $A_k = A$ and $\phi = 0$, the maximum amplitude grows linearly with the number of tones (i.e., $\max|x_{Tx,I}(t)| = NA$). Since the DAC can only reproduce a finite amplitude, the number of tones must be limited or their amplitude reduced in order to avoid clipping that would distort the signal. This represents a reduction in the power of the tones. One of the most commonly used metrics to measure the relationship between the maximum amplitude of a multi-tone signal and the power of each tone is called the Peak-to-Average Power Ratio (PAPR), and it is defined as

$$PAPR = \frac{P_{peak}}{P_{rms}} = \frac{max\{|x_(t)|\}^2}{\frac{1}{T}\int_0^T |x(t)|^2 dt}. \tag{5.5}$$

In the numerator, the peak power P_{peak} of the signal $x(t)$ is represented, while the denominator represents the RMS power P_{rms}. This factor must be considered during generation in order to use the DAC full scale efficiently, and during reception to avoid saturating the

ADC, as we will see later. Nowadays, there are several methods to reduce this factor, based on the selection of the phase of each tone ϕ_k, and they should be implementable by the comb generator [151].

Once the position and power of the readout tones are located, the signal generator must remain static. The solution that best adapts to these needs with the least resource consumption is to store the samples of the signals (given by equations 5.1 and 5.2) in memory and cyclically reproduce them at the rate required by the DAC. The frequency resolution achieved Δf_{gen} depends on the number of samples stored N and the sampling frequency f_s:

$$\Delta f_{gen} = \frac{f_s}{N}. \tag{5.6}$$

The implementation of this block was carried out using asynchronous dual-port block RAM (BRAM). One of its ports is connected to the AXI4-Lite control interface, through which the memory is sequentially filled sample by sample. The other port is associated with the clock of the DAC and provides the 16-bit words to the DAC via an AXI4-stream [152].

5.3.2 Channelization and Digital-Down Conversion

The frequency comb given by equation 5.4 is transmitted to the cryostat where the MUX modulates each of the tones. The signal recovered from the cryostat at the output of the Rx port (see Figure 4.20) takes the form

$$x_{Rx}(t) = \sum_{k=1}^{N} A'_k(t) \cos\left[2\pi(f_{LO} + f_k)t + \phi'_k(t)\right]. \tag{5.7}$$

The objective of the SDR system is to measure the quantities $A'_k(t)$ and $\phi'_k(t)$ for all the channels. Similar to the transmission, another I/Q mixer is used to down-convert $x_{Rx}(t)$ to baseband. Equivalent to equations 5.1 and 5.2, the in-phase and quadrature components of the received signal can be written as

$$x_{Rx,I}(t) = \sum_{k=1}^{N} \frac{A'_k(t)}{2} \cos\left[2\pi f_k t + \phi'_k(t)\right], \tag{5.8}$$

$$x_{Rx,Q}(t) = -\sum_{k=1}^{N} \frac{A'_k(t)}{2} \sin\left[2\pi f_k t + \phi'_k(t)\right]. \tag{5.9}$$

At this point, although the signals are at a frequency that can be processed by the programmable logic, the information from each detector is still contained around each tone at the frequency f_k. Therefore, to arrive at an expression equivalent to that presented in equation 4.1, a final frequency translation must be performed for each tone, followed by low-pass filtering. Mathematically, this is represented as

$$z_k(t) = \left\langle \left[x_{Rx,I}(t) + j x_{Rx,Q}(t)\right] e^{-j2\pi f_k t} \right\rangle = A'_k(t) e^{j\phi'_k(t)}, \tag{5.10}$$

where $e^{-j2\pi f_k t}$ is the complex local oscillator for each tone at frequency f_k, and $\langle\rangle$ represents the required low-pass filtering to eliminate signals from other channels and noise. $z_k(t)$ is the complex envelope of each channel, and from it, the information from each detector can be extracted using the methods described in Section 4.2.

The implementation of this channelization scheme is not feasible in the digital domain for a large number of channels. This is because all operations must be performed at the data rate imposed by the ADCs, and filters with a high number of taps are required to achieve the desired cutoff frequencies. Advanced DSP techniques provide more efficient solutions in the use of digital resources through pipelining and progressive down-sampling. This reduces

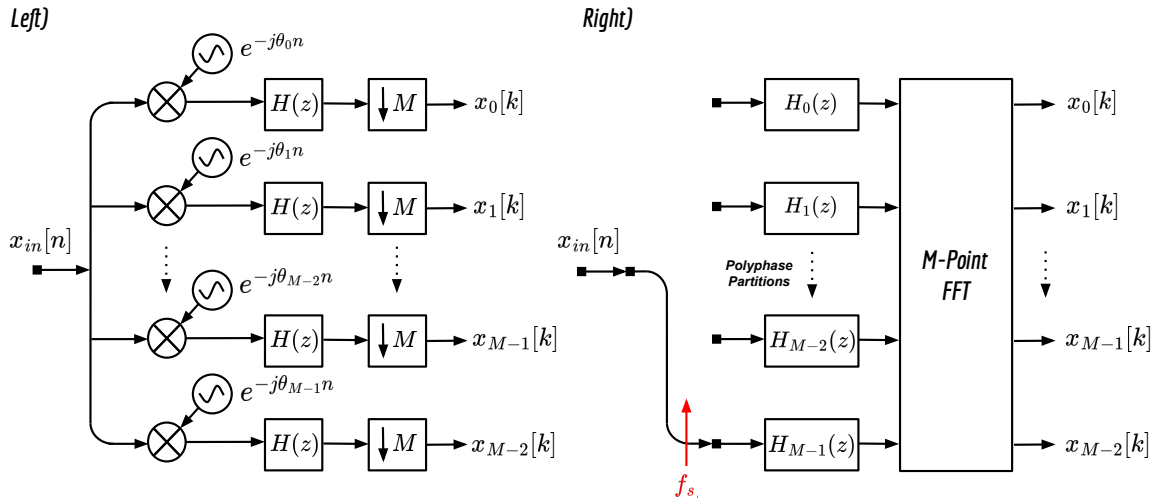

Figure 5.7: Polyphase Filter Bank block Diagram. **Left)** Bank of M-path Down-Converters followed by Low-pass filters and Decimators. **Right)** Polyphase Implementation of the M-path filter Bank.

the logic operating frequency and enables parallel processing of the different channels. The scheme used in our firmware is detailed below.

Polyphase filter Banks

The natural solution for channel separation or channelization is to use a bank of M *Digital Down-Converters* (DDC). As shown on the left side of Figure 5.7, each channel is composed of a mixer and an NCO tuned to the frequency f_k, a low-pass filter with response $H(z)$, and a decimator by M [153]. This approach is not suitable for FPGA implementation due to the enormous amount of memory resources and operations that must be performed simultaneously. Additionally, given the decimation, this system is inefficient since many of the operations performed will not affect the outputs. A more efficient implementation is achieved by reordering the blocks, using the *equivalency theorem*, the *Noble identity*, and leveraging the Fast Fourier Transform (FFT). This results in the Polyphase Filter Bank (PFB), which is shown on the right side of Figure 5.7. Details of the transformations used can be found in the following references [153, 154]. Its name comes from the fact that the prototype low-pass filter $H(z)$ was partitioned into its different phases $H_i(z)$. The Polyphase Filter Bank not only requires fewer processing and memory resources but also allows each phase to operate at a rate of f_s/M, where f_s is the sampling rate and M is the number of polyphase partitions.

The firmware used employs four PFBs with $M = 32$ channels for the first stage of coarse channelization. These four PFBs cover a total bandwidth of 1 GHz across $N = 128$ channels. As mentioned above, each pair of ADCs provides the logic with two complex streams at a rate of $f_s = 500$ MSPS, and each of them is associated with two PFBs. Each PFB with $M = 32$ channels has a channel separation of $\Delta f_p = f_s/M = 15.625$ MHz and a bandwidth of $BW \approx 11$ MHz at 0.2 dB. The stop-band attenuation is $\approx$ 89 dB at $\pm\Delta f_{\text{stop}} \approx 10$ MHz from the center of each channel. This attenuation factor is sufficient to avoid cross-talk with the tones present in neighboring channels. Figure 5.8 shows the detailed response of the two PFBs (i.e., PFB0 and PFB1). As a result of the PFB design, there are blind intervals between channels, which is why one of the channelizers is preceded by a spectrum shift block that shifts the entire band by $\Delta f_c \approx 7.8125$ MHz. These channels are represented with a dashed line in Figure 5.8.

To avoid aliasing of signals outside the first Nyquist zone, a pair of low-pass filters with

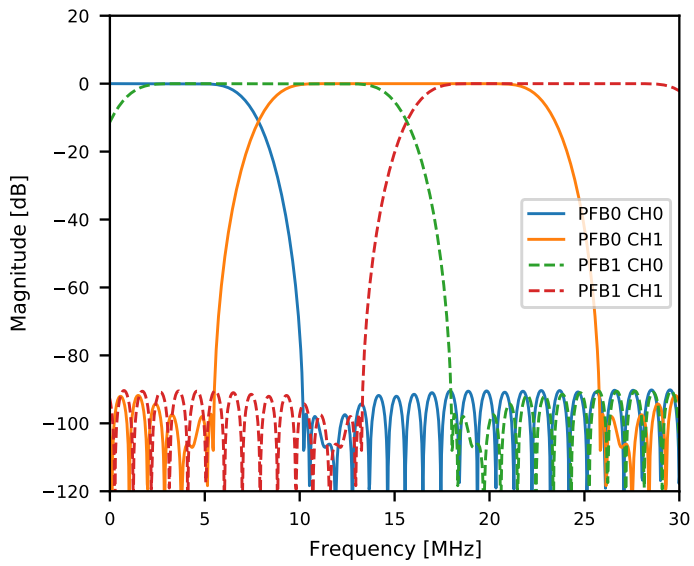

Figure 5.8: Detailed view of the frequency response of the PFB Channels. PFB0 channels CH0 and CH1 are separated $\Delta f_p \approx 15.625$ MHz and 0.2dB bandwidth of $BW \approx 11$ MHz. The stop-band attenuation is $\approx$ 89dB at a $\pm\Delta f_{\text{stop}} \approx 10MHz$ form the channel center frequency. In order to cover blind intervals, PFB1 is frequency shifted $\Delta f_c \approx 7.8125$ MHz.

a cutoff frequency of $f_c \approx 400$ MHz provides a transition margin of 100 MHz, which is reasonable to achieve more than 40 dB of stopband attenuation. Given these filters, the effective bandwidth that can be observed is 800 MHz, representing $N = 100$ channels. As an example, Figure 5.9 shows the frequency response of just two PFBs and represents a total of $N = 50$ channels. The other two remaining PFBs were not plotted for clarity, but they cover blind intervals between the channels.

The implementation of two channelizers involves the use of the Xilinx® FIR Compiler for the implementation of the multi-channel filter and two pipelined 32-point Fourier transforms from Xilinx® [155, 156]. The modules operates at a clock frequency of 500 MHz with an output bit width of 16 Bits, sufficient to keep the required SNR. More details of the implementation can be found in reference [152]. Although the number of channels implemented is not sufficient for the improvements to the QUBIC project, it is enough to carry out the characterization of the SDR prototypes. Nevertheless, work is underway to expand the number of channels, either by scaling the current PFB or by using other types of channelizers based on Goertzel filters [118].

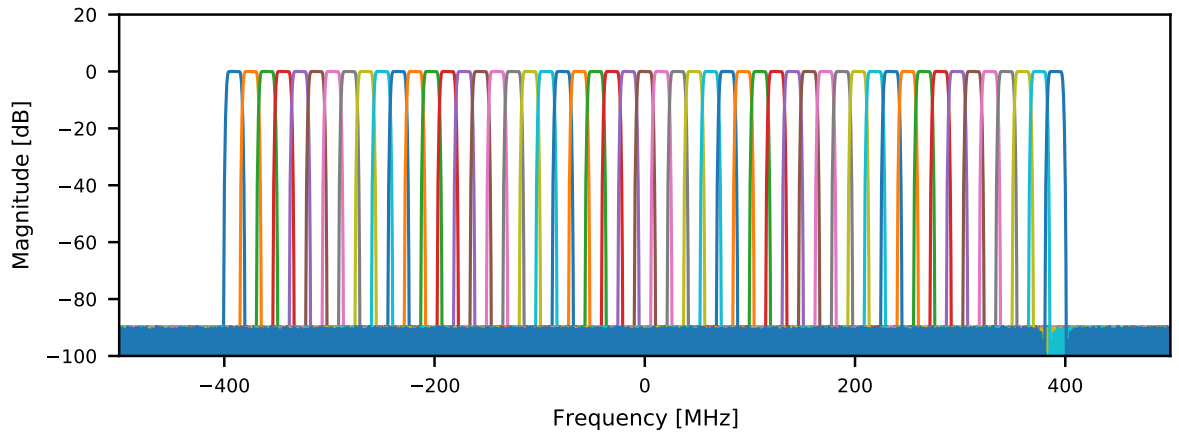

Figure 5.9: Simulated Frequency response of the two Polyphase Filter Banks (PFB) covering the positive and negative frequencies. Only the channels inside the band of interest where represented (800 MHz). For sake of simplicity, the rest of the PFB that covers the blind intervals where not represented, therefore, only 50 of the total 100 are shown.

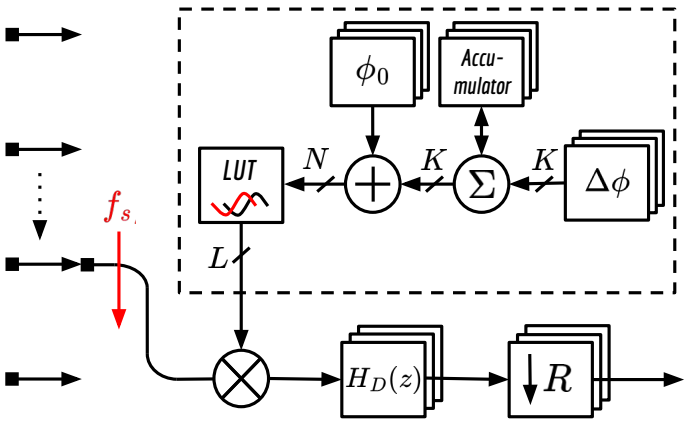

Figure 5.10: Multi-channel Digital-Down Converter Block Diagram, comprised of a Complex Mixer, a Numerically Controlled Oscillator (NCO) and a low-pass Filter $H_D(z)$. An optional decimator can be included after the filter. The NCO components are represented inside the dashed black rectangle.

Multi-channel DDC

The first coarse channelization separates the total bandwidth into $N = 128$ channels centered at $f_i = i\Delta f_c$, which are sampled at a rate of $f_s = 15.625$ MHz. This presents two issues. First, any frequency shifted with respect to the center of the channel must be shifted to baseband before demodulation. Second, the sampling rate is high compared to the bandwidth of the information, which contains the sidebands of the readout tones. These are generally located at multiples of f_{mod}, as detailed in Section 4.2.2. Typically, the bandwidth required for bolometric applications is of the order of $\approx$ 200 KHz [135]. This provides a margin to further reduce the signal bandwidth and decimate the sampling rate of $f_s = 15.625$ MHz.

In the firmware used, frequency translation, filtering, and decimation for each channel (fine channelization) are performed using a Multi-channel Digital-Down Converter (DDC). There is one multi-channel DDC per PFB, as shown in Figure 5.6. The multi-channel DDC shown in Figure 5.10 consists of four parts: a mixer, an NCO, a low-pass filter, and a down-sampler. In the mixer, the signal from each of the channels is multiplied by a complex oscillator, then filtered by $H_D(z)$ and decimated by a factor of R. The multi-channel DDC uses a Time Division Multiplexing (TDM) scheme, represented by the switch, to sequentially convert each of the $M = 32$ channels of the PFB. Each PFB channel requires a distinct NCO frequency due to the randomness of the interrogation tones. Therefore, the multi-channel NCO uses three buffers that stores the frequency values $\Delta\phi_i$ and phase ϕ_i, as well as the accumulator Σ_i, corresponding to each channel i. Instant by instant, the mixer multiplies a sample from each channel with its corresponding sample from the local oscillator, and the result enters a multi-channel filter and decimator. The multi-channel uses two LUTs, where phase values are converted into amplitudes of $\cos(\dot{})$ and $\sin(\dot{})$. For a phase accumulator with K-bits, the resolution of the NCO is calculated as

$$\Delta f_{NCO} = \frac{f_s}{2^K}. \tag{5.11}$$

The implemented DDCs use a sampling rate of$f_s = 15.625$ MHz and an accumulator width of $K = 32$ Bits, resulting in a frequency resolution of $\Delta f_{NCO} \approx 3.7$ mHz. This resolution is sufficient for most cases. However, increasing the resolution could be considered to compensate for small frequency deviations in other oscillators in the system.

After the multiplication, the real and imaginary parts are sent to two multi-channel FIR filters. The filter was created using the Xilinx® FIR Compiler [155]. A symmetric 12-coefficient structure is used for $H_(Z)$. This design achieves a stop-band attenuation of $>$ 80 dB at $f_{stop} \approx 4$ MHz and a pass-band of $f_c \approx$ 1MHz with 3 dB attenuation at the pass-band edge. The details of the filter response are shown in Figure 5.11. The multi-channel DDC

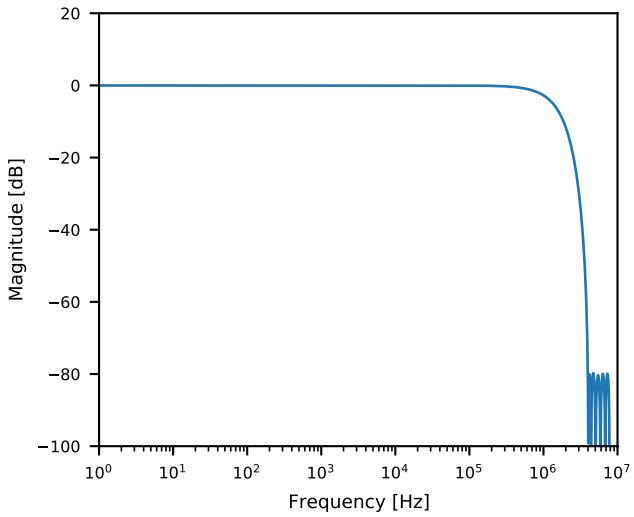

Figure 5.11: Frequency Response $|H_D(f)|$ of the Digital-Down Converter Filter. The filter was designed with a frequency of 3 dB cut-off frequency of $f_c \approx 1$ MHz and a stop-band attenuation of > 80 dB for frequencies greater than $f_{\text{stop}} > 4$ MHz.

can optionally be configured with a decimation factor of $R = 2$, where the filter is configured as a decimation filter. Additionally, a short FIFO buffer is added to collect the samples after low-pass filtering and transfer them to another clock domain. The decimation factor will be increased in future designs in order to achieve lower data rates per channel as required for bolometric applications [135].

5.3.3 Miscellaneous Modules

Here, we will briefly explain the purpose of the blocks shown in Figure 5.6, which, although not part of the DSP used in this thesis, are necessary to provide all the functionalities required by a modern SDR reading system.

IQ Imbalance Correction

IQ imbalances produce image tones at the opposite frequency of the tone that generates them, as explained in Appendix E. These tones can interfere with another channel if they are within the demodulation bandwidth. As a result, this causes crosstalk and reduces the SNR. In the case of transmission, IQ imbalances are corrected using the amplitudes and phases of the stored tones in the comb-generator block. For reception, the process is more complex, as it requires applying corrections to the received data stream. Generally, corrections are applied using FIR filtering to the signals [157, 158]. Unfortunately, this requires significant DSP resource usage due to the high data rates involved and the need to compensate for a large bandwidth.

To address this issue, colleagues at IPE proposed the development of an IQ compensation block (see Figure 5.6), which can be applied after the PFB. Here, the entire spectrum (i.e., desired frequencies and images) can be accessed, and the data rate is lower [152]. During the development of this thesis, the IQ correction module was in the evaluation and resource optimization phase. Therefore, it will not be used throughout this work, but it will be integrated into the system in the future.

Flux-Ramp Modulation and Demodulation

Both the generation of the flow ramp modulation and the demodulation are tasks that the SDR readout system must be capable of performing. In the case of generation, the flux-ramp is a low-frequency signal and generally requires higher quality than RF signals. Typically, high-speed RF DACs are suitable for generating the flow ramp, while external low-frequency

DACs with a higher number of bits are required. These typically have much lower sampling rates than 500 MHz and resolutions greater than 16 bits. With this objective, both members of the ITeDA institute and IPE have developed various prototypes of add-on boards for this purpose. These boards are connected to the SDR devices via available FMC connectors and use the available high-speed LVDS lines. As shown in Figure 5.6, within the programmable logic, a generation block based on LUTs or Direct Digital Synthesis (DDS) is responsible for generating the ramp values (Flux-ramp Generation), and another handles the physical communication between devices (LVDS PHY).

For the case of demodulation, the firmware must perform all the tasks described in Section 4.2. The processing begins by processing the IQ traces for the calculation of the domain θ or γ. This is generally done efficiently and with few resources using a COordinate Rotation DIgital Computer (CORDIC). Then, a NCO provides the reference signals, which are multiplied with the window used $w(t)$ and the desired signal (i.e. θ or γ). These are then accumulated over a number of full periods to obtain the result [114]. Synchronization signals are used to maintain coherence between the ramp generation module and the demodulation, as well as to control the temporal delay between the generated ramp and the reference signals. It is worth mentioning that all the elements within the firmware, such as the DAC and ADC, are all locked to the same reference (CLK104) to avoid frequency differences that would result in low-frequency signals after demodulation [152].

The development and optimization of the hardware for the generation of the flux ramp and its associated firmware for modulation/demodulation is being carried out by another colleague at *ITeDA* by the time of writing of this thesis. Additionally, previously developments designed for colorimetric applications only considers the amplitude γ demodulation not allowing the resonator phase θ demodulation [152]. For this reason, in later chapters, a commercial Arbitrary Waveform Generator (AWG) will be used for generation, and the demodulation will be performed offline. It is important to mention that several of the capabilities of the demodulation system were derived from the work presented in Chapter 4. Therefore, its evaluation will be performed through software demodulation before it is implemented in firmware.

Time Stamping

The scientific data acquired by the readout system must be associated with the position in the sky the telescope was pointing at. Therefore, there must be a synchronization system that provides both a temporal and spatial reference to allow the association of data collected by the different subsystems. Generally, synchronization is accomplished with precise timestamps distributed to the bolometer readout, telescope encoders, and other housekeeping subsystems. Typically, a high-quality GPS-disciplined oscillator (GPSDO) is used, which provides a 10 MHz frequency reference and a 1 pulse-per-second (PPS) signal. These signals are distributed to all sub-systems. Other more complex protocols, such as IRIG-B, can be used to distribute time-codes [159]. Timestamps are also important in calorimetric applications or single-photon counting, where timestamps with microsecond resolution are required [140].

While this module is still under development at the time of writing of this thesis, it is proposed to use the PPS and 10 MHz signals generated from a Rubidium (Rb) frequency standard [160]. The 10 MHz signal feeds the CLK104 clock board, while the PPS signal enters an NTP (Network Time Protocol) server to which the processing system can access. The UTC timestamp provided by the NTP is used to tag the data. The length required for the UTC timestamp has not yet been determined.

Data acquisition and control interface

The firmware and software architecture previously presented was developed to meet the needs of the ECHo project [45]. The required functionalities are not very different from those needed for the QUBIC project or other projects that use cryogenic sensors [29, 135, 18]. Both projects require the SDR readout system to be controllable and capable of performing acquisitions both locally and remotely. Additionally, the system must operate in two modes: calibration mode and acquisition mode. In the first mode, the proper functioning of each subsystem is diagnosed and the readout parameters are optimized to meet scientific objectives. In the acquisition mode, the previously determined parameters are used to acquire scientific data during the measurement campaign. In this mode, the data is transmitted to a server where data from all subsystems is collected (e.g., telescope pointing system, cooling systems, weather station, calibration source, etc.). All these functionalities were easily implemented in the SoC architecture (i.e., MPSoC and RFSoC). To do so, the data streams generated by the modules within the programmable logic are collected using a AXI Stream Switch, and then sent to a custom Direct Memory Access (DMA) module (see Figure 5.6) [152]. This module is responsible for receiving the data and storing it in the RAM memory attached to the PL or PS. From there, the data can be accessed by the PL, which can process it locally or forward it over the network.

For calibration, control, and data acquisition, the SDR group at IPE developed a user interface that uses network-capable Remote Procedure Calls (RPCs) [161]. It is called ServiceHub and allows for the configuration of the firmware and hardware of the measurement system. The user interface can control the modules in the programmable logic via the system bus or external hardware components using kernel modules that interface with I2C or SPI buses. It can also monitor and reset the firmware through the Information and Management Core (PIMC) [152].

Finally, it is important to mention that for the design, synthesis, and implementation of the firmware in the RFSoC, AMD Vivado™ Design Suite[3] was used, while for the development of the software and the compilation of the Linux distributions, a custom build system based on Yocto[4] was employed.

5.4 Zero-IF RFSoC-Based SDR Prototype System

The first prototype of the SDR reading system reuses the hardware structure proposed for the ECHo project [139]. A complete schematic of the Zero-IF RFSoC-Based SDR Prototype System is detailed in Figure 5.12 [105]. On the left side, the ZCU216 evaluation kit is responsible for generating and acquiring the frequency comb, as well as performing the channelization and demodulation of the channels. This is done using the firmware presented earlier and detailed in Figure 5.6. The evaluation kit makes use of three external boards. First, the CLK104 to generate the sampling clocks and synchronize the different local oscillators. Second, a Balun board for the differential-to-single-ended conversion required to access the converters. Finally, the Flux-Ramp Generation board (FRM Board). In the center of Figure 5.12, the Multi-Band RF Mixing board is located. During transmission, it is responsible for converting the different bands to the operating frequency, combining them, and sending them with the appropriate power to the cryostat. During reception, the different bands are amplified, separated, and filtered, before being converted to base-band for acquisition by the SDR system. On the right side, the cryogenic detection system is shown. It consists of the cryostat equipped with the RF cryogenic chain shown in Figure 4.20. At the lowest temperatures, the focal plane of detectors is placed, which are connected to the different channels of the µMUX, as detailed in Figure 3.7.

[3] https://www.amd.com/en/products/software/adaptive-socs-and-fpgas/vivado.html
[4] https://www.yoctoproject.org/

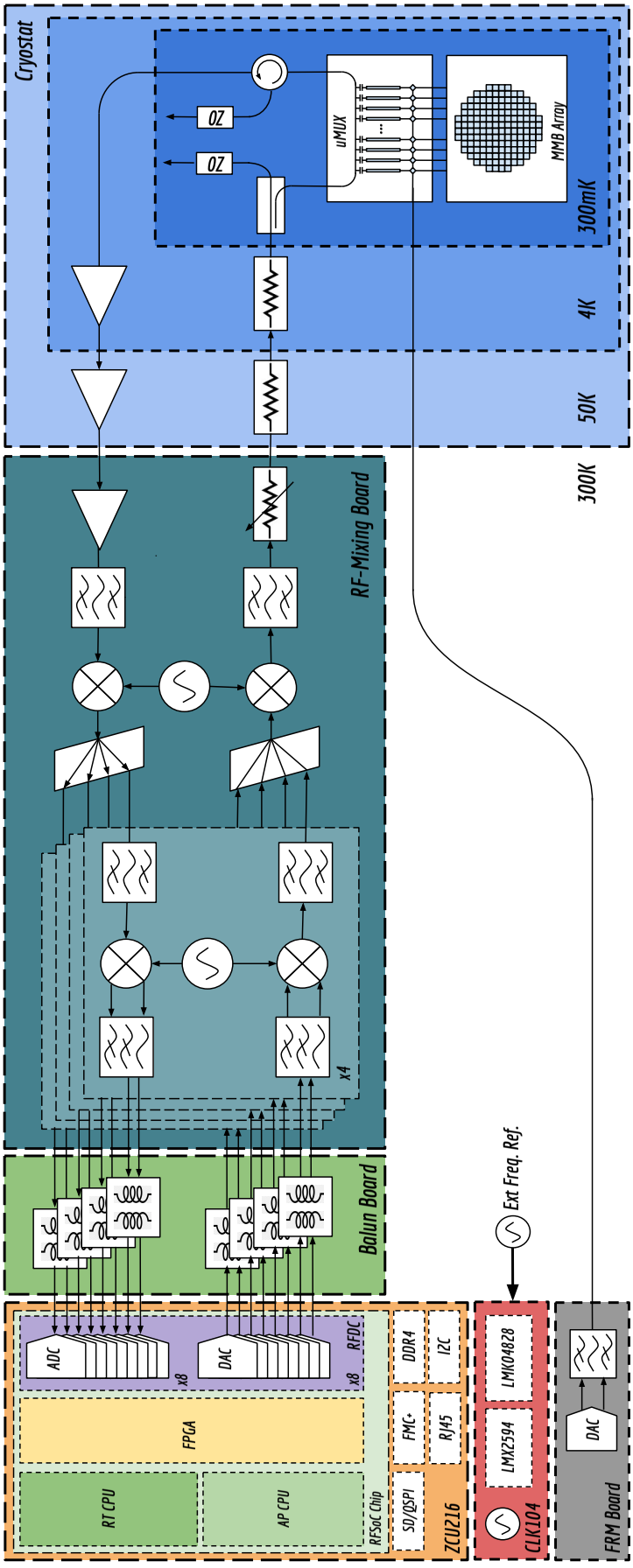

Figure 5.12: Block diagram of the Zero-IF RFSoC-Based SDR Readout System Prototype. **Left)** ZCU216 Evaluation KIT, Clock Board and Flux-Ramp Board. **Middle)** Multi-band IQ Mixing Board. **Right)** Cryogenic Microwave Multiplexing Systems and Detectors.

5.4.1 Multi-Band IQ mixing Board

The scheme used by the ECHo project divides the bandwidth between 4 and 8 GHz into five 800 MHz bands using an innovative Multi-band IQ Mixing board [148]. This design avoids the use of expensive IQ mixers and commercially available IQ modulators and demodulators. While these devices have a limited frequency range, their performance and functionalities are superior. Hence, modulation and demodulation are performed by wireless communications integrated circuits (*LTC5588* and *LTC5586*). The limited operating range of these circuits is compensated with a second real mixing stage using the *LTC5549*. A-priori band combination before the second conversion avoids duplicating the number of oscillators. In the reception path, the reverse process occurs. Filters and amplifiers remove unwanted signal components and adapt the required power levels. Oscillator generation begins in the *ADCLK948* chip, where the clock signal is buffered and fanned out to a series of PLL synthesizers. The local oscillators for all RF mixing stages consist of *LMX2594* chips, as in the CLK104.

To better understand the Multi-band IQ Mixing board, we will explain its operation using Figure 5.13. At the top of the figure, a pair of DACs generate the signals $x_{Tx,I}(t)$ and $x_{Tx,Q}(t)$ at a rate of $f_{DAC} = 1$ GHz. A pair of low-pass filters removes out-of-band signals. Then, an IQ mixer shifts the signals to an intermediate frequency f_{IF}. A bandpass filter removes the harmonic signals generated by the mixer. For the purposes of this thesis, we will consider the implementation of only four bands to simplify the direct comparison with the Mixer-Less prototype, since adding an additional band to the scheme is trivial. In the middle of Figure 5.13, a set of eight DACs and four IQ mixers generate four complex bands centered at $f_{IF} = 1.5 + 1 \cdot n$ GHz with $n \in [0, 3]$. These bands are combined and up-converted using a real mixer with $f_{RF} = 9$ GHz. The result is shown at the bottom of Figure 5.13, where the four bands located at $f_{IF} = 4.5 + 1 \cdot n$ GHz with $n \in [0, 3]$ are displayed after filtering the upper sideband. The reception process is similar, except that the four bands are acquired by four pairs of ADCs, as shown in Figure 5.12.

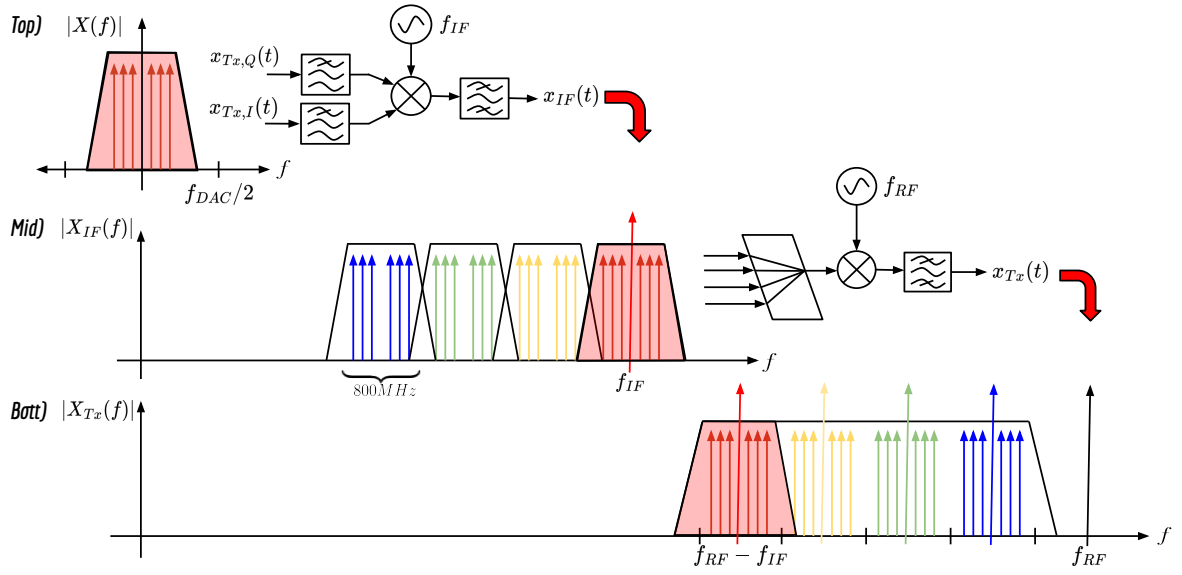

Figure 5.13: Frequency Planning using the Multi-band IQ Mixing Board. **Top)** A single complex band is up-converted to a specific intermediate frequency f_{IF} using an IQ mixer and filtered. **Middle)** The four different bands are combined and up-converted again to the final frequency using a real mixer. **Bottom)** The four bands are filtered again in order to eliminate image tones above the local oscillator f_{RF}.

For the development of the presented work, a single-band version of the Multi-band

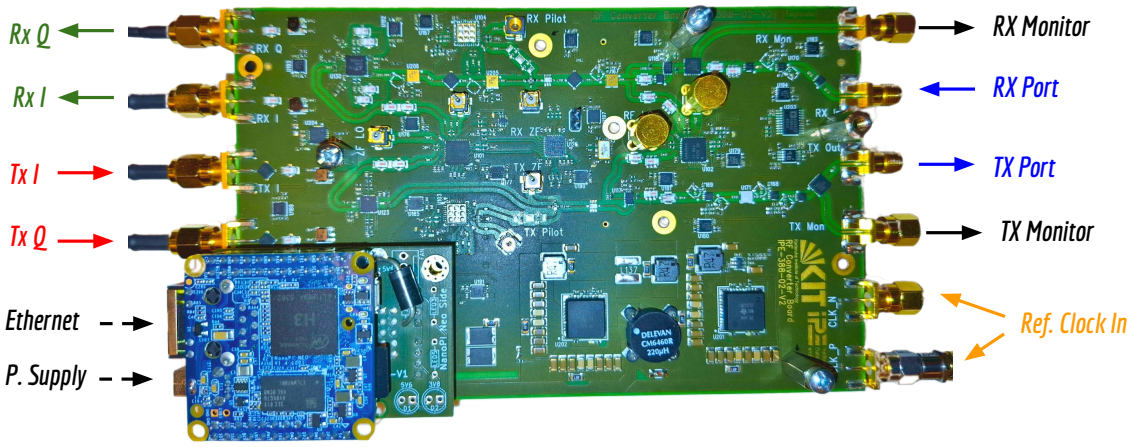

Figure 5.14: Photograph of the Multi-band IQ Mixing Board PCB.

IQ Mixing board was used. A photo of the PCB of this board can be seen in Figure 5.14. This version is equipped with SMA connectors and provides all the required functionalities, such as adjustable gain and monitoring ports for both Tx and Rx [162]. Its control is done via Ethernet through a *NanoPi* single-board computer, which is connected to the SPI and I2C communication ports of the board. Regarding frequency synchronization, it has a clock input that allows locking all the local oscillators (LO) to an external reference.

5.4.2 IQ Signal Generation

For the Zero-IF RFSoC-Based SDR, four pairs of DACs (IQ pairs) out of the eight pairs available are used. The configuration of the DACs within the RFDC core is shown at the top of Figure 5.15. It uses two individual ADCs in Real-to-Real mode, sampling at $f_{DAC} = 1$ GHz to generate $x_{Tx,I}(t)$ and $x_{Tx,Q}(t)$. These signals feed the IQ mixers on the mixing board. The $f_{DAC} = 1$ GHz clock is externally generated by the CLK104 and distributed to the DACs through DAC Tile 2 (DAC229 [146]). Each DAC, operating as a slave, receives samples from the PL via an AXI4-stream that carries 16 words per AXI4-stream clock at $f_{DAC}^{AXI} = 62.5$ MHz. Since each word is 16 bits wide, the bus width is 256 bits. A FIFO gearbox handles the alignment of the samples before sending them to the DAC, after being compensated by the Inverse-Sinc, as explained in Appendix A. It should be mentioned that the comb-generator block was designed to provide a complex data stream (interleaved IQ samples). To be compatible with the interface required by the RFDC, an additional IQ split block was added to the schematic shown in Figure 5.6. This block creates two real AXI streams from a single complex sample stream.

At the bottom of the figure, the spectrum of the DAC output signals is shown, as given by equations 5.1 and 5.2. The elimination of spurious tones generated outside the Nyquist zone due to the NRZ reconstruction waveform (see Appendix A) is achieved using two low-pass filters *Mini-circuits LFCN-400+* located in the mixing board.

5.4.3 IQ Signal Acquisition

Equivalently to the generation process, for reception, four pairs of ADCs are planned to be used out of the eight available pairs. The digital datapath is shown in Figure 5.16. The signals $x_{Tx,I}(t)$ and $x_{Tx,Q}(t)$ coming from the IQ down-mixer are sampled at $f_{ADC} = 1$ GHz after being filtered by two low-pass filters, *LFCN-320+*. The sampling clock is provided by the

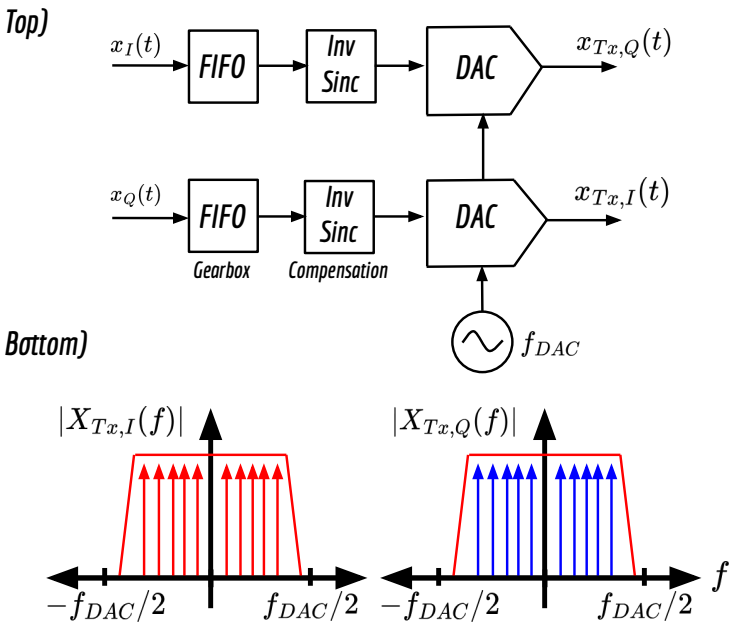

Figure 5.15: Top) Zero-IF SDR RFDC DAC configuration. Each DAC is configured as Real-to-Real and sampling at $f_{DAC} = 1$ GHz. **Bottom)** Spectrum of the in phase $x_{Tx,I}(t)$ and Quadrature components $x_{Tx,Q}(t)$ generated by the DACs.

CLK104 through the ADC Tile 2 (ADC225 [146]). Unlike the DACs, the mixers operate in Dual-Band Complex-to-Complex mode. Using the CrossBar, the signals from both ADCs are distributed to two DDCs. Each DDC selects the positive or negative frequency band. For this, the NCOs of each DDC are configured in fine mode with frequencies $f_{NCO,1} = 200$ MHz and $f_{NCO,2} = -200$ MHz. Both the real and imaginary parts are subsequently decimated before being filtered by the decimating filters provided by the RFDC, which offer a bandwidth protected from aliasing of 400 MHz [146]. In contrast to the DACs, the ADC data is transferred to the logic using two master AXI4-streams of complex samples. Each AXI4-stream has a width of 128 Bits, transporting eight words per AXI clock configured at $f_{ADC}^{AXI} = 125$ MHz. The bottom panel of Figure 5.16 shows the complex spectrum of the received comb $|X(f)|$ and how it is split into two bands $|X_1(f)|$ and $|X_2(f)|$ by the DDCs. Each band is sampled at a rate of $f_s = 500$ MHz, compatible with the firmware scheme developed for ECHo and shown in Figure 5.6.

It is worth mentioning that the clocks f_{DAC}^{AXI} and f_{ADC}^{AXI} are generated by the RFDC from the sampling clocks f_{DAC} and f_{ADC} provided by the CLK104. These clocks are also used in the PL for the DSP modules.

5.5 Mixer-Less RFSoC-Based SDR Prototype System

The previous scheme is widely used by various SDR reading systems. Some variations of it propose the use of a single IQ conversion stage [114, 98]. While this scheme easily demodulates complex signals, it has the drawbacks mentioned in E, requiring a tedious and frequent calibration process [99]. Nowadays, commercially available high-speed ADCs and DACs, such as those in the RFSoC, offer a solution to this problem. These are equipped with DDCs and DUCs, which allow digital implementation of IQ modulation without suffering from the problems associated with analog mixers. Additionally, the high sampling rates allow direct access to the medium at RF frequencies or intermediate frequencies, where the process can be completed

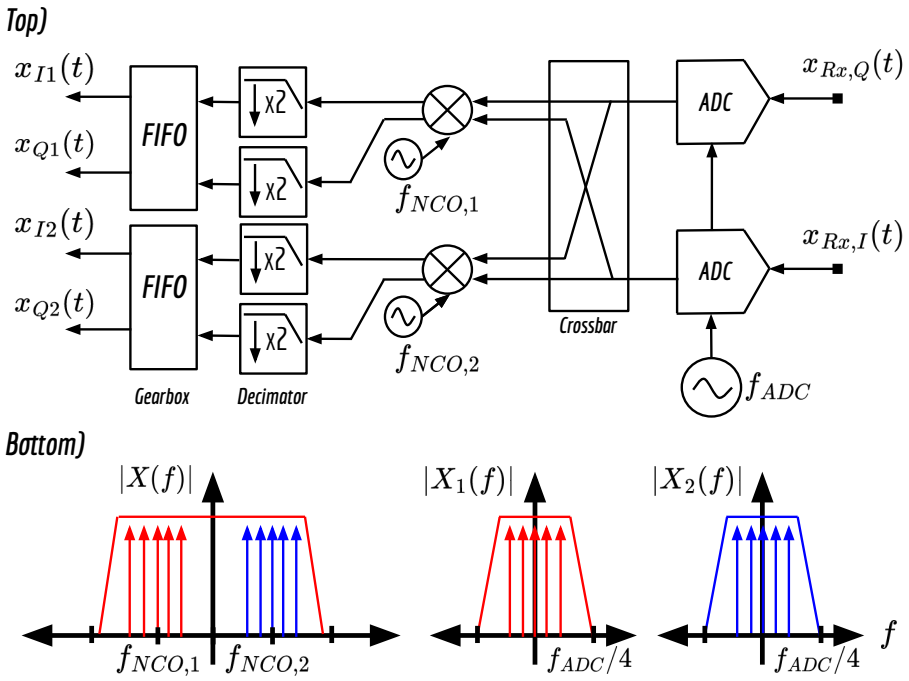

Figure 5.16: Top) Zero-IF SDR RFDC ADC configuration. Each ADC is configured as Complex-to-Complex and sampling at $f_{ADC} = 1$ GHz. **Bottom)** Spectrum of the sub-bands $|X_1(f)|$ and $|X_2(f)|$ generated by the ADCs.

using real mixers. Some examples of these systems can be found in the following references [135, 163, 164, 165].

In line with these new technologies, a SDR prototype based on RFSoC, called the Mixer-Less SDR, was developed. This prototype fully exploits the unique features of the RFSoC, and its development is less complex since it only uses amplifiers and filters. The general schematic of the Mixer-Less RFSoC-Based SDR Prototype System is shown in Figure 5.17. On the left side, the ZCU216 evaluation kit is responsible for generating and acquiring the frequency comb, as well as performing the channelization and demodulation of the channels. This is done using the firmware presented earlier and detailed in Figure 5.6. The evaluation kit makes use of three external boards: the CLK104, the Balun board, and the FRM Board. Unlike the previous scheme, the signals are generated and acquired directly in the operating band, as we will detail below. In the center of Figure 5.17, the Multi-Band Combiner and signal conditioning Board is located. During transmission, it is responsible for heavily filtering unwanted signals, combining the different bands, and sending them with the appropriate power to the cryostat. During reception, the different bands are amplified, separated, and filtered again before being acquired by the SDR system. On the right side, we can see the cryogenic detection system comprising the microwave cryogenic chain shown in Figure 4.20, the µMUX chips, and the focal plane.

5.5.1 Direct-RF Signal Generation

The third generation RFSoC DACs allow maximum sampling rates of $f_{DAC} = 9.85$ GHz and are equipped with reconstruction waveforms capable of generating signals in the second Nyquist zone. Making use of these qualities, the Mixer-less SDR intends to use four DACs sampling at $f_{DAC} = 8$ GHz to generate four bands of 800 MHz between 4 and 8 GHz. This is

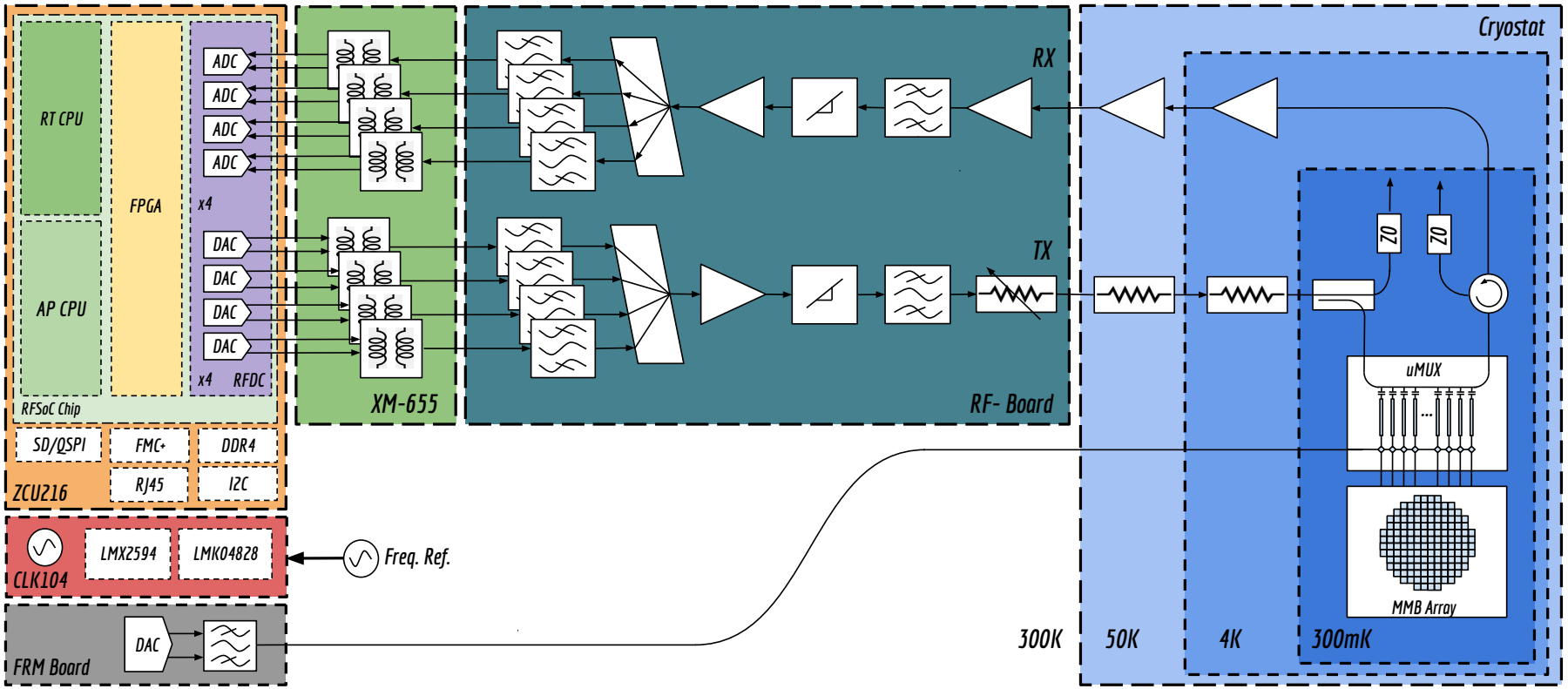

Figure 5.17: Block diagram of the Mixer-Less RFSoC-Based SDR Prototype System. **Left)** ZCU216 Evaluation kit, Clock Board and Flux-Ramp Board. **Middle)** Multi-Band Combiner and signal conditioning Board. **Right)** Cryogenic Microwave Multiplexing Systems and Detectors.

compatible with the previously presented Zero-IF SDR and the requirements of the cryogenic microwave chain. The configuration of the DACs is shown in the upper part of Figure 5.18. In this case, the comb-generator feeds the DAC via a complex AXI4-Stream with a bus width of 256 bits. It transports sixteen words per AXI clock at $f_{DAC}^{AXI} = 125$ MHz. The complex data at a rate of $f_s = 1$ GHz (see the middle of Figure 5.18) is interpolated by a factor of 4 and enters the complex mixer, where it up-converts with the NCO signal to a frequency of f'_{NCO}. In this case, the DUC feeds a single DAC, so it operates in IQ-to-Real mode. Since the DUC cannot operate at frequencies higher than 6 GHz, an additional x2 interpolation provided by the Image Rejection Filter (IMR) is used [146]. It must be configured as a low-pass or high-pass filter, depending on the desired operating frequency. This can be between 4 and 6 GHz or between 6 and 8 GHz. It should be noted that the effective rate at which the frequency comb will be shifted is $f_{NCO} = 2f'_{NCO}$ as shown in the lower part of Figure 5.18. Once the required rate for the DAC (x8 total interpolation factor) is reached, it is sent to the DAC. Since operation in the second Nyquist zone is required, a mix-mode reconstruction waveform is applied as explained in Appendix A. Therefore, before send it to the DAC, compensation for the mix-mode is applied. It is important to note that operation in the second Nyquist zone entails a mirroring effect that must be compensated by either selecting $f_{NCO} = -f_{NCO}$ or by mirroring the frequency comb during generation.

As we will see later, the frequency planning of this prototype is intimately related to the acquisition. For this reason, four bands were defined for both prototypes. Again, and for this case, the bands will be centered at $f_{NCO} = 4.5 + 1n$ GHz with $n \in [0, 3]$. Although the set NCO frequency f'_{NCO} is not equal to the effective f_{NCO}, this is transparent to the user since the RFDC configuration interface automatically calculates f'_{NCO} from f_{NCO} [146].

5.5.2 High-Order Nyquist Zone Signal Acquisition

Unlike the DACs, the third generation of RFSoC provides two types of devices with a different number of ADCs: ZU48DR and ZU49DR. The difference between both lies in the fact that the ZU48DR has a structure of two ADCs per tile, which can sample up to $f_s = 5$ GHz, while the ZU49DR has four ADCs per tile, limiting operation to 2.5 GHz. Since we have the ZCU216 kit equipped with the ZU49DR, we are limited to $f_s = 2.5$ GHz.

The acquisition of the frequency comb in the Mixer-Less SDR is based on the concept of bandpass sampling. It takes advantage of aliasing to acquire signals in high Nyquist zones. The associated theory can be found in Appendix B. The ADC configuration diagram is shown at the top of Figure 5.19. The received signal $x_{Rx}(t)$ is sampled at a rate of $f_{DAC} = 2$ GHz. Based on sampling theory, all signal components in the different Nyquist zones will be folded onto the first one. If we ensure that only one Nyquist zone contains the signal, it will fold onto the first zone and can be acquired. This effect is shown in the middle part of Figure 5.19, where signals in the sixth Nyquist zone ($NZ6$) are folded onto the first zone ($NZ1$). For $f_{DAC} = 2$ GHz, each zone has a bandwidth of $f_s/2 = 1$ GHz. Therefore, each of the bands generated by the DAC, centered at $f_{NCO} = 4.5 + 1n$ GHz with $n \in [0, 3]$, can be acquired after unwanted bands are eliminated. While not having mixers is an advantage, it requires sharp filters at microwave frequencies and guard bands between the bands. This limitation led to the implementation of only four bands. Since the folding process reflects signals in even zones, this must be taken into account during acquisition to correctly assign the received frequencies.

Once the information is contained in the first zone, the ADC splits the signal into two DDCs operating in Real-to-Complex mode. The spectrum of the real signal at the output of the ADC is shown at the bottom of Figure 5.19. It is equivalent to the signal in Figure 5.16, but centered at an intermediate frequency $f_{IF} = 500$ MHz. Therefore, the oscillators are set at $f_{NCO,1} = 300$ MHz and $f_{NCO,2} = 700$ MHz to separate the upper and lower bands of the frequency band. Then, a decimator x4 reduces the data rate, and the data is transferred to the logic. As in the Zero-IF SDR prototype, two complex AXI streams with a width of 128 bits

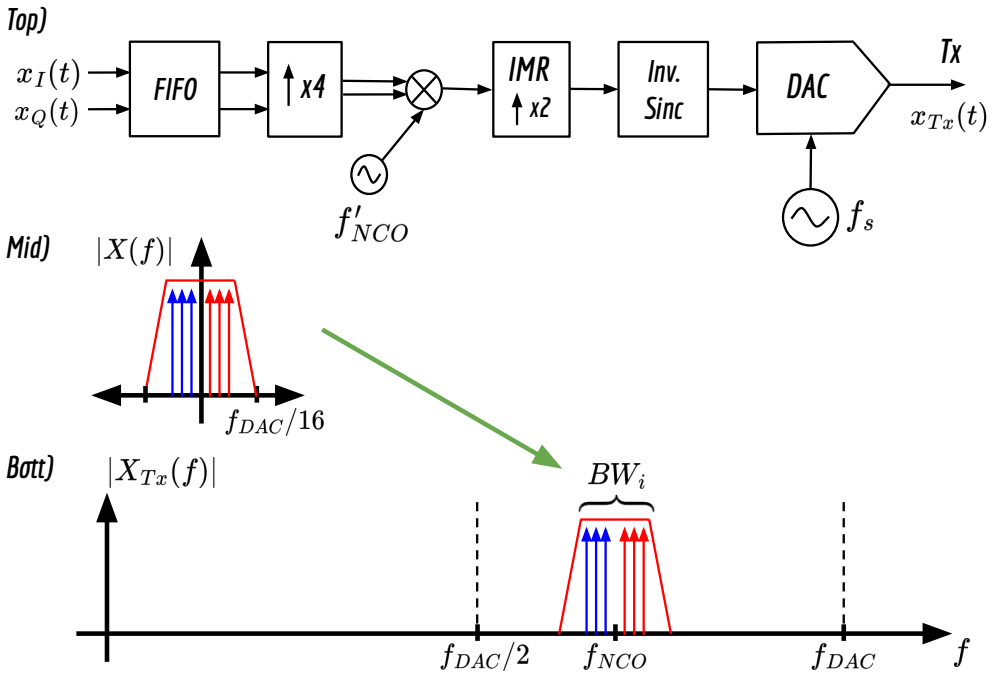

Figure 5.18: Top) Mixer-Less SDR RFDC DAC configuration. The DAC is configured as Complex-to-Real and sampling at $f_{DAC} = 8$ GHz. **Middle)** Spectrum of the frequency comb at baseband $|X(f)|$. **Bottom)** Spectrum of the frequency comb $|X_{Tx}(f)|$ generated by the DACs.

carry 8 words per AXI4 clock at $f_{ADC}^{AXI} = 125$ MHz.

As in the previous prototype, the sampling clocks for f_{DAC} and f_{ADC} are provided by the CLK104 and fed into tile 2 of the DAC (DAC229) and tile 2 of the ADC (ADC225). Both AXI clocks are generated by the RFDC and distributed within the PL. It is worth noting that the datasheet for the third generation of RFSoC specifies an analog bandwidth of 6 GHz for both the DACs and ADCs. However, characterizations performed show proper operation at frequencies up to 8 GHz. The details of the characterization are presented in Appendix C.

5.6 Resources Utilization Report

In order to evaluate the resources used by each SDR prototype, the firmware design shown in Figure 5.6 for a single band was implemented. Since some blocks specific to the QUBIC project are still under development, equivalent blocks already designed for the ECHo project and reported in the references [152, 116] were implemented. It is expected that the resource consumption will be of the same order for both applications (i.e., Calorimetric and Bolometric). The only blocks not implemented were the IQ-correction and the Flux-Ramp generator. Clearly, the blocks for implementing the JEDEC JESDx standard to communicate with the converters were not necessary. The resources used by the firmware for both prototypes are listed in Table 5.2.

Regarding the resources available in the RFDC, the Mixer-less prototype uses half the number of converters compared to the Zero-IF. This does not provide any comparative advantage, as both prototypes use nearly the same amount of DDCs and DUCs. The RFSoC only provides one DDC and one DUC per ADC and DAC respectively, as shown in Table 5.1. In terms of PL resources, both prototypes use the same processing chain and consume approximately the same amount of resources. From these results, we can conclude that the implementation of

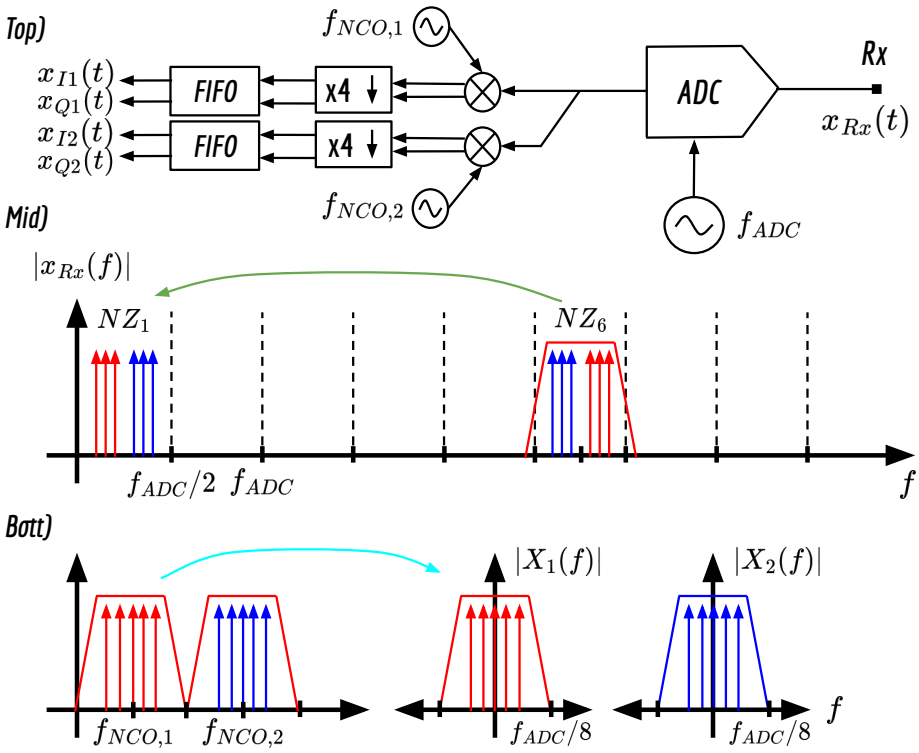

Figure 5.19: Top) Mixer-Less SDR RFDC ADC configuration. The ADC is configured as Real-to-Complex and sampling at $f_{ADC} = 2$ GHz. **Middle)** Bandpass Sampling of the received signal $x_{Rx}(t)$. **Bottom)** Spectrum of the sub-bands generated by the ADC.

Table 5.2: Summary of resources utilization for the Single-Band Gen3 RFSoC-Based SDR prototype systems.

Resource	Zero-IF SDR	Mixer-Less SDR	Available
DACs	2	1	16
ADCs	2	1	16
DUCs	2	1	16
DDCs	2	2	16
LUT	73K (17.4%)	75K (17.5%)	425K
LUTRAM	11K (5%)	11K (5%)	425K
FFs	105K (12.4%)	107K (12.6%)	850K
BRAM	270 (24.9%)	270 (24.9%)	1080
UltraRAM	1 (1.25%)	1 (1.25%)	80
DSP Slices	256 (6%)	256 (6%)	4272
IO	102 (25%)	102 (25%)	408
BUFG	15 (2.2%)	14 (2%)	696
MMCM	2 (25%)	2 (25%)	8
PLL	2 (12.5%)	2 (12.5%)	16

a total of four bands is feasible for both prototypes, as none of the available resources exceed 25% utilization. However, a rigorous implementation analysis is required to ensure that none of the blocks resources usage does not scale linearly with the number of bands. It should also be verified that the congestion caused by the high resource density does not generate timing issues. In future implementations, the use of blocks that leverage the large number of DSPs

and alleviate the consumption of other resources will be explored.

In the next chapter, the analog performance of the previously described SDR prototypes will be characterized. This will be done using the single-band versions and utilizing available RF components in the laboratory. This will allow for the identification of the pros and cons of both architectures and the analysis of the feasibility of implementing a custom hardware design based on one of them.

6. Characterization of the SDR Prototype Systems

Several factors are analyzed when selecting a SDR for reading superconducting detectors. Some of these include low cost, high integration level, ease of implementation and use, functionality, and versatility [18]. While all these factors are important, the decisive factor for selecting the SDR is its analog performance. It must be ensured that the readout system is capable of generating, acquiring and demodulating high-quality signals without deteriorating the intrinsic performance of the detection system, as detailed in Chapter 2. Since the analog performance of the SDR depends on the number of detectors, we must ensure that the performance requirements are met for the number of detectors required for the experiment.

In this chapter, we present the characterization of the performance of both SDR prototypes described in Chapter 5. The characterization will allow us to compare the advantages and disadvantages of each scheme and determine which is more appropriate for application in the QUBIC project upgrade. In Section 6.1, we begin by describing the composition of the characterization setup for both prototypes outlined in 5.4 and 5.4. Then, in Section 6.2, we demonstrate the capability of the prototypes to generate signals in different bands, before focusing on the detailed characterization of a single band. Finally, in Section 6.3, using the generated signals and a loopback configuration, we characterize the total noise performance of the SDR.

6.1 Characterization Set-Up

Figure 6.1 shows the hardware setup for the characterization of both prototypes. On the left, the ZCU216 evaluation kit equipped with the CLK104 clock board and the XM655 Balun board is shown. The different cables coming from the left provide power, Ethernet connection, and UART. Since the same kit is used for both prototypes, the appropriate RFDC tiles were selected to allow simultaneous access to both configurations. For the Zero-IF SDR case, the four *Minicircuits TCM2-33WX+* baluns were used, and they were connected via SMA-SMA coaxial cables to the mixing board. An additional SMA cable provides the $f_{OUT} = 10$ MHz output reference to the mixing board for LO generation (see Figure 5.14). For this prototype, the transmission and reception ports (*Zero-IF Tx* and *Zero-IF Rx*) are identified in blue in Figure 6.1.

In contrast to the Zero-IF SDR system, the Mixer-Less system uses the *Anaren BD3150N50100AHF* and *Anaren BD4859N50100AHF* baluns for the 4 to 5 GHz and 5 to 8 GHz bands, respectively. Additionally, two *Minicircuits VBFZ-5550-S+* bandpass filters and a wideband LNA *Minicircuits ZX60-83LN12+* are added. These provide gain and filtering of image tones. Here, the transmission and reception ports (*Mixer-Less Tx* and *Mixer-Less Rx*) are identified in green in Figure 6.1.

The characterization process was divided into two parts: the generation of the tone comb and the acquisition of the same in loopback. The frequency comb characterization process

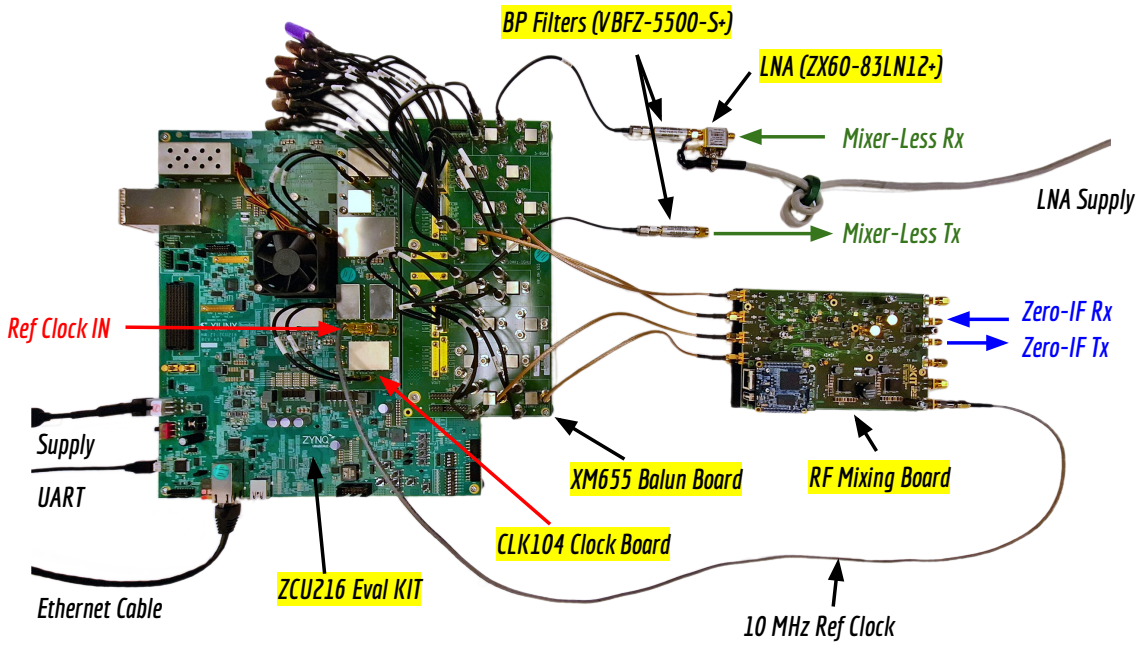

Figure 6.1: Hardware implementation of the two different RFSoC-Based SDR prototype systems. The ADC/DAC tiles and Balun configuration were properly selected allowing the evaluation of both prototypes. The Single-band Mixing board is used for the Zero-IF SDR Prototype, while Filters and LNA for the Mixer-Less SDR Prototype.

aims to determine the system's ability to generate tones, as well as the gain and filtering requirements necessary to achieve the power and signal quality required by the µMUX. On the other hand, characterizing the signal acquisition aims to evaluate how the system affects the frequency comb and its quality.

The block diagram shown in Figure 6.2 presents the characterization setup for the Zero-IF SDR system. During transmission, the stored frequency comb is reproduced at a rate of $f_{DAC} = 1$ GHz and sent to the Mixing Board, where it is shifted to the operating frequency $f_{LO} = f_{RF} - f_{IF}$. The power and quality of the generated frequency comb are analyzed by connecting the system's output to a spectrum analyzer (Tx to SA). In this work, the R&S FSWP 50 [166] was used. Once the tone quality and power were ensured, a loop-back measurement (Tx to RX) was performed. The tones were down-converted and acquired by the ADCs, to later be processed by the PFB, and converted back to base-band through the DDCs. At this point, the complex envelope of each tone is available for characterization as $x(t) = x_I(t) + jx_Q(t)$. As shown in the figure, all LOs, ADCs, and DACs are connected to the internal reference of the CLK104.

In a similar manner, Figure 6.3 shows the block diagram corresponding to the characterization of the Mixer-Less SDR system. The frequency comb is generated directly at the operating frequency f_{NCO} by a single DAC sampling at $f_{DAC} = 8$ GHz. In order to analyze the spectral components produced by the DAC sampling at high speeds, the Tx transmitter was connected directly to the SA without prior filtering. Previous results are used to determine the filtering characteristics necessary to eliminate unwanted signals. Once the generation characteristics are determined, a loop-back measurement of RF (i.e., Tx - Rx) is carried out. Amplifiers and filters condition the signal to be later acquired in a high Nyquist zone by the ADC sampling at $f_{ADC} = 2$ GHz. Similarly to the other prototype, the signals are processed by the PFB

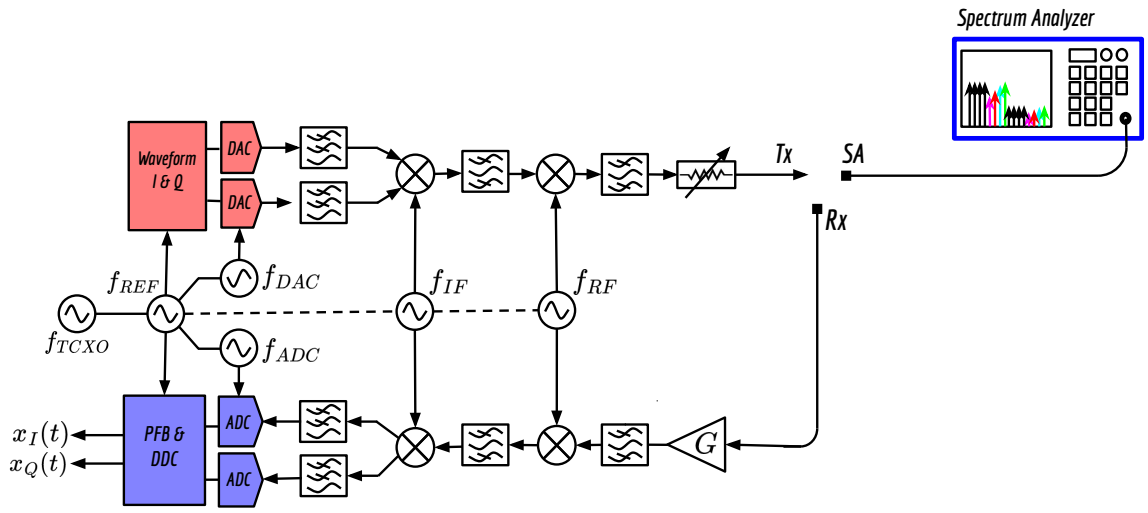

Figure 6.2: Block diagram of the Zero-IF SDR Characterization Set-Up.

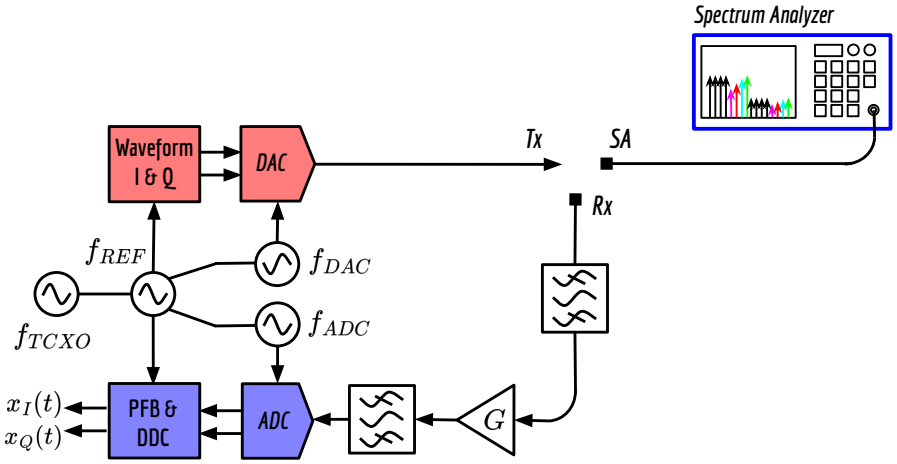

Figure 6.3: Block diagram of the Mixer-Less SDR Characterization Set-Up.

and converted to base-band by the DDCs. The complex envelope $x(t) = x_I(t) + jx_Q(t)$ will be used later to characterize phase and amplitude errors of each tone. Both sampling clocks are generated by the CLK104 from its internal reference.

6.2 Signal Generation Characterization

The Microwave SQUID Multiplexer (μMUX) encodes the information from the detectors in the phase and amplitude of the interrogation tones. As we saw in Chapter 4, the noise performance is determined by the power of the interrogation tones and the noise present in them. Noise or spurious signals present in either of these coordinates cannot be distinguished from the detector signals and lead to a degradation in sensitivity. Therefore, the tones must be generated with high spectral purity and acquired with minimal added noise or distortion. In the following Subsection 6.2.1, we will characterize the capability of our prototypes to generate the frequency comb with the appropriate power. Later, in Subsection 6.2.2, we will present the

results of the characterization of the sampling clocks.

6.2.1 Frequency Comb Generation

The first test conducted on the prototypes was the ability to generate the required frequency combs to cover the entire bandwidth. For this, $N = 100$ tones were generated with a Gaussian frequency distribution, with a mean spacing of $\mu_f = 7.8120$ MHz and a standard deviation of $\sigma_f = 200$ kHz. The choice of $N = 100$ is justified based on the number of channels that can be processed using the available firmware. Hence, the average separation between tones μ_f corresponds to the separation between channels of the channelizer, as shown in Figure 5.8. The randomness introduced in the tones has two objectives. First, to emulate the actual resonance frequency distribution of a µMUX given the variations in the manufacturing process σ_f. Second, to ensure that neither the inter-modulation products nor the image frequencies of the tones are located at the same frequency as the desired signals, so they can be distinguished. For more details, see Section 4.4.3 and Appendix E.

Figure 6.4 shows the spectrum of the tones generated by the Zero-IF prototype and measured by a spectrum analyzer over the bandwidth between 0 and 12 GHz. This bandwidth was chosen because it allows for an adequate evaluation of spurious signals located within the band as well as 4 GHz above and below the operating band. This is sufficient for our application since the highest frequency signals have low power and are filtered by the cryogenic microwave chain itself. It should be noted that the prototypes can generate a single band, and each band was generated and measured independently. A previous characterization of the converters presented in C, demonstrated that the use of the High Linearity Decoder (HL) provides the best SFDR. Although the highest SFDR was achieved for $P_{out} \equiv -10$ dBFs, it represents a considerable reduction in power for the gain in SFDR. Therefore, the next measurements will employ the HL and an output power of $P_{out} \equiv -5$ dBFs. It is worth noting that for the Zero-IF case, the maximum available gain power in the transmission path is used [162].

As seen in Figure 6.4, the frequency combs are centered at $f_{LO} = 4.5 + 1 \cdot n$ GHz with $n \in [0, 3]$ and represented in different colors. At the center of each comb, a high-power tone can be distinguished, which is produced by the LO leakage of the IQ modulator (see appendix E), while the other tones with comparable power are produced by the LO leakage from the real mixer present in the Mixing-board. The remaining spurious signals are images and/or inter-modulation products generated by both the frequency conversion processes and the non-linearities of the Mixing board. While the components outside the band between 4 and 8 GHz can be filtered, this is not the case for the in-band signals. Using measurements from the Zero-IF SDR, a SFDR > 50 dB was determined. This is because, during the design of the µMUX, dedicated guard bands can be considered where no channels will be located, thus preventing their interference. In the case of IQ images, they can be removed during calibration, as we will see later. The aforementioned SFDR value can be improved either by reducing the tone power, using more linear components, or increasing the selectivity of the filters used. Thus, it is well below the level of the inter-modulation products produced by the cryogenic microwave chain, which is the limiting factor.

Similarly, measurements were repeated for the case of the Mixer-less SDR prototype using the setup shown in Figure 6.3. In this case, instead of modifying the local oscillators (LO), f_{NCO} frequencies were adjusted to center the frequency combs at the desired frequencies. These frequencies are given by: $f_{NCO} = 4.5 + 1 \cdot n$ GHz, with $n \in [0, 3]$. Although the NCO configuration can be done at runtime, at the time this work was conducted, there was no available driver to perform this operation. Therefore, different bitstreams were created for each configuration and used according to the operating band.

Two major differences can be observed compared to the previous case. First, there are no tones at the center of the band. Second, a series of high-power image tones appear on both sides of the operating band. The absence of LO leakage is due to the fact that this issue does

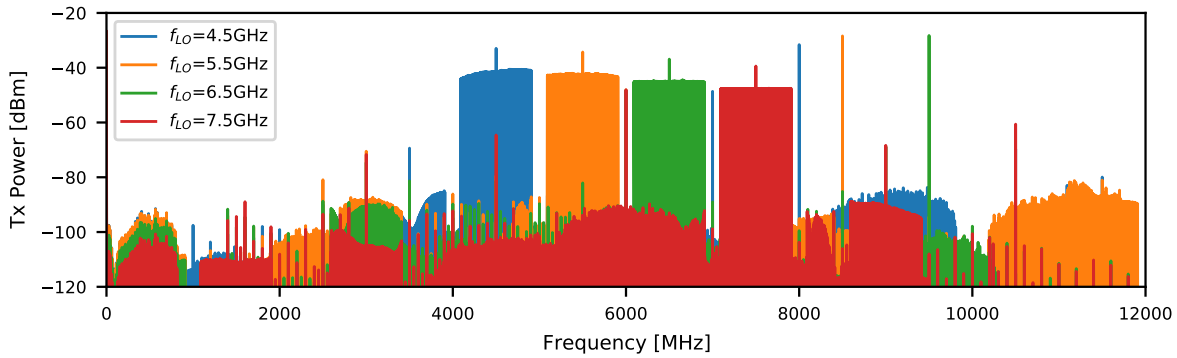

Figure 6.4: Measured Spectrum of $N = 100$ tones generated by the Zero-IF Scheme. Different colors represent the frequency comb up-converted to four different local oscillator frequencies f_{LO}.

not occur in the case of digital mixers. On the other hand, the appearance of spectral replicas is due to the nature of the reconstruction process. As explained in Appendix A, the output signal of the DAC consists of all the replicas of the analytic signal, weighted by the frequency response of the used reconstruction waveform.

In this case, since the signal is sampled at $f_{DAC} = 8$ GHz, each Nyquist zone spans 4 GHz, and each replica is mirrored in the odd zones. This gives rise to one of the most significant drawbacks of this scheme: The tones at both edges of the Nyquist zone will have their replicas close in frequency. While this problem imposes strict requirements on the filters used, there are commercially available solutions. Some examples include the cavity filter family provided by *K&L Microwave*[1], such as the models *11ED30-4500_U800, 11ED30-5500_U800, 11ED30-6500_U800, and 11ED30-7500_U800*, or the quadruplexer family provided by *Lark Engineering*, which has shown demonstrated performance in similar systems, according to the references in [135] and [167]. Another approach is to use different sampling frequencies that allow the separation of replicas and easy filtering. Since this requires the use of internal PLLs and involves a more complex configuration of the RFDC [146], it will be explored in future work. In any case, the use of guard bands between sub-bands should be considered in order to provide a transition margin for the filters. For this configuration, a similar SFDR of approximately 50 dB was determined for the operating band between 4 and 8 GHz.

In addition to spectral purity, the readout SDR prototypes must be capable of generating the power levels required by the μMUX. This depends on several factors such as the RF system gain, which conditions the signals, the output power of the DACs, the number of tones, and the generation algorithm used. The first two factors depend on the analog characteristics of the DACs, the type of reconstruction waveform used, and the frequency response of the RF components (i.e., amplifiers, cables, filters, etc.). The presence of these factors is reflected in the separation of approximately -8 dB between the edges of the operating band (i.e., 4 and 8 GHz), which is shown in Figures 6.4 and 6.5. This behavior can be compensated by using equalizers and amplifiers. However, throughout this work, we characterize the prototypes using the components shown in Figure 6.1. Overcoming the limitations found in both prototypes is beyond the scope of this work and will be part of future hardware designs.

As mentioned, the output power also depends on the number of tones and the generation algorithm used to minimize the PAPR. The maximum power with which a single tone can be generated corresponds to the full-scale amplitude of the DAC, A_{FS}. For the configuration used, this corresponds to a maximum current of $I_{FS} = 32$ mA, which is reached when all 14 bits of resolution have a value of 1. This current translates into a determined power in Watts

[1] https://www.klfilterwizard.com/

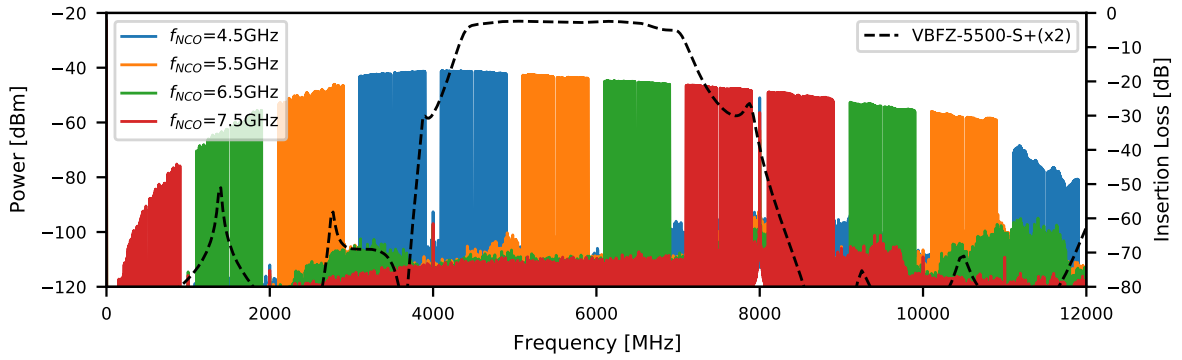

Figure 6.5: Measured Spectrum of $N = 100$ tones generated by the Mixer-Less Scheme. Different colors represent the frequency comb up-converted to four different NCO frequencies f_{NCO}. The DAC sampling frequency used is $f_{DAC} = 8$ GHz. The right Y axis corresponds to the insertion loss response of the Band-Pass filter used for the characterization and is represented with a dashed black line.

depending on the DAC coupling mode and the termination impedance shown by the Balun. For the case of generating a multitonal signal, the total amplitude of the tones, A_{tot}, is selected so that it equals $A_{FS} - A_m$, where A_m is a margin used to avoid working at full scale, where the DAC does not have a good SFDR. In the general case of a N-tone comb of equal amplitudes, the power of each tone, P_{tone}, can be calculated as

$$P_{tone}(N) = P_{FS} - M - PAPR(N) - 10\log_{10}(N). \tag{6.1}$$

Here P_{FS} is the full-scale power in dBm, M is the margin with respect to full scale in dBFS, and $PAPR(N)$ is the Peak-to-Average Power Ratio achieved by the algorithm used as a function of the number of tones, also expressed in dB. This relationship is very important since, in combination with the attenuation of the microwave readout chain, it defines the maximum excitation power, $P_{exc}(N)$, and consequently the flux noise $\sqrt{S_\Phi(N)}$ (see Figure 4.13). Since P_{FS} depends on the analog characteristics of the DAC and is a function of frequency, a single band was selected for the characterization. The band selected for both prototypes is centered at $f_{LO} = f_{NCO} = 6.5$ GHz. This band is located near the center of the possible frequency range of the μMUX, and therefore represents an intermediate condition for the evaluation of the prototypes. At the same time, this band hosts one of the multiplexer's channels that will be evaluated in Chapter 7.

For the power characterization, the same configuration as in Figures 6.2 and 6.3 was used, with the only difference being that the available spectrum analyzer in *ITeDA* was used: *Agilent N9000A CXA* [168]. As in the previous measurement, it involved the generation of N randomly spaced tones with a margin of $M = -5$ dBFS, generated using random initial phases for each tone. The phases are uniformly distributed in the range $[0, 2\pi)$ [151]. The use of this $PAPR(N)$ minimization method is justified by several factors, in addition to emulating the position of the readout tones required by a real μMUX. One factor is that all advanced $PAPR$ minimization methods converge to the same $PAPR(N)$ value provided by the random-phase method when the tones are randomly spaced in frequency. This was experimentally confirmed and through simulations [105, 169]. The second factor is that it mimics the characteristics of the frequency comb modulated by the μMUX. This is because both the RF component phases and the modulation produced by each resonator create a pseudo-random modulation of the phases of each tone. The consequence of this modulation is that the signals received by the SDR will have $PAPR$ values similar to those obtained with the random initial phase method. We will use this to our advantage in the following sections when characterizing the frequency

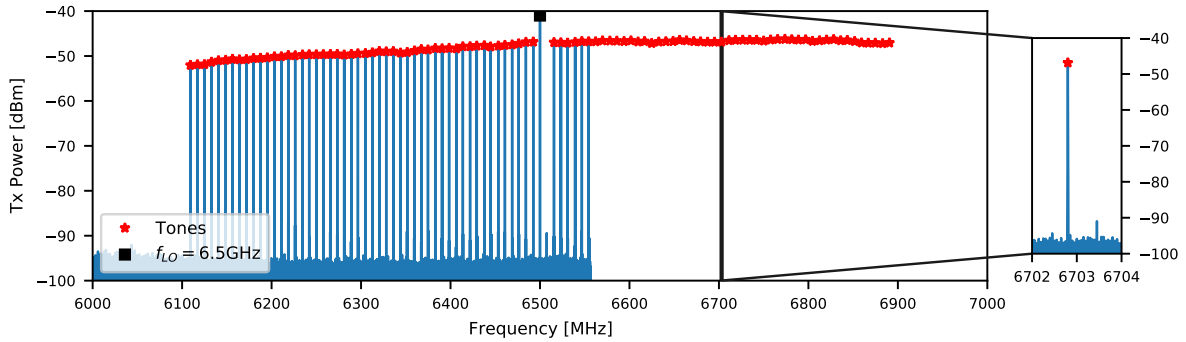

Figure 6.6: $N = 100$ tones centered at $f_{LO} = 6.5$ GHz generated by the Zero-IF SDR prototype.

comb via the Loopback.

Figures 6.6 and 6.7 show a zoom of the frequency combs with N_{100} tones generated by both prototypes, centered at $f_c = 6.5$ GHz. These figures show some details that are not noticeable in the previous figures. In the case of Figure 6.6, the tones are identified by red stars, while the LO leakage is marked with a black square. The inset on the right shows the spectrum in detail around a tone at $f_{tone} \approx 6.703$ GHz. The small tone located to the right of the main tone corresponds to one of the images produced by the IQ imbalance.

In contrast, the results shown in Figure 6.7 demonstrate that although the Mixer-less SDR does not present an output power ≈ 3 dB lower than the Mixer-based SDR, it does not suffer from the drawbacks of analog IQ mixing. This represents an advantage as it does not require any calibration, unless tone power equalization is needed.

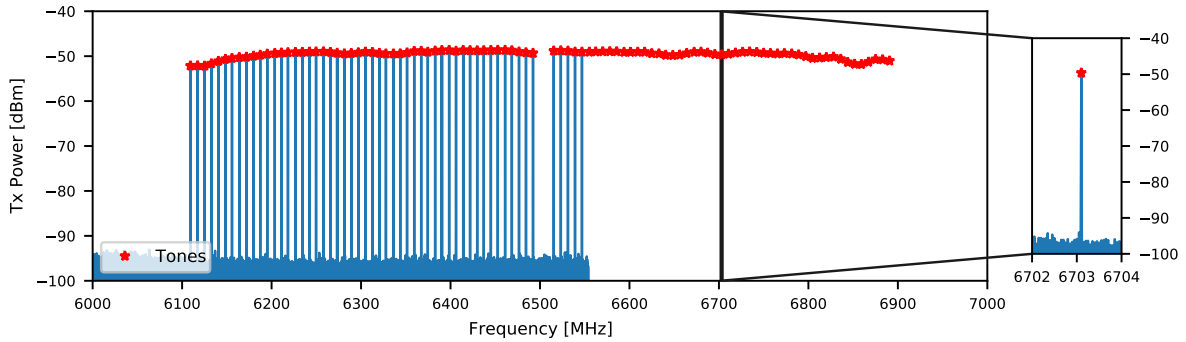

Figure 6.7: $N = 100$ tones centered at $f_{NCO} = 6.5$ GHz generated by the Mixer-Less SDR prototype.

The previous measurements were repeated by generating a number of tones $N = 1, 2, 4, 8, 16, 32, 64, 100$, and the power of the generated tones was measured. In all cases, the maximum amplitude was adjusted to satisfy $P_{peak} = -5$ dBFS. Figure 6.9 shows the power of a tone, P_{tone}, located at $f_{tone} \approx 6.55$ GHz as a function of the number of generated tones, N. These results follow from Equation 6.1. A fitting of the results reflects a $PAPR(N) \approx 5 \cdot \log_{10}(N)$, which is consistent with the experimental results and previous simulations [105, 169]. The small variations in the measurements are due to the fact that the $PAPR$ in the case of random initial phases is a random variable, and the results shown in the figure represent an average of different realizations. This value of $PAPR(N)$ will be used in later chapters to estimate the readout power, $P_{exc}(N)$.

In the following Section 6.3, the phase and amplitude noise of the tones generated by the SDR prototypes will be characterized. In addition to the power reduction between the different

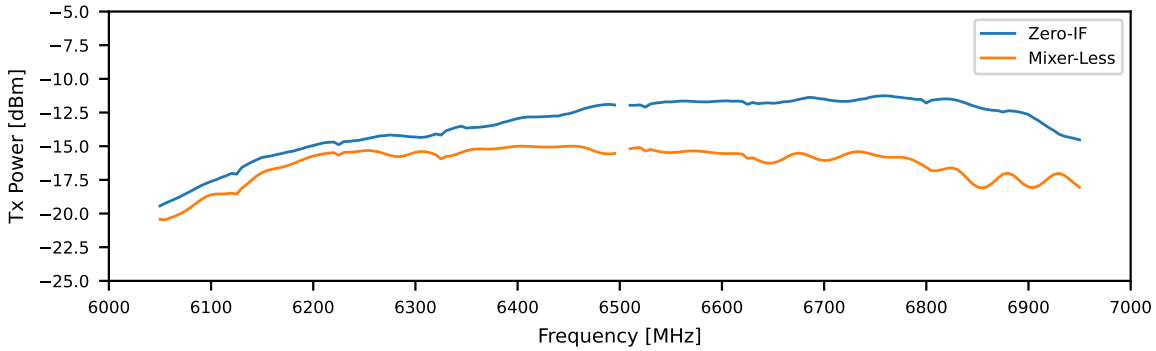

Figure 6.8: Measured transmitted power over a bandwidth of 900 MHz and centered at $f_c = 6.5$ GHz for both SDR prototypes. The tone was generated at a constant power of $P_{tone} = -1$ dBFs.

bands, Figures 6.6 and 6.7 show that there is a reduction in the power of the tones at the band edges compared to the center. In the case of the Zero-IF SDR, this is due to the combination of the DAC response (see appendix C), the filters, and cables connecting the XM655 with the Mixing Boards, as well as the response of the IQ modulator. For the Mixer-less SDR, this is primarily due to the response of the interpolating filters and the baluns of the XM655. Since the noise is dependent on the power of each tone, the correct characterization of the noise requires evaluating both prototypes at the same output power, P_{Tx}. To achieve this, a power calibration was performed, which allows setting a known power level exactly at the transmission (Tx) port at the desired frequency. The calibration process consisted of performing a frequency sweep over a bandwidth of 900 MHz centered around $f_c = 6.5$ GHz and measuring the power for each frequency. The sweep was performed with a single tone at $P_{tone} = -1$ dBFS and in steps of $\Delta f_{tone} = 5$ MHz, which is sufficient to compensate for the ripples present in the band. The difference between the measured power and the set power, $P_{Tx} - P_{tone}$, is used in a subsequent step to obtain the desired power.

It is important to note that since these signals will be transmitted to the receiver (Tx-Rx loop-back), the interfering components must be removed. In the case of the Zero-IF, the filtering of these components is done in the Mixing-Board, while in the Mixer-less system, it is achieved by including two band-pass filters, *Minicircuits VBFZ-5500-S+*. These filters shown in Figure 6.5 provide more than 50 dB of rejection for the lower replica located at $f_{inf} = 1.5$ GHz and more than 80 dB for the upper replica located at $f_{inf} = 9.5$ GHz. The previous calibration process included one of these filters between the transmitter and the spectrum analyzer.

Similar to spurious signals, the image tones produced by IQ imbalances will be acquired and cannot be separated from the desired signals. Moreover, due to their power, they can combine with other tones to produce additional inter-modulation products beyond those generated by the interrogation tones. To prevent the images from being acquired in the Zero-IF SDR, IQ imbalance calibration was performed. After power calibration, N equalized tones were generated. The spectrum was acquired, and a script was used to calculate the power of the tones and their images. In an iterative process, amplitude and phase imbalances were applied to the IQ components of each tone while measuring the Image-Rejection Ratio (IMRR) for each tone. The iterative process was completed once $IMRR > 50$ dB was achieved [170]. More details on the IQ calibration process can be found in Appendix E.

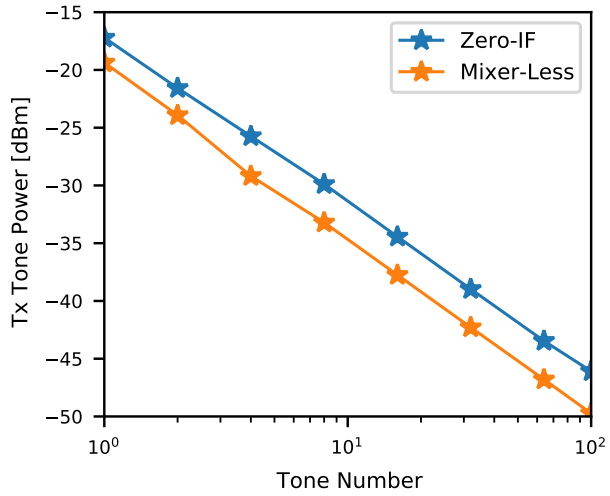

Figure 6.9: Measured transmitted tone power P_{tone} as a function of the number of tones N for both SDR prototypes. The tones generation were generated with Random Phases and the measurements were taken using a center frequency of $f_c = 6.5$ GHz considering a $P_{peak} = -5$ dBFs.

6.2.2 Sampling Clock Characterization

As seen earlier, the generation of a large number of tones leads to the creation of a vast amount of spurious signals. These are generated both by the DACs and the RF components. Although they may have powers of $\sim$ 60 dBc, they are frequency-localized, which allows them to be identified and avoided through proper modulation frequency selection, as mentioned in Section 4.2.2 [106]. This is not the case for multiplicative noise, both in the phase and amplitude of the readout tones, reflecting the need to include it within the simulation frameworks presented in Chapter 4. The main source of multiplicative noise in SDR systems comes from the direct transfer of phase noise from the sampling clock of the converter to the generated/acquired tones. In the case of a DAC with a clock at f_{CLK} and phase noise $S_\phi^{CLK}(f)$, the phase noise $S_\phi^{sig}(f)$ of a signal generated at f_{sig} is related to the phase noise of the clock $S_\phi^{CLK}(f)$ through the following expression [171]

$$S_\phi^{sig}(f) = S_\phi^{CLK}(f) + 20\log_{10}\left(\frac{f_{sig}}{f_{CLK}}\right), \tag{6.2}$$

where S_ϕ is expressed in logarithmic units. This expression highlights the importance of selecting the required clock for the converters. For the case of Zero-IF, the relation $f_{sig}/f_{CLK} < 1/2$ provides an improvement greater than 6 dB. In contrast, for the Mixer-Less case, $1/2 < f_{sig}/f_{CLK} < 1$, the improvement is less than 6 dB. Although the *CLK104* was equipped with low phase noise synthesizers, it must be characterized to verify its performance and be optimized for the required application. To do this, one of the outputs of the *CLK104* was connected to the *R&S FSWP 50* instrument. This instrument is not only a spectrum analyzer but also an excellent phase noise analyzer [166]. Once connected, each of the clocks required by the prototypes (i.e., 1, 2, and 8 GHz) was configured, and their phase noise $S_\phi(f)$ was measured. The results of the phase noise measurements are presented in Figure 6.10. The green-shaded region represents the frequency range where the flux-ramp modulation may be located, and in which the phase noise of the clock was optimized.

For the generation of $f_s = 1$ GHz, the standard configuration of the *CLK104* was used, where the *LMK04828B* provides a reference signal of $f_{REF} = 250$ MHz, and within the *LMX2594*, this reference signal is divided by 10 to feed the phase detector with a signal of $f_{PD} = 25$ MHz. In the case of the clocks at $f_s = 2$ GHz and $f_s = 8$ GHz, the phase detector frequency was increased to $f_{PD} = 250$ MHz to reduce the phase noise within the green region. Increasing the phase detector frequency was not a trivial decision. The phase noise in a PLL is determined by the noise added by each of its components and the external reference. For

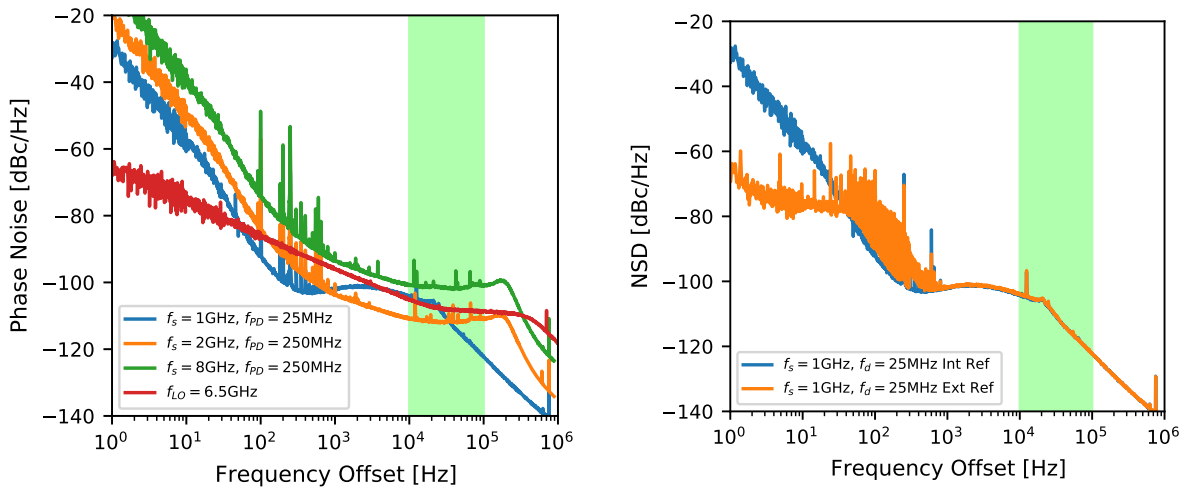

Figure 6.10: Left) Phase noise measured at each of the clock signals used in the SDR prototypes. **Right)** Phase noise measured at the $f_s = 1$ GHz clock with and without the use of the external reference to the CLK104. The shaded region in green represents the possible flux-ramp modulation frequencies spectral location.

the frequencies used, the noise in the shaded region is dominated by the noise produced by the Voltage Controlled Oscillator (VCO) and the closed-loop transfer of the PLL. Since it was decided not to make hardware modifications to the *CLK104*, the loop transfer was modified by changing the frequency of the phase detector. This change modifies the transfer coefficient of the phase detector, and consequently increases the bandwidth of the filter and reduces the closed-loop gain, attenuating the VCO component noise component. This modification can be seen in Figure 6.10 by comparing the phase noise profile plotted in blue with the others. Although this optimization can also be applied to the case of $f_s = 1$ GHz, the phase noise values are acceptable for the relations $f_{sig}/f_{CLK} < 1/2$, so f_{PD} was not modified.

Another of the presented tests aimed at evaluating the behavior of the *CLK104* when using an external reference. On the right side of Figure 6.10, the measurement result is shown using an external reference at $f_{EXT} = 10$ MHz provided by an*ERASynth+*[2] synthesizer from *ERA Instruments*, compared to using the internal TXCO. While an external reference provides better frequency accuracy and lower phase noise at low frequency offsets (e.g., *FS725* [160]), which is important for MKIDs or Open-Loop readout (see Section 4.3.1), it does not influence the phase noise at the frequencies of interest when using FRM, as seen in Section 4.3.2. We reiterate that this is due to the fact that the VCO dominates over the other sources of noise. To better understand these concepts, you can refer to D, where the operation and sources of phase noise in a PLL are detailed. Future tests include modifying the hardware of the *CLK104* as well as its configuration parameters to further optimize the phase noise profile. This would involve the joint optimization of the *LMK04828B* and both *LMX2594* using an external reference.

In addition to the sampling clock, the phase noise of the local oscillators of the Mixing Board was also characterized. This phase noise can be transferred to the tones during the mixing process. Since two local oscillators are used, the effect of both has to be characterized simultaneously. To achieve this, the Mixing Board was configured to generate a $f_{LO} = 6.5$ GHz, and the tone produced by the LO leakage was measured at the transmission (Tx) port (see Appendix E) with tone generation disabled. While this tone does not have high power, it is sufficient to measure phase noise values at the frequencies of interest. The result of this

[2] https://raw.githubusercontent.com/erainstruments/erasynth-docs/master/erasynth-datasheet.pdf

measurement is shown in red in Figure 6.10. In this case, no phase noise profile optimization was made, as the values were already optimized for the application, and the results were already shown in [162]. It should be noted that in this case, the *CLK104* was used as the external reference for the Mixing Board.

6.3 Signal Acquisition Characterization

In the previous section, the characteristics of the frequency combs generated by both prototypes were determined. Some of these characteristics include power, spurious levels, and phase noise levels given the sampling clock signals. This ensures the quality of the signal for interrogating the µMUX, as well as for characterizing the reception path of our SDR systems. To achieve this, a direct connection was made between the transmitter and receiver (Tx-Rx) of the SDR, also known as the RF loopback. This configuration can be observed in the diagrams of Figures 6.2 and 6.3. Next, we will characterize the prototype's ability to perform the channelization of the different channels. Later, we will determine the additive and multiplicative noise levels of a single tone.

6.3.1 Frequency Comb Channelization

As detailed in the previous section, a frequency comb of $N = 100$ tones with random frequencies was generated with each of the prototypes, and its power was equalized at the transmitter level to achieve a tone power of $P_{tone} \approx -45$ dBm. These initial measurements were conducted with the aim of verifying the operation of the prototypes and their ability to channel the signals.

In order to do this, using the firmware from Figure 5.6, $N_s = 2^{19}$ samples of the signal from each channel $x(t) = x_I(t) + x_Q(t)$ were acquired, and its spectrum $S_x(f)$ was computed. Prior to being acquired, they were channelized by the PFB and down-converted to baseband by the Multi-channel DDC. The results in Figure 6.11 show the spectrum of the $N = 100$ channelized tones for the Zero-IF prototype case. The center of the horizontal axis (x) corresponds to the frequency $f_{LO} = f_{NCO} = 6.5$ GHz. As can be seen, each color represents a channel from the PFB explained in Section 5.3.2 and depicted in Figure 5.9. This figure does not include the other channels covering the blind bands. The vertical axis (y) in Figure 5.6 is normalized with respect to the ADC full-scale power and shows a maximum power of ≈ -37 dBFs.

Considering that the received tones have the same $PAPR$ as the generated ones, the peak power of the tones $P_{peak} = P_{tone} + PAPR(100) + 10\log_{10}(100)$ yields a value of $P_{peak} \approx -7$ dBFs. This confirms the correct reception without clipping, given the adequate margin of $M = 7$ dB with respect to full scale, as verified during the characterization of the ADCs presented in Appendix C. Even so, spurious signals are observed near each tone, which originate from the combination of spurious signals and image tones generated by imperfections in the IQ demodulator. As in transmission, a reduction in power at the edges of the band is also observed, caused by analog components between the IQ demodulator and the ADCs.

The same procedure described previously was repeated for the Mixer-less prototype. The spectrum of the tones acquired by the Mixer-less prototype is shown in Figure 6.12. The received power values are similar to the previous case, with values of ≈ -38 dBFs, representing a margin of $M = 7$ dB. This is due to the inclusion of the LNA *ZX60-83LN12+*, which provides a gain of $G \approx 20$ dB at $f \approx 6.5$ GHz. The need for this amplifier was determined during the characterization process due to the high attenuation at those frequencies when using bandpass sampling. This characterization is detailed in Appendix C. In contrast to the Zero-IF SDR, the spectral density and level of spurious signals is much lower due to the absence of IQ imbalances. This can be attributed to the higher linearity of the reception chain, given the reduced number of active components compared to the Zero-IF SDR. Nevertheless, this

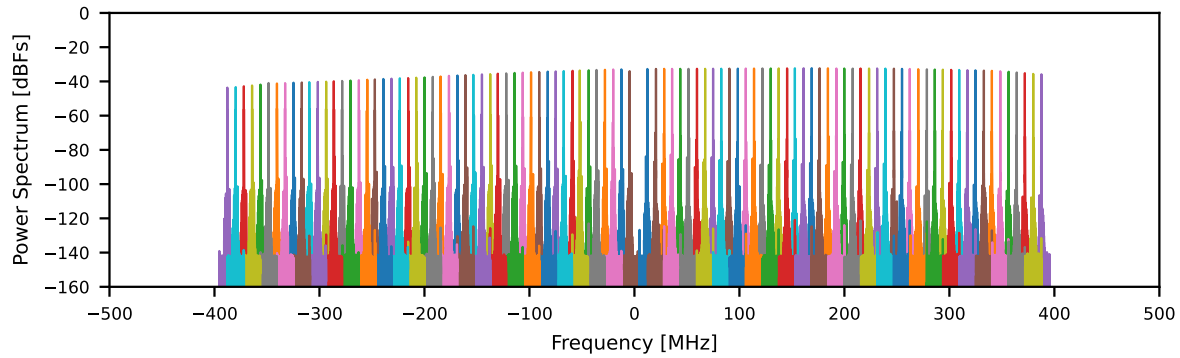

Figure 6.11: $N = 100$ tones centered at $f_{LO} = 6.5$ GHz acquired and channelized by the Zero-IF SDR prototype. The tones were generated by the Zero-IF SDR at a constant power of $P_{tone} = -45$ dBm.

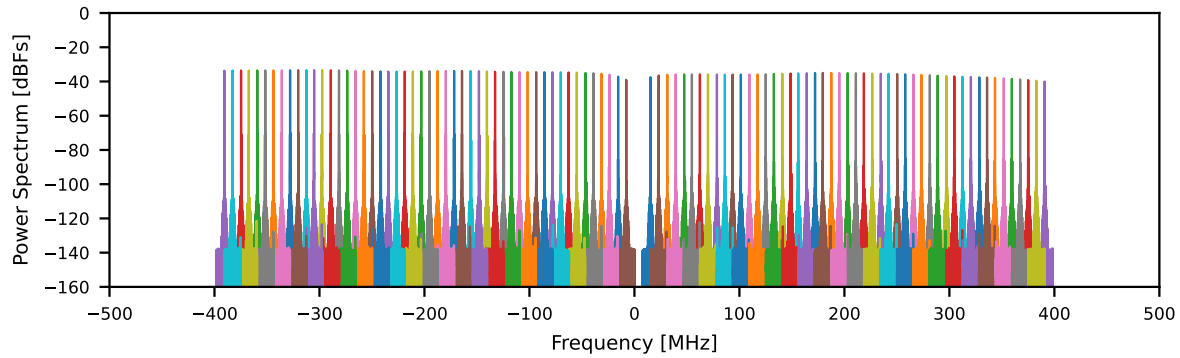

Figure 6.12: $N = 100$ tones centered at $f_{NCO} = 6.5$ GHz acquired and channelized by the Mixer-Less SDR prototype. The tones were generated by the Mixer-Less SDR at a constant power of $P_{tone} = -45$ dBm.

characteristic will be evaluated in detail in future work.

Before proceeding with the noise characterization, two important aspects of Figures 6.11 and 6.12 should not go unnoticed. The first is to note the small spurious signals at the bottom of each spectrum, aligned with the neighboring tone. These spurious signals are produced by the neighboring channel, which cannot be completely eliminated by the channelizer. However, these values correspond to the stopband attenuation > 80 of the PFB (see Figure 5.8). The second aspect to note is the slope in the tone power. This is introduced by the frequency response of the analog components of the receiver and the decimation filters of the RFDC. Although it can be compensated, this slope does not have a direct effect on noise reduction, as it is applied at the end of the chain where both signal and noise are affected, without representing a gain in the signal-to-noise ratio (SNR). Therefore, it should be reduced through hardware design optimization.

6.3.2 SDR System Noise Characterization

The readout simulation model of the µMUX, described in Section 4.1, takes as input the additive and multiplicative noise parameters of the readout system and uses them to determine the flux noise level at the SQUID. These noise parameters must be determined beforehand through the characterization of the readout system. While the readout system consists of the SDR system and the cryogenic microwave chain, we begin by determining the noise param-

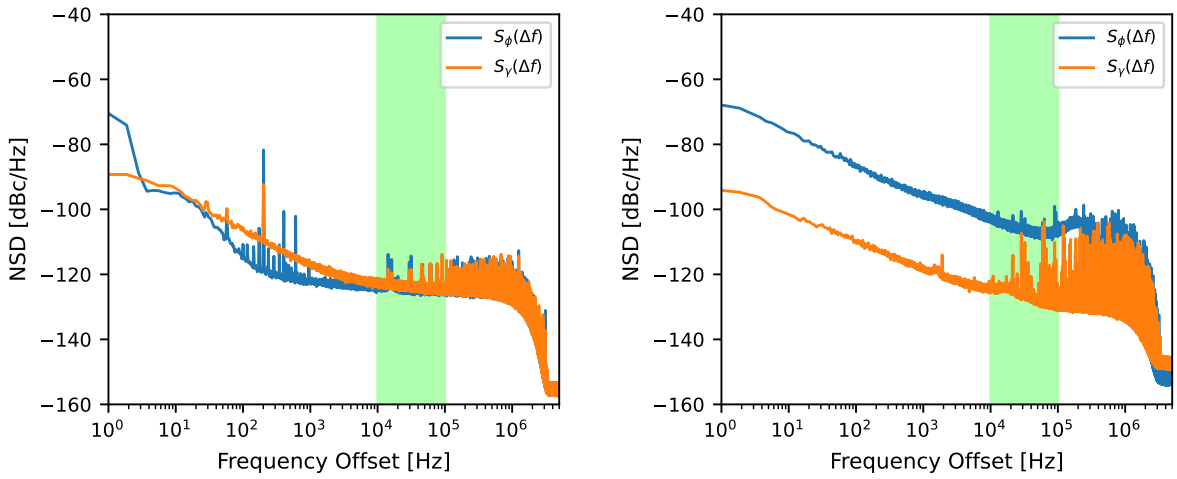

Figure 6.13: Right:) Tx-Rx Loopback phase and amplitude noise spectra for the Zero-IF SDR Prototype System. **Left)** Tx-Rx Loopback phase and amplitude noise spectra for the Mixer-Less SDR Prototype System. Both measurements were performed at $f_{\text{exc}} \approx 6.4$ GHz and $P_{Tx} \approx -25$ dBm.

eters of the SDR systems in loop-back configuration. The individual characterization of the cryogenic microwave chain and the SDR system allows minimizing the contribution of each component in the noise temperature budget shown in Figure 4.22.

For the characterization of the additive and multiplicative noise of the SDR systems, the setups shown in Figures 6.2 and 6.3 were used again, employing the Tx-Rx loopback. The characterization was carried out at a single frequency of $f_{\text{exc}} \approx 6.4$ GHz, which coincides with the location of one of the available μMUX channels and it will be characterized in the following chapter.

The measurement process consists of generating a single tone at a frequency of $f_{\text{exc}} \approx 6.4$ GHz with a known power P_{Tx} at the Transmitter (Tx) output. This tone was channelized, down-converted to base-band, and acquired. Using the probing tone complex envelope $x(t) = x_I(t) + jx_Q(t)$, the readout phase $\phi(t) = \arctan(x_Q(t)/x_I(t))$ and amplitude $\gamma(t) = |x_I(t) + jx_Q(t)|$ time traces were computed. By means of Python scripts, $N_s = 2^{24}$ samples were used to calculate the readout system phase $S_\phi^{\text{meas}}(f)$ and amplitude $S_\gamma^{\text{meas}}(\Delta f)$ noise spectra. In order to avoid spectral leakage, a Blackman–Harris window was applied, achieving a spectral resolution of around ≈ 1 Hz. To reduce the variance in the spectrum estimation, $M = 100$ spectra were averaged. The resulting readout phase $S_\phi^{\text{meas}}(\Delta f)$ and amplitude $S_\gamma^{\text{meas}}(\Delta f)$ noise spectra for a transmitted power of $P_{Tx} \approx -25$ dBm are shown in Figure 6.13. The left-side plot corresponds to the Zero-IF SDR, while the right-side plot corresponds to the Mixer-Less SDR. As in previous figures, the green region represents the region of possible modulation frequencies f_{mod}. The samples were acquired at a rate of $f_s = 15.625$ MHz, so the maximum frequency represented is 7.8125 MHz.

At frequencies below 10 kHz, both prototypes show a frequency dependency described by the power law presented in 4.8. The phase noise shows trends of -10 dB/dec and -20 dB/dec for the Zero-IF and the Mixer-Less prototypes, while in the case of amplitude noise, both show -20 dB/dec. At frequencies between 10 kHz and 100 kHz (green region), there is a plateau in which both noise parameters are constant but present different noise levels for both prototypes. Finally, the roll-off observed at higher frequencies is consistent with the cutoff frequency of the low-pass filter used in the DDC, which is $f_{\text{cut}} \approx 1.6$ MHz.

From the previous figures, it is not possible to fully identify the sources of additive and

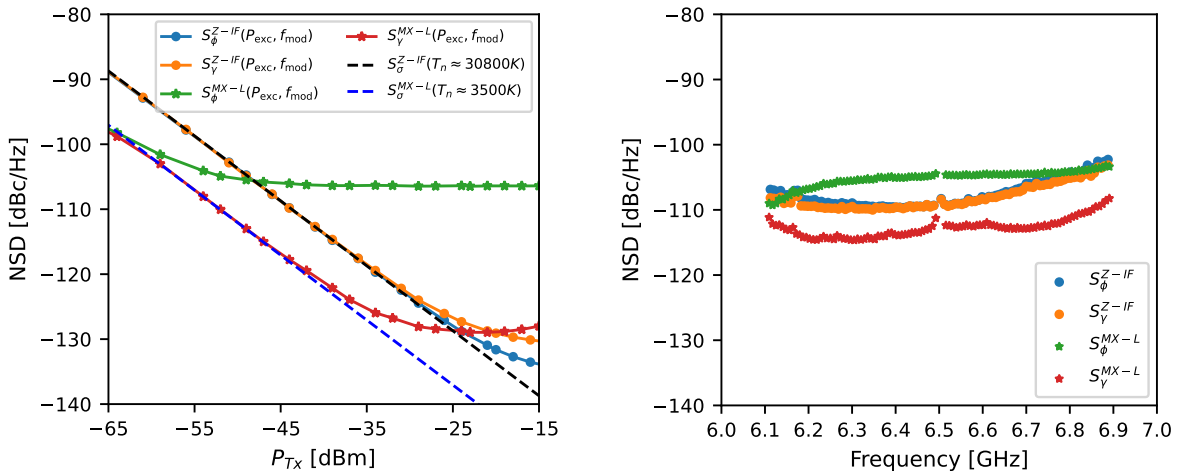

Figure 6.14: Phase and amplitude noise measured in Tx-Rx Loop-back configuration for both SDR prototype Systems. **Left:)** Phase and amplitude noise as a function of power for a tone at $f_{exc} \approx 6.4$ GHz. $S_\phi^{Z-IF}(P_{Tx}, f_{\text{mod}})$ and $S_\gamma^{Z-IF}(P_{Tx}, f_{\text{mod}})$ correspond to the Zero-IF prototype, while $S_\phi^{MX-L}(P_{Tx}, f_{\text{mod}})$ and $S_\gamma^{MX-L}(P_{Tx}, f_{\text{mod}})$ to the Mixer-Less prototype. **Right)** Phase and amplitude noise measured with both prototypes for the frequency combs shown in figures 6.11 and 6.12.

multiplicative noise. Equivalently to equation 4.1 with $S_{21} \approx 1$ (i.e., Tx-Rx loopback), additive and multiplicative noise are measured simultaneously and cannot be distinguished. This is because the additive noise (orange noise cloud in Figure 4.2) can also be interpreted as simultaneous variations in phase and amplitude. In this case, the readout phase $S_\phi^{\text{meas}}(f)$ and amplitude $S_\gamma^{\text{meas}}(f)$ measured spectra consist of the two contributions and can be expressed as

$$S_\phi^{\text{meas}}(\Delta f) = S_\phi(\Delta f) + \frac{k_B T_n^{Tx-Rx}}{P_{Tx}}, \tag{6.3}$$

$$S_\gamma^{\text{meas}}(\Delta f) = S_\gamma(\Delta f) + \frac{k_B T_n^{Tx-Rx}}{P_{Tx}}. \tag{6.4}$$

Here, P_{Tx} is the transmitted power and T_n^{Tx-Rx} is the ADC additive noise temperature referred to the transmitter output (Tx). The terms on the left side of equations 6.3 and 6.4 are the pure multiplicative spectra, while the additives are on the right side. In order to extract the pure multiplicative phase and amplitude noise levels, a power sweep was performed until the dependence on power vanishes (i.e., $S_\phi^{\text{meas}}(\Delta f) \approx S_\phi(\Delta f)$ and $S_\gamma^{\text{meas}}(f) \approx S_\gamma(f)$ [101]. The power sweep was performed by modifying the DAC output power, P_{DAC}. Although it would be preferred to work at full scale of the DAC to avoid quantization noise [138], modifying the DAC power is equivalent to what happens when generating a comb of N frequencies, where each tone decreases its power as N increases. This fact will be used later in conjunction with equation 6.1 to calculate the flux noise for different numbers of tones $\sqrt{S_\Phi(N)}$. The result of these measurements is shown in Figure 6.14. Since we are interested in the values taken by the additive and multiplicative noise in the region of possible modulation frequencies, f_{mod}, the phase and amplitude noise values were averaged within this window. The results of the power sweep are shown on the right side of Figure 6.14. $S_\phi^{Z-IF}(P_{Tx}, f_{\text{mod}})$ and $S_\gamma^{Z-IF}(P_{Tx}, f_{\text{mod}})$ correspond to the phase and amplitude noise for the Zero-IF SDR, while $S_\phi^{MX-L}(P_{Tx}, f_{\text{mod}})$ and $S_\gamma^{MX-L}(P_{Tx}, f_{\text{mod}})$ correspond to the Mixer-Less SDR.

At lower powers, both phase and amplitude spectra are dominated by the additive noise, following the trajectory indicated by the straight dashed blue and black lines. On the contrary, at high powers, phase and amplitude noise densities are dominated by the multiplicative noise and reach a constant value. As a result, the true phase S_ϕ and amplitude S_γ multiplicative noise values obtained from the measurement are listed in Table 6.1 for both prototypes. These values are similar to those used in the example shown in Section 5.1, with the difference that they reflect the average in the desired frequency region. Interestingly, the results show a higher phase noise for the Mixer-Less SDR system compared to the Zero-IF SDR. These results are consistent with those obtained in the characterization of the sampling clocks shown in Figure 6.10, and are dominated by the VCO of the *LMX2594*. Several factors contribute to amplitude noise, such as spurious signals inherent to the NCOs [138], fluctuations in temperature, and supply voltages of the circuits. The latter factor is also associated with the appearance of peaks in the spectrum, typically at 50 Hz or at frequencies related to the DC-DC converters [171].

It is important to highlight that the noise measured by the system in Loop-back is also specifically referred to as *Residual Noise*. This name is based on the ability of some RF systems to remove the phase noise they themselves introduce by using locally coherent oscillators and clocks (e.g., locked to the same frequency reference). In this way, they can introduce and remove noise during the up/down conversion or signal generation/acquisition processes. The measured phase noise is the "Residual" noise from these processes and depends on the coherence level [107, 109]. We base our justification for the observed noise reduction in the Zero-IF SDR, as compared to the Mixer-Less SDR. The symmetric scheme of frequency generation and conversion using the same frequencies has a higher coherence degree than using two different frequencies for generation and acquisition.

Additionally, this procedure allows us to determine the additive noise level from the linear trend given by the blue and black dashed lines in Figure 6.14. These lines correspond to equation 4.7 expressed in logarithmic units and were fitted to the data where P_{Tx} is the independent variable. The fitting parameters yielded the additive noise temperatures listed in Table 6.1. In the case of the Zero-IF SDR, the result yielded $T_n^{Tx-Rx} = 30800$ K, while for the Mixer-Less SDR, $T_n^{Tx-Rx} = 3500$ K.

Table 6.1: Summary of the additive and multiplicative noise levels for both Single-Band RFSoC-Based SDR prototype systems measured in Tx-Rx loop-back. Multiplicative noise is the average value within the range between 10 kHz and 100 kHz representing the possible location of the modulation frequency f_{mod}

Noise Parameter	Zero-IF SDR Prototype	Mixer-Less SDR Prototype
T_n^{Tx-Rx}	30800 K	3500 K
$S_\phi(f_{\text{mod}})$	-131 dBc/Hz	-105 dBc/Hz
$S_\gamma(f_{\text{mod}})$	-134 dBc/Hz	-129 dBc/Hz

These noise temperature values allow for a comparison of the performance of both systems and determine that the Mixer-Less SDR system shows much lower additive noise values than the Zero-IF SDR. As seen in Chapter 4, additive noise dominates over multiplicative noise and must be minimized. Although the difference between the noise temperatures of both systems is on the order of ~ 10, it cannot be stated that the same difference exists in the total noise temperature when the system is integrated into the cryogenic microwave chain. This is because the temperature measured in Tx-Rx loopback is the sum of the equivalent noise temperatures of the transmitter T_n^{Tx} and the receiver T_n^{Rx} (i.e. $T_n^{Tx-Rx} = T_n^{Tx} + T_n^{Rx}$). Therefore, according to equation 4.29, the total noise temperature of the system referred to the output port of the µMUX is calculated by,

$$T_n^{tot} = T_n^{Tx} G_{Tx} + T_n^{cryo} + T_n^{Rx} / G_{Rx} \tag{6.5}$$

Where G_{Tx} and G_{Rx} are the transmission and reception path gains, respectively, and T_n^{cryo} is the equivalent noise temperature of the cryogenic microwave chain shown in Figure 4.20, with measured values presented in Figure 4.24. Determining each of the individual noise contributions would require additional tests, which would need a calibrated noise source [131]. Since these instruments are not available in the laboratory, in the following chapter, we will limit ourselves to finding the total noise temperature by integrating the SDR with the cryogenic microwave chain.

The values obtained previously are valid for a single frequency, and their variation across the operating band must be verified. As an example, phase and amplitude noise values were measured for all the channels present in Figures 6.11 and 6.12. The results are shown on the right side of Figure 6.14. As seen, the values for both prototypes are close to those calculated earlier, except for the values near both ends of the band. The causes of this variation include the frequency-dependent attenuation shown in Figures 6.11 and 6.12, as well as the variation in phase noise given by equation 6.2. An additional factor that could also contribute to differences between both results is the inclusion of inter-modulation products created by the frequency comb. Unlike the results with a single tone, the frequency comb creates a pseudo-random noise which increases the measured noise value over the band of interest. Nevertheless, these values show uniform performance across the band for both prototypes.

In the following chapter, we will evaluate the noise performance of the SDR system integrated into the cryogenic microwave chain. We will then demonstrate the readout of a single µMUX channel in order to assess the performance of both prototypes in a real measurement. These results will be extrapolated to the case of N channels to verify the feasibility of using the SDR prototypes for the readout of MMBs.

7. Readout Demonstration of a Microwave SQUID Multiplexer

The noise performance of the bolometric detection system is determined by the performance of the detectors and the multiplexing and readout systems. For this reason, in Chapter 2 we presented the noise budget of the proposed detectors (i.e., MMBs), and from the total detector noise, an upper bound for the noise of the readout and multiplexing system is defined. One of the objectives of this thesis is to determine if the RFsoc-Based SDR prototypes, along with the previously presented cryogenic microwave chain, meet this condition. The simulation framework presented in Chapter 4 aims to answer this question by estimating the noise level from the design parameters of the μMUX and the noise characterization results of the readout system. It also aims to determine the optimal parameters and readout domain that minimize the demodulated noise.

Although the results obtained are consistent with theoretical calculations and experimental results found in the literature [102, 92], there is no detailed readout demonstration of a μMUX that can be directly compared with the obtained simulation results[101]. Thus, this chapter will complete the noise characterization of the readout system and provide the experimental demonstration of readout a μMUX channel.

In Section 7.1, the experimental setup used for the readout demonstration of a μMUX and the determination of the system's noise performance is presented. Then, in Section 7.2, the characterization process of a μMUX channel is described in order to obtain the optimal readout parameters. Later, in Section 7.3, the readout noise parameters is determined, including the SDR prototype systems and the cryogenic chain. Finally, in Section 7.4, the demodulated flux noise measurement is carried out using various readout parameters, and the results are compared with those from Chapter 4 to verify their validity. These results will later be used to estimate the expected performance of the proposed readout and multiplexing system for the QUBIC project upgrade using MMBs.

7.1 Experimental Set-Up

The experimental demonstration of the readout of a μMUX was carried out in the cryogenics laboratory of *ITeDA* at the *Centro Atómico Constituyentes*. The complete experimental setup is shown in Figure 7.1. In the right, the *LD250* dilution cryostat is shown, which contains the cryogenic microwave chain shown in Figure 4.20. On the left side of Figure 7.1, there are two racks housing all the characterization instruments along with the SDR readout systems. The electrical connections to the cryostat are made through coaxial cables or twisted pairs, which are accessible from the racks either via the SMA connector panel or the DC Breakout box. Additionally, extra lines are also accessible through the top flange of the cryostat. The most important components of the readout system, essential for the development of this work, are

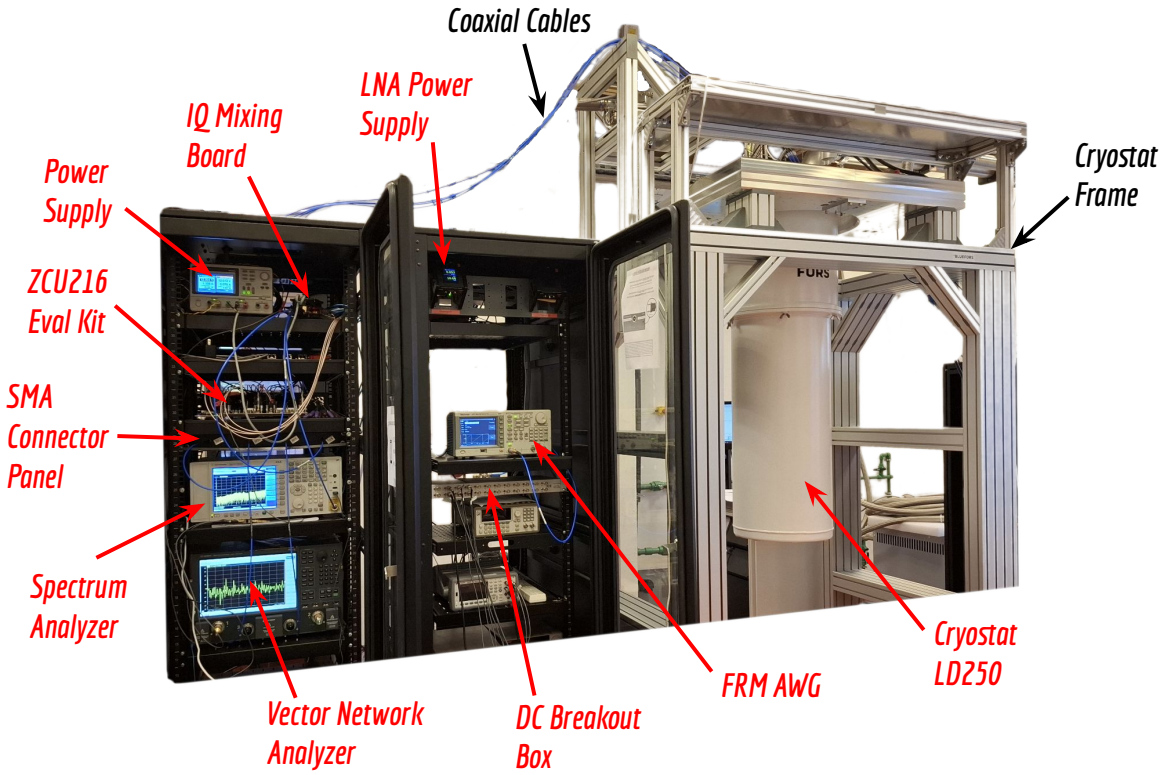

Figure 7.1: Hardware set-up for the readout of cryogenic detectors. The racks on the left side houses the SDR and Microwave Instruments. The Microwave SQUID Multiplexer is placed inside the dilution refrigerator shown on the left side.

the SDR, which includes the *ZCU216* evaluation kit and the Single-Band IQ mixing board, the Arbitrary Waveform Generator (AWG), the power supplies for both the cryogenic LNAs and the SDR, the Vector Network Analyzer (VNA), and the Spectrum Analyzer (SA).

The proposed upgrade for the QUBIC project requires that the detectors and the multiplexing system be cooled to temperatures below 300 mK [42]. To achieve this, it is necessary to mount the devices on the coldest stage of the cryostat (MXC flange), ensuring good thermal contact between the device and the associated flange. This is done using a copper sample holder, which also provides mechanical support for the device. At the same time, it adapts the electrical interfaces to allow the chip to connect with the available coaxial lines and TPW. Figure 7.2 shows the details of the sample holder used. It consists of a machined copper block, with two attached printed circuit boards (PCBs) and the chips under test. The upper PCB (RF PCB) handles the transmission of radio frequency signals and facilitates the transition from coaxial (SMA connectors) to planar (CPW) transmission. It is designed using high-frequency techniques and controlled dielectric substrates to ensure proper impedance matching between the chip and the PCB. In contrast, the lower PCB is used to provide polarization and flux modulation signals (DC and FRM PCB). Since it only carries low-frequency signals, it is made from traditional substrates. It includes pads for soldering the cables that will be used for the connections. Particularly, this sample holder and μMUX prototype were designed and manufactured by several colleagues at the *Institute of Micro- and Nanoelectronic Systems* (IMS).

It is worth noting that the sample holder has a copper cover, which allows the devices to be enclosed and provides proper shielding to ensure electromagnetic compatibility, as well as protecting the device from external electric fields. Once the sample holder was covered, it was properly screwed onto the MXC flange, and the electrical connections were made. After

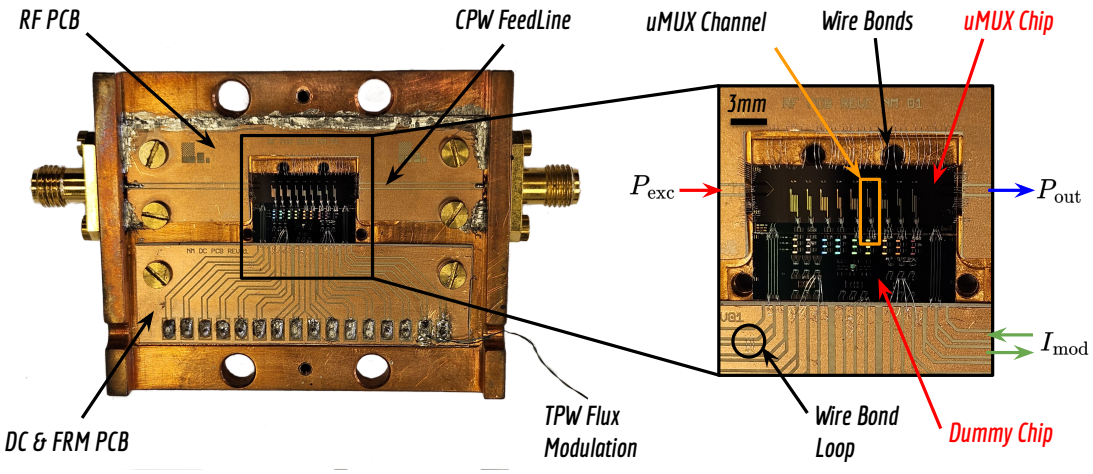

Figure 7.2: µMUX Chip Mounting Details in a Sample Holder. The µMUX is mounted over a Cooper Sample holder and glued with rubber cement. The CPW lines of RF PCB are connected to the µMUX feedline using Al Wire bounds and accessed using SMA connectors. The Flux-Ramp signals are injected using a TWP cable connected to the FRM board using the lines on the left.

verifying the mounting of the devices to the microwave chain shown in Figure 4.20, all the cryostat vessels were placed, and the system was powered on. Once the base temperature was reached, the Proportional-Integral-Derivative (PID) temperature control was activated to ensure temperature stability during the measurements. For the measurements carried out in this chapter, a base temperature of $T_{\text{base}} = 100$ mK was selected.

After verifying the proper functioning of the μMUX using the VNA, the SDR was connected to the cryogenic chain. The connection diagram used for the characterization and reading of the μMUX with the Zero-IF prototype is shown in Figure 7.3. In this setup, the Zero-IF SDR is connected to the microwave chain via the transmission and reception ports using a pair of coaxial cables. For simplicity, only a single μMUX channel is depicted, and the various stages of the cryostat are omitted. Since the FRM Board is still under development, an Arbitrary Waveform Generator (AWG) from *Tektronix*, model *AFG3021B*, was used to generate the required flux modulation. Both the Mixing Board and the AWG were frequency-synchronized with the SDR using the external output from the *CLK104* and a power splitter. The modulation scheme used for the μMUX employs a differential line to inject the modulation current I_{mod}, while the AWG is a voltage generator with a single-ended output. To convert from voltage to current and from single-ended to differential, a resistive divider was designed, providing a voltage-to-current conversion of $G_{VI} \approx 4950$ µA/V. This divider was connected to an Unshielded Twisted Pair (UTP) cable and then to the TWP line mounted in the cryostat. Considering a modulation mutual inductance of $M_{\text{mod}} \sim 10$ pH (see Table 3.1), the current required to generate Φ_0 is approximately $I_0 = \Phi_0 / M_{\text{mod}} \sim 200$ µA. Therefore, the AWG must be capable of generating $V_0 = I_0 / G_{VI} \sim 100$ mV. Since this value is close to the AWG's resolution limits, a 10 dB attenuator (voltage attenuation) was added to increase the generator's amplitude, allowing it to operate at higher amplitudes with a considerable margin over the noise floor. This attenuator results in a final conversion factor of $G_{VI} \approx 495$ µA/V. Additionally, to eliminate high-frequency noise and spurious signals, a low-pass filter from *Minicircuits*, model *SLP-1.9+*, was added, with a cutoff frequency of $f_c \approx 2$ MHz.

Unlike the noise from the SDR, the noise present in the flux modulation directly couples into the SQUID at the same frequency range as the detector signal. In order to determine an upper bound for the modulation noise, the characterization of the AWG was performed in

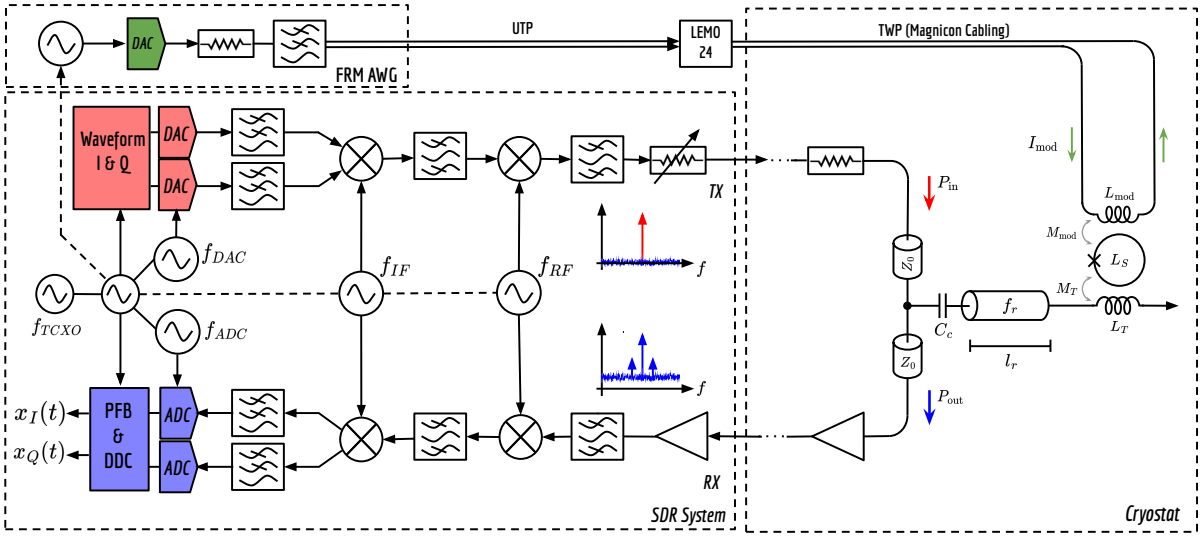

Figure 7.3: Diagram of the µMUX channel characterization using the Zero-IF SDR prototype system. The AWG is used in order to generate the flux modulation. It is frequency locked to the SDR frequency reference and connected to the µMUX modulation line through a twisted-pair cable. A set of attenuators and filters are used in order to increase the AWG's noise performance.

conjunction with the attenuator and filter. Given the low frequencies involved ($f < 1$ MHz) and the noise levels to be measured, the use of our SA was not possible. The only available solution in the lab capable of measuring densities of the order of $\sim 1\ \mu V/\sqrt{Hz}$ at frequencies near DC is the acquisition board *Red-Pitaya stemlab-125-14*[1]. The measurements were carried out acquiring $N = 2^{25}$ voltage samples at a rate of $f_s = 2.5$ MHz. The first measurement consisted of generating a signal with the AWG of 1 Vpp and a frequency of $f_{\text{mod}} = 10$ kHz. The second measurement involved connecting a 50 Ω load to verify the noise baseline of the measurement instrument. From the voltage traces, the voltage noise spectral density $\sqrt{S_V(f)}$ was calculated and then referred to the SQUID using $G_{VI} = 495\ \mu A/V$ and $M_{\text{mod}} = 10$ pH. The results of both measurements are shown in Figure 7.4. The blue trace represents the AWG noise $\sqrt{S_\Phi^{AWG}(f)}$, while the orange one represents the noise baseline of the *Red-Pitaya* $\sqrt{S_\Phi^{RP}(f)}$. Both results coincide, reflecting that the measurement is limited by the *Red-Pitaya*, so we cannot determine the flux noise produced by the AWG, only that it is lower than the limit imposed by the *Red-Pitaya*. Therefore, this value represents the upper bound of the flux noise produced by the flux modulation system.

Although the noise of the generator cannot be determined, it is possible to set a bound for the thermal noise produced by the passive components (i.e., filter, attenuator, and voltage-to-current converter). $\sqrt{I_n(f)} \sim 10\ pA/\sqrt{Hz}$ at a temperature of $T_{\text{amb}} = 300$ K. This corresponds to a value of $\sqrt{S_\Phi(f)} \approx 0.05\ \mu\Phi_0/\sqrt{Hz}$ and represents the lower bound of the flux noise produced by the flux modulation system.

The setup shown in the Figure 7.3 was also implemented using the Mixer-less SDR prototype. It was not shown to avoid repeating two figures with redundant content. This only requires connecting the Tx and Rx ports to the corresponding ones on the Mixer-less SDR, as shown in Figure 6.1. The diagram of the SDR would correspond to that in Figure 6.3. Having presented the diagram of the complete readout system, we can proceed with the full characterization of the µMUX using only the SDR.

[1] https://redpitaya.readthedocs.io/en/latest/developerGuide/hardware/125-14/top.html

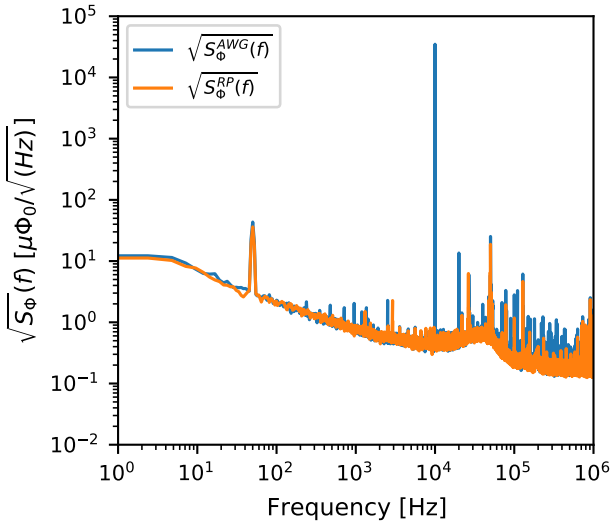

Figure 7.4: AWG flux-noise Characterization. $\sqrt{S_\Phi^{AWG}(f)}$ represents the equivalent flux-noise spectral density produced by the AWG (Blue trace), while $\sqrt{S_\Phi^{RP}(f)}$ represents the flux-noise density baseline measured with the *Red-Pitaya* connected to a terminating impedance $Z_0 = 50\,\Omega$.

7.2 µMUX Characterization

Before demonstrating the readout of a µMUX, it is necessary to characterize it in order to determine the optimal readout parameters for each channel. As explained in Section 4.3.2, these parameters depend both on the frequency response of the resonator $S_{21}(f_{\text{exc}})$, as well as the Power and flux dependence of the resonance frequency $f_r(P_{\text{exc}})$. The Figure 7.5 shows the transmission parameter of the nine-channel µMUX, as shown in Figure 7.2 at a temperature of $T_{base} = 100$ mK. The measurement was carried out with a VNA using an excitation power of $P_{\text{exc}} \approx -75$ dBm at the input port of the µMUX. Using the SDR, the characterization of channel 5 of the µMUX, indicated with red letters, was performed. Particularly, the input coil L_{in} of this channel is not connected to the dummy chip and is left open-circuited.

The multidimensional characterization consisted of generating a tone at a constant power P_{Tx} and performing a frequency sweep centered at $f_{\text{center}} = 6.44940$ GHz with a span of 1 MHz. For the case of the implemented firmware, the frequency resolution achieved is $\Delta_{\text{gen}} \approx 7629$ kHz. The sweep was repeated for different excitation powers P_{exc} and modulation fluxes Φ_{mod} generated by the AWG. On the receiver side, the acquired power was measured for each frequency and normalized with respect to the maximum value in order to remove the

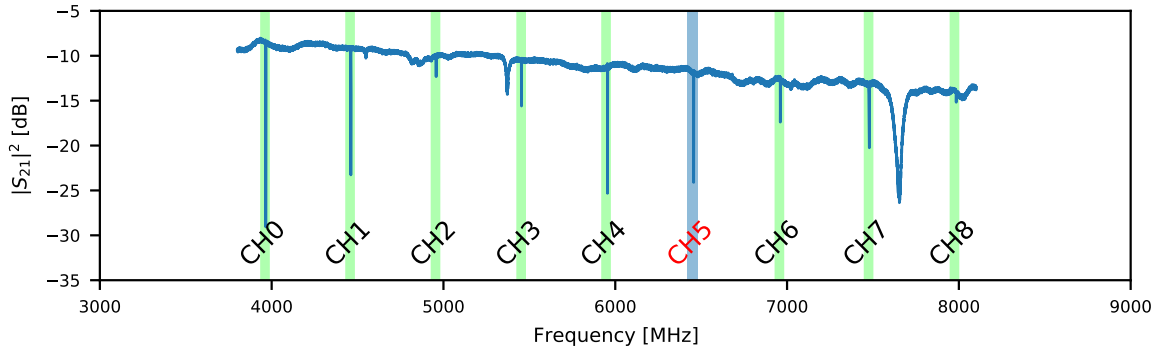

Figure 7.5: Transmission Scattering parameter of a nine channel µMUX measured using the Vector network Analyzer. The characterization was done at $P_{\text{exc}} \approx -75$ dBm. Channel 5, located at $f \approx 6.4$ GHz was taken as an example for the readout demonstration.

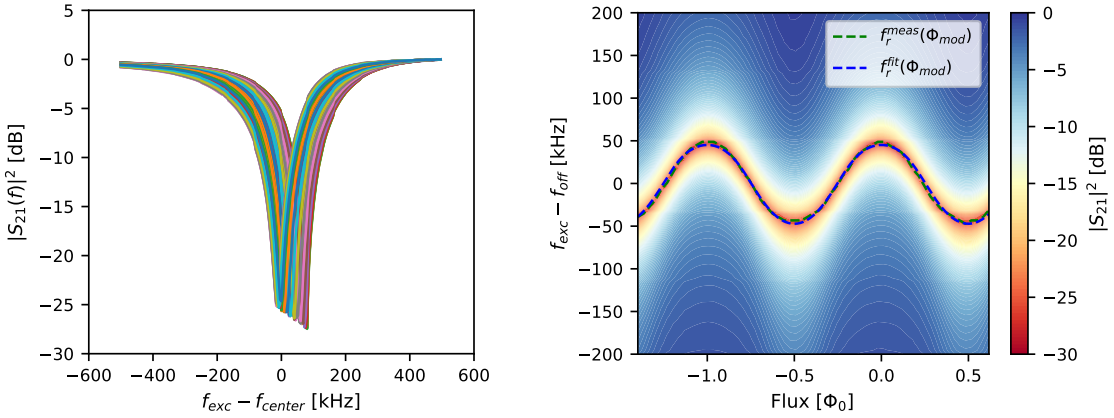

Figure 7.6: Left) Magnitude of the transmission scattering parameter $|S_{21}(f)|^2$ measured as function of the modulation flux Φ_{mod}. **Right)** Measured f_r^{meas} and fitted resonance f_r^{fit} frequencies as a function of the modulation flux Φ_{mod}. Both measurements were performed at a constant excitation power of $P_{\text{exc}} \approx -70$ dBm.

baseline attenuation. On the left side of Figure 7.6, the frequency response of the resonator $|S_{21}(f)|^2$ as a function of the external modulation flux is shown for an excitation power of $P_{\text{exc}} \approx -70$ dBm. This power value was calculated considering $A_{Tx} = 45$ dB and is equivalent to a $P_{Tx} \approx -25$ dBm.

The AWG was configured to generate $N = 61$ voltage values between $-450 < V_{\text{mod}} < 450$ mV, equivalent to modulation currents between $-200 < I_{\text{mod}} < 200$ µA. Considering $M_{\text{mod}} \approx 10$ pH, these values correspond to $\sim 2\Phi_0$, which is sufficient to represent the periodicity of the resonance frequency as a function of the flux. Using the traces $|S_{21}(f)|^2$, the resonance frequency for each flux value $f_r^{\text{meas}}(\Phi_{\text{mod}})$ was determined, and from these, a fitting of the model given by equation 3.32 was carried out. In this case the parameters presented in Table 3.1 were used as starting point for the fitting. The fitting result $f_r^{\text{fit}}(\Phi_{\text{mod}})$ is shown on the right side of Figure 7.6. The x-axis corresponds to the modulation flux Φ_{mod}, while the y-axis corresponds to measured frequencies relative to the unaltered resonance frequency $f_{\text{exc}} - f_{\text{off}}$. According to predictions, two periods can be observed in the resonance frequency. This procedure was repeated for different excitation powers P_{exc} in the range $[-100, -60]$ dBm, and the values of the maximum $f_r^{\text{max}}(P_{\text{exc}})$ and minimum resonance frequencies $f_r^{\text{min}}(P_{\text{exc}})$ as a function of power were recorded. The results are shown on the left side of Figure 7.7. The blue trace corresponds to $f_r^{\text{max}}(P_{\text{exc}})$, while the orange trace corresponds to $f_r^{\text{min}}(P_{\text{exc}})$. Combining the previous results yield a bandwidth of $BW_{res} \approx 180$ kHz and a peak resonance frequency variation of the order of $\Delta f_r \approx 165$ kHz yields $\eta_0 \approx 0.92$. This result, together with the insensitivity in the response observable at $P_{\text{exc}} \approx -65$ dBm, is consistent with the design parameters shown in Table 3.1.

From these curves, and based on the simulation results presented in Section 4.3.2, it is possible to find the trajectories $(f_{\text{exc}}, P_{\text{exc}})$ that represent the minimum demodulated flux noise. In the case of resonator phase demodulation, the trajectory for minimum noise is approximated by $f_\theta \approx 0$, while for amplitude demodulation, we have $f_\gamma^{\text{low}} \approx f_r^{\text{min}}$ and $f_\gamma^{\text{up}} \approx f_r^{\text{max}}$. These curves cannot be directly configured in the SDR because they are referenced to f_{off}, which is a function of power. Therefore, the curves were referenced to the center frequency f_{center}, used as the reference in our SDR. The use of a center frequency has the sole purpose of avoiding working with absolute frequencies. The frequency graph shows the optimal trajectories referenced to the center frequency used in the SDR, which is $f_{\text{center}} = 6.44940$ GHz.

It is important to note that the stars shown in Figure 7.7 represent the measured values,

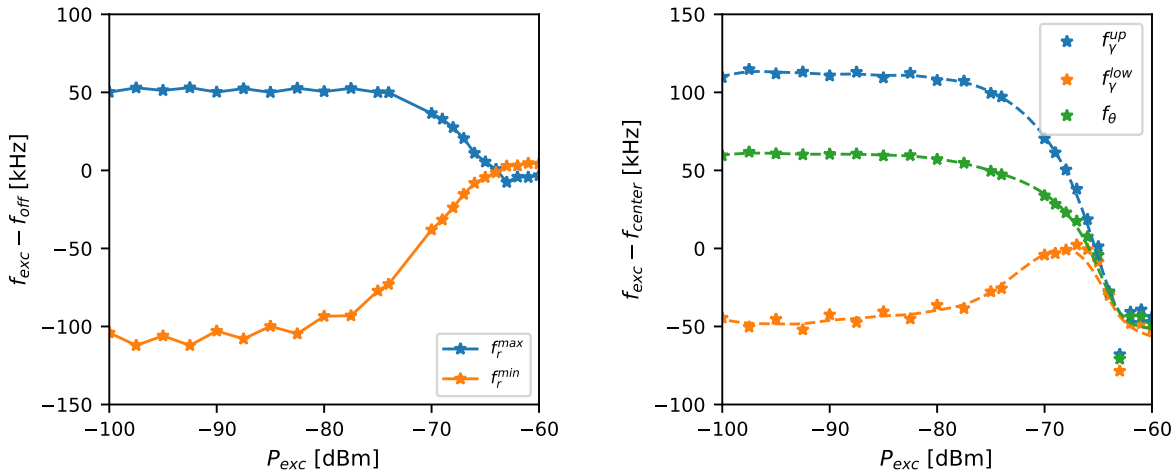

Figure 7.7: Left) Maximum $f_r^{\max}$ and Minimum $f_r^{\min}$ resonance frequencies for the μMUX channel referenced to the unaltered resonance frequency f_{off}. **Right)** Approximated optimum $(P_{\text{exc}}, f_{\text{exc}})$ trajectories for minimum demodulated flux noise $\sqrt{S_\Phi}$. f_γ^{up} and f_γ^{low} correspond to the optimum trajectories for amplitude demodulation while f_θ for resonator phase demodulation. Stars represent the measurements while dashed lines the smoothed interpolation using splines.

while the dashed lines are a smoothed interpolation using splines. The spline approximation was performed with the goal of conducting subsequent measurements with better power resolution, avoiding an increase in the number of powers used during the time-consuming flux characterization.

As expected, the characterization results showed a behavior of the channel approximating that of the μMUX with the parameters listed in Table 2.1. The only unexpected behavior found during the characterization was the dependence of the parameter $|S_{21}^{\min}|^2$ on the readout power, as shown in Figure 7.8 for two different flux values. In the simulations presented in Chapter 4, this was considered constant with a value of -18 dB. In contrast, the measurement shows a variation between -13 and -25 dB. The variation of the $|S_{21}^{\min}|$ with respect to the flux is attributed to the sub-gap conductance of the Josephson Junction [93], while the variation as a function of the excitation power is potentially attributed to the losses caused by the Two-Level Systems (TLS), which modify Q_i [172, 173]. Explaining this behavior and including it in the simulations is beyond the scope of this thesis, and it will be considered in future work.

7.3 Readout System Noise Characterization

In this section, the noise characterization of the complete readout system was carried out, which integrates the SDR with the cryogenic microwave chain. The characterization consisted of repeating the complete procedure described in Section 6.3, with the only difference being that the loopback in this case included the μMUX. Here, an interrogation tone was generated at an off-resonance frequency with excitation powers P_{exc} in the range of $[-100, -60]$ dBm. Specifically, the tone frequency was set 2 MHz below the frequency f_{off}. This value would represent the midpoint between two channels using the channel separation planned for the QUBIC project of $\Delta f_{res} = 4$ MHz. The results of the phase and amplitude noise measurement, performed at a power of $P_{\text{exc}} \approx -70$ dBm and using both prototypes, are shown in Figure 7.9.

The results are similar to those shown in Figure 6.13. During these measurements, differ-

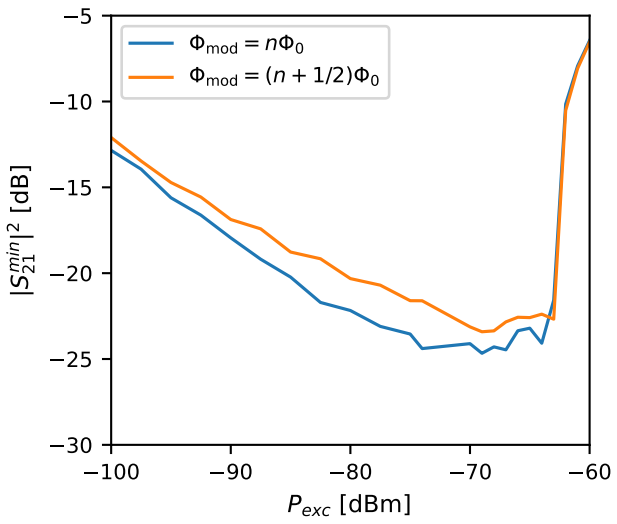

Figure 7.8: Minimum Transmission Scattering Parameter $|S_{21}^{min}|^2$ as a function of the probing power P_{exc} for two different modulation fluxes $\Phi_{\text{mod}} = n\Phi_0$ and $\Phi_{\text{mod}} = (n + 1/2)\Phi_0$.

ent factors were observed that contributed to an increase in the level of spurious signals. These factors included excessive ground loops, and electronic devices that induced electromagnetic interference. As a result, all unnecessary devices were turned off, the number of ground loops was reduced, and the cryogenic LNA was configured to operate in floating mode. Figure 6.13 represents the best case, where existing interference was minimized as much as possible.

The results of the phase and amplitude noise measurement as a function of power are shown in Figure 7.10. As in the previous chapter, the levels measured in both prototypes reflect the average within the green-shaded region in Figure 6.13. The dashed curves are the result of the fitting in the region dominated by additive noise, according to equations 6.3 and 6.4. Table 7.1 lists the measurement results for both prototypes. Among the most important results are the additive noise temperatures, which are $T_n^{Z-IF} = 8.1$ K for the Zero-IF SDR prototype and $T_n^{MX-L} = 6.5$ K for the Mixer-Less SDR prototype. These can be compared to the cryogenic chain noise temperature results shown in Figure 4.24, which reflect $T_n^{cryo} = 4.6$ K at the frequency of $f_{\text{exc}} = 6.5$ GHz. Therefore, the prototypes show an increase of 3.5 K and 2.1 K for the Zero-IF SDR and the Mixer-Less SDR, respectively. In the case of multiplicative noise, both phase and amplitude noise remained approximately constant, and the small differences are attributed to mechanical and thermal variations of components and the delay τ imposed by the microwave chain, which degrades the coherence between LOs [121, 174].

The measured additive noise temperatures T_n^{Z-IF}, T_n^{MX-Z}, and T_n^{cryo} can be used in conjunction with equation 6.5 to determine the contributions of the transmitter and receiver noise of each prototype. The resolution of the equations requires considering that $G_{Tx} = -45$ dB, $G_{tot} = G_{Tx} + G_{Rx} = -12.5$ dB (see Figure 4.23) and $T_n^{Tx-Rx} = T_n^{Tx} + T_n^{Rx}$. The calculated temperature results are listed in Table 7.1. The contribution of both noise temperatures can be reduced by lowering the attenuation level of the cryogenic microwave chain, increasing the gain, and reducing the noise figure of the receiver components. The objective of this thesis is not only to develop a low-noise readout system but also to propose a characterization method that allows determining the noise contributions of each component in order to enable optimization. Therefore, for the purpose of this thesis, the results obtained are acceptable and in agreement with other comparable readout systems [103, 148]. The optimization of the noise will be part of future work.

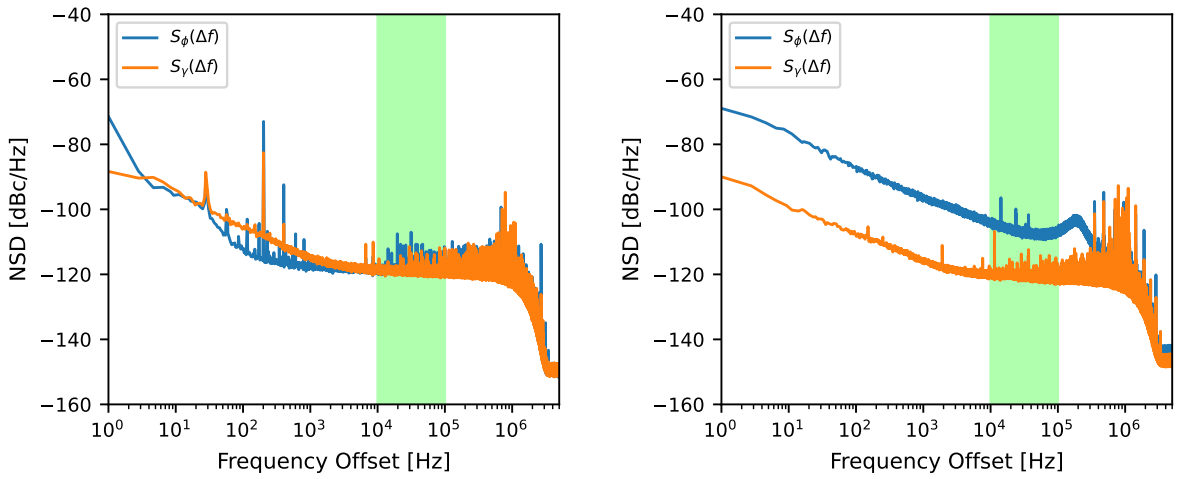

Figure 7.9: Right:) Off-resonance phase and amplitude noise spectra for the Zero-IF SDR Prototype System. **Left)** Off-resonance phase and amplitude noise spectra for the Mixer-Less SDR Prototype System. Both measurements were performed at a frequency $f_{\text{exc}} \approx 6.4$ GHz and $P_{\text{exc}} \approx -70$ dBm.

Table 7.1: Summary of the additive and multiplicative noise levels for both Single-Band RFSoC-Based SDR prototypes measured in Cryo-loopback. Multiplicative noise is the average value within the range between 10 kHz and 100 kHz representing the possible location of the modulation frequency f_{mod}. The additive noise temperatures were referred to the μMUX output considering a $A_{Tx} = 45$ dB. T_n^{Tx} and T_n^{Rx} were calculated using the values shown in Table 6.1, considering $T_n^{cryo} = 4.6$ K and $G_{tot} = -12.5$ dBm as described in Section 4.4.

Noise Parameter	Zero-IF SDR Prototype	Mixer-Less SDR Prototype
T_n	8.5 K	6.1 K
T_n^{cryo}	4.6 K	4.6 K
T_n^{Tx}	0.8 K	0.03 K
T_n^{Rx}	3.10 K	1.47 K
$S_\phi(f_{\text{mod}})$	−124 dBc/Hz	−102 dBc/Hz
$S_\gamma(f_{\text{mod}})$	−122 dBc/Hz	−122 dBc/Hz

7.4 Flux-Ramp Demodulated Noise Performance

Once the optimal readout parameters of the μMUX have been determined for both readout domains and the noise performance of the readout system have been characterized, we can proceed to demonstrate the readout of the μMUX channel. The objective of this section is to determine the demodulated flux noise level for different readout conditions and then compare it with the predictions from the simulation model presented in Chapter 5. We will first describe the process of selecting the flux modulation frequency and then configure our SDR to demodulate the signals present in the SQUID.

7.4.1 Flux-Ramp Modulation Placement

As mentioned in Section 4.2.2, the μMUX requires the application of a unique flux modulation φ_{mod} to all channels to prevent any of them from being at an insensitive point to the detector's

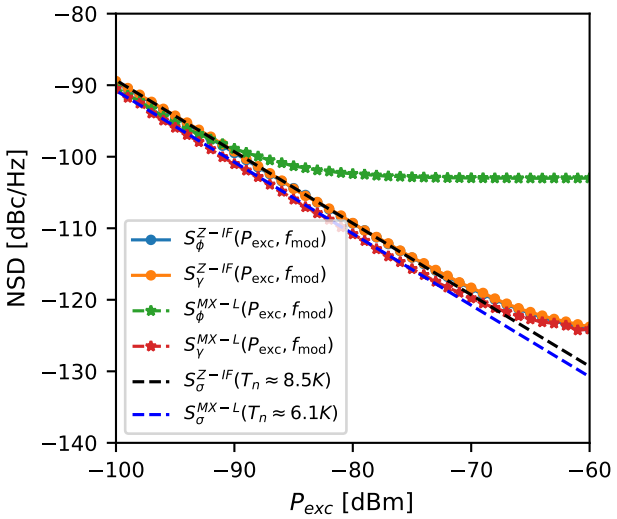

Figure 7.10: Phase and amplitude noise measured in cryogenic Loop-back configuration for both proposed SDR prototypes. Phase and amplitude noise as a function of power for a tone at $f_{exc} \approx 6.4$ GHz. $S_\phi^{Z-IF}(P_{exc}, f_{\mathrm{mod}})$ and $S_\gamma^{Z-IF}(P_{exc}, f_{\mathrm{mod}})$ correspond to the Zero-IF prototype, while $S_\phi^{MX-L}(P_{exc}, f_{\mathrm{mod}})$ and $S_\gamma^{MX-L}(P_{exc}, f_{\mathrm{mod}})$ to the Mixer-Less prototype.

flux φ_{det}. This modulation, in turn, allows us to shift the detector signal in frequency, thus avoiding the high noise level present at low frequencies. Some examples include TLS noise or phase noise in the system, as shown on the right side of Figure 7.9 [175, 101]. During the development of this thesis the flux-ramp modulation was considered to be set at frequencies between 10 kHz and 100 kHz, its selection should be made based on the measured noise levels at resonance.

The process for determining the optimal modulation frequency f_{mod} requires the measurement of phase and amplitude noise at resonance. This is necessary to determine the spectral structure of the noise and thus locate the region where the noise is minimal. For this, using the AWG, a flux of $\Phi_{\mathrm{mod}} \approx \Phi_0/4$ was applied, and the μMUX was interrogated with a power of $P_{\mathrm{exc}} \approx -70$ dBm. These values ensure that the SQUID is at its most sensitive point and at a power level below the point where the SQUID becomes insensitive (see Figures 3.8 and 3.8). Locating the SQUID at a sensitive point allows all flux noise sources threading the SQUID to be amplified and observed in the noise spectrum.

The measurement results using the Zero-IF SDR are shown on the left side of Figure 7.11. The blue and orange curves correspond to the off-resonance phase noise $S_\phi^{\mathrm{off}}(\Delta f)$ and amplitude noise $S_\gamma^{\mathrm{off}}(\Delta f)$, respectively. Meanwhile, the green and red curves correspond to the on-resonance phase noise $S_\phi^{on}(\Delta f)$ and amplitude noise $S_\gamma^{\mathrm{on}}(\Delta f)$, respectively. In this case, the spectra were calculated from $N = 2^{25}$ IQ samples and averaged over $M = 100$ spectra. These results show an increase in the measured noise, which is due to two factors. The first is the reduction of output power due to the attenuation of the resonator, and the second is the flux noise coupled to the SQUID, either from the modulation lines or from various external sources (i.e., cell phones, motors, computers, Wi-Fi routers). The shape of the on-resonance noise spectrum has not been fully explained, but it is believed to be related to the bandwidth of the resonator or one of the flux lines, which modulates the interrogation tone with the flux noise.

After verifying the noise in resonance, we proceeded to apply a flux modulation with an amplitude $n_{\Phi_0} = 4$ and a ramp-reset frequency $f_{\mathrm{ramp}} = 1 \cdot 10^9/2^{17} \approx 7629$ Hz. The choice of this frequency is not trivial, as it is a frequency that can be correctly generated and synchronized with the sampling frequency at the output of the DDC. This measurement was carried out to verify whether the noise profile has any dependence on the applied modulation or not. The result of the measurement after injecting the modulation is shown on the right side of Figure 7.11. It can be seen that the modulation sideband is at $f_{\mathrm{mod}} = f_{\mathrm{ramp}} n_{\Phi_0} \approx 30.517$ kHz, along with its harmonics, as the phase trace $\gamma(t)$ and amplitude trace $\gamma(t)$ are not exactly sinusoidal. The other components at frequencies $f_{\mathrm{mod}}/2$ and $f_{\mathrm{mod}}/4$ are produced as a consequence of the

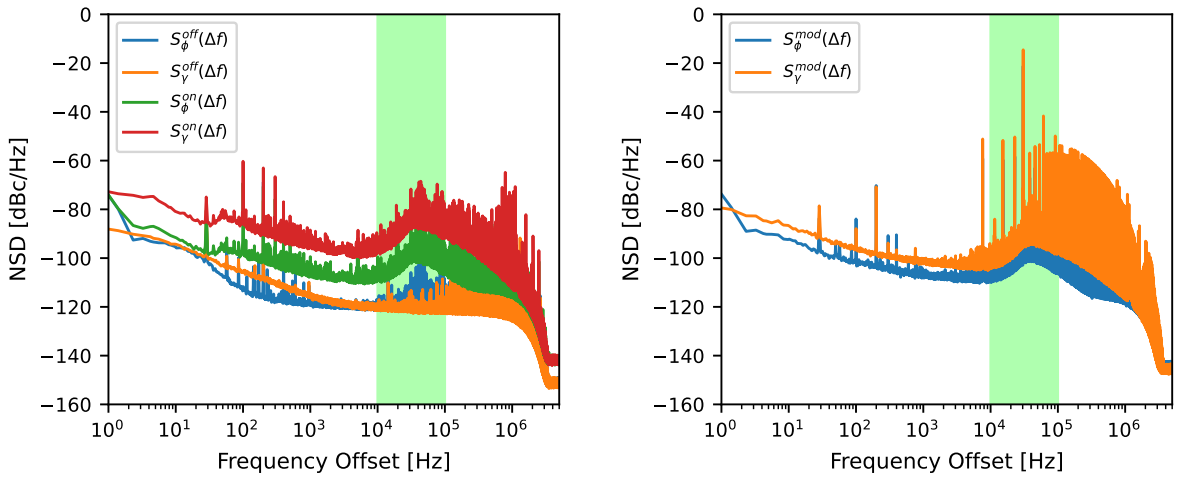

Figure 7.11: Left) On and Off-Resonance phase and amplitude noise comparison. Right) Phase and amplitude noise spectra with and without flux modulation. The flux-modulation frequency is $f_{\text{mod}} = f_{\text{ramp}} n_{\Phi_0} \approx 30.517$ kHz, where $f_{\text{ramp}} \approx 7629$ Hz and $n_{\Phi_0} = 4$.

ramp transients and the fact that the flux ramp amplitude is not exactly $n_{\Phi_0} = 4$.

Since the noise spectra do not change with modulation, the ramp frequency f_{ramp} was reduced until reaching the valley present at frequencies between 1 and 10 kHz, while maintaining the amplitude at $n_{\Phi_0} = 4$. Figure 7.12 shows the reduction in both phase and amplitude noise for three different modulation frequencies. The black dashed line is a guideline. In this measurement, the noise reduction was verified, while ensuring that the amplitude of the sideband remained at constant levels, thereby effectively increasing the SNR (see the red dashed line in Figure 7.12). The optimal modulation frequency used in the following sections corresponds to $f_{\text{mod}} = 1 \cdot 10^9/2^{17} \approx 7629$ Hz (i.e., $f_{\text{ramp}} = 1 \cdot 10^9/2^{19} \approx 1907$ Hz).

In the following section, we will perform the demodulation of the detector signal in order to determine the noise level. Since we do not have the capability to inject signals to emulate the detector, the modulation line was used for this purpose. Given that adding a detector signal $\Phi_{\text{det}}(t)$ to the modulation ramp $\Phi_{\text{mod}}(t)$ is equivalent to a phase modulation [87], the phase modulation of the AWG was activated in order to emulate a detector with a known amplitude. Specifically, the AWG was configured to generate a detector signal with $f_{\text{det}} = 135$ Hz and amplitude $A_{\text{det}} = 10\ \text{m}\Phi_0$. This signal is used to verify the correct operation of the demodulation.

On the right side of Figure 7.12, the spectral content around the modulation sideband $f_{\text{mod}} \approx 7629$ Hz is shown. As explained in Section 4.2.2, the effective sampling rate of the detector is given by the reset rate of the ramp $f_{\text{ramp}} \approx 1907$ Hz. The shaded area in green represents the set of frequencies that correspond to the first Nyquist zone after demodulation. In agreement with Figure 4.7, the carrier is located at f_{mod} and the modulation sidebands are positioned at a distance f_{det} on both sides of the carrier. The remaining present signals are either harmonic signals of the detector signal or spurious signals generated by the AWG. These will be taken into account if observed after demodulation.

7.4.2 Minimum-Noise Optimum Readout Parameters

The results of the simulations presented in Chapter 4 suggest that the optimal readout parameters are derived from the characteristics of the μMUX channels. The first step in validating the simulation results was the determination of the μMUX characteristics presented in Sec-

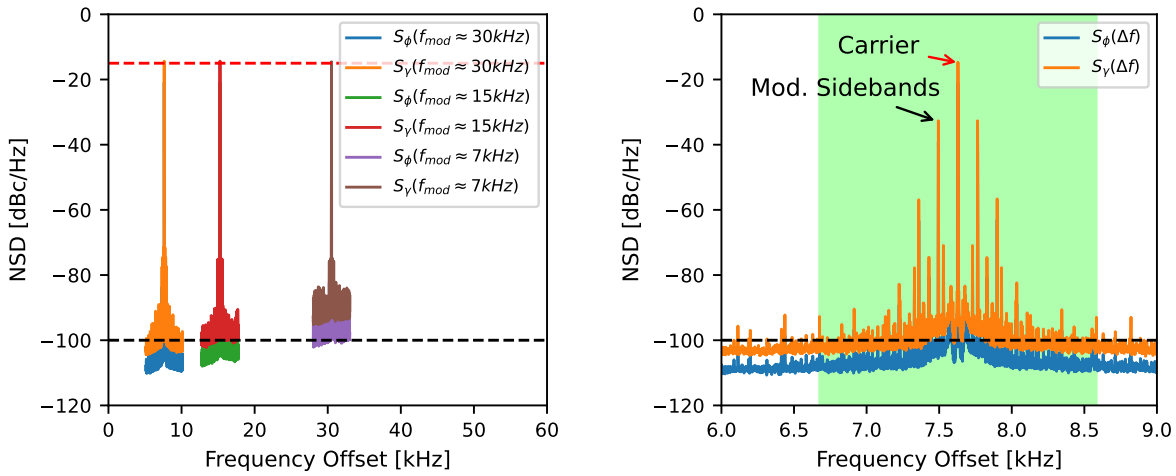

Figure 7.12: Left) Phase and amplitude noise measured at different modulation frequencies f_{mod}. **Right)** Phase and amplitude noise spectra close to the modulation sideband located at $f_{\text{mod}} \approx 7629$ Hz, phase modulated with $f_{\text{det}} = 135$ Hz and $A_{\text{det}} = 10$ mΦ_0. The dashed red line represents the sideband amplitude while dashed back line is used as a guideline. The green regions span 1907 Hz around the sideband and represents the Nyquist zone after the FRD.

tion 7.2. The trajectories (P_{exc},f_{exc}), shown in Figure 7.7, according to the readout simulation model, allow achieving the minimum demodulated noise for both readout domains using flux modulation. In order to validate the simulation framework, a flux-ramp demodulation was performed, and the white flux noise $\sqrt{S_{\Phi,\text{white}}}$ was estimated for different readout parameter configurations.

The measurement of the demodulated noise $\sqrt{S_{\Phi,\text{white}}}$ follows the same steps described in Section 4.2, including the generation of a tone at power P_{exc} and frequency f_{exc} and the application of flux modulation with the previously mentioned parameters (i.e., $f_{\text{ramp}} \approx 1907$ Hz and $n_{\Phi_0} = 4$). These measurements were performed using both SDR readout prototypes in the configuration shown in Figure 7.3. For each readout parameter configuration, an IQ trace of the channel $x(t) = x_I(t) + x_Q(t)$ was obtained with a total of $N = 2^{25}$ samples, and the phase trace of the resonator $\theta(t)$ and amplitude trace $\gamma(t)$ were calculated off-line. On the left side of Figure 7.13, the IQ traces obtained for the condition of $P_{\text{exc}} \approx -70$ dBm and $f_{\text{exc}} \approx f_\theta(P_{\text{exc}})$ are shown. Starting from yellow, going through green, and ending in blue, the motion of the resonator along the resonance circle, represented by a red dashed line, is shown. This circle was fitted based on the IQ samples and shows a radius of $r \approx 0.465$ and a minimum transmission parameter $|S_{21}^{\text{min}}|^2 \approx -24$ dB, both consistent with the results from Figures 7.6 and 7.8. From the IQ traces and the fitting parameters, the resonator phase $\theta(t)$ and amplitude $\gamma(t)$ were calculated and are shown in the upper right part of Figure 7.13. These results allow observing the periodicity given by $f_{\text{ramp}} \approx 1907$ Hz and the discontinuity caused by the ramp reset (shaded green area). The traces of both domains were demodulated, and the flux spectral density was calculated in order to estimate the white noise level for each domain. To simplify the demodulation, a boxcar window $w(t)$ was used, and no periods were discarded ($n_{\text{disc}} = 0$). In the lower right part of Figure 7.13, the flux densities for each readout domain $\sqrt{S^\theta_{\Phi,\text{white}}}$ and $\sqrt{S^\gamma_{\Phi,\text{white}}}$ are shown. The black star represents the calibration signal at $f_{\text{det}} = 135$ Hz, and the red and black dashed lines represent the noise estimates in the resonator phase and amplitude domains, respectively.

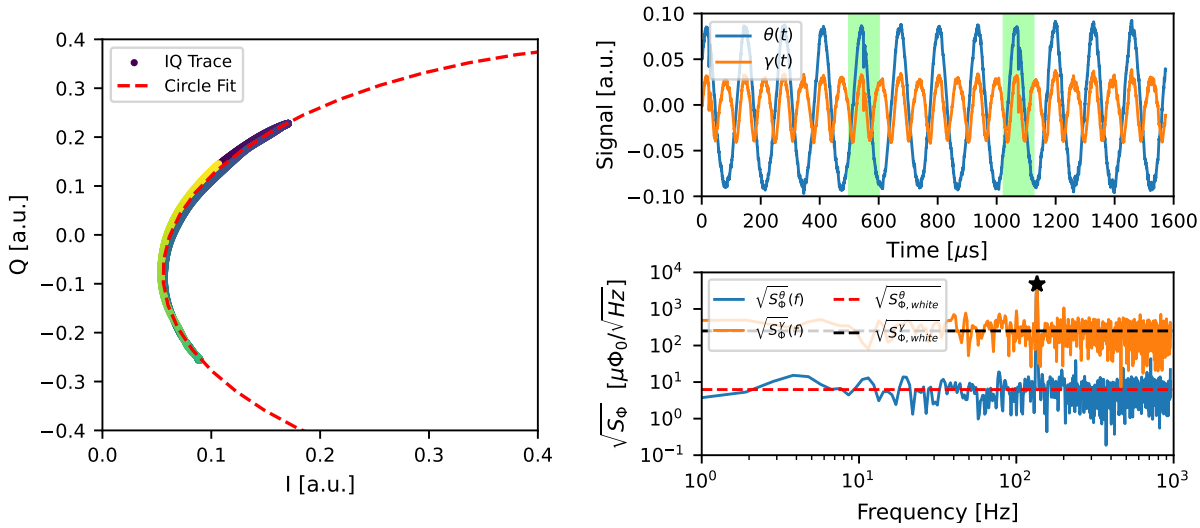

Figure 7.13: Measured IQ, phase and amplitude traces **Left)** IQ traces fitted by a circle used for resonator phase θ calculation **Right)** Phase and amplitude time-traces and demodulated flux-noise spectral density. All traces uses $f_{\text{mod}} = f_{\text{ramp}} n_{\Phi_0} \approx 7629$ Hz, where $f_{\text{ramp}} \approx 7629$ Hz and $n_{\Phi_0} = 4$, $P_{\text{exc}} \approx -70$ dBm and $f_{\text{exc}} \approx f_\theta(P_{\text{exc}})$. Green regions contain the flux-ramp transients, while dashed red and black lines represent the white flux-noise levels for both demodulation domains.

This process was repeated for excitation powers P_{exc} in the range of $[-100, -60]$ dBm and frequencies f_{exc} in the range of $[-250, 250]$ kHz with respect to the reference frequency used, $f_{\text{center}} \approx 6.4494$ GHz. The results of the demodulated noise $\sqrt{S_{\Phi,\text{white}}}$ in this range for both demodulation domains, using the Zero-IF SDR prototype, are shown in Figure 7.14. The left side of the figure shows the demodulated noise for the phase of the resonator, while the right side shows the demodulated noise for the amplitude. These results validate the simulation results shown in Figure 4.13, where the local minima of the noise for each domain are found below the optimal trajectories presented in Figure 7.7. Each point in the figure represents the average of $N = 5$ noise measurements. Since the Mixer-Less prototype showed similar results, these are not shown to avoid redundancy.

The previous measurement verified the validity of the optimal noise trajectories obtained through the characterization of the μMUX. To obtain a better estimate of the noise level under these trajectories and avoid consuming the measurement time required to obtain the results shown in Figure 7.14, the demodulated noise estimation was repeated for two particular cases, averaging $N = 20$ spectra.

For one of the cases, the demodulated noise was measured as a function of the excitation frequency for only two power values. Specifically, $P_{\text{exc}} \approx -70$ dBm and $P_{\text{exc}} \approx -90$ dBm. The results for the Zero-IF SDR prototype and the Mixer-Less SDR are shown on the left and right sides, respectively. For the Zero-IF SDR case, the demodulated noise in the resonator phase domain $\sqrt{S^{\theta}_{\Phi,\text{white}}}$ is always lower than the noise in the amplitude $\sqrt{S^{\gamma}_{\Phi,\text{white}}}$, in accordance with a reading system dominated by additive noise. In contrast, the Mixer-Less SDR shows a higher noise level in the phase than in the amplitude for high excitation powers. This was predicted by the simulation framework and is due to the multiplicative noise in the phase presented by the Mixer-Less SDR. However, this effect is only observed at high powers, while at low powers both systems are dominated by additive noise. The peak observed in the amplitude domain can be explained by the spectral components of the amplitude trace $\gamma(t)$. At frequencies $f_{\text{exc}} \approx f_{\text{off}}$, the spectral component with the highest power is $2f_{\text{mod}}$, and demodu-

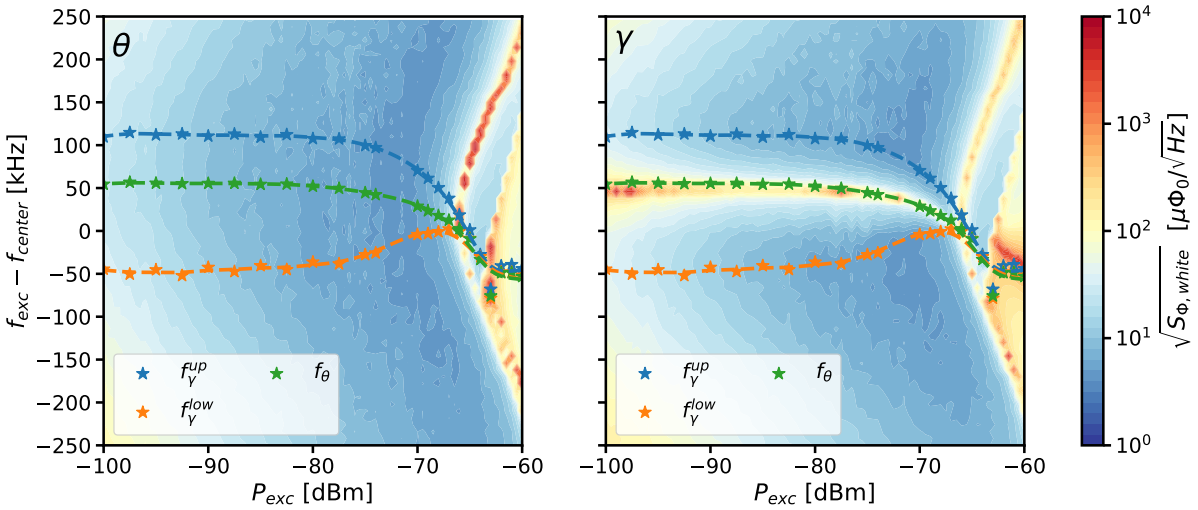

Figure 7.14: Measured flux-ramp demodulated white flux noise density $\sqrt{S_{\Phi,\text{white}}}$ as a function of the excitation power P_{exc} and frequency f_{exc} using the Zero-IF SDR prototype. **Left)** Measured flux-ramp demodulated white flux noise density $\sqrt{S_{\Phi,\text{white}}}$ for the resonator phase domain. **Right)** Measured flux-ramp demodulated white flux noise density $\sqrt{S_{\Phi,\text{white}}}$ for the amplitude domain. Blue and Orange trajectories represent the upper f_γ^{up} and lower f_γ^{low} minimum noise trajectories for amplitude demodulation, while green trace the optimum trajectory for resonator phase demodulation f_θ.

lation based on the first harmonic f_{mod} yields unfavorable results. This is clearly observed in the upper-right part of Figure 7.13, where the amplitude trace $\gamma(t)$ has twice the frequency of the resonator phase $\theta(t)$. All the results obtained are consistent with the qualitative simulation results shown in Figure 4.14.

The second case represented the measurement of the flux noise following the optimal noise trajectories as a function of the excitation power (i.e., $f_\theta(P_{\text{exc}})$, $f_\gamma^{\text{low}}(P_{\text{exc}})$, and $f_\gamma^{\text{up}}(P_{\text{exc}})$). As in the previous case, $N = 20$ noise values were averaged. The results obtained are shown in Figure 7.16. On the left side, the results corresponding to the Zero-IF SDR are shown, which are in agreement with the results obtained in Figure 4.16 for a system dominated by additive noise, such as the Zero-IF SDR. The minimum noise value $\sqrt{S_\Phi^\theta} \approx 4\ \mu\Phi_0/\sqrt{Hz}$ is reached in the resonator phase domain at an excitation power of $P_{\text{exc}} \approx -73$ dBm. Similar results were obtained for the Mixer-Less SDR, but it can be observed that at high powers, the multiplicative noise in the phase increases the noise in the resonator phase domain, and it reaches values comparable to that of the amplitude. This result validates the simulation results shown in Figure 4.18, which used the noise parameters found for the Mixer-Less SDR, as reflected in Table 6.1. It is important to note that both graphs differ in the excitation power resolution used. Different technical issues during the measurements prevented performing the second sweep with better resolution using the Mixer-Less SDR. Nevertheless, the results obtained are valid and reflect the noise behavior of the μMUX up to excitation powers of $P_{\text{exc}} \approx -70$ dBm. Above this power, the behavior of the μMUX cannot be represented due to the lack of data points near the insensitive point.

Although the qualitative analysis of the results reflects the validity of the simulations, the quantitative differences in the noise levels should be explained. The simulation results in Figure 4.16 show noise levels of the order of $\sqrt{S_\Phi^\theta} \approx 0.71\ \mu\Phi_0/\sqrt{Hz}$ for an additive noise temperature of $T_n \approx 4$ K, $P_{\text{exc}} \approx -70$ dBm, using a *Hamming* window and discarding $n_{\text{disc}} = 1$ periods of $n_{\Phi_0} = 4$ (i.e. $\kappa = 1.37$ and $\alpha = 3/4$). Given the high excitation powers, these noise

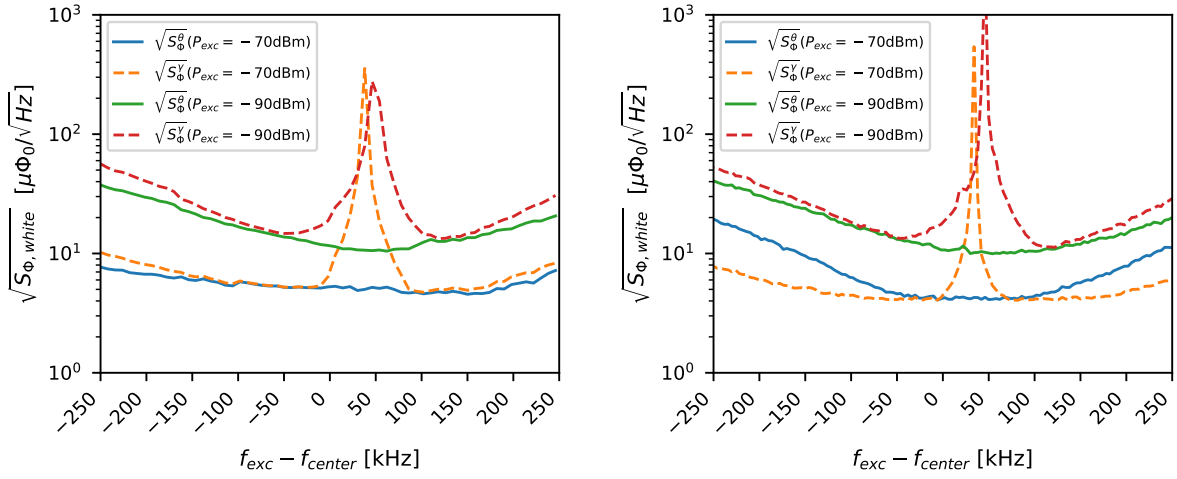

Figure 7.15: Flux-ramp demodulated white flux noise density $\sqrt{S_{\Phi,\text{white}}}$ as a function of the excitation frequency f_{exc} for both demodulation domains and measured using both SDR prototypes at constant power P_{exc}. **Left)** Flux-ramp demodulated white flux noise density $\sqrt{S_{\Phi,\text{white}}}$ for both resonator phase and amplitude domains measured for two different excitation powers P_{exc} using the Zero-IF SDR prototype. **Right)** Flux-ramp demodulated white flux noise density $\sqrt{S_{\Phi,\text{white}}}$ for both resonator phase and amplitude domains measured for two different excitation powers P_{exc} using the Mixer-Less SDR prototype.

levels are consistent with the analytical results provided by the expression 4.26. This expression considered a fundamental component of the resonator phase $\theta(t)$ equal to $\Theta_1 = 0.63$. For the case of the measurements in this section, we used $\alpha = 1$, $\kappa = 1$, and the observed value of the fundamental phase component shown in the top part of Figure 7.13 is $\Theta_1 = 0.085$. Using expression 4.26, for an excitation power of $P_{\text{exc}} \approx -70$ dBm, the demodulated noise results are approximately $\sqrt{S^{\theta}_{\Phi}} \approx 6.16\ \mu\Phi_0/\sqrt{Hz}$ for the Zero-IF SDR case and $\sqrt{S^{\theta}_{\Phi}} \approx 5.22\ \mu\Phi_0/\sqrt{Hz}$ for the Mixer-less SDR prototype. Based on these results, we can conclude that the discrepancies between both simulation and measurement results are due to the fact that the peak amplitudes of the resonator's amplitude and phase traces (i.e., Θ_1 and Γ_1) are considerably lower than in the simulated case, which leads to an increase in the noise level. Although the exact cause of this reduction was not precisely determined, the characterization of the μMUX reveals two possible factors. The first is the difference between the values of the transmission parameter used in the simulation $|S^{\text{min}}_{21}| \equiv -18$ dB and the measured value, which is not only lower but also dependent on the power (see Figure 7.8). The second is the reduced factor $\eta_0 \approx 0.92$, whereas during the simulations, it was set to $\eta_0 = 1$. Understanding the origin of these discrepancies is important, as it could represent an optimization of the demodulated noise by approximately ~ 5 times, relaxing the requirements imposed on the SDR and the cryogenic microwave chain. In the future, the effects observed during the characterization will be included and verified to determine if they are the cause of these discrepancies.

7.4.3 Expected Detection System Noise Performance

In this section, the results from the characterization of the SDR prototypes and the demodulated flux noise will be used to estimate the performance of the detection system proposed for the QUBIC project. The results presented in Figure 7.16 show a minimum flux noise level

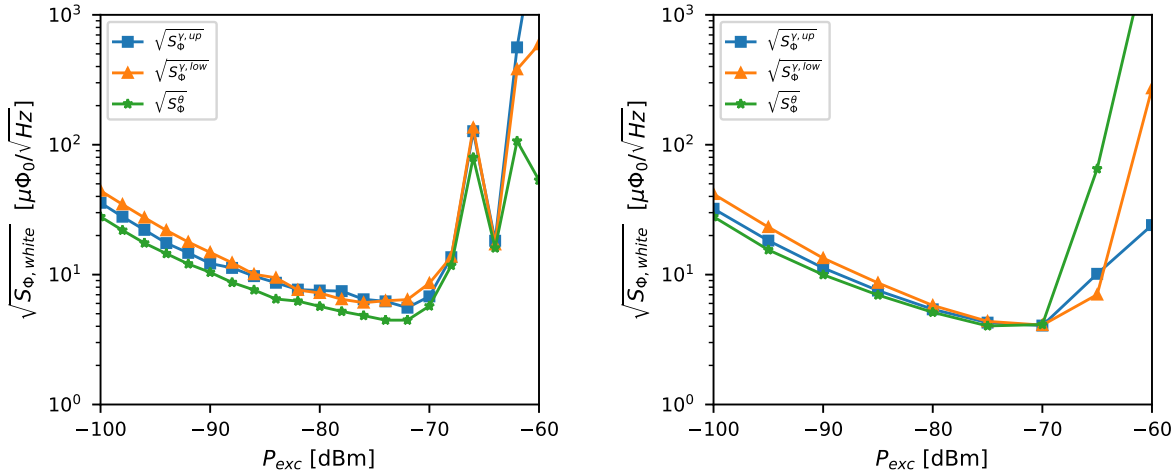

Figure 7.16: Flux-ramp demodulated white flux noise density $\sqrt{S_{\Phi,\text{white}}}$ as a function of the excitation power P_{exc} for both demodulation domains and measured over the optimum (P_{exc},f_{exc}) trajectories using both SDR prototypes. **Left)** Flux-ramp demodulated white flux noise density $\sqrt{S_{\Phi,\text{white}}}$ for both demodulation domains measured under the minimum noise trajectories (P_{exc},f_{exc}) using the Zero-IF SDR prototype. **Right)** Flux-ramp demodulated white flux noise density $\sqrt{S_{\Phi,\text{white}}}$ for both demodulation domains measured under the minimum noise trajectories (P_{exc},f_{exc}) using the Mixer-Less SDR prototype.

of $\sqrt{S_\Phi^{\min}} \approx 4\ \mu\Phi_0/\sqrt{Hz}$ for both SDR prototypes, using demodulation in the phase domain of the resonator. This value was obtained for a probing power of $P_{\text{exc}} \approx -73$ dBm. On the other hand, for the amplitude domain, the optimal noise values were similar, around $\sqrt{S_\Phi^{\min}} \approx 4.5\ \mu\Phi_0/\sqrt{Hz}$, but these will not be considered for further analysis. Under the assumption that all channels of the µMUX will behave the same, and using the results from Figure 6.9, it is possible to estimate the maximum number of channels that can be optimally read with the SDR. To do this, we must verify the maximum number of tones that the SDR can generate with a power of $P_{\text{exc}} \approx -73$ dBm at the µMUX level. Considering an attenuation of $A_{Tx} = 45$ dB, this corresponds to a transmitted tone power of $P_{Tx} = -28$ dBm. Based on the results from Figure 6.9, this would correspond to a maximum number of $N_{max}^{Z-IF} = 8$ and $N_{max}^{MX-L} = 4$, which can be read while maintaining the minimum achievable flux noise.

Clearly, this number of channels is not consistent with the requirement for the QUBIC project, which plans for approximately $N \sim 1000$ detectors. Therefore, to achieve this, it is necessary to tolerate some degradation in the readout noise to compensate for the limited power capacity of the SDR prototypes. Considering the maximum channel capacity that both prototypes can handle, $N = 100$, the maximum power per tone that both prototypes can generate is $P_{Tx}^{Z-IF} = -47$ dBm and $P_{Tx}^{MX-L} = -50$ dBm. These correspond to excitation powers at the µMUX level of $P_{\text{exc}}^{Z-IF} = -92$ dBm and $P_{\text{exc}}^{MX-L} = -95$ dBm. From the curves shown in Figure 7.16, these power values correspond approximately to $\sqrt{S_\Phi^{\min}} \approx 15\ \mu\Phi_0/\sqrt{Hz}$ for both prototypes. Interestingly, the power difference between the two prototypes compensates for the difference in their noise temperatures, resulting in the same noise level. This number of channels could be doubled in both cases by using some optimization method for $PAPR$ or reducing the safety margin $M = 5$ dB used for the SFDR [151]. If we consider that the final version of each SDR could cover four bands, this would represent a total of approximately 800

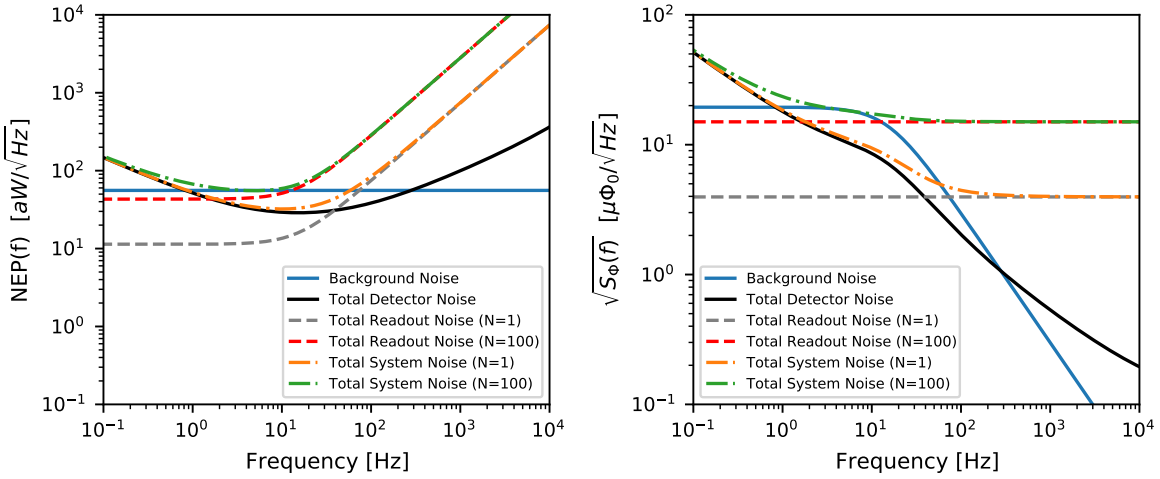

Figure 7.17: Left) Different NEP contributions for the detection System. **Right)** Flux noise contributions at the SQUID level for the proposed MMB detector with antenna-coupled scheme including the μMUX and SDR Readout System Noise. The solid blue line represents the background NEP/flux noise as a function of the frequency, while the solid black line represents the total detector NEP/flux noise without considering the multiplexing and readout noise. Red and gray Dashed lines represent the μMUX and SDR readout system NEP/flux noise considering the simultaneous readout of $N = 1$ and $N = 100$ detectors respectively. Orange and Green dash-dotted lines are the total detection system NEP/Flux noise for both cases.

channels. Although this total number of channels is below the required one, it far exceeds the maximum number of channels imposed by the linearity of the cryogenic microwave chain presented in Section 4.4.3. Therefore, the SDR does not represent the most important limitation in the early stages of development.

Once the noise levels have been determined, we can proceed to analyze whether the obtained values are acceptable for CMB observation in the QUBIC project. Answering this question is one of the most important results of this work, and as explained in Chapter 2, it requires calculating the total noise of the bolometric detection system and comparing it with the requirements for CMB observation. The result of this comparison is presented in Figure 7.17. It shows the different noise contributions of the detection system compared to the limit set by Background Noise. On the left, the contributions are expressed in NEP, while on the right, they are expressed in flux noise referred to the SQUID. The solid blue and black traces represent the Background noise and the total detector noise, respectively. Both contributions were determined in Chapter 2 for the case of the QUBIC project using MMBs and are shown in Figure 2.7. The dashed gray and red traces represent the noise of the SDR readout and multiplexing system determined throughout this thesis for the cases of $N = 1$ and $N = 100$ channels. Finally, the dotted lines represent the total noise of the detection system (i.e., detectors, multiplexing system, and SDR readout system) for both numbers of channels.

For the case of a single tone, the noise of the reading and multiplexing system is below the noise of the detector, which dominates the noise of the bolometric detection system. In contrast, for the case of $N = 100$ tones and at frequencies above 1 Hz, the noise from the readout and multiplexing system exceeds the noise from the detector but is still below the noise imposed by the Background noise. For frequencies below 1 Hz, the detector noise, dominated by the *Er* excess $1/f$ Noise, exceeds all contributions.

At this point in the analysis, we must note that the total noise of the detector marginally meets the BLIP condition, representing an unfavorable condition for the readout and multi-

plexing system. Nevertheless, for the maximum number of channels, the total noise of the detection system is on the order of the background noise, as seen in Figure 7.17 with the dotted green trace. Furthermore, the analysis conducted is very conservative as it is based on estimates of the detector noise that is still under development and on the behavior of the first version of the µMUX, which likely does not reflect the performance of an optimized µMUX.

Based on this fact, we can conclude that both SDR prototypes along with the cryogenic microwave chain meet the requirements of the QUBIC project. While the detection system marginally meets the BLIP condition, any optimization of either the bolometer, µMUX and readout system would ensure the BLIP condition. Within the scope of the detector, increasing the responsivity $\mathfrak{R}_{MMB}$ and reducing the excess 1/f noise of the *Er* are some of the most important objectives, and their optimization would exponentially improve the system's performance. In relation to the µMUX, phase and amplitude variations should be maximized through η_0 and the attenuation produced by the resonator should be minimized by reducing $|S_{21}^{\min}|$. As mentioned earlier, this would lead to a reduction in the demodulated noise.

Regarding the systems developed and evaluated during this thesis, there are two factors that can be optimized and would lead to a direct reduction in noise. The first is the noise temperature of the system T_n, which can be reduced by including an additional amplification stage after the cryogenic LNA, either at cryogenic temperatures or at room temperature. This additional amplification stage would compensate for the attenuation caused by the long cables connecting the cryostat with the SDR, allowing for a reduction in the noise introduced by the SDR while maintaining the noise temperature imposed by the cryogenic LNA. After this work, it was verified that the addition of an extra LNA at the output of the Rx path achieved system noise temperatures of $T_n \approx 4.8$ K. While this amplifier reduced the noise temperature, its implications on the linearity of the RF chain should be checked in the future. The second factor to optimize is the transmission power, which can be increased by reducing the *PAPR* or including an amplifier in the Tx path. This has not yet been tested, but attention must be paid to the degradation of the readout tone quality and whether the linearity of the RF chain can handle the elevated RF power. This analysis would lead to verifying whether the optimal solution is to increase the number of channels per band or to increase the number of bands to be covered with the SDR.

8. Conclusion and Outlook

The detection of the B-mode polarization in the CMB would confirm "inflation", proposed as a solution to the main problems of the standard Big Bang model of cosmology: the horizon, flatness, and monopole problems. Given the low intensity of the signal and the various contaminants that affect the signal from its origin to its detection, its observation represents one of the most challenging experimental tasks in observational cosmology. The Q & U Bolometric Interferometer for Cosmology (QUBIC) is a novel type of polarimeter specially designed to address these observational issues with an innovative approach that combines the advantages of interferometry in terms of control of instrumental systematic effects with those of low-temperature bolometric detectors in terms of wide-band, background-limited sensitivity [29].

During the development phase of the QUBIC technological demonstrator, several limitations were encountered that hindered progress towards the final instrument. Some of these limitations include the difficulty of micro-fabrication of the TES bolometers, the high Noise Equivalent Power (NEP) achieved by the detection system, and the reduced multiplexing factor, limited by the complex and costly cryogenic time-domain multiplexing (TDM) system. With the goal of improving the instrument's capabilities and overcoming the limitations described above, the *ITeDA* institute, in collaboration with several institutes from *KIT*, is driving the development of a novel detection chain using three new technologies. The proposed detection chain incorporates an array of Multichroic Antenna Coupled Magnetic Microbolometers (MMB), multiplexed in the frequency domain with a Microwave SQUID Multiplexer (µMUX), and read out by a Software-Defined Radio (SDR) system based on Radio-Frequency System on Chip (RFSoC) platforms. This new detection chain would represent a significant advancement in the instrument's sensitivity due to the large number of detectors with multichroic capabilities and exquisite NEP [176, 177]. This thesis focuses on the development of SDR technologies, exploiting the unique features of RFSoC devices, which combine powerful processing systems with high-speed RF data converters.

The development of SDR readout technologies requires a thorough description of the principles and operating parameters of the blocks they apply to, in this case, the MMB and the µMUX. Given the parallel development of the different technologies, this thesis extracts the requirements of the SDR readout system from two simulation frameworks developed by the working group at *ITeDA*, *IPE* and *IMS*. Simulations of the MMB prototype were used to obtain the required noise levels for Background Limited Performance (BLIP) [42, 178]. In addition, a dedicated simulation framework for the µMUX was developed as part of this thesis [101], which enables the estimation of readout noise performance based on its constitutive parameters and different noise sources. From this, the dominant noise sources and the readout parameters that optimize noise performance across different readout domains were identified. These simulation results were validated through the successful readout demonstration of a µMUX using the developed SDR prototypes.

In addition, two functional SDR prototypes exploiting the characteristics of the RFSoC devices were developed. The prototypes were characterized individually and in conjunction

with the cryogenic microwave readout chain following a characterization methodology developed in the context of this thesis. This methodology, aligned with the previously developed simulation framework, allowed for the discrimination of different noise contributions and facilitated a comparison of the performance of both SDR systems. Both the *Zero-IF SDR* prototype and the *Mixer-Less SDR* prototype successfully demonstrated the readout of a µMUX and achieved the noise performance necessary to reach BLIP condition. Considering their final version of four bands, along with a slight optimization in noise temperature and output power, they can easily reach the order of $\mathcal{O}(1000)$ multiplexed channels required by QUBIC. Additionally, the prototypes reflected the characteristics inherited from previous developments, combined with the high level of integration, great availability of processing resources, and excellent analog performance provided by RFSoC devices [105, 179]. As a summary of the unique features of each prototype, the *Zero-IF SDR* offers higher output power and greater flexibility in selecting the frequencies to be used. On the other hand, the *Mixer-Less SDR* does not require external analog frequency converters, such as IQ mixers, reducing system complexity and eliminating the complex and time-consuming process of calibrating IQ imbalances. Furthermore, it is important to note that the *Mixer-Less SDR* aligns with the current market trend in SDR system development and is favored by the release of new versions of SoC devices (e.g., *AMD Versal RF* [180] and *Intel Agilex 9* [181]).

Building on the results of this thesis and continuing the development of SDR systems, the final hardware design of the multi-band SDR systems will be defined based on the available components and subsequently manufactured. Additionally, the simultaneous development of firmware and hardware, carried out by other colleagues, specifically for the bolometric application, will be integrated into the RFSoC-based SDR system. This includes the channelizer based on the Goertzel filter and the low-noise Flux-Ramp board add-on [118, 182]. As part of the future work related to the integration of the bolometric detection chain, the demonstration of the first MMB readout using the µMUX and SDR readout systems is scheduled for 2025. The first readout results of an MMB will validate the detector performance predicted by the simulation frameworks and enable the refinement of the noise requirements for the multiplexing and SDR readout systems.

A. DAC Reconstruction Waveforms

An Analog-to-Digital Converter (DAC) is a device that receives numerical data through a digital interface (samples) and converts them to a voltage at the output. A linear relationship is assumed between the digital value and the corresponding analog value, and the samples are converted to analog values at a constant rate given by the sampling rate f_s. The spectrum of the analog signal $v(t)$ at the output of the DAC can be expressed as:

$$v(t) = \left[x(t) \sum_{n=-\infty}^{\infty} \delta(t - kT_s) \right] * r(t). \tag{A.1}$$

Where $x(t)$ is the analytical representation of the signal reproduced by the DAC, $T_s = 1/f_s$ is the sampling period, and $(*)$ represents convolution in time. $r(t)$ describes how the voltage output of the DAC behaves between different samples and is nonzero only for $0 \leq t < T_s$. The corresponding frequency spectrum of the DAC voltage output is:

$$V(f) = R(f) \left[X(f) * \sum_{n=-\infty}^{\infty} \delta(f - kf_s) \right]. \tag{A.2}$$

Here, $V(f)$, $R(f)$ and $X(f)$ denote the Fourier transform of $v(t)$, $r(t)$ and $x(t)$. The expression between brackets represents a series of replicas of the spectrum of the original signal $X(f)$ located at integer multiples of the sampling frequency. This formula is analog to the spectrum of discrete time signal presented in appendix B except for a frequency-dependent attenuation factor $r(f)$ given by the reconstruction waveform $r(t)$ that manifests as a frequency-dependent attenuation. Therefore, the properly choice of $r(t)$ can be used to maximize power in the required Nyquist zones. Modern High-speed DACs exploit this effect and allowing the selection of different reconstruction waveforms depending on the desired Nyquist zone operation. Three common functions for $r(t)$ are shown in the left side of Figure A.1 including the non-return-to-zero (NRZ), return-to-zero (RZ), and mix-mode/RF-mode (MIX). The NRZ waveform is the most common and is often referred to as a zero-order hold, this reconstruction waveform hold the output value constant for T_s until the next sample (blue). More advanced waveforms can drive the output to zero or invert the output exactly at $Ts/2$. The former describes the RZ mode (orange) and the latter describes the mix mode (dashed green). Although this represents an advantage, it requires the analog core of the DAC to have a higher sampling rate. In the case of the RFSoC DACs, the supported modes are NRZ and MIX. The analytical expression for the attenuation imposed by the NRZ mode is

$$R_{NRZ}(f) = T_s e^{-j2\pi f T_s/2} \operatorname{sinc}\left(\frac{2\pi f T_s}{2} \right), \tag{A.3}$$

while for the MIX mode, it is

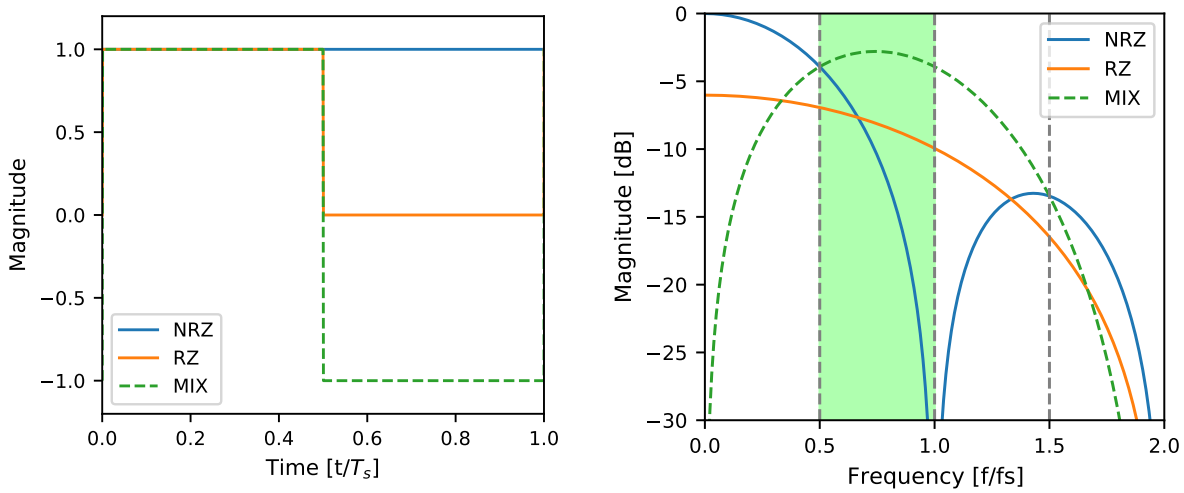

Figure A.1: Reconstruction Waveforms used by High Speed Digital-to-Analog Converters. **Left)** Time Domain Waveforms. **Right)** Power Spectrum of the Reconstruction Waveforms. The second Nyquist zone is highlighted in green.

$$R_{MIX}(f) = \frac{2\pi f T_s^2}{4} e^{-j(2\pi f T_s - \pi)/2} \operatorname{sinc}^2\left(\frac{2\pi f T_s}{4}\right). \tag{A.4}$$

The right side of Figure A.1 shows the attenuation imposed by the reconstruction waveforms previously mentioned. In the case of the blue curve (NRZ), it represents the least attenuation for signals in the first Nyquist zone ($0 < f_s/2$), while the dotted green curve (MIX) shows the least attenuation for the generation in the second Nyquist zone ($f_s/2 < f_s$). The frequency-dependent attenuation may lead to distortion in the generated signals, which is why the RFSoC provides compensation filters that exhibit attenuation $|H(f)| \approx 1/|R(f)|$ in order to achieve flat total attenuation [146]. A detailed analysis of the derivation of the mathematical expressions used in this appendix can be found in the following references [164, 183, 184].

B. Band-Pass Sampling

In signal processing, band-pass sampling or under-sampling is a technique that allows to sample a band-pass signal at a sample rate below its Nyquist rate but is still able to reconstruct the signal [154]. Consider an analog signal $x_a(t)$ sampled at a sampling rate $f_s = 1/T_s$. The spectrum of the discrete-time signal $X(f)$ can be expressed in terms of the spectrum of the analog signal $X_a(f)$ as follows:

$$X(f) = f_s \sum_{k=-\infty}^{\infty} X_a(f - kf_s). \tag{B.1}$$

It consists of the summation of infinite replicas of the analog spectrum $X_a(f)$, scaled by f_s and separated by a distance of f_s. Based on this expression, the sampling theorem states that an analog signal with finite bandwidth B must be sampled at a frequency $f_s > 2B$ to avoid the overlapping of replicas, which would cause aliasing. In this way, the signal can be reconstructed exactly [154]. Band-pass sampling, or under-sampling, uses aliasing to our advantage to sample signals with frequencies higher than the sampling frequency f_s.

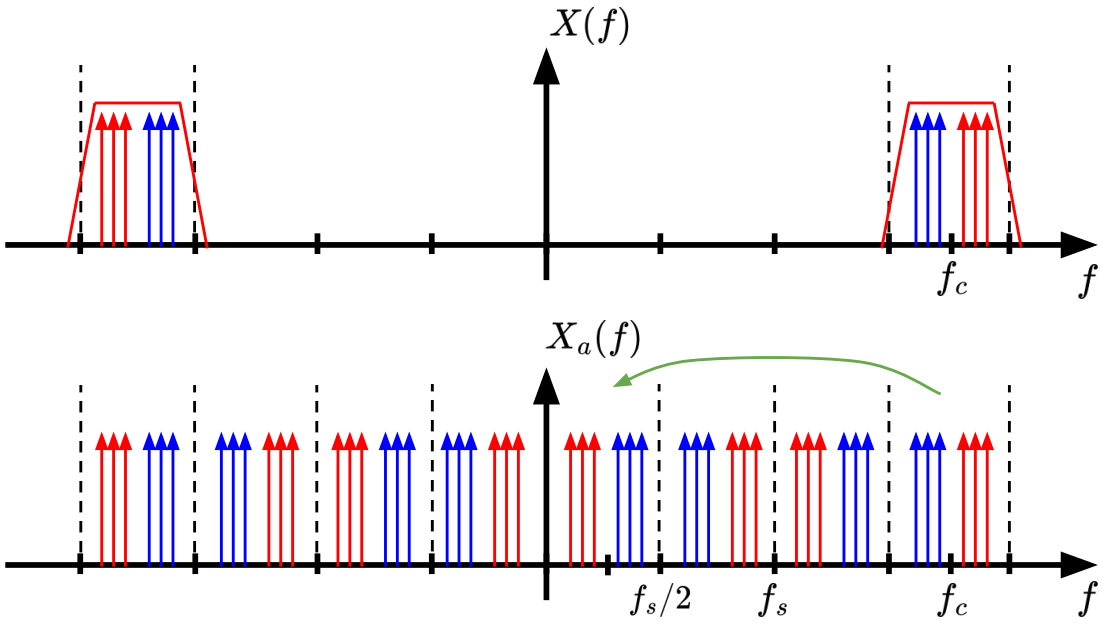

Figure B.1: Band-Pass Sampling of a Band-pass Signal centered at f_c and with bandwidth $B < f_s/2$. **Top)** Analog signal spectrum $X_a(f)$ centered at f_c and bandwidth $B < f_s/2$. **Bottom)** Discrete-time signal spectrum $X_(f)$ where the spectrum signal is replicated.

As an example, consider the signal shown at the top of Figure B.1, which is centered at a frequency $f_c > f_s/2$ and has a bandwidth of $B < f_s/2$ (i.e. a band-pass signal). Using equation B.1, it is possible to demonstrate that the replicas of the signal are centered at positions $f_c - kf_s$, and at least one of them will be positioned in the first Nyquist zone, between $0 < f < f_s$, without any aliasing. This is shown in the lower part of Figure B.1. This effect is called "spectrum folding", as all signals in the different Nyquist zones are folded onto the first zone. In this particular example the signal located in the fourth Nyquist zone was folded to the first one. While band pass sampling allows acquiring signals outside the first zone, it is important to note that any unfiltered spectral component outside the bandwidth of the signal $X_a(f)$ will also fold into the first zone, affecting the desired signal. For this reason, proper filtering of out-of-band signals must be ensured.

C. RFSoC Data Converters Characterization

The readout of multiplexed superconducting detectors in the frequency domain requires the generation/acquisition of high-frequency and high-purity signals. One of the most widely used metrics to define the quality of DACs and ADCs processing high-purity signals is the Spurious-Free Dynamic Range (SFDR), defined as the power difference between the desired signal and the highest power spur within the desired operational bandwidth. Since this parameter is not specified in the datasheets for various configuration parameters, the characterization of the DACs and ADCs of the RFSoC was performed under different operating parameters using microwave top-bench instruments. Along with SFDR, the output power of the DACs and the frequency response of the ADCs at different frequencies were also characterized.

C.1 DAC Characterization

The characterization was carried out using the ZCU216 evaluation kit along with the clock generation board CLK104 and the balun board XM655. Using the evaluation tool provided by AMD (RF Data-Converters Evaluation Tool[1]), a Python script was created, which through socket communication allows generating a tonal signal at different frequencies and power levels. Given the desired frequency range, the required Balun was selected, and its SMA output connector was connected to a spectrum analyzer R&S model FSWP50 [166]. The characterization was performed with the goal of evaluating the performance of the converters when used in the two SDR systems proposed in Sections 5.4 and 5.5. Therefore, the characterization was carried out at the sampling frequencies of $f_{DAC} = 1$ GHz and $f_{DAC} = 8$ GHz. For both cases the selected output current is $i_{out} = 32$ mA.

Figure C.1 shows the results for a frequency of $f_{DAC} = 1$ GHz. The left graph corresponds to the output power as a function of frequency, measured by the spectrum analyzer for two different amplitudes relative to the full scale of the DAC. Along the measurements, the compensation required by the NRZ reconstruction waveform (see equation A.3) was activated. For this sampling rate, the *Minicircuits TCM2-33WX+* Balun is used. The blue curve shows $P_{out} = -5$ dBFS, while the orange curve shows $P_{out} = -10$ dBFS. These values correspond approximately to -2 and -7 dBm, respectively. The results show a slope of approximately 1 dB over the Nyquist zone. The right side of Figure C.1 presents the SFDR results for previously mentioned power levels and using the two available decoders (High-Linearity and SDR Optimized). The highest SFDR is achieved using the HL decoder and $P_{out} = -10$ dBFS. These previous results are consistent with the results provided by the manufacturer [185].

The results for the frequency of $f_{DAC} = 8$ GHz are shown in Figure C.2. The left graph corresponds to the output power as a function of frequency, measured by the spectrum ana-

[1] https://docs.amd.com/r/en-US/ug1433-zcu216-rfsoc-eval-tool

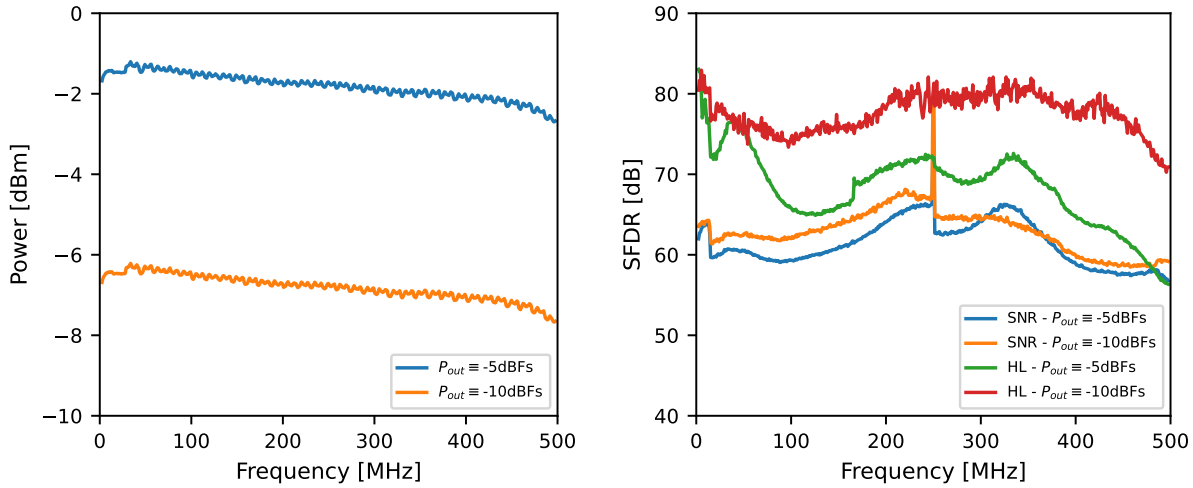

Figure C.1: Left) DAC output power vs. frequency for different tone amplitudes. **Right)** DAC Spurious-Free Dynamic Range vs. frequency for different tone amplitudes using the High SNR and High Linearity DAC decoders. The DAC is sampling at $f_{DAC} =$ 1 GHz.

lyzer for two different amplitudes relative to the full scale of the DAC. Here, the compensation required by the MIX reconstruction waveform (see equation A.4) was used. The blue curve shows $P_{out} = -5$ dBFS, while the orange curve shows $P_{out} = -10$ dBFS. For the 4 to 5 GHz band, the Balun *Anaren BD3150N50100AHF* was used, while for the 5 to 8 GHz band, the Balun *Anaren BD4859N50100AHF* was used. A total slope of 7 dB is observed, with only 3 dB from 4 to 6 GHz, consistent with the maximum operating frequency at -3 dB specified by the manufacturer [185]. The output power is also consistent with the manufacturer's specification for a DAC output current of 32 mA. For each frequency, the full spectrum from 0 to 12 GHz was acquired, and using a script, the SFDR was calculated. Since the bandwidth of interest for the SDR Mixer-Less prototype is 1 GHz, the SFDR was only evaluated at 1 GHz wide bands (i.e., from $4-5$, $5-6$, $6-7$, and $7-8$ GHz). The right side of the Figure C.2 shows the SFDR for the two types of available encoders (SNR and High-Linearity) and for the previously used power levels. As expected, the high-linearity mode and low power operation achieve the highest SFDR. Although all show irregular behavior at the edges of the band and between 5 and 6 GHz, the cause of this behavior is unknown.

C.2 ADC Characterization

The characterization of the ADCs was performed by connecting a microwave generator, the R&S model SMA100B [186], to the corresponding balun for the band to be analyzed. The same baluns used for the DAC were employed in this case. We started configuring the ADC with a sample frequency of $f_{ADC} = 1$ GHz, and a high-quality tonal signal was injected, performing a sweep in the first Nyquist zone (specifically between 10 and 500MHz). The quality of the SMA100B ensures that there are no in band or out-of-band signals that could inferred as a spur [186]. The results for $f_{ADC} = 1$ GHz are shown in Figure C.4. The graph on the left of figure shows the required power from the generator to achieve a constant amplitude value at the ADC output. The blue trace corresponds to $P_{in} = -5$ dBFS, while the orange trace corresponds to $P_{in} = -10$ dBFS. These values correspond to -4 and -9 dBm of input power respectively. The frequency response has a total slope of 1 dB over the 500 MHz range.

The graph on the right in Figure C.4 shows the SFDR of the ADC. It was calculated

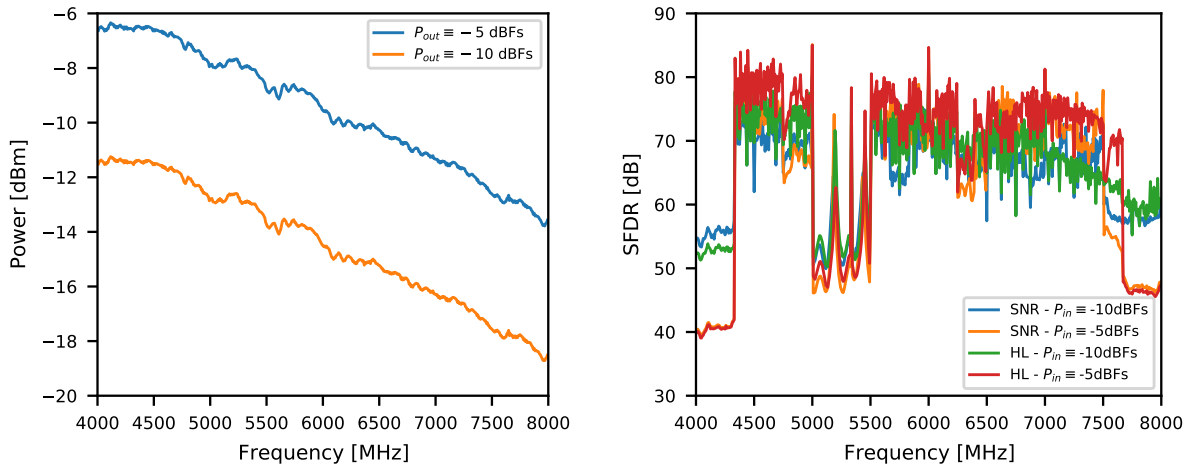

Figure C.2: Left) DAC output power vs. frequency for different tone amplitudes. **Right)** DAC Spurious-Free Dynamic Range vs. frequency for different tone amplitudes using the High SNR and High Linearity DAC decoders. The DAC is sampling at $f_{DAC} = 8$ GHz.

based on the FFT of the acquired time trace. It shows a flat SFDR for both powers with a minimum of 72 dB within the 10 to 400 MHz band. A reduction in the SFDR is observed at low frequencies due to the lower limit of the balun and at higher frequencies due to the proximity to $f_{ADC}/2 = 500$ MHz. These results are also consistent with the datasheet [185] and other articles[179].

For the characterization of the ADC performing bandpass sampling at at $f_{ADC} = 2$ GHz, the tone signal was swept between 4 and 8 GHz. Depending on the Nyquist zone, acquired signals may appear mirrored. The measurement script used is capable of identifying the bands where the spectrum is folded and calculating the corresponding RF frequency. For this measurement, the automatic calibration mode (Autocal) [146] was used. The graph on the left of Figure C.4 shows the required power from the generator to achieve a constant amplitude value at the ADC output. The blue trace corresponds to $P_{in} = -5$ dBFS, while the orange trace corresponds to $P_{in} = -10$ dBFS. The frequency response presents a total slope of 5 dB over the 4 GHz range.

The graph in the right in Figure C.4 shows the SFDR of the ADC. It was calculated based on the FFT of the acquired time trace. As with the input power, the SFDR was calculated for the two constant amplitude values previously used. Again, it is observed that at low power and low frequencies, the ADC achieves higher SFDR. The glitches present in the graph correspond to spurious signals generated when the signal is located near the limits between Nyquist zones or to interleaving spurs near the frequencies $f_{ADC}/2$ and $f_{ADC}/4$.

It is worth noting that for all measurements performed on the ADCs, the required background calibration was maintained to minimize interleaving spurs [146], and at the same time, the Dither addition was enabled [187].

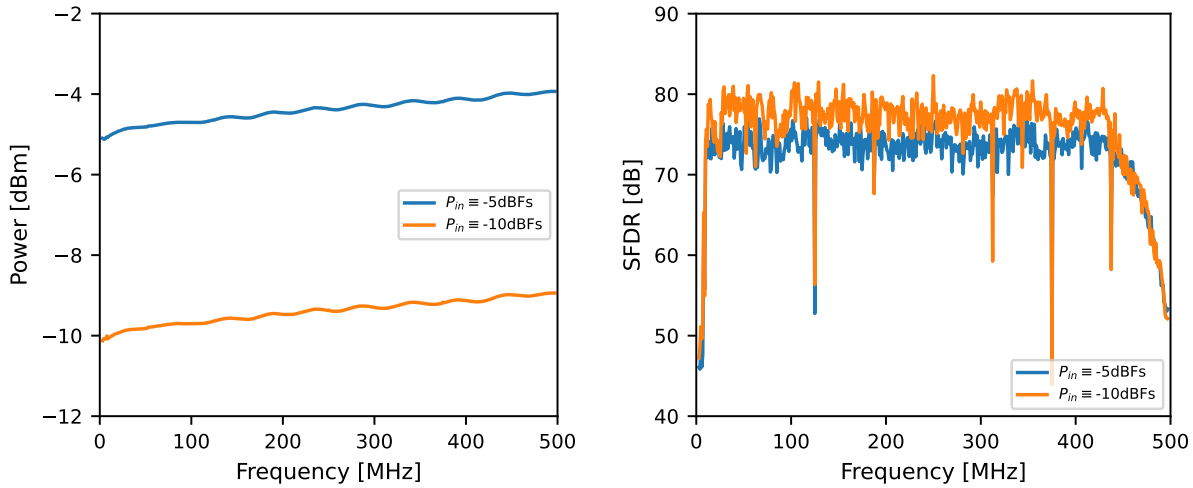

(a)
t

Figure C.3: Left) ADC input power vs. frequency required for constant output amplitude. **Right)** ADC Spurious-Free Dynamic Range vs. frequency for constant output amplitude. The ADC is sampling at $f_{ADC} = 1$ GHz.

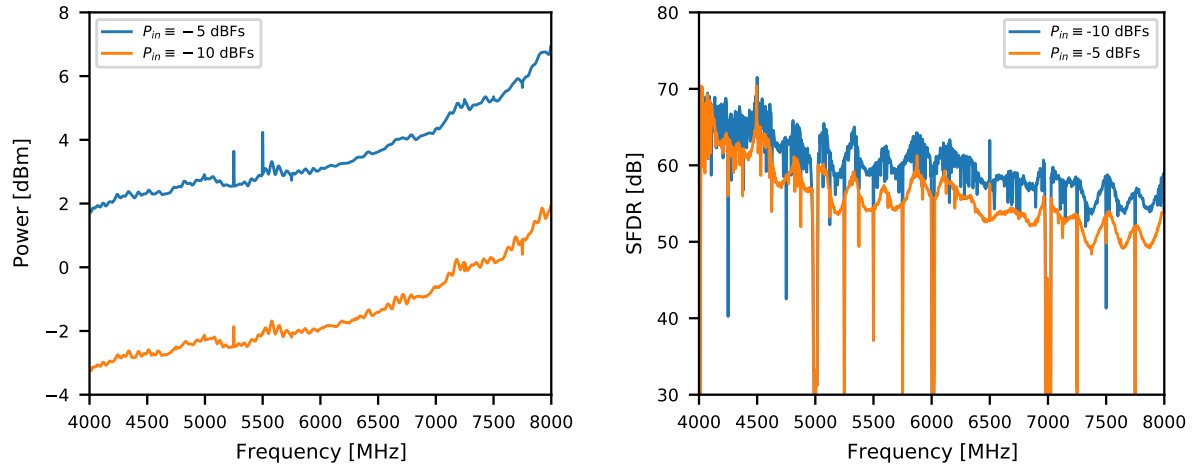

Figure C.4: Left) ADC input power vs. frequency required for constant output amplitude. **Right)** ADC Spurious-Free Dynamic Range vs. frequency for constant output amplitude. The ADC is sampling at $f_{ADC} = 2$ GHz.

D. PLL Synthesizer Phase Noise

The CLK104 Add-on Board is equipped with two wideband Phase-Locked Loop (PLL) synthesizers (*LMX2594*) used to generate DAC and ADC sampling clocks (see Figure 5.5). Most of the phase noise characteristics of the sampling clocks are determined by the PLL components. A simplified block diagram of a PLL is shown in Figure D.1. It comprises five blocks: 1) a Reference Oscillator, 2) a Voltage-Controlled Oscillator (VCO), 3) a frequency N Divider. 4) a Loop-Filter, and 5) a Phase Detector.

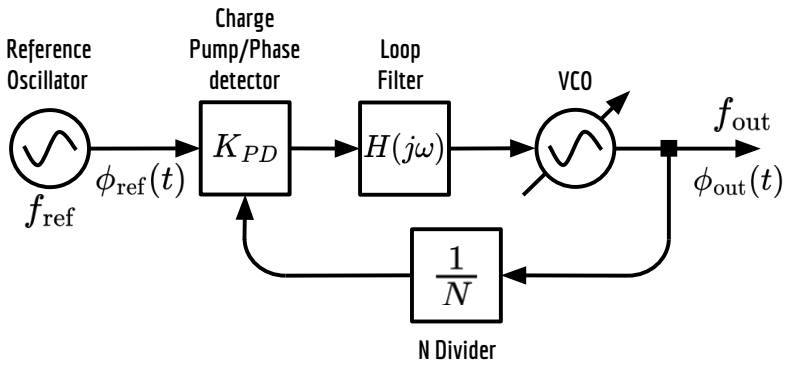

Figure D.1: Phase-Locked Loop (PLL) block diagram. The synthesizer creates a frequency f_{out} from a reference oscillator of N times lower frequency f_{ref}. The feedback system allows the output phase ϕ_{out} to be locked to the reference phase $\phi_{\text{ref}}(t)$. The phase noise response is determined by the noise contributed by each block and the closed-loop gain between each point in the system and the output $\phi_{\text{out}}(t)$.

When the system is locked, the VCO generates an output frequency f_{out} which is divided N times and sent to the phase detector. The phase detector compares the phases of the signal coming from the divider $\phi_{\text{out}}(t)/N$ with that of the reference oscillator $\phi_{\text{ref}}(t)$. At its output, the phase detector (usually implemented as a charge pump) generates a voltage proportional to the phase difference $V_{PD}(t) = K_{PD}[\phi_{\text{ref}}(t) - \phi_{\text{out}}(t)/N]$. This signal is filtered and used to close the loop by adjusting the VCO voltage $V_{VCO}(t)$ such that the generated frequency is in phase with that of the reference oscillator. In this condition we can state that the output signal is an exact multiple of the frequency of the reference oscillator $f_{\text{out}} = Nf_{\text{ref}}$ and follows its phase variations. Typically the control loop is designed to have the phase error in the steady state at zero (i.e. $\phi_{\text{ref}}(t) - \phi_{\text{out}}(t)/N = 0$).

The total phase noise $S_{\phi}^{tot}(\Delta f)$ at the PLL output is determined by the contribution of each of the PLL components. Using the closed-loop gain between each system component and the output $G_i(f)$, it is possible to calculate the total phase noise by adding all noise components $S_{\phi}^{i}(\Delta f)$. Using the simulation software provided by the manufacturer, the phase noise

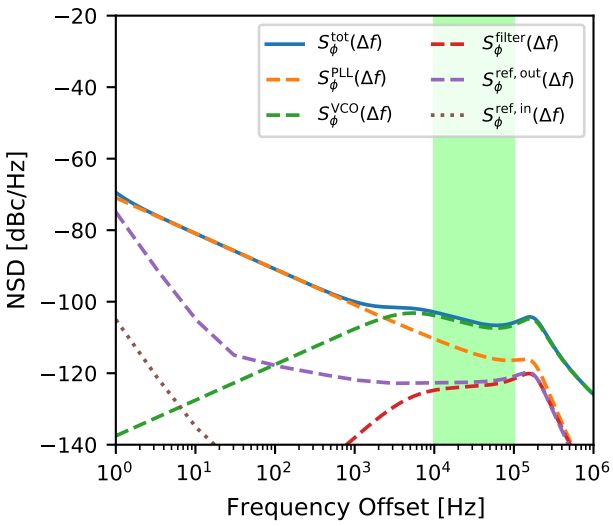

Figure D.2: Phase locked loop phase noise contributions for a frequency $f_{DAC} = 8$ GHz generated from a reference frequency of $f_{ref} = 250$ MHz. The solid blue line represents the total phase noise $S_\phi^{tot}(\Delta f)$, while dashed lines are the phase noise contributions $S_\phi^{i}(\Delta f)$ of each block shown in D.1. The dotted brown line corresponds to the reference oscillator phase noise at the input $S_\phi^{in,out}(\Delta f)$, while $S_\phi^{ref,out}(\Delta f)$ is the oscillator phase noise referred to the output.

of each component of the LMX2594 synthesizer was estimated for the configuration used in the CLK104 [188, 147]. For demonstration purposes, a $f_{\text{ref}} = 250$ MHz reference oscillator with phase noise characteristics $S_\phi^{\text{ref,in}}(\Delta f)$ equivalent to a Rubidium oscillator was adopted for the simulations [160]. The simulation results for a frequency of $f_{\text{out}} = 8$ GHz are shown in Figure D.2. In this case the synthesizer parameters were optimized to obtain the minimum phase noise in the green shaded region. Only software configurable parameters were modified, to avoid modifying the CLK104 hardware.

The results show that the total phase noise $S_\phi^{\text{tot}}(\Delta f)$ for this configuration is determined by the internal components of the synthesizer. At low frequencies, it is dominated by the PLL (Divider and Phase Detector) noise $S_\phi^{PLL}(\Delta f)$ (dashed orange line), while at higher frequencies it is dominated by the VCO phase noise $S_\phi^{VCO}(\Delta f)$ (dashed green line). Furthermore, we can conclude that even with the use of a Rubidium oscillator the phase noise is dominated by the PLL circuitry. This is mainly due to three factors: First, the integrated VCO has high noise level at the operating frequency. Second, the high output frequency imposes a division factor $N = 32$ amplifying both the divider and reference noise by $20\log_{10}(N)$ (see magenta line in the Figure D.2). Third, the PLL generates an electrical noise at the input of the VCO which creates a strong $1/f$ component given the integrating characteristics of the VCO [189]. Therefore, the phase noise can only be improved by using a higher quality PLL and VCO as well as reducing the value of N by using a higher frequency reference. This previous analysis can also be performed using the phase noise characteristics of the *LMK04828B* with the internal 10 MHz TXCO reference oscillator. However, there is no difference at the frequencies of interest (green region) since the total phase noise is dominated by the *LMX2594* PLL components.

Phase noise present in the ADC or DAC sampling clocks is directly transferred to the generated/acquired tone. In this case the phase noise is dominated by the DAC sampling at $f_{\text{out}} = 8$ GHz. This is consistent with the measurement results shown in Figure 4.3 and with experimental results shown in other articles related with Direct-RF SDR systems based on RFSoC devices used in the field of Quantum Computing [163, 100]. More details about phase noise in PLLs and its optimization can be found in the following references [190, 189].

E. IQ Imbalance and Local Oscillator Leakage

Consider the case in which we use a real IQ mixer to convert a single tone to frequency at a frequency f_1 amplitude A_1 and phase ϕ_1. In this case, the input signals are $x_{Tx,I}(t) = A_1 \cos(2\pi f_1 t + \phi_1)$ and $x_{Tx,Q}(t) = A_1 \sin(2\pi f_1 t + \phi_1)$. In a real IQ mixer, two undesired effects arise. The first is that both local oscillators are not in perfect quadrature and have different amplitudes. These imbalances can be included in the reference signals to evaluate their effect. The output signal of the real IQ mixer can be written as:

$$x_{Tx}(t) = A_1 \cos(2\pi f_1 t + \phi_k)\alpha \cos(2\pi f_{LO} t - \frac{\theta}{2}) - A_1 \sin(2\pi f_1 t + \phi_k)\beta \sin(2\pi f_{LO} t + \frac{\theta}{2}). \quad \text{(E.1)}$$

Where $\epsilon = \alpha/\beta$ and θ are the gain and amplitude imbalances. Using trigonometric identities, these expressions can be regrouped to identify two frequency components. One is the desired component at $f_{LO} + f_1$, and the other, called the image frequency, is at $f_{LO} - f_1$. The powers of these two components can be calculated using the following expressions:

$$P_{f_{LO}+f_1} = \frac{1}{2} A_1^2 \left[\epsilon^2 + 1 + 2\epsilon \cos(\theta)\right], \quad \text{(E.2)}$$

$$P_{f_{LO}-f_1} = \frac{1}{2} A_1^2 \left[\epsilon^2 + 1 - 2\epsilon \cos(\theta)\right]. \quad \text{(E.3)}$$

In the case of an ideal mixer, where $\epsilon = 1$ and $\theta = 0$, the image frequency vanishes, i.e., $P_{f_{LO}-f_1} = 0$, as expected. For the general case where $\epsilon \neq 1$ and $\theta \neq 0$, the ratio between the power of the desired tone and the power of the image frequency defines the Image Rejection Ratio (IMRR)

$$IMRR = \frac{P_{f_{LO}+f_1}}{P_{f_{LO}-f_1}} = \frac{\epsilon^2 + 1 - 2\epsilon \cos(\theta)}{\epsilon^2 + 1 + 2\epsilon \cos(\theta)}. \quad \text{(E.4)}$$

This factor is widely used by mixer manufacturers to express the quality of the device. Sometimes also called Sideband Suppresion Ratio (SSR). Typically, an IMRR factor greater than 30 dB indicates a good balance. Higher values can be achieved by applying small amplitude and phase imbalances to the tones in order to compensate for the imbalances ϵ and θ. It is important to mention that both $\epsilon(f)$ and $\theta(f)$ are frequency-dependent, so corrections must be applied individually to each tone.

The second problem present in IQ mixers is the low isolation between the local oscillator port and the RF output. This causes a copy of the local oscillator, A_{leak}, to leak into the output

$x_{Tx}(t)$. While it is an attenuated version, the local oscillator is several dB more powerful than the signals to be converted. Therefore, in some cases, it may even be more powerful. This can be observed in Figure 6.4. To explain its origin and compensation, let us consider the following equation:

$$x_{Tx}(t) = x_I \cos(2\pi f_{LO} t) - x_Q \sin(2\pi f_{LO} t) + A_{leak} \cos(2\pi f_{LO} t + \theta_{leak}). \tag{E.5}$$

The calibration process considers the conversion of two continuous signals, x_I and x_Q, along with the inclusion of the Local-Oscillator leakage, $A_{leak} \cos(2\pi f_{LO} t + \theta_{leak})$. The proper selection of x_I and x_Q should be capable of generating an out-of-phase signal with equal amplitude that cancels out the LO. By solving the equation for $x_{Tx}(t) = 0$, the following is obtained:

$$x_I = -A_{leak} \cos(\theta_{leak}), \tag{E.6}$$

$$x_Q = -A_{leak} \sin(\theta_{leak}). \tag{E.7}$$

In summary, the calibration of IQ imbalances and LO leakage should be carried out by adjusting the amplitude and phase values of each tone and adding DC offsets to each component [170]. For the calibration process, a spectrum analyzer is typically used, which allows measuring the oscillator power and the image tones while the calibration algorithm is being executed.

Bibliography

[1] N. Deruelle, J.-P. Uzan, and P. de Forcrand-Millard, *Relativity in Modern Physics*. Oxford University Press, 2018.

[2] A. A. Penzias and R. W. Wilson, "A measurement of excess antenna temperature at 4080 mc/s.," , vol. 142, pp. 419–421, 1965.

[3] M. D. Niemack, Ade, and others., "ACTPol: a polarization-sensitive receiver for the atacama cosmology telescope," in *Millimeter, Submillimeter, and Far-Infrared Detectors and Instrumentation for Astronomy V*, SPIE, 2010.

[4] S. Masi, P. De Bernardis, G. De Troia, and G. et al., "The BOOMERanG experiment and the curvature of the universe," *Progress in Particle and Nuclear Physics*, vol. 48, no. 1, p. 243–261, 2002.

[5] G. F. Smoot, "Cobe observations and results," in *Conference on 3K cosmology*, ASCE, 1999.

[6] Planck Collaboration, Aghanim, N., Akrami, Y., Arroja, F., Ashdown, M., Aumont, J., Baccigalupi, C., Ballardini, M., Banday, A. J., Barreiro, R. B., Bartolo, N., Basak, S., and others., "Planck 2018 results - I. overview and the cosmological legacy of planck," *AA*, vol. 641, p. A1, 2020.

[7] K. Abazajian, G. Addison, P. Adshead, Z. Ahmed, , and others., "CMB-S4 Science Case, Reference Design, and Project Plan," 2019.

[8] Z. A. S. A. Peter Ade, James Aguirre and others., "The Simons Observatory: science goals and forecasts," *Journal of Cosmology and Astroparticle Physics*, vol. 2019, no. 02, p. 056, 2019.

[9] Z. A. S. W. A. Kevork N. Abazajian, Peter Adshead and others., "CMB-S4 science book, first edition," 2016.

[10] de Bernardis, P. and Ade, P. A. R. and Bock, J. J. and Bond, J. R. and Borrill, J. and Boscaleri, A. and Coble, K. and Crill, B. P. and De Gasperis, G. and Farese, P. C. and Ferreira, and others., "A Flat universe from high resolution maps of the cosmic microwave background radiation," *Nature*, vol. 404, pp. 955–959, 2000.

[11] Planck Collaboration, Akrami, Y., Ashdown, M., Aumont, J., Baccigalupi, C., Ballardini, M., and a. Banday, A. J., "Planck 2018 results - VII. Isotropy and statistics of the CMB," *AA*, vol. 641, p. A7, 2020.

[12] S. Dodelson, *Modern Cosmology*. Amsterdam: Academic Press, 2003.

[13] A. H. Guth, "Inflationary universe: A possible solution to the horizon and flatness problems," *Phys. Rev. D*, vol. 23, pp. 347–356, 1981.

[14] A. Readhead, S. Myers, T. Pearson, Sievers, and others., "Polarization Observations with the Cosmic Background Imager," *Science (New York, N.Y.)*, vol. 306, pp. 836–44, 2004.

[15] G. Hinshaw, D. N. Spergel, L. Verde, R. S. Hill, S. S. Meyer, and others., "First-Year Wilkinson Microwave Anisotropy Probe (WMAP) Observations: The Angular Power Spectrum," *The Astrophysical Journal Supplement Series*, vol. 148, no. 1, p. 135, 2003.

[16] J. T. Sayre, C. L. Reichardt, J. W. Henning, P. A. R. Ade, A. V., and others., "Measurements of *B*-mode polarization of the cosmic microwave background from 500 square degrees of SPTpol data," *Phys. Rev. D*, vol. 101, p. 122003, 2020.

[17] E. J. Baxter, R. Keisler, S. Dodelson, K. A. Aird, S. W. Allen, and Ashby, "A measurement of gravitational lensing of the cosmic microwave background by galaxy clusters using data from the south pole telescope.," *The Astrophysical Journal*, vol. 806, no. 2, p. 247, 2015.

[18] M. H. Abitbol, Z. Ahmed, and others., "CMB-S4 technology book, first edition," 2017.

[19] R. C. L. H. J. W. A. Sayre, J. T. and others., "Measurements of B-mode polarization of the cosmic microwave background from 500 square degrees of SPTpol data," *Physical Review D*, vol. 101, no. 12, 2020.

[20] T. P. Collaboration *et al.*, "A Measurement of the Cosmic Microwave Background B-mode Polarization Power Spectrum at Subdegree Scales from Two Years of polarbear Data," *The Astrophysical Journal*, vol. 848, no. 2, p. 121, 2017.

[21] P. A. R. Ade, Z. Ahmed, R. W. Aikin, Alexander, and others., "Constraints on Primordial Gravitational Waves Using Planck, WMAP, and New BICEP2/*Keck* Observations through the 2015 Season," *Phys. Rev. Lett.*, vol. 121, p. 221301, 2018.

[22] S. Dahal, M. Amiri, J. Appel, B. D., and et al., "The CLASS 150/220 GHz polarimeter array: Design, assembly, and characterization," *Journal of Low Temperature Physics*, vol. 199, pp. 289–297, 2020.

[23] A. Suzuki, P. Ade, Y. Akiba, *et al.*, "The Polarbear-2 and the Simons Array experiments," *Journal of Low Temperature Physics*, vol. 184, 2016.

[24] S. Henderson, R. Allison, J. Austermann, Baildon, and others., "Advanced ACTPol cryogenic detector arrays and readout," *Journal of Low Temperature Physics*, vol. 184, 2016.

[25] J. A. Grayson, P. A. R. Ade, Z. Ahmed, K. D. Alexander, Amiri, and others., "BICEP3 performance overview and planned Keck Array upgrade," vol. 9914 of *Society of Photo-Optical Instrumentation Engineers (SPIE) Conference Series*, p. 99140S, 2016.

[26] T. P. Collaboration *et al.*, "A Measurement of the Cosmic Microwave Background B-mode Polarization Power Spectrum at Subdegree Scales from Two Years of polarbear Data," *The Astrophysical Journal*, vol. 848, no. 2, p. 121, 2017.

[27] T. L. collaboration, "The large scale polarization explorer (LSPE) for CMB measurements: performance forecast," *Journal of Cosmology and Astroparticle Physics*, vol. 2021, no. 08, p. 008, 2021.

[28] M. Hazumi, P. A. R. Ade, Y. Akiba, D. Alonso, Arnold, and others., "LiteBIRD: A Satellite for the Studies of B-Mode Polarization and Inflation from Cosmic Background Radiation Detection," *Journal of Low Temperature Physics*, vol. 194, no. 5-6, pp. 443–452, 2019.

[29] T. Q. collaboration et al., "QUBIC I: Overview and science program," *Journal of Cosmology and Astroparticle Physics*, vol. 2022, no. 04, p. 034, 2022.

[30] P. de Bernardis, P. Ade, G. Amico, Auguste, and others., "QUBIC: Measuring CMB polarization from Argentina," *Boletin de la Asociacion Argentina de Astronomia La Plata Argentina*, vol. 60, pp. 107–114, 2018.

[31] S. Ali, P. Rossinot, L. Piccirillo, W. K. Gear, P. Mauskopf, P. Ade, V. Haynes, and P. Timbie, "MBI: Millimetre-wave bolometric interferometer," *AIP Conf. Proc.*, vol. 616, no. 1, p. 126, 2002.

[32] P. T. Timbie, G. S. Tucker, P. A. R. Ade, Ali, and others., "The Einstein polarization interferometer for cosmology (EPIC) and the millimeter-wave bolometric interferometer (MBI)," , vol. 50, no. 11-12, pp. 999–1008, 2006.

[33] G. Polenta, M. Calvo, L. Conversi, P. de Bernardis, , and others., "The Brain Experiment," in *The Eleventh Marcel Grossmann Meeting On Recent Developments in Theoretical and Experimental General Relativity, Gravitation and Relativistic Field Theories*, pp. 1680–1688, 2008.

[34] P. Timbie and G. Tucker, "Adding interferometry for CMBPol," *Journal of Physics: Conference Series*, vol. 155, p. 012003, 2009.

[35] T. Q. collaboration et al., "QUBIC V: Cryogenic system design and performance," *Journal of Cosmology and Astroparticle Physics*, vol. 2022, no. 04, p. 038, 2022.

[36] T. Q. collaboration et al., "QUBIC VI: Cryogenic half wave plate rotator, design and performance," *Journal of Cosmology and Astroparticle Physics*, vol. 2022, no. 04, p. 039, 2022.

[37] T. Q. collaboration et al., "QUBIC VII: The feedhorn-switch system of the technological demonstrator," *Journal of Cosmology and Astroparticle Physics*, vol. 2022, no. 04, p. 040, 2022.

[38] T. Q. collaboration et al., "QUBIC VIII: Optical design and performance," *Journal of Cosmology and Astroparticle Physics*, vol. 2022, no. 04, p. 041, 2022.

[39] T. Q. collaboration et al., "QUBIC IV: Performance of TES bolometers and readout electronics," *Journal of Cosmology and Astroparticle Physics*, vol. 2022, no. 04, p. 037, 2022.

[40] G. D'Alessandro *et al.*, "QUBIC Experiment Toward the First Light," *J. Low Temp. Phys.*, vol. 209, no. 5-6, pp. 839–848, 2022.

[41] M. Piat *et al.*, "QUBIC: Using NbSi TESs with a Bolometric Interferometer to Characterize the Polarization of the CMB," *Journal of Low Temperature Physics*, vol. 200, pp. 363–373, 2020.

[42] J. M. Geria, M. R. Hampel, S. Kempf, J. J. Bonaparte, and others., "Suitability of magnetic microbolometers based on paramagnetic temperature sensors for CMB polarization measurements," *Journal of Astronomical Telescopes, Instruments, and Systems*, vol. 9, no. 1, pp. Art.–Nr.: 016002, 2023.

[43] J. Mates, *The Microwave SQUID Multiplexer*. PhD thesis, University of Colorado, 2011.

[44] AMD, *Zynq UltraScale+ RFSoC Data Sheet: Overview*, 2022.

[45] L. Gastaldo *et al.*, "The electron capture in 163Ho experiment – ECHo," *The European Physical Journal Special Topics*, vol. 226, pp. 1623–1694, 2017.

[46] W. Hu and S. Dodelson, "Cosmic microwave background anisotropies," *Annual Review of Astronomy and Astrophysics*, vol. 40, no. Volume 40, 2002, pp. 171–216, 2002.

[47] J. M. Kovac, E. M. Leitch, C. Pryke, Carlstrom, and others., "Detection of polarization in the cosmic microwave background using DASI," *Nature*, vol. 420, no. 6917, p. 772–787, 2002.

[48] W. Hu and M. White, "A CMB polarization primer," *New Astronomy*, vol. 2, no. 4, pp. 323–344, 1997.

[49] Hamilton, J.-Ch., Charlassier, R., Cressiot, C., Kaplan, J., Piat, M., and Rosset, C., "Sensitivity of a bolometric interferometer to the cosmic microwave backgroud power spectrum," *AA*, vol. 491, no. 3, pp. 923–927, 2008.

[50] C. Kittel and H. Kroemer, *Thermal Physics*. W. H. Freeman, 1980.

[51] P. L. Richards, "Bolometers for infrared and millimeter waves," *Journal of Applied Physics*, vol. 76, no. 1, pp. 1–24, 1994.

[52] C. Perbost, *Matrices de bolomètres supraconducteurs pour la mesure de la polarisation du fond diffus cosmologique : application à l'expérience QUBIC*. PhD thesis, Université Paris Diderot, 2016.

[53] J. M. Lamarre, "Photon noise in photometric instruments at far-infrared and submillimeter wavelengths," *Appl. Opt.*, vol. 25, no. 6, pp. 870–876, 1986.

[54] J. Clarke and A. Braginski, *The SQUID Handbook: Fundamentals and Technology of SQUIDs and SQUID Systems*. Wiley, 2006.

[55] S. Kempf, A. Fleischmann, L. Gastaldo, and C. Enss, "Physics and Applications of Metallic Magnetic Calorimeters," *Journal of Low Temperature Physics*, vol. 193, no. 3, pp. 365–379, 2018.

[56] C. Enss, A. Fleischmann, K. Horst, J. Schönefeld, J. Sollner, J. Adams, Y. Huang, Y.-H. K. Kim, and G. Seidel, "Metallic Magnetic Calorimeters for Particle Detection," *Journal of Low Temperature Physics*, vol. 121, pp. 137–176, 2000.

[57] A. Fleischmann, C. Enss, and G. Seidel, *Metallic Magnetic Calorimeters*, pp. 151–216. Berlin, Heidelberg: Springer Berlin Heidelberg, 2005.

[58] N. E. Phillips, "Low-temperature heat capacity of metals," *C R C Critical Reviews in Solid State Sciences*, vol. 2, no. 4, pp. 467–553, 1971.

[59] S. Hanany, A. H. Jaffe, and E. Scannapieco, "The effect of the detector response time on bolometric cosmic microwave background anisotropy experiments," *Monthly Notices of the Royal Astronomical Society*, vol. 299, no. 3, pp. 653–660, 1998.

[60] J. C. Mather, "Bolometer noise: nonequilibrium theory," *Appl. Opt.*, vol. 21, no. 6, pp. 1125–1129, 1982.

[61] C. L. Kuo, J. J. Bock, G. Chattopadthyay, A. Goldin, S. Golwala, *et al.*, "Antenna-coupled TES bolometers for CMB polarimetry," in *Millimeter and Submillimeter Detectors and Instrumentation for Astronomy III* (J. Zmuidzinas, W. S. Holland, S. Withington, and W. D. Duncan, eds.), vol. 6275, p. 62751M, International Society for Optics and Photonics, SPIE, 2006.

[62] C. M. Posada, P. A. R. Ade, Z. Ahmed, Anderson, and others., "Fabrication of Detector Arrays for the SPT-3G Receiver," *Journal of Low Temperature Physics*, vol. 193, no. 5-6, pp. 703–711, 2018.

[63] S. Kempf, A. Ferring, A. Fleischmann, and C. Enss, "Direct-current superconducting quantum interference devices for the readout of metallic magnetic calorimeters," *Superconductor Science and Technology*, vol. 28, no. 4, p. 045008, 2015.

[64] K. D. Irwin, "Shannon Limits for Low-Temperature Detector Readout," *AIP Conference Proceedings*, vol. 1185, no. 1, pp. 229–236, 2009.

[65] H. Hui, P. A. R. Ade, Z. Ahmed, K. D. Alexander, M. Amiri, D. Barkats, Benton, and others., "BICEP3 focal plane design and detector performance," in *Millimeter, Submillimeter, and Far-Infrared Detectors and Instrumentation for Astronomy VIII* (W. S. Holland and J. Zmuidzinas, eds.), vol. 9914 of *Society of Photo-Optical Instrumentation Engineers (SPIE) Conference Series*, p. 99140T, 2016.

[66] M. A. Dobbs, M. Lueker, K. A. Aird, A. N. Bender, B. A. Benson, L. E. Bleem, and others., "Frequency multiplexed superconducting quantum interference device readout of large bolometer arrays for cosmic microwave background measurements," *Review of Scientific Instruments*, vol. 83, no. 7, p. 073113, 2012.

[67] J. W. Fowler, W. B. Doriese, G. Hilton, K. Irwin, D. Schmidt, G. Stiehl, D. Swetz, J. N. Ullom, and L. Vale, "Optimization and Analysis of Code-Division Multiplexed TES Microcalorimeters," *Journal of Low Temperature Physics*, vol. 167, no. 5-6, pp. 713–720, 2012.

[68] J. Zmuidzinas, "Superconducting Microresonators: Physics and Applications," *Annual Review of Condensed Matter Physics*, vol. 3, pp. 169–214, 2012.

[69] K. D. Irwin and K. W. Lehnert, "Microwave SQUID multiplexer," *Applied Physics Letters*, vol. 85, pp. 2107–2109, 2004.

[70] B. Dober, Z. Ahmed, and others., "A Microwave SQUID Multiplexer Optimized for Bolometric Applications," 2020.

[71] S. Kempf, M. Wegner, A. Fleischmann, L. Gastaldo, F. Herrmann, M. Papst, D. Richter, and C. Enss, "Demonstration of a scalable frequency-domain readout of metallic magnetic calorimeters by means of a microwave SQUID multiplexer," *AIP Advances*, vol. 7, no. 1, p. 015007, 2017.

[72] J. Gao, *The Physics of Superconducting Microwave Resonators*. PhD thesis, California Institute of Technology, 2008.

[73] S. Kempf, *Development of a microwave SQUID multiplexer based on non-hysteretic rf-SQUIDs for the readout of metallic magnetic calorimeters*. PhD thesis, Heidelberg University, 2012.

[74] M. Wegner, *Development, fabrication and characterization of a metallic magnetic calorimeter based 64 pixel detector array with integrated microwave SQUID multiplexer*. PhD thesis, Heidelberg University, 2018.

[75] C. Kittel, *Introduction to Solid State Physics, 7th Ed*. Wiley India Pvt. Limited, 2007.

[76] J. Bardeen, "Two-Fluid Model of Superconductivity," *Phys. Rev. Lett.*, vol. 1, pp. 399–400, 1958.

[77] J. Bardeen, L. N. Cooper, and J. R. Schrieffer, "Microscopic Theory of Superconductivity," *Phys. Rev.*, vol. 106, pp. 162–164, 1957.

[78] D. C. Mattis and J. Bardeen, "Theory of the Anomalous Skin Effect in Normal and Superconducting Metals," *Phys. Rev.*, vol. 111, pp. 412–417, 1958.

[79] R. Barends, *Photon-detecting superconducting resonators*. PhD thesis, Kavli Institute of NanoScience (AS) (TU Delft), 2009.

[80] R. Collin, *Foundations for Microwave Engineering*. IEEE Press series on electromagnetic wave theory, McGraw-Hill, 1992.

[81] M. Göppl, A. Fragner, M. Baur, R. Bianchetti, S. Filipp, J. M. Fink, P. J. Leek, G. Puebla, L. Steffen, and A. Wallraff, "Coplanar waveguide resonators for circuit quantum electrodynamics," *Journal of Applied Physics*, vol. 104, no. 11, p. 113904, 2008.

[82] D. Pozar, *Microwave Engineering*. Wiley, 2011.

[83] B. D. Josephson, "Possible new effects in superconductive tunnelling," *Physics Letters*, vol. 1, no. 7, pp. 251–253, 1962.

[84] B. D. Josephson, "Coupled Superconductors," *Rev. Mod. Phys.*, vol. 36, pp. 216–220, 1964.

[85] S. M. Anlage, "Microwave Superconductivity," *IEEE Journal of Microwaves*, vol. 1, no. 1, pp. 389–402, 2021.

[86] S. Kempf, A. Ferring, A. Fleischmann, L. Gastaldo, and C. Enss, "Characterization of the reliability and uniformity of an anodization-free fabrication process for high-quality Nb/Al–AlOx/Nb Josephson junctions," *Superconductor Science and Technology*, vol. 26, no. 6, p. 065012, 2013.

[87] J. A. B. Mates, K. D. Irwin, L. R. Vale, G. C. Hilton, J. Gao, and K. W. Lehnert, "Flux-Ramp Modulation for SQUID Multiplexing," *Journal of Low Temperature Physics*, vol. 167, pp. 707–712, 2012.

[88] M. Wegner, C. Enss, and S. Kempf, "Analytical model of the readout power and SQUID hysteresis parameter dependence of the resonator characteristics of microwave SQUID multiplexers," *Superconductor Science and Technology*, vol. 35, no. 7, p. 075011, 2022.

[89] M. Abramowitz and I. Stegun, *Handbook of Mathematical Functions: With Formulas, Graphs, and Mathematical Tables*. Applied mathematics series, Dover Publications, 1965.

[90] F. K. Ahrens, *Cryogenic read-out system and resonator optimisation for the microwave SQUID multiplexer within the ECHo experiment*. PhD thesis, Heidelberg University, 2022.

[91] S. Probst, F. Song, P. Bushev, A. Ustinov, and M. Weides, "Efficient and robust analysis of complex scattering data under noise in microwave resonators," *The Review of scientific instruments*, vol. 86, 2014.

[92] C. Schuster, M. Wegner, and S. Kempf, "Simulation framework for microwave SQUID multiplexer optimization," *Journal of Applied Physics*, vol. 133, no. 4, p. 044503, 2023.

[93] Sebastian Kempf and Mathias Wegner and Andreas Fleischmann and Loredana Gastaldo and Felix Herrmann and Maximilian Papst and Daniel Richter and Christian Enss, "Demonstration of a scalable frequency-domain readout of metallic magnetic calorimeters by means of a microwave squid multiplexer," *AIP Advances*, vol. 7, p. 015007, 2017.

[94] J. A. B. Mates, D. T. Becker, D. A. Bennett, B. J. Dober, J. D. Gard, G. C. Hilton, D. S. Swetz, L. R. Vale, and J. N. Ullom, "Crosstalk in microwave SQUID multiplexers," *Applied Physics Letters*, vol. 115, no. 20, p. 202601, 2019.

[95] X. Liu, W. Guo, Y. Wang, M. Dai, L. F. Wei, Dober, *et al.*, "Superconducting microresonator arrays with ideal frequency spacing," *Applied Physics Letters*, vol. 111, no. 25, p. 252601, 2017.

[96] M. S. Rao, M. Silva-Feaver, A. Ali, K. Arnold, P. Ashton, B. J. Dober, and others., "Simons Observatory Microwave SQUID Multiplexing Readout – Cryogenic RF Amplifier and Coaxial Chain Design," *Journal of Low Temperature Physics*, vol. 199, pp. 807–816, 2020.

[97] C. Yu, Z. Ahmed, J. M. D'Ewart, J. C. Frisch, S. W. Henderson, and M. Silva-Feaver, "A simulation suite for readout with SMuRF tone-tracking electronics," in *Millimeter, Submillimeter, and Far-Infrared Detectors and Instrumentation for Astronomy XI* (J. Zmuidzinas and J.-R. Gao, eds.), vol. 12190, p. 121900V, International Society for Optics and Photonics, SPIE, 2022.

[98] J. van Rantwijk, M. Grim, D. van Loon, S. Yates, and others., "Multiplexed Readout for 1000-Pixel Arrays of Microwave Kinetic Inductance Detectors," *IEEE Transactions on Microwave Theory and Techniques*, vol. 64, no. 6, pp. 1876–1883, 2016.

[99] J. Herrmann and others., "Frequency Up-Conversion Schemes for Controlling Superconducting Qubits," 2022.

[100] C. Ding *et al.*, "Experimental advances with the QICK (Quantum Instrumentation Control Kit) for superconducting quantum hardware," *Phys. Rev. Res.*, vol. 6, p. 013305, 2024.

[101] M. E. García Redondo, N. A. Müller, J. M. Salum, L. P. Ferreyro, J. D. Bonilla-Neira, J. M. Geria, J. J. Bonaparte, T. Muscheid, R. Gartmann, A. Almela, M. R. Hampel, A. E. Fuster, L. E. Ardila-Perez, M. Wegner, M. Platino, O. Sander, S. Kempf, and M. Weber, "Optimal demodulation domain for microwave SQUID multiplexers in presence of readout system noise," *Journal of Applied Physics*, vol. 136, no. 11, p. 114401, 2024.

[102] M. Malnou, J. A. B. Mates, M. R. Vissers, L. R. Vale, D. R. Schmidt, D. A. Bennett, J. Gao, and J. N. Ullom, "Improved microwave SQUID multiplexer readout using a kinetic-inductance traveling-wave parametric amplifier," *Applied Physics Letters*, vol. 122, no. 21, p. 214001, 2023.

[103] M. Sathyanarayana Rao and others., "Simons Observatory Microwave SQUID Multiplexing Readout - Cryogenic RF Amplifier and Coaxial Chain Design," *J. Low. Temp. Phys.*, vol. 199, no. 3-4, pp. 807–816, 2020.

[104] N. Zobrist, B. H. Eom, P. Day, B. A. Mazin, S. R. Meeker, B. Bumble, H. G. LeDuc, G. Coiffard, P. Szypryt, N. Fruitwala, I. Lipartito, and C. Bockstiegel, "Wide-band parametric amplifier readout and resolution of optical microwave kinetic inductance detectors," *Applied Physics Letters*, vol. 115, no. 4, p. 042601, 2019.

[105] M. E. G. Redondo, T. Muscheid, R. Gartmann, J. M. Salum, and others., "RFSoC Gen3-Based Software-Defined Radio Characterization for the Readout System of Low-Temperature Bolometers," 2023.

[106] J. M. Salum, M. E. García Redondo, L. P. Ferreyro, Bonilla-Neira, and others., "Spectral Engineering for Optimal Signal Performance in the Microwave SQUID Multiplexer," *Journal of Low Temperature Physics*, vol. 214, 2024.

[107] E. Rubiola, *Phase Noise and Frequency Stability in Oscillators*. The Cambridge RF and Microwave Engineering Series, Cambridge University Press, 2008.

[108] Rohde & Schwarz GmbH & Co. KG, *White paper: Understanding phase noise measurement techniques*, 2021.

[109] Rohde & Schwarz GmbH & Co. KG, *White paper: Understanding phase noise fundamentals*, 2021. Version 01.01.

[110] J. Gao, B. A. Mazin, P. K. Day, J. Zmuidzinas, and H. G. LeDuc, "Noise Properties of Superconducting Coplanar Waveguide Microwave Resonators," 2006.

[111] S. Kumar and others., "Temperature dependence of the frequency and noise of superconducting coplanar waveguide resonators," *Applied Physics Letters*, vol. 92, p. 123503, 03 2008.

[112] A. Papoulis and S. Pillai, *Probability, Random Variables, and Stochastic Processes*. International student edition, McGraw-Hill, 2002.

[113] AMD, "ZCU216 Evaluation Board User Guide (UG1390)," 2022.

[114] J. D. Gard, D. T. Becker, D. A. Bennett, J. W. Fowler, G. C. Hilton, J. A. B. Mates, C. D. Reintsema, D. R. Schmidt, D. S. Swetz, and J. N. Ullom, "A Scalable Readout for Microwave SQUID Multiplexing of Transition-Edge Sensors," *Journal of Low Temperature Physics*, vol. 193, pp. 485–497, 11 2018.

[115] D. Becker, D. Bennett, M. Biasotti, M. Borghesi, *et al.*, "Working principle and demonstrator of microwave-multiplexing for the HOLMES experiment microcalorimeters," *Journal of Instrumentation*, vol. 14, no. 10, p. P10035, 2019.

[116] N. Karcher, T. Muscheid, T. Wolber, D. Richter, C. Enss, S. Kempf, and O. Sander, "Online Demodulation and Trigger for Flux-ramp Modulated SQUID Signals," *Journal of Low Temperature Physics*, vol. 209, pp. 581–588, 2022.

[117] J. M. Salum, T. Muscheid, A. Fuster, M. E. Garcia Redondo, and others., "Aliasing Effect on Flux Ramp Demodulation: Nonlinearity in the Microwave Squid Multiplexer," *Journal of Low Temperature Physics*, vol. 213, p. 223–236, 2023. 54.12.02; LK 01.

[118] L. P. Ferreyro, M. G. Redondo, M. R. Hampel, A. Almela, A. Fuster, J. Salum, J. M. Geria, J. Bonaparte, J. Bonilla-Neira, N. Müller, N. Karcher, O. Sander, M. Platino, and A. Etchegoyen, "An Implementation of a Channelizer based on a Goertzel Filter Bank for the Read-Out of Cryogenic Sensors," 2023.

[119] P. Welch, "The use of fast Fourier transform for the estimation of power spectra: A method based on time averaging over short, modified periodograms," *IEEE Trans. Audio Electroacoust.*, vol. 15, no. 2, pp. 70–73, 1967.

[120] C. M. Caves, "Quantum limits on noise in linear amplifiers," *Phys. Rev. D*, vol. 26, pp. 1817–1839, 1982.

[121] M. Silva-Feaver, Z. Ahmed, and others., "Phase Drift Monitoring for Tone Tracking Readout of Superconducting Microwave Resonators," 2022.

[122] Oxford Instruments, *Principles of dilution refrigeration: A brief Technology Guide*, 2015.

[123] F. Pobell, *Matter and Methods at Low Temperatures*. Springer-Verlag, 1996.

[124] G. White, *Experimental Techniques in Low-temperature Physics*. Monographs on the physics and chemistry of materials, Clarendon Press, 1987.

[125] S. Krinner, S. Storz, P. Kurpiers, P. Magnard, J. Heinsoo, R. Keller, J. Luetolf, C. Eichler, and A. Wallraff, "Engineering cryogenic setups for 100-qubit scale superconducting circuit systems," *EPJ Quantum Technology*, vol. 6, pp. 1–29, 2018.

[126] Coax Co., LTD., *Semi-Rigid Coaxial Cable CouplerLine Catalog*, 2018.

[127] L. N. Factory, "LNF-LNC4-8C," 2012.

[128] H. Friis, "Noise Figures of Radio Receivers," *Proceedings of the IRE*, vol. 32, no. 7, pp. 419–422, 1944.

[129] H. B. Callen and T. A. Welton, "Irreversibility and Generalized Noise," *Phys. Rev.*, vol. 83, pp. 34–40, 1951.

[130] Keysight Technologies, Inc., *Keysight 2-Port and 4-Port PNA-X Network Analyzer*, 2024.

[131] Keysight Technologies, Inc., *High-Accuracy Noise Figure Measurements Using the PNA-X Series Network Analyzer*, 2024.

[132] Keysight Technologies, Inc., *Making Accurate Intermodulation Distortion Measurements with the PNA-X Network Analyzer, 10 MHz to 26.5 GHz*, 2024.

[133] S. W. Henderson, Z. Ahmed, J. Austermann, D. Becker, D. A., and others., "Highly-multiplexed microwave SQUID readout using the SLAC Microresonator Radio Frequency (SMuRF) electronics for future CMB and sub-millimeter surveys," in *Millimeter, Submillimeter, and Far-Infrared Detectors and Instrumentation for Astronomy IX* (J. Zmuidzinas and J.-R. Gao, eds.), vol. 10708, p. 1070819, International Society for Optics and Photonics, SPIE, 2018.

[134] H. S. H. J. M. J. A. B. S.-F. M. U. J. Y. C. Groh John C., Ahmed Zeeshan, "Crosstalk effects in microwave SQUID multiplexed TES bolometer readout," *Journal of Low Temperature Physics*, vol. 216, no. 225, p. 236, 2024.

[135] C. Yu, Z. Ahmed, J. C. Frisch, and others., "SLAC microresonator RF (SMuRF) electronics: A tone-tracking readout system for superconducting microwave resonator arrays," *Review of Scientific Instruments*, vol. 94, no. 1, p. 014712, 2023.

[136] S. S. Haykin, *Communication systems, 4th ed*. Wiley India Pvt. Limited, 2006.

[137] C. Mack, "The Multiple Lives of Moore's Law," *IEEE Spectrum*, vol. 52, no. 4, pp. 31–31, 2015.

[138] A. Wyglinski, R. Getz, T. Collins, and D. Pu, *Software-Defined Radio for Engineers*. Artech House mobile communications series, Artech House, 2018.

[139] O. Sander, N. Karcher, O. Krömer, S. Kempf, M. Wegner, C. Enss, and M. Weber, "Software-Defined Radio Readout System for the ECHo Experiment," *IEEE Transactions on Nuclear Science*, vol. 66, no. 7, pp. 1204–1209, 2019.

[140] J. P. Smith, I. Bailey, John I., A. Cuda, N. Zobrist, and B. A. Mazin, "MKIDGen3: Energy-resolving, single-photon-counting microwave kinetic inductance detector readout on a radio frequency system-on-chip," *Review of Scientific Instruments*, vol. 95, no. 11, p. 114705, 2024.

[141] L. Crockett, D. Northcote, and R. Stewart, *Software Defined Radio with Zynq Ultrascale+ RFSoC*. Strathclyde Academic Media, 2023.

[142] Analog Devices, Inc., *JESD204B Survival Guide*, 2013.

[143] D. Mayhew and V. Krishnan, "PCI express and advanced switching: evolutionary path to building next generation interconnects," in *11th Symposium on High Performance Interconnects, 2003. Proceedings.*, pp. 21–29, 2003.

[144] L. Crockett, R. Elliot, M. Enderwitz, and R. Stewart, *The Zynq Book: Embedded Processing Withe ARM® Cortex®-A9 on the Xilinx® Zynq®-7000 All Programmable SoC*. Strathclyde Academic Media, 2014.

[145] AMD, *Zynq UltraScale+ MPSoC Data Sheet: Overview*, 2022.

[146] AMD, *Zynq UltraScale+ RFSoC RF Data Converter v2.6 Gen 1/2/3/DFE LogiCORE IP Product Guide (PG269)*, 2023.

[147] AMD, *CLK104 RF Clock Add-on Card User Guide (UG1437)*, 2022.

[148] T. Muscheid, R. Gartmann, N. Karcher, F. Schuderer, M. Neidig, M. Balzer, L. E. Ardila-Perez, S. Kempf, and O. Sander, "Full-Scale Readout Electronics for the ECHo Experiment," *Journal of Low Temperature Physics*, vol. 217, no. 3-4, p. 456–463, 2024.

[149] N. Karcher, D. Richter, F. Ahrens, R. Gartmann, M. Wegner, O. Krömer, S. Kempf, C. Enss, M. Weber, and O. Sander, "SDR-Based Readout Electronics for the ECHo Experiment," *Journal of Low Temperature Physics*, vol. 200, pp. 261–268, 2020.

[150] T. Muscheid, A. Boebel, N. Karcher, T. Vanat, L. Ardila-Perez, I. Cheviakov, M. Schleicher, M. Zimmer, M. Balzer, and O. Sander, "DTS-100G — a versatile heterogeneous MPSoC board for cryogenic sensor readout," *Journal of Instrumentation*, vol. 18, no. 02, p. C02067, 2023.

[151] Y. Shibasaki, K. Asami, R. Aoki, A. Hatta, A. Kuwana, and H. Kobayashi, "Analysis and Design of Multi-Tone Signal Generation Algorithms for Reducing Crest Factor," in *2020 IEEE 29th Asian Test Symposium (ATS)*, pp. 1–6, 2020.

[152] N. Karcher, *Ausleseelektronik für magnetische Mikrokalorimeter im Frequenzmultiplexverfahren*. PhD thesis, Karlsruher Institut für Technologie (KIT), 2022.

[153] F. Harris, C. Dick, and M. Rice, "Digital receivers and transmitters using polyphase filter banks for wireless communications," *IEEE Transactions on Microwave Theory and Techniques*, vol. 51, no. 4, pp. 1395–1412, 2003.

[154] J. Proakis and D. Manolakis, *Digital Signal Processing: Principles, Algorithms, and Applications*. Prentice-Hall International editions, Prentice Hall, 1996.

[155] Advanced Micro Devices, Inc., *FIR Compiler v7.2 LogiCORE IP Product Guide*, 2022.

[156] Advanced Micro Devices, Inc., *Fast Fourier Transform v9.1 LogiCORE IP Product Guide*, 2022.

[157] B. Jovanovic and S. Milenkovic, "IQ Imbalance Correction in Wideband Software Defined Radio Transceivers," *Radioengineering*, vol. 32, pp. 479–491, 2023.

[158] J. Tubbax, B. Côme, L. Van Der Perre, S. Donnay, and M. Engels, "Joint compensation of iq imbalance, frequency offset and phase noise," in *Multi-Carrier Spread-Spectrum* (K. Fazel and S. Kaiser, eds.), (Dordrecht), pp. 473–480, Springer Netherlands, 2004.

[159] P. A. Z. A. Kevork N. Abazajian, Graeme Addison and others., "CMB-S4 Science Case, Reference Design, and Project Plan," 2019.

[160] S. R. Systems, *FS725 — Benchtop rubidium frequency standard*.

[161] N. Karcher, R. Gebauer, R. Bauknecht, R. Illichmann, and O. Sander, "Versatile Configuration and Control Framework for Real-Time Data Acquisition Systems," *IEEE Transactions on Nuclear Science*, vol. 68, no. 8, pp. 1899–1906, 2021.

[162] R. Gartmann, N. Karcher, R. Gebauer, O. Krömer, and O. Sander, "Progress of the ECHo SDR Readout Hardware for Multiplexed MMCs," *Journal of Low Temperature Physics*, vol. 209, pp. 726–733, 2022.

[163] L. Stefanazzi, K. Treptow, N. Wilcer, C. Stoughton, C. Bradford, S. Uemura, S. Zorzetti, S. Montella, G. Cancelo, S. Sussman, A. Houck, S. Saxena, H. Arnaldi, A. Agrawal, H. Zhang, C. Ding, and D. I. Schuster, "The QICK (Quantum Instrumentation Control Kit): Readout and control for qubits and detectors," *Review of Scientific Instruments*, vol. 93, no. 4, p. 044709, 2022.

[164] W. D. Kalfus, D. F. Lee, G. J. Ribeill, S. D. Fallek, A. Wagner, B. Donovan, D. Ristè, and T. A. Ohki, "High-Fidelity Control of Superconducting Qubits Using Direct Microwave Synthesis in Higher Nyquist Zones," *IEEE Transactions on Quantum Engineering*, vol. 1, pp. 1–12, 2020.

[165] C. Liu, Z. Ahmed, S. W. Henderson, R. Herbst, L. Ruckman, and T. Satterthwaite, "Development of RFSoC-based direct sampling highly multiplexed microwave SQUID readout for future CMB and submillimeter surveys," 2024.

[166] Rohde & Schwarz GmbH & Co. KG, *RS®FSWP PHASE NOISE ANALYZER AND VCO TESTER Specifications*, 2024. Version 06.00.

[167] C. Liu, Z. Ahmed, S. W. Henderson, R. Herbst, and L. Ruckman, "Higher Order Nyquist Zone Sampling with RFSoC Data Converters for Astronomical and High Energy Physics Readout Systems," 2023.

[168] Keysight Technologies, *CXA X-Series Signal Analyzer N9000A*, 2018. 9 kHz to 7.5 GHz Version.

[169] L. Ferreyro, *Back-end Design of the Readout System for Cryogenic Particle Detectors*. PhD thesis, Karlsruher Institut für Technologie (KIT), 2024.

[170] Analog Devices Inc., *Correcting Imperfections in IQ Modulators to Improve RF Signal Fidelity*, 2009. AN-1039 APPLICATION NOTE.

[171] Analog Devices Ic., *Analyzing and Managing the Impact of Supply Noise and Clock Jitter on High Speed DAC Phase Noise*, 2017. Analog Dialogue 51-03.

[172] K. D. Crowley, R. A. McLellan, A. Dutta, N. Shumiya, A. P. M. Place, X. H. Le, Y. Gang, T. Madhavan, M. P. Bland, R. Chang, N. Khedkar, Y. C. Feng, E. A. Umbarkar, X. Gui, L. V. H. Rodgers, Y. Jia, M. M. Feldman, S. A. Lyon, M. Liu, R. J. Cava, A. A. Houck, and N. P. de Leon, "Disentangling Losses in Tantalum Superconducting Circuits," *Phys. Rev. X*, vol. 13, p. 041005, 2023.

[173] M. C. de Ory, V. Rollano, D. Rodriguez, M. T. Magaz, D. Granados, and A. Gomez, "Low loss hybrid Nb/Au superconducting resonators for quantum circuit applications," 2024.

[174] R. Kalra, A. Laucht, J. P. Dehollain, D. Bar, S. Freer, S. Simmons, J. T. Muhonen, and A. Morello, "Vibration-induced electrical noise in a cryogen-free dilution refrigerator: Characterization, mitigation, and impact on qubit coherence," *Review of Scientific Instruments*, vol. 87, no. 7, p. 073905, 2016.

[175] J. Gao, J. Zmuidzinas, B. A. Mazin, H. G. LeDuc, and P. K. Day, "Noise properties of superconducting coplanar waveguide microwave resonators," *Applied Physics Letters*, vol. 90, no. 10, p. 102507, 2007.

[176] M. Hampel, A. Almela, J. Bonaparte, J. B. Neira, L. Ferreyro, A. Fuster, M. G. Redondo, R. Gartmann, J. Geria, N. Müller, T. Muscheid, J. Salum, M. Platino, L. Ardila, O. Sander, M. Wegner, S. Kempf, M. Weber, and A. Etchegoyen, "The Magnetic Microbolometer: A Proposal for QUBIC Next Gen," *Journal of Low Temperature Physics*, vol. 217, no. 3, pp. 401–408, 2024.

[177] M. Platino, M. E. García Redondo, L. P. Ferreyro, J. M. Salum, N. A. Müller, J. D. Bonilla-Neira, T. Muscheid, R. Gartmann, J. M. Geria, J. J. Bonaparte, D. A. Almela, L. E. Ardila-Pérez, M. R. Hampel, A. E. Fuster, O. Sander, M. Weber, and A. Etchegoyen, "The Magnetic Microbolometer Detection Chain: A Proposed Detection System to Observe the B Modes of the Cosmic Microwave Background," *Journal of Low Temperature Physics*, vol. 217, no. 5, pp. 762–771, 2024.

[178] J. Geria, A. Almela, J. Bonaparte, J. Bonilla-Neira, L. Ferreyro, A. Fuster, M. García Redondo, M. Hampel, N. Müller, M. Platino, J. Salum, S. Kempf, M. Weber, and A. Etchegoyen, "Antenna-Coupled Magnetic Microbolometers for CMB Polarization Surveys," *Journal of Low Temperature Physics*, vol. 217, no. 3, pp. 472–480, 2024.

[179] R. Gartmann, T. Muscheid, M. G. Redondo, M. Fuchs, L. Ardila-Perez, and O. Sander, "Evaluating the RFSoC as a Software-Defined Radio readout system for Magnetic Microcalorimeters," *Journal of Instrumentation*, vol. 19, no. 02, p. C02078, 2024.

[180] AMD, *AMD VERSAL™ RF SERIES Wideband Spectrum, Massive DSP Compute, Single Chip. Product Brief*, 2024.

[181] Intel, *Altera® Direct RF-Series FPGAs Product Brief*, 2023.

[182] L. P. Ferreyro, M. E. García Redondo, J. M. Salum, T. Muscheid, M. Hampel, A. Almela, A. Fuster, J. M. Geria, J. Bonaparte, J. Bonilla-Neira, L. E. Ardila-Perez, R. Gartmann, N. Müller, M. Wegner, O. Sander, M. Platino, S. Kempf, A. Etchegoyen, and M. Weber, "Advances in the Goertzel Filter Bank Channelizer for Cryogenic Sensors Readout," *Journal of Low Temperature Physics*, vol. 217, no. 3, pp. 409–417, 2024.

[183] U. Singhal, S. Kalipatnapu, P. K. Gautam, S. Majumder, V. V. L. Pabbisetty, S. Jandhyala, V. Singh, and C. S. Thakur, "SQ-CARS: A Scalable Quantum Control and Readout System," *IEEE Transactions on Instrumentation and Measurement*, vol. 72, pp. 1–15, 2023.

[184] K. H. Park, Y. S. Yap, Y. P. Tan, C. Hufnagel, L. H. Nguyen, K. H. Lau, P. Bore, S. Efthymiou, S. Carrazza, R. P. Budoyo, and R. Dumke, "ICARUS-Q: Integrated control and readout unit for scalable quantum processors," *Review of Scientific Instruments*, vol. 93, no. 10, p. 104704, 2022.

[185] AMD, *Zynq UltraScale+ RFSoC Data Sheet: DC and AC Switching Characteristics (DS926)*, 2023.

[186] Rohde & Schwarz GmbH & Co. KG, *RS®SMA100B RF AND MICROWAVE SIGNAL GENERATOR Specifications*, 2024. Version 08.01.

[187] Analog Devices Ic., *ADC Input Noise: The Good, The Bad, and The Ugly. Is No Noise Good Noise?*, 2004. Vol 40.

[188] T. Instruments, *PLLatinum Simulator Tool*.

[189] A. Hajimiri, "Noise in phase-locked loops," in *2001 Southwest Symposium on Mixed-Signal Design (Cat. No.01EX475)*, pp. 1–6, 2001.

[190] A. Hajimiri and T. Lee, "A general theory of phase noise in electrical oscillators," *IEEE Journal of Solid-State Circuits*, vol. 33, no. 2, pp. 179–194, 1998.

List of Publications

- **Geria J.M. et al.**, "*Suitability of magnetic microbolometers based on paramagnetic temperature sensors for CMB polarization measurements.*", JATIS, 2023, DOI:10.1117/1.JATIS.9.1.016002.
- **Ferreyro L. P., García Redondo M.E. et al.**, "*An Implementation of a Channelizer based on a Goertzel Filter Bank for the Read-Out of Cryogenic Sensors.*", JINST, 2023, DOI:10.1088/1748-0221/18/06/P06009.
- **Salum J. M. et al.**, "*Aliasing Effect on Flux Ramp Demodulation: Nonlinearity in the Microwave SQUID Multiplexer.*", Journal of Low Temperature Physics, 2023, DOI:10.1007/s10909-023-02993-z.
- **Salum, J.M., García Redondo M.E., Ferreyro, L.P. et al.**, "*Spectral Engineering for Optimal Signal Performance in the Microwave SQUID Multiplexer*", Journal of Low Temperature Physics 217, 272–279 (2024), DOI:10.1007/s10909-024-03049-6.
- **García Redondo M.E. et al.**, "*RFSoC Gen3-Based Software-Defined Radio Characterization for the Readout System of Low-Temperature Bolometers.*", Journal of Low Temperature Physics 217, 2024, DOI:10.1007/s10909-024-03079-0.
- **Gartmann R., Muscheid T., García Redondo M.E. et al.**, "*Evaluating the RFSoC as a Software-Defined Radio readout system for Magnetic Microcalorimeters.*", Journal of Instrumentation, 2024, DOI:10.1088/1748-0221/19/02/C02078.
- **García Redondo M.E. et al.**, "*Optimal Demodulation Domain for Microwave SQUID Multiplexers in Presence of Readout System Noise.*", Journal Applied Physics, 2024, 10.1063/5.0222656.
- **Geria J.M. et al.**, "*Antenna-Coupled Magnetic Microbolometers for CMB Polarization Surveys.*", Journal of Low Temperature Physics 217, 472–480, 2024, DOI:10.1007/s10909-024-03217.
- **Hampel M. R. et al.**, "*The Magnetic Microbolometer: A Proposal for QUBIC Next Gen.*", Journal of Low Temperature Physics 217, 401–408, 2024, DOI:10.1007/s10909-024-03203-0.
- **Ferreyro, L.P., García Redondo M.E., Salum, J.M. et al.**, "*Advances in the Goertzel Filter Bank Channelizer for Cryogenic Sensors Readout.*", Journal of Low Temperature Physics 217, 409–417, 2024, DOI:10.1007/s10909-024-03204-z.
- **Platino, M., García Redondo M.E., Ferreyro, L.P. et al.**, "*The Magnetic Microbolometer Detection Chain: A Proposed Detection System to Observe the B Modes of the Cosmic Microwave Background.*", Journal of Low Temperature Physics 217, 762–771, 2024, DOI:10.1007/s10909-024-03230-x.

List of Figures

List of Tables

List of Abbreviations

ADC Analog-to-Digital Converter

API Application Programming Interface

APU Application Processor

ASIC Application-Specific Integrated Circuit

AWG Arbitrary Waveform Generator

BLIP Background Limited Performance

BRAM Block RAM

CDM Code-Division Multiplexing

CLB Configurable Logic Block

CMB Cosmic Microwave Background

CORDIC Coordinate Rotation Digital Computer

CSU Configuration Security Unit

DAC Digital-to-Analog Converter

DDC Digital Downconversion

DDS Direct Digital Synthesis

DESY Deutsches Elektronen Synchrotron

DFT Discrete Fourier Transform

DMA Direct Memory Access

DSP Digital Signal Processing

ECHo Electron Capture in Holmium-163

FDM Frequency-Division Multiplexing

FF Flip-Flops

FFT Fast Fourier Transform

FIFO First-In-First-Out

FIR Finite Impulse Response

FLL Flux-Locked Loop

FMC FPGA Mezzanine Card

FPGA Field-Programmable Gate Array

FWHM Full Width Half Maximum

GPIO General-Purpose Input/Output

GUI Graphical User Interface

I2C Inter-Integrated Circuit Bus

IMS Institute of Micro- and Nanoelectronic Systems

IPE Institute for Data Processing and Electronics

ITeDA Instituto de Tecnologías en Detección y Astropartículas

KIT Karlsruhe Institute of Technology

LO Local Oscillator

LUT Look-Up Table

LVDS Low-Voltage Differential Signaling

MKID Microwave Kinetic Inductance Detector

NCO Numerically Controlled Oscillator

NEP Noise Equivalent Power

NET Noise Equivalent Temperature

NSD Noise Spectral Density

PIMC Platform Information and Management Core

PL Programmable Logic

PLL Phase-Locked Loop

PMU Platform Management Unit

PS Processing System

QUBIC Q & U Bolometric Interferometer for Cosmology

RFDC Radio-Frequency Data Converter

RFSoC Radio-Frequency System on Chip

RPC Remote Procedure Call

RPU Real-Time Processor

SDR Software-Defined Radio

SFDR Spurious-Free Dynamic Range

SNR Signal-to-Noise Ratio

SoC System-on-Chip

SPI Serial Peripheral Interface

SQUID Superconducting Quantum Interference Device

TDM Time-Division Multiplexing

TES Transition Edge Sensor

VCXO Voltage-Controlled Crystal Oscillator

VCO Voltage-Controlled Oscillator

VNA Vector Network Analyzer

TCXO Temperature-Compensated Voltage-Controlled Crystal Oscillator

TLS Two-Level Systems

uMUX Microwave SQUID Multiplexer